2013

Photometric variability of X-ray sources in the galactic bulge

Christopher Tillman Britt
Louisiana State University and Agricultural and Mechanical College

Recommended Citation

Britt, Christopher Tillman, "Photometric variability of X-ray sources in the galactic bulge" (2013). *LSU Doctoral Dissertations*. 1079.
https://digitalcommons.lsu.edu/gradschool_dissertations/1079

PHOTOMETRIC VARIABILITY OF X-RAY SOURCES IN THE GALACTIC BULGE

A Dissertation

Submitted to the Graduate Faculty of the
Louisiana State University and
Agricultural and Mechanical College
in partial fulfillment of the
requirements for the degree of
Doctor of Philosophy

in

The Department of Physics and Astronomy

by
Christopher T. Britt
B.S., Louisiana State University, 2008
M.S., Louisiana State University, 2012
December 2013

To my family, past, present, and future.

Acknowledgements

This work was enabled by the incredible support of my family and friends. There are too many people who helped to put me on the path I now find myself to name them all individually, but I would like to give special acknowledgement to my grandfather Arthur deVries, affectionately called Doc, who constantly showed the importance of keeping a sharp mind and sense of humor; my parents, David and Viola Britt, who encouraged science learning and provided my first view of the planets through a small 2 inch refractor; my aunt, Lorinda deVries, for humoring my many requests to visit the science museum growing up until she could probably have recreated the exhibits herself from memory; my brother, Jeb, for many discussions growing up; my many teachers at Brandeis Elementary and beyond who challenged me and provided a chance to explore the scientic method; my friends Andrew, James, DT, and many others for refining nerdery beyond the usual social limits, and my many comrades-in-arms in the trenches of graduate school.

I would like to thank my advisor, Rob Hynes, who struck an excellent balance between letting me figure things out own my own and making my own mistakes and with offering his aid and guidance when it was needed. I would like to thank my collaborators Peter Jonker, Manuel Torres, and Tom Maccorone for their many comments and suggestions on papers and questions of interpretation. I would also like to thank my committee for their support.

I give special thanks to my wife, Bonnie, whose support and understanding of late nights I greatly appreciate. I have been out of the country on observing trips for 2 out of our 5 anniversaries, and worked through the most recent one preparing this document. Her support has enabled the completion of this work more than any other, even though it has meant that she has had to take care of more than her share of putting the house on the market and preparing for moving. She has sacrificed to allow me to finish this work, and it is greatly appreciated.

This work was supported by the National Science Foundation under Grant No. AST-0908789, the Louisiana State Board of Regents Fellowship, the Louisiana Space Consortium

Graduate Student Research Assistanceship, and by NASA/Louisiana Board of Regents grant NNX07AT62A/LEQSF(2007-10) Phase3-02. Dissemination of these results was aided by the LSU Graduate School Coates Conference Travel Award.

Table of Contents

List of Tables

List of Figures

Abstract

The Chandra Galactic Bulge Survey (GBS) undertakes to find and classify X-ray sources in the Galactic Bulge. Of these X-ray sources, there is likely a significant minority which are Low Mass X-ray Binaries: systems containing either a neutron star or black hole that is accreting matter from a roughly stellar mass companion via Roche-Lobe overflow. I use optical time-series photometry from the Mosaic-II instrument on the Blanco 4m telescope at the Cerro Tololo Inter-American Observatory to identify counterparts to new X-ray sources in the GBS. Of those that are variable in brightness, I use the morphology of the changes and the relative proportion of optical and X-ray light, to identify high inclination systems through eclipses, to determine what periodicity, if any, is present in the optical light, and use these properties to partially or fully classify X-ray sources. The GBS contains a variety of X-ray sources, including Low Mass X-ray Binaries, Cataclysmic Variables, Intermediate Polars, Active Galactic Nuclei, W Ursa Majoris stars, RS Canum Venaticorum stars, active stars, and flare stars. Spectroscopy greatly aids the classification of the X-ray source and is used, where available, to distinguish between source types and identify promising objects for further study. Only a handful of sources are identified as potential new Low Mass X-ray Binaries in quiescence, which places limits on the number of such systems in the Galaxy and on their outburst duty cycle.

In addition to the GBS, I have done work on echo-tomography of Scorpius X-1, the brightest extra-solar X-ray source in the sky. I have found that reprocessing is dominated by the accretion disk in all observations, and that the companion is not reliably distinguishable in reprocessing of continuum light. I also found that reprocessing mainly occurs in the Flaring Branch of the Z-diagram, turning off in other X-ray states.

1. Introduction

In this chapter, I will discuss the background of the science topics comprising my work, beginning broadly with the life of a star and binary evolution. I will then focus more on the particular science questions addressed by my work and previous attempts to answer them before moving on to the outline of the projects I have undertaken. There is an explanation of common astronomy terms and units at the end of this chapter in Section 1.10, covering the magnitude system and distance units like the parsec, broadband filters, colors, and reddening.

1.1 Basics of Binary Evolution

1.1.1 Single Star Evolution

Stars are born when they start fusing hydrogen in their cores. As long as this core hydrogen burning continues, the star is said to be on the Main Sequence. Massive stars evolve off of the main sequence quickly, on a timescale of only a million years. By comparison, stars like the Sun take 10 billion years to evolve off the main sequence. The least massive stars take much more time to finish burning hydrogen in their cores than the universe has existed. After hydrogen core burning, stars continue burning hydrogen in a shell around a helium core. The star then begins to swell and leave the Main Sequence to follow the Red Giant Branch (RGB). Eventually, enough helium is produced to ignite helium burning in the core, until it, too, is depleted followed by shell helium burning when the star enters the Asymptotic Giant Branch (AGB). Lighter stars finish life by being unable to fuse carbon, nitrogen, and oxygen in their cores, blowing off the outer layers in a planetary nebula, and becoming White Dwarfs (WD). The heaviest stars ($\gtrsim 8$ Solar Masses) will continue piling up the ash of the previous fusion reactions in their cores, then igniting them, until they reach iron. Fusing iron loses energy, so stars cannot burn it and survive. When enough iron has accumulated in the core, the star's core collapses and a supernova begins. As a crude guide, intermediate mass star supernovae leave neutron stars (NS) behind while more massive stars result in a black hole (BH) (Tauris & van den Heuvel, 2006).

White dwarfs are composed primarily of either helium or carbon and oxygen. They are deficient in hydrogen, being the remnant of the old core of the star in which the hydrogen fuel was used up. They range in mass from tenths of a solar mass up to the Chandrasekar Mass Limit of $1.4\,\mathrm{M}_{\odot}$, which is the maximum mass that electron degeneracy pressure can support (Warner, 2003). The radius of a WD is approximately the same as the Earth, though there is a dependence on the mass (Warner, 2003). Counterintuitively, more massive WDs have smaller radii, which is true for any degenerate matter. Neutron stars are also degenerate, and have a mass distribution that peaks around the Chandrasekar Mass, with an upper limit that is still unknown but is in the range of $2-3\,\mathrm{M}_{\odot}$. Composed primarily of neutrons, the exact inner structure of NSs is still an open question though it is thought that below the outer crust the neutrons form a superfluid. Supported by neutron degeneracy, NSs are much more compact than WDs, reaching densities 4-5 times nuclear density. Typical NS radii are the order of 10 km, but precise measurements of NS radius have not yet been made. Black holes, having collapsed beyond what any pressure can support as the speed of the pressure wave would have to exceed c, have a radius well defined by General Relativity that depends only on the mass and spin of the BH. The radius of a BH with zero spin with the mass of the Sun is 3 km and scales linearly with mass.

1.1.2 Binary Evolution

We often find these end products of stellar life in binary star systems. In a binary system, the effective gravitational potential in the rotating frame of the system is called the Roche Potential.

$$\Phi_{\mathrm{R}}(\overrightarrow{r}) = -\frac{GM_1}{|\overrightarrow{r}-\overrightarrow{r_1}|} - \frac{GM_2}{|\overrightarrow{r}-\overrightarrow{r_2}|} - \frac{1}{2}(\overrightarrow{\omega} \times \overrightarrow{\mathrm{r}})^2$$

Where $\overrightarrow{r}$ is the displacement from the center of mass, $\overrightarrow{r_1}$ is the distance to M_1, and $\overrightarrow{r_2}$ is the distance to M_2. Fig. 1.1 shows a cross section of the equipotential surfaces in the orbital plane; force is perpendicular to these equipotentials. There are 5 equilibrium points called "Lagrange points." The saddle point in between the two stars, L_1, is particularly important. This is known as the inner Lagrange point. The equipotential intersecting this saddle-point is called the Roche-Lobe. As the more massive star in the binary sequence evolves, it can expand past its Roche-Lobe and matter can begin pouring off the more massive star and onto the less massive star. When the mass ratio of the two stars, $q = \frac{M_{donor}}{M_{accretor}}$, exceeds a certain value depending on the equation of state of the donor, this mass transfer is unstable and mass transfer results in the accretion rate increasing, creating a positive feedback loop. This leads to an atmosphere of gas surrounding both stars, which is called the common envelope. While in this phase of binary evolution, the system loses energy and angular momentum, and the stars get much closer together (Paczynski, 1976). When both stars fill the Roche-Lobe, the system is called a contact binary. If neither do, it is called a detached binary. If one star does, it is called a semi-detached binary.

When a more massive star finishes its evolution in a supernova, the binary may become unbound. The change in the orbit from the companion due to mass loss is called the "Blaauw kick" (Blaauw, 1961). If the binary loses $\geq 1/2$ its mass in the ejection, the Blaauw kick will unbind the system. For example, the typical NS mass is $1.4\mathrm{M}_\odot$, which is $\sim 8\mathrm{M}_\odot$ less than the progenitor star. If mass loss were the only determinant in whether the system remains bound, there should be no NSs with low mass companions. However, the size of the core determines the end state of the star, and the core size is determined before the common envelope stage. During the common envelope phase, the primary may expel more mass from the system through the outer Lagrange points than the supernova later blows away allowing the system to remain bound. The other factor that needs to be accounted for is the presence of assymmetries in the supernova explosion, or "kick." The kick is oriented randomly with respect to the binary motion, so it could serve either to remove or add angular momentum and could serve to cancel the Blauuw kick.

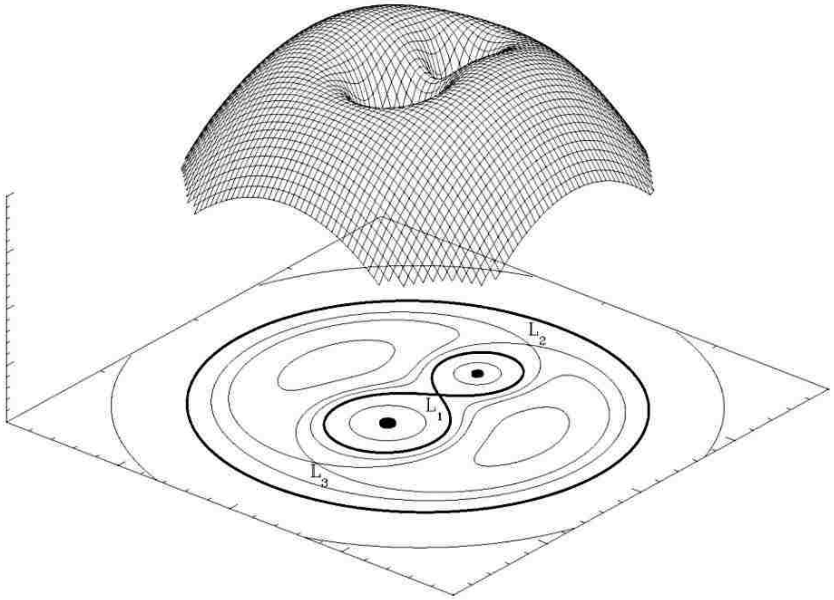

Figure 1.1: A cross section of the orbital plane, showing the intersection of the plane with equipotential surfaces of the effective gravitational potential between two stars in a binary. The saddle point in the middle marks the equipotential surface called the Roche-Lobe. Matter can flow across this saddle point to accrete onto the companion star. Figure reproduced with permission from van der Sluys (2006).

1.1.3 Types of Binaries

If the system remains bound, it can get closer together still through magnetic braking, which occurs when the magnetic field of the companion star interacts with its stellar wind, accelerating material above Keplerian velocities and serving to remove angular momentum from the system, bringing the binary closer together (Ivanova & Taam, 2003). For very close binaries, gravitational radiation becomes an important mechanism for removing angular momentum from the system.

If the system remains bound and the donor star ends up filling its Roche Lobe, it is called an X-ray Binary (XRB), which contains a NS or a BH primary. Binaries with low mass companions ($\lesssim 1\,\mathrm{M}_\odot$) are Low Mass X-ray Binaries (LMXB), while those with high mass companions are High Mass X-ray Binaries (HMXB). Systems with intermediate mass companions ($\gtrsim 8\,\mathrm{M}_\odot$) are called Intermediate Mass X-ray Binaries (IMXBs). LMXBs accrete through Roche-Lobe overflow once the companion gets close enough through angular momentum loss or evolves to fill the Roche-Lobe itself. As material accretes, it forms a stream out of L_1 which then forms an accretion disk of material around the compact object. The size of the star is then the size of the Roche-Lobe, approximated by Paczyński (1971) as

$$R_{RL} = 0.462\, a \left(\frac{M_2}{M_1 + M_2} \right)^{1/3}$$

where a is the binary separation. Initially, accretion through Roche-Lobe overflow in neutron star IMXBs is not stable because of the high mass ratio in these systems, though advances in computing have shown that the evolution of the donor in NS IMXBs can lead to a state of stable mass accretion (Pfahl et al., 2003). BH IMXBs can stably transfer matter through Roche Lobe, e.g. in the system GRO J1655-40 (Orosz & Bailyn, 1997). HMXBs accrete material through high stellar winds from the companion, or from Roche-Lobe overflow, or some combination of the two. Be XRBs are a type of HMXB that consist of a spectral class Be star showing hydrogen emission lines and a neutron star in orbit around it. These systems can form an excretion disk in the equatorial plane of the star, which is not in general the same as the orbital plane of the system. The neutron star can interact with this disk; for example, it can pass through the disk as it approaches the closest point of its orbit (periastron). The high mass companions of HMXBs do not live for long and so these systems trace regions of recent star formation (Grimm et al., 2003). They are also optically very bright because of the high mass companion.

If the primary is not massive enough to undergo a core collapse supernova and form a NS, it will become a WD system. A WD accreting material is called a Cataclysmic Variable (CV) and can show many different types of dramatic changes in light output. The most dramatic event is when enough hydrogen has accreted onto the surface of the WD to ignite fusion, which results in a classical nova eruption in which the system brightens optically by several orders of magnitude. There is also a possible event called a Dwarf Nova (DN), which is totally different from a classical nova and happens in the accretion disk. The disk is composed primarily of atomic hydrogen, but when part of the disk is heated above the ionization temperature of hydrogen, the gas in the disk becomes much more viscous (Warner, 2003; Frank et al., 2002). The heat energy from the increase in viscosity causes a heating wave to propagate through the disk, ionizing the remainder of it. The high viscosity disk then accretes at a much higher rate, dumping material onto the WD, which is observed as a sudden brightening of roughly an order of magnitude and decline to the original brightness over the course of days to weeks (Warner, 2003).

If the WD has a strong magnetic field, accreting matter will not form a disk but will follow magnetic field lines from L_1 to the pole of the WD. In the process, magnetic braking slows the spin of the WD until it is tidally locked with the donor star, so that its spin period is the same as the orbital period (Warner, 2003; Frank et al., 2002). This type of system is called a Polar. A moderately strong magnetic field can result in a slower magnetic braking process, which leaves the WD with a spin period slower than its birth spin, but still faster than the orbital period (Patterson, 1994). These systems are called Intermediate Polars (IPs), and can also have an outer disk before magnetic pressure dominates gravitational pressure, and the matter again follows field lines to the pole. The peak in the spin distribution of IPs roughly follows the relation $P_{Orb} \sim 10\, P_{Spin}$ (Scaringi et al., 2010).

NS or BH systems in which the companion is hydrogen and/or helium deficient are called Ultra Compact X-ray Binaries (UCXB). When the primary is a WD, the system is called an AM Canum Venaticorum (AM CVn), named for the first such system discovered. These all have orbital periods below 70 minutes, sometimes as short as 5 minutes (Nelemans & Jonker, 2010). In order to fit inside an orbit this fast, the disk is obviously quite small. Because of the extremely compact sizes of these systems, they are very optically faint. The only possible components of these binaries are WDs, NSs, BHs, and the cores of evolved giant stars whose hydrogen has been stripped in the CE phase.

Stellar remnants are not the only sources of X-rays. Other types of systems emit X-rays as well. RS Canum Venaticorum (RS CVn) stars are cool, late-type, close binaries with deep convection zones, high rotation, and active magnetic fields. Contact binaries sharing a common envelope that are eclipsing are called W Ursa Majoris (W UMa) stars. Algol systems form when enough matter accretes from an initially more massive star to move the companion up to a bluer spectral class, while itself evolving off the main sequence. This results in a system with a less massive, more evolved star and a more massive, less evolved star. Single M dwarf stars (red dwarfs) and K stars can also have large flares and coronal mass ejections that emit X-rays. The X-ray luminosity for these objects is closely related to the spin period of the star. Most stars, including the Sun, emit X-rays at some level, and can be detected if they are close enough to Earth.

1.2 Binary Population Models

Currently, models of binary evolution predict wildly divergent end populations, consisting of white dwarfs, neutron stars, and black holes with and without companion stars (Ivanova et al., 2005; Kalogera, 1999; Pfahl et al., 2003; Kiel & Hurley, 2006). We only know of a relatively small number of each type of end scenario within the galaxy, which allows many models of binary evolution to offer predictions of population size differing by orders of magnitude while still avoiding conflict with existing data. Many of these end scenarios are semi-detached binary systems, which will tend to give off X-rays as matter from one star accretes onto the degenerate stellar remnant.

The largest uncertainty in these models is in the Common Envelope (CE) phase of binary evolution. The energy lost in ejecting the envelope strongly influences mass and period distributions of LMXBs (Pfahl et al., 2003). It is in this phase that the system loses much of its angular momentum, allowing the formation of a close binary (Taam & Sandquist, 2000). Uncertainties also arise from the magnitude of “kicks” objects receive during a supernovae. A large enough asymmetry in the explosion, or the ejection of enough mass, can unbind the system. Finding out just how many of these systems remain bound can significantly constrain models for these kicks.

The mass distributions of both NSs and BHs are also important contraints on supernova models. The mass distribution of neutron stars peaks around 1.4 times the mass of the Sun (Özel et al., 2012), with the most massive neutron star found to be 1.94 ± 0.04 solar masses (Demorest et al., 2010). Instead of the continuous mass distribution one naively expects from supernovae remnants, however, the best measurements of the black hole mass distribution cutoff at $\sim 5\,\mathrm{M}_\odot$ at the low end, resulting in a gap between $2 - 5\,\mathrm{M}_\odot$ with no BHs or NSs (Bailyn et al., 1998; Farr et al., 2011; Özel et al., 2012). This distribution is plagued by numerous uncertainties in mass estimates and low number statistics. If the gap between NSs and BHs is real, however, it must be accounted for by supernova models especially since the mass distribution of supernova progenitors is continuous. Surprisingly, the kicks imparted to BHs by supernovae appear to result in similar velocity distributions to that of NSs, rather than similar momenta (Janka, 2013; Repetto et al., 2012).

1.3 Neutron Star Equation of State

The nature of one of these end states, neutron stars, is not well understood. Neutron stars contain material at densities unlike anything found on Earth, fitting 1.4-2.0 times the mass of the Sun in a sphere with a radius of only 10-15 kilometers. Material at this density offers an excellent probe of the strong nuclear force at regions of phase space that are simply unattainable here on Earth (Lattimer & Prakash, 2001). There are many different ideas about how material behaves at these densities, but so far there are not enough systems with known parameters to constrain the Equation of State (EoS) of neutronic material to any high degree (Özel, 2006). One reason for this is that some measurement must be made of both the mass and the radius of the neutron star, or some relationships between the two (Özel et al., 2009). These have been only weakly constrained for a handful of systems (Özel et al., 2010a). Alternatively, the maximum NS mass varies depending upon the model used, so finding heavy NSs would eliminate some EoSs. Indeed, a $1.97 \pm 0.04 M_\odot$ NS, which is a millisecond pulsar, has been identified since this project began by Demorest et al. (2010). This level of certainty rules out "soft" equations of state. There is still, however, merit in searching for NS masses both to fill out a mass distribution and because there is a chance we could find a higher mass NS. Fig. 1.2 shows some of the proposed EoS predictions for Mass-Radius relationships. The EoSs that do not reach close to $2M_{\odot}$ have been eliminated (Demorest et al., 2010).

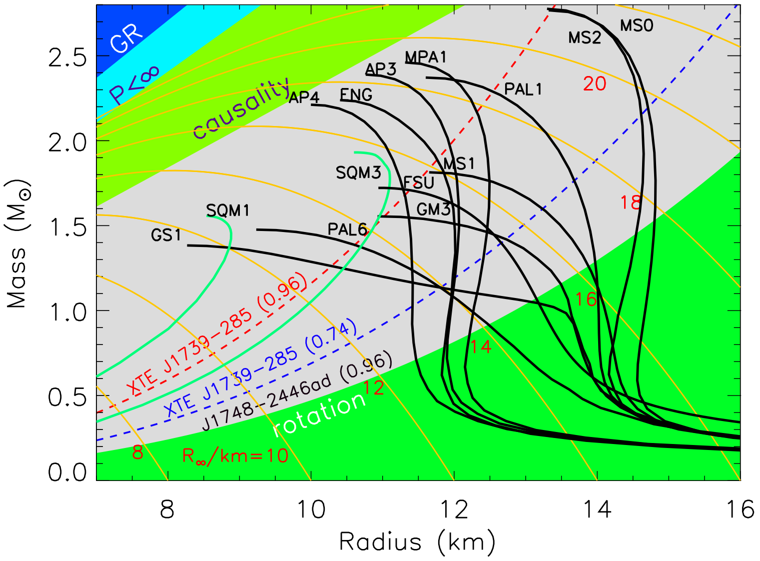

Figure 1.2: A plot of various NS EoS predictions for both maximum NS mass and the predicted mass-radius relation, reproduced with permission from Lattimer & Prakash (2007)

1.4 Previous X-ray Surveys

Previous surveys of Galactic X-ray sources, such as ChaMPlane (Grindlay et al., 2005), have concentrated on the Galactic Plane or the Galactic Center region (Muno et al., 2003). The reason for this is that source density is much higher here, so telescope time can be used more efficiently (Muno et al., 2003). Because extinction is so high in the disk of the Milky Way ($A_V \sim 30$) the search for counterparts in this region is conducted in the infrared. These surveys have run into problems with source crowding; so many possible counterparts are present for each detected X-ray source that it is difficult and time consuming to identify the true counterpart, and successful identifications have occurred largely in low extinction windows (Mauerhan et al., 2009; Hong et al., 2012). ChaMPlane is a serendipitous survey relying on existing deep exposures of the Galactic Plane and Bulge regions, with exposures from $\gtrsim 20 - 100\,\mathrm{ks}$ (Grindlay et al., 2005), and using follow up data from optical telescopes on the ground. The Bulge Latitude Survey (BLS) is conducted by the ChaMPlane team, and extends above and below the Galactic Center in narrow strips at $|l| < 0.35°$ to $|b| < 1.5°$. The BLS measured the fall-off of the faint X-ray point source population with height above and below the plane of the disk. Optical instruments are in many respects superior to infrared instruments today, being a more mature technology, but IR detectors are gaining ground. Establishing an optical/infrared counterpart is a necessary first step for characterizing the properties of most X-ray emitting objects.

Studies of X-ray sources in Globular Clusters (GC) can escape the problem of high extinction, but the crowding of possible counterparts is much worse and the formation mechanism in GCs is different than in the rest of the Galaxy. LMXBs in GCs are formed primarily through interactions between stars in the cluster; binaries do not remain intact through the entirety of binary evolution that would be seen in the sparser Galactic population. They cannot, therefore, be used as a probe of binary evolution elsewhere. Because of the age and lack of any post-birth star formation in GCs, the stars in them are exclusively low mass. Black holes therefore should sink to the center of the cluster, and dynamic interactions should eject all but one of these. GCs are therefore not a good place to search for BH candidates, though Strader et al. (2012) had a surprising result of finding 2 possible BHs in a GC in the Milky Way, identified through radio observations. The crowding of possible counterparts is too high to estimate their masses through spectroscopy, however.

Some surveys focus on high energy X-rays because they are affected less by absorption than lower energy X-rays (Hands et al., 2004; Sugizaki et al., 2001). Surveys with instruments like INTEGRAL at the energies > 17 keV, suffer from very poor angular resolution ($\sim 12'$) compared to the focusing X-ray telescopes at lower energies (Krivonos et al., 2012). These surveys focus primarily on HMXBs because the counterparts are so luminous, but the low angular resolution in X-rays severely limits their sensitivity.

1.5 The Chandra Galactic Bulge Survey, Survey Design

The Chandra Galactic Bulge Survey (GBS) undertakes to conduct a census of X-ray sources in the Galactic Bulge (Jonker et al., 2011). The GBS intends to avoid as much as possible the problems of crowding and extinction present in previous surveys of the Galactic Center, while giving up as little as possible in the way of number of sources. The GBS makes use of both optical and X-ray imaging of two $6^\circ \times 1^\circ$ strips located 1.5° above and below the Galactic Plane, cutting out the region $b < 1^\circ$ to avoid copious amounts of dust in the Galactic Plane, as shown in Fig. 1.3. Also marked in Fig. 1.3 are the X-ray sources discovered by the Chandra X-ray Observatory in the full survey region. The Chandra X-ray Observatory is a focusing telescope using oblique reflections off of parabolic mirrors to focus the X-rays and operates in the soft X-rays from $0.5 - 8\,\mathrm{keV}$. The resolution of CXO is quite good, getting to ~ 0.6" for sources close to the optical axis. For observations of sources that are more off-axis, the resolution lowers to 10" at $10'$ off-axis using the formula in Hong et al. (2005). Most GBS sources have errors on the order of $1 - 2$".

The X-ray observations were made in 2 main epochs, the first being the northern 3/4 which found 1234 X-ray sources (Jonker et al., 2011), though there are 18 duplicates that made it through screening leaving 1216 unique X-ray sources (Hynes et al., 2012). Observations of the last southernmost section of the survey area bring the total to 1640 X-ray sources (Jonker et al, in prep). I will be focusing on the counterparts to the 1234 sources first discovered in the northern 3/4 of the survey.

The GBS aims to greatly expand the known number of Galactic X-ray binaries, including discovery of the first Galactic eclipsing black hole binary (BHB). By greatly increasing the number of known LMXBs, we are bound to increase correspondingly the number of LMXBs for which mass determinations are possible. Filling out the BH mass distribution also has consequences for models of the history of our Galaxy (Kalogera, 1999). Currently, there are

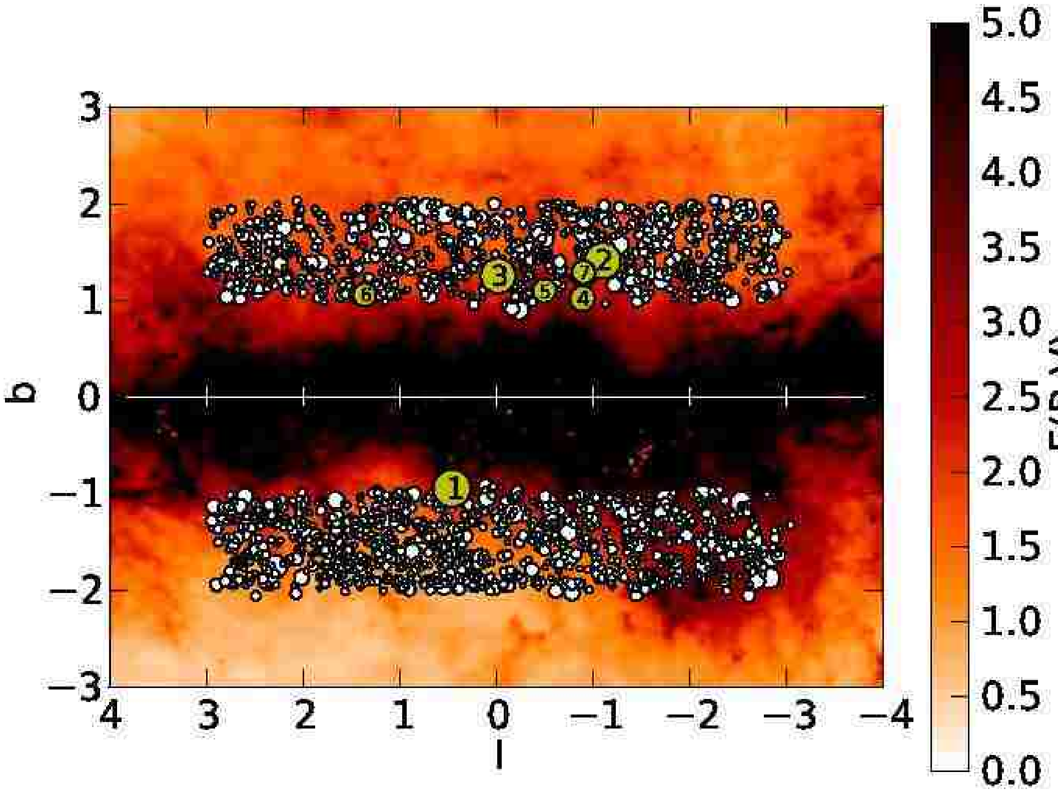

Figure 1.3: A map of reddening using values from Gonzalez et al. (2012) in the Galactic Plane, with the GBS sources marked. The size of the marker is proportional to the X-ray brightness of the source. We avoid the worst of the extinction in the Plane.

only 24 sources that are confirmed to be BHBs (Özel et al., 2010b; Kennea et al., 2012). Of these 24, 16 have some constraint on the mass ratio, q. This is a large enough population to raise questions about the lack of BHs with $M < 5M_{\odot}$ (Özel et al., 2010b). In particular, the mass gap between the most massive NSs and the least massive BHs, if real, is a puzzle that has serious implications for supernova models and binary evolution. It has been suggested by Farr (2012) that the mass gap is a result of systematic errors in estimating the inclination angle of BHBs through ellipsoidal modulations. This uncertainty could be removed by finding eclipsing BH systems as $\sin i \approx 1$ for these. There are currently no eclipsing BHBs known in our galaxy, though there is an eclipsing HMXB in M33 (Orosz et al., 2007). Because known stellar mass BHs have all been discovered in outburst and followed into a fainter quiescent state, it is possible that the accretion disk rim blocks the view of the outburst originating in the inner accretion disk (Narayan & McClintock, 2005). In quiescence, the disk rim is thinner, allowing a direct view of the central accretion disk (Nowak et al., 2001).

X-ray observations in the GBS are intentionally shallow, since the objects we are primarily interested in, active and quiescent LMXBs (qLMXBs), are typically more luminous in X-rays than other types of sources which give off X-rays such as RS CVn stars and CVs. By keeping X-ray observations shallow, we keep the proportion of LMXBs higher than it would otherwise be. Previous surveys have been deep, narrow "pencil beam" surveys, whereas the GBS is a wide, shallow survey. The proportion of LMXBs and qLMXBs to CVs should be much higher in the GBS than in previous surveys (Jonker et al., 2011). We should have a good chance of discovering the first eclipsing BHB.

The primary goal of the GBS is to constrain models of binary evolution, particularly regarding the CE phase, by conducting a census of LMXBs in the Galactic Bulge. In Jonker et al. (2011), it was predicted that we would find 120 new qLMXBs with official counterparts. Because the systems are quiescent, the donor star should make up $\sim 1/2$ of the continuum light which means that ellipsoidal variations should be visible for these systems (see Section 1.6).

At the Galactic latitudes where we observe, $A_V \lesssim 5$. Observing in r' and i' lowers this, since shorter wavelengths are more affected by scattering than longer, redder wavelengths. To be more precise, $A_{r'} = 0.84 A_V$ and $A_{i'} = 0.6 A_V$ Schlegel et al. (1998).

The spectroscopic follow-up campaign is being led by Peter Jonker and Manuel Torres at SRON in Utrecht, Netherlands. They have so far collected ~ 600 spectra with the VLT, NTT, Magellan and Gemini telescopes. Danny Steeghs and Sandra Greiss at Warwick, UK, are investigating IR counterparts primarily using VVV. Thomas Maccarone at Texas Tech is using serendipitous UV and radio observations of GBS sources. The population synthesis used for the GBS's population estimates were produced by Gijs Nelemans and his students at

Radboud University, Netherlands. I am searching for optical variability of GBS counterparts using data collected with my advisor, Dr. Robert Hynes.

1.6 Importance of Photometric Variability

Optical variability is a key tool in identifying the optical counterpart to the X-ray source, identifying high inclination systems via eclipses, and constraining orbital parameters such as period and inclination angle. Almost all optical counterparts to X-ray sources are expected to be variable, except for emission from massive stars, isolated NSs, and coronal emission from nearby Main Sequence stars.

Accreting systems such as LMXBs and CVs are far more likely to be optically variable than normal binaries. Accretion is ultimately driven by angular momentum loss from magnetic braking or gravitational wave radiation, but small timescale changes can be driven by changes in heating the donor star's atmosphere. Local changes in accretion rate and in the disk can cause aperiodic variability, or flickering, while periodic variability can be caused by ellipsoidal variations, the accretion stream point of impact on the disk (hotspot) or the face of the companion being heated by X-rays and becoming more or less visible to our line of sight as it orbits the compact object, or by partial or total eclipses of either the disk or the companion star.

Ellipsoidal variations can be especially important. When a companion star is near enough to its more massive partner, gravitational tidal effects elongate the companion star along the line towards the primary. The companion star winds up shaped more or less as a tear drop, with the pointed end at L_1. As the secondary star orbits, its projected cross-sectional area changes with phase. When it is directly in our line of sight to the primary, a minimum of its surface is visible, while at right angles to our line of sight, a maximum of its surface is visible. The light we see is therefore modulated with the phase of the system as a sine wave with a period 1/2 that of the orbital period. The amplitude of ellipsoidal modulations depends on the inclination angle of the system and to a lesser extent the degree of tidal distension, which depends on the mass ratio $q = \frac{M_1}{M_2}$. Tidal stresses circularize orbits quickly compared to the lifetime of the system, so orbits of Roche-Lobe accreting systems should be circular. The form of Kepler's 3^{rd} law that is of most use for mass determinations is

$$\frac{P_{orb}K_2^3}{2\pi G} = \frac{M_1 \sin^3 i}{(1+q)^2}$$

as P_{orb}, K_2, are observables, while i and q can be deduced less directly from observables. Since the inclination angle is usually difficult to determine for most systems, Kepler's 3^{rd} law becomes a lower limit on the mass, called the mass function.

$$f(M) = \frac{M_1^3 \sin^3 i}{(M_1 + M_2)^2} M_{\odot} = \frac{K_2^3 P_{orb}}{2\pi G}$$

It is also important to note that the same tidal stresses should lock the rotational period of the companion in sync with the orbital period of the system, as the Moon is tidally locked to the Earth. This tidal locking, combined with the fact that the companion's radius is R_L, is important in that it means the rotational broadening of absorption lines $v \sin i$ is related to the radial velocity amplitude K_2 of the system by

$$\frac{v \sin i}{K_2} = 0.46[(1+q)^2 q]^{1/3}$$

Hence, measurement of $v \sin i$ and K_2 allows q to be deduced. From measured ellipsoidal modulations it is possible to model inclination angle, which combined with K_2, P_{orb}, and q yields dynamical masses of the object and its companion via Kepler's 3^{rd} law. Without knowing the inclination angle, all that can be determined is the mass function of the primary, which sets a lower limit on the mass.

Identification of eclipsing systems is important because it offers concrete constraints on the inclination of the system, i.e. that it must be near 90° and therefore that $\sin i \approx 1$, $\frac{d(\sin^3 i)}{di} \approx 0$ and what uncertainties exist in the inclination angle do not propogate through to the mass estimate. It is also important to note that this is independent from the lightcurve models used to find inclination angle from ellipsoidal modulations. Further, we have a good chance of finding the first eclipsing Galactic Black Hole binary in our galaxy. We expect to find on the order of 10 new BH LMXBs (Jonker et al., 2011) which would greatly improve the mass-distribution of stellar-mass blackholes in the galaxy, as it would represent an increase in the population of known Galactic BHs by $\sim 50\%$. There is currently a dearth of high inclination Galactic black hole systems, which is probably due to selection effects in finding outbursting systems in that to be able to see the X-ray outburst, the disk cannot be in the line of sight (Narayan & McClintock, 2005). Since we are identifying many systems while they are in quiescence instead of finding them in outburst, and because the disk is much thinner in quiescence than in outburst (Nowak et al., 2002), we neatly escape this problem and expect to find $15 - 20\%$ eclipsing systems.

1.7 Classification of X-ray Sources

Different types of systems that produce X-rays do so by very different mechanisms, which produce very different levels of X-rays compared to optical light. The ratio of the energy being emitted in X-ray wavelengths to the energy being emitted in optical wavelengths is very important since it can distinguish between different source categories. It is independent of distance, since the brightness drops off as $\frac{1}{r^2}$ for both. The ratio $\frac{F_X}{F_{Opt}}$ is therefore a major tool in our diagnostic kit. Actively accreting LMXBs and UCXBs have $\frac{F_X}{F_{Opt}} \sim 100$. HMXBs, and IPs have $\frac{F_X}{F_{Opt}} \sim 1$. Non-magnetic CV's in quiescence have $\frac{F_X}{F_{Opt}} \sim 1/100$ while RS CVns, Algols, and W UMas can be even lower. X-ray emission from main sequence stars is ubiquitous, and originates from high temperature corona confined by magnetic field lines generated by a combination of a dynamo effect from the star's rotation and a convective envelope. F_X is limited to $\sim 10^{-3} \times F_{Bol}$, and tends to drop as stars spin down and age. For most stars, most of the star's energy is emitted at optical wavelengths so $F_{opt} \lesssim F_{Bol}$, but for red dwarfs, whose spectrum peaks in the infrared, $\frac{F_X}{F_{Opt}}$ can be significantly higher than 10^{-3}. For close binaries like RS CVns and W UMas, the stars in the binary are spun up faster than an isolated star of the same spectral type, and the dynamo effect generating the corona and X-ray emission is stronger than for an isolated star. A high $\frac{F_X}{F_{Opt}}$ is immediately interesting because it cannot be produced by any kind of active star. For this work, optical flux is defined as

$$F_{Opt} = \nu F_\nu = F_{\nu r'0} \times 10^{-0.4 m_{r'}} \times \frac{c}{\lambda_{cent}}$$

where $F_{\nu r'0}$ is the flux density of a magnitude 0 star for the SDSS r' filter, designed to be $3631\, W\, m^{-2}\, Hz^{-1}$, and λ_{cent} is the central wavelength of the filter.

For accreting systems, if an orbital period can be determined, P_{orb} constrains the size of the companion via Kepler's 3rd law, $\frac{P_{orb}}{2\pi} = \sqrt{\frac{a^3}{G(M_1+M_2)}}$ since $R_2 = R_L$. Typically, systems accreting by Roche-Lobe overflow that have orbital periods of days have a giant or subgiant companion. Those with periods of hours have a main sequence companion, while orbital periods of minutes imply a UCXB. For Main Sequence stars, mass and radius are more tightly related, leading to the relation $M_2 \approx 0.11 P_{\rm hr} {\rm M}_\odot$ (Frank et al., 2002).

Lightcurve morphology and spectroscopy are critically important, since for accreting binaries it can tell us whether the system's light is being dominated by the disk or the companion. For example, if no ellipsoidal modulations are present and only flickering is seen, the disk is outshining the companion or the system has a low inclination. A stellar spectrum can tell us not only how hot a star is, but what it is composed of and how fast it is moving, both in its orbit and rotation. For quiescent systems, the spectrum should be primarily that of the companion star rather than the accretion disk and so can be used to determine the spectral type of the companion, but disk dominated systems do exist.

Spectroscopy of individual sources is also a vital tool in characterizing objects. The relative strength of emission lines from different elements and ionization states can discriminate between qLMXBs and CVs, and partially discriminate between CVs and IPs as discussed in Table 1.1. Lines can be broadened by Doppler shifting as the emitting regions move in the system. The Full Width Half Maximum (FWHM) of each line is therefore a measure of velocity dispersion in the emitting regions. The distance from the rest frame line emission position and the central point of the line profile is the mean velocity of the emitting region along the line of sight. For absorption features from the donor, observing the variations in the radial velocity at different phases allows the construction of a radial velocity curve and the measurement of K_2. The radial velocity of the emission lines does not, in general, provide the semi-amplitude of either of the components but on average they provide the system's velocity relative to Earth.

All of these properties together can distinguish between different types of X-ray sources. Each source class is listed with its distinguishing characteristics in Table 1.1.

1.8 Reprocessed X-ray Variability

Optical variability can also occur as X-rays are reprocessed into optical light. As X-rays are emitted by accreting matter, they strike the accretion disk and the companion star and are reprocessed into optical light. At higher energies, the X-ray photons are not photoelectrically absorbed but are more often scattered through Thompson and Compton scattering. Because the photon is not absorbed, it is not emitted as electrons fall into low energy orbits, and it is not reprocessed into optical light. Reprocessing of X-rays takes ≤ 0.6s (Pedersen et al., 1982), so delays between X-ray emission and seeing optical reprocessing are caused primarily by light travel times within the system. By simultaneously observing a source in X-ray and optical wavelengths, one can correlate changes in X-ray flux with changes in optical brightness to determine the geometry of the system.

The accretion disk is approximately axisymmetric, so it should reprocess light in the same way independent of phase. Since the light travel time between the compact object, the companion star, and the observer changes with phase it is in theory possible to separate light reprocessed by the disk from light reprocessed by the companion. The mean lag between X-ray light and reprocessed optical light is the binary separation of the system in light-seconds, while the amplitude of the variation in travel time with phase is determined by inclination angle, as shown in Figures 1.4 and 1.5 reproduced from O'Brien et al. (2002).

Table 1.1: This table presents a rubric by which X-ray sources can be identified using optical and X-ray properties from existing X-ray data and optical follow-up. References: (1) Warner (2003); (2) Echevarria (1988); (3)Silber (1992); (4)Hynes et al. (2004); (5)Zurita et al. (2003); (6)Remillard & McClintock (2006); (7)Marsh et al. (1994); (8)Menou et al. (1999); (9)Lasota (2001); (10)Casares et al. (1991); (11) Grindlay (1999); (12)Shara et al. (2005); (13)Grindlay (2006); (14)Nelemans (2005); (15)Véron-Cetty & Véron (2000); (16)Güdel (2004); (17)Schmitt et al. (1995); (18)Dempsey et al. (1997); (19)Kupfer et al. (2013); (20)Nelemans et al. (2006); (21)Hynes et al. (2012)

Category	$\frac{F_x}{F_{Opt}}$	Optical Spectral lines	$\lvert RV \rvert$ offset ($\mathrm{km\,s^{-1}}$)	Possible Variability	References
CV	0.01 - 1	$\frac{\mathrm{HeI4471}}{\mathrm{H}\beta} = 0.22 \pm 0.09^1$, $\frac{\mathrm{HeII4686}}{\mathrm{H}\beta} < 0.4$	< 500	Flickering, sinusoidal, ellipsoidal, DN	1,2,3,11,13
IP	0.1 - 10	0.17 ± 0.04^1, $\frac{\mathrm{HeII4686}}{\mathrm{H}\beta} > 0.4$	< 600	Flickering plus reprocessed X-ray pulsation, rare DN	1,2,3,11,12
qLMXB (NS)	0.1 - 1	$\frac{\mathrm{HeI4471}}{\mathrm{H}\beta} = 0.12^3$, He II absent ^{3}	< 1000	Flickering, ellipsoidal, flares on timescale of minutes or longer	7,8
qLMXB (BH)	0.01 - 0.1	$\frac{\mathrm{HeI4471}}{\mathrm{H}\beta} = 0.12^3$, He II absent ^{3}	< 1000	Flickering, ellipsoidal, flares on timescale of minutes or longer	5,7,8
LMXB	≥ 100	$\frac{\mathrm{HeI4471}}{\mathrm{H}\beta} = 0.3^3$, $\frac{\mathrm{HeII4686}}{\mathrm{H}\beta} = 0.8^3$	< 1000	Flickering, disk dominated, outbursts on timescale of a week to months, reprocessed thermonuclear bursts in case of NS primaries	4,6,9,10
UCXB	10^3 - 10^5	C/O-He/N emission, H deficient	< 3000	Flickering	20
AM CVn	1	He I+II emission, no H	< 1000	Flickering, $\mathrm{P_{Orb}} < 1$ hour Outbursts < 4 magnitudes	14, 19
AGN	10 - 1000	Broad or narrow emission lines from both allowed and forbidden transitions	> 1000	Aperiodic variability on a timescale of days or longer	15
RS CVn	0.001 - 0.01	Ca II H & K, Mg II emission	< 100	Sinusoidal, P_{Orb} days	16,18
W UMa	10^{-3} - 10^{-2}	Broadened stellar absorption features of F, G, K stars	< 300	Broad eclipses of nearly equal depth, can appear ellipsoidal, $\mathrm{P_{Orb}} < 1$ day	16
Flare Stars	10^{-3} - 1	M,K stellar spectra	< 100	Sinusoidal variations & flares on timescale of minutes, $\mathrm{P_{Orb}}$ days	17
Coronal	10^{-6} - 10^{-3}	F,G stellar spectra	< 100	not variable in optical	16
Wind emission	10^{-6} - 10^{-4}	O,B stellar spectra	< 100	Irregular or none	16,21

---

[a] Average and standard deviation of reported EW ratios in Echevarria (1988)

[b] For systems where EW(Hβ) > 20 Å. This is not a definitive test, as it is based on tens of systems. The defining characteristic of IPs is an X-ray spin period for the WD that is less than the orbital period. Our X-ray observations are too shallow to permit detection of a spin period in most cases.

[c] Reported values are average of observed EW ratios for the systems A0620-00 and V404 Cyg in quiescence and outburst, respectively.

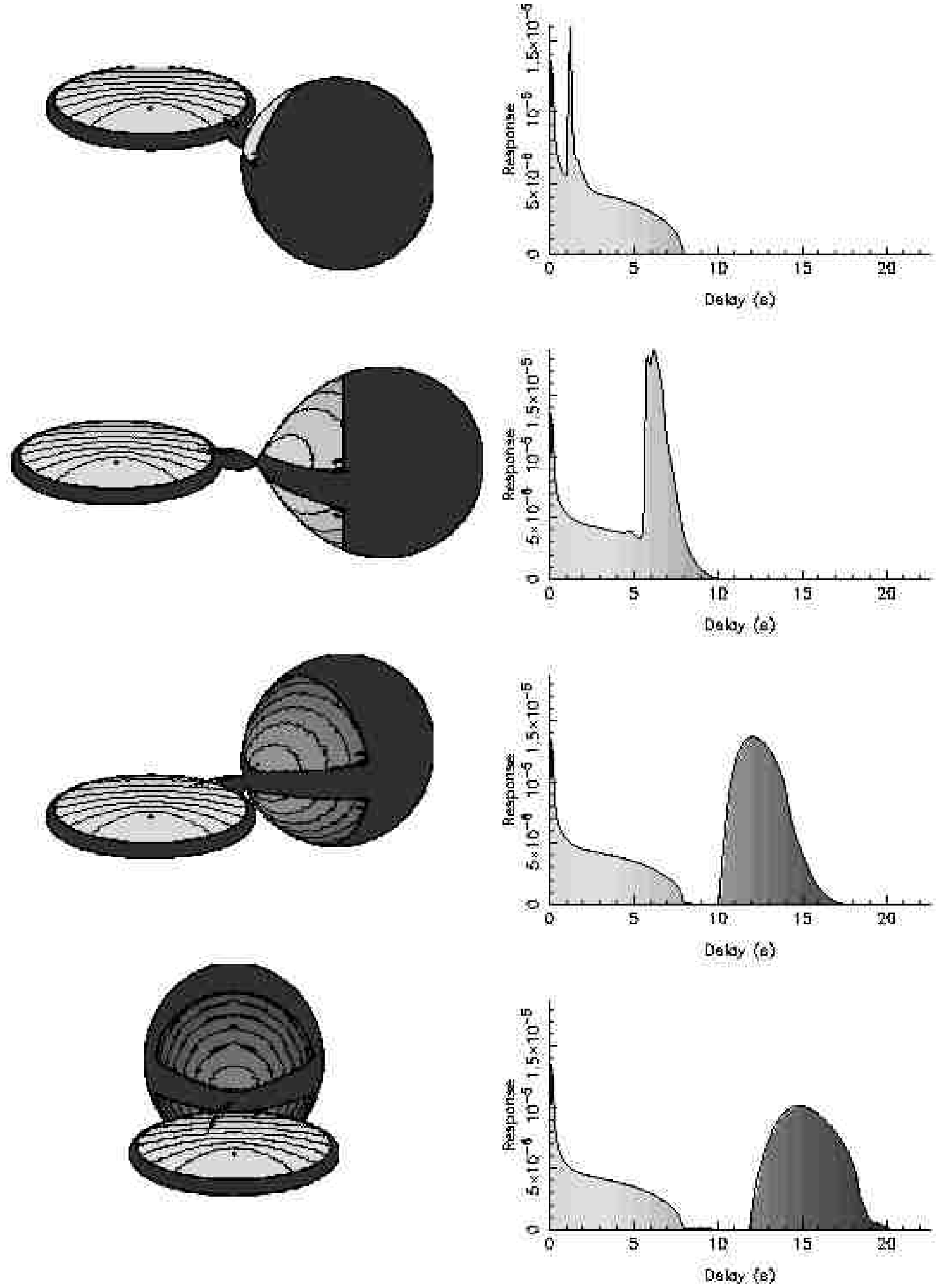

Figure 1.4: Modeled optical responses to a delta function X-ray emission as a function of phase. The contribution from the accretion disk is the same, but the contribution from the companion star depends on phase for both the time delay and strength of the response. Figure reproduced with permission from O'Brien et al. (2002).

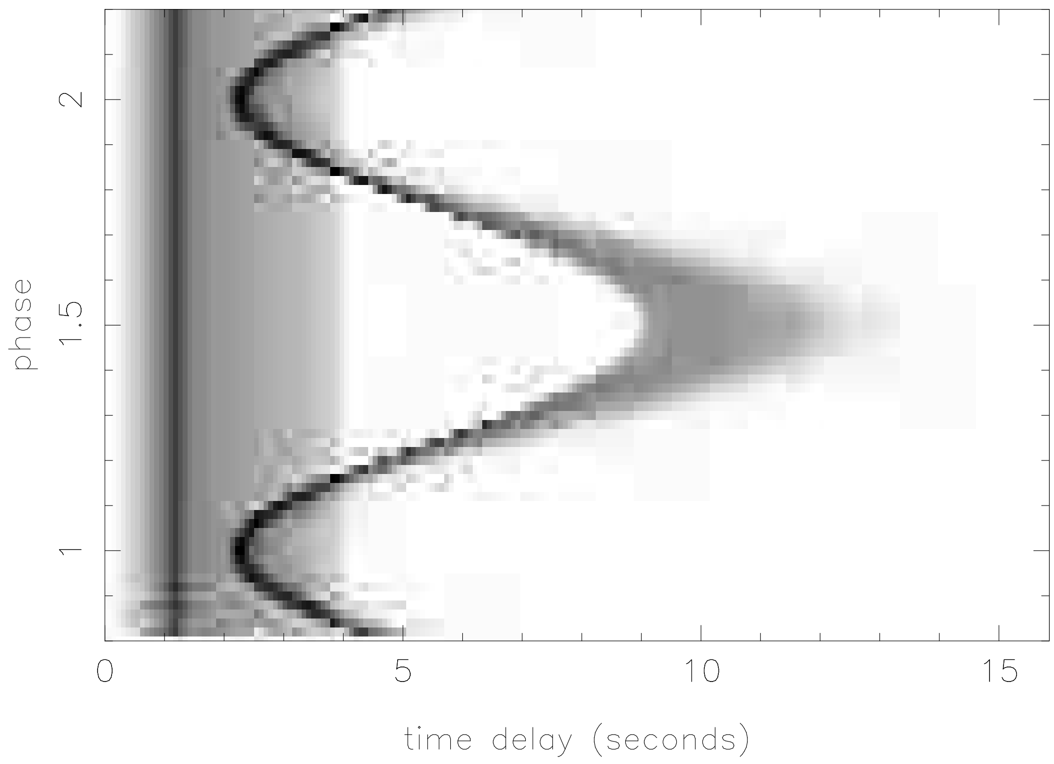

Figure 1.5: The time delay from the companion star traces a sine wave with phase, with an average at the binary separation distance and an amplitude determined by inclination angle. Figure reproduced with permission from O'Brien et al. (2002).

1.9 Sco X-1 and Z sources

Sco X-1, the brightest persistent known extra-solar X-ray source, is one of 6 known Z-sources, so called because they change state to trace out a *Z* shape in an X-ray color-color diagram (Hasinger et al., 1989; Hjellming et al., 1990). An X-ray color is just a ratio of the amount of high-energy (bluer) light to the amount of lower energy (redder) light. In optical astronomy, colors have long been used to classify and understand the nature of stars as they stand in as a crude spectrum. In X-ray astronomy, they can be used the same way. The three branches of the *Z* are called, from top to bottom, the horizontal branch (HB), normal branch (NB), and flaring branch (FB). Futhermore, Z-sources are divided into 2 categories: "Sco-like" after Sco X-1, and "Cyg-like" after Cygnus X-2. Sco-like sources spend most of their time in the FB, and very little time in the HB. The Z-tracks for both a Sco-like and Cyg-like Z source are shown in Figure 1.6, from Church & Bałucińska-Church (2012).

Not much is known of the reasons for this behavior, but Church et al. (2006) suggests that a change in the rate of mass accretion on the NB and HB drives an increase in luminosity in the Accretion Disk Corona (ADC) and blackbody radiation disrupting the inner accretion disk. Lin et al. (2012) suggest that the entirety of the Z-track can be effectively modeled at a constant mass accretion rate. Church & Bałucińska-Church (2012) offers a review of Z-sources. At one time, it was thought that the inclination angle of the binary was responsible for the differences in Sco-like and Cyg-like Z sources, but XTE J1701-462 was observed to outburst, and in the decay transform between being a Cyg-like source to a Sco-like source and finally an atoll source (Homan et al., 2007), demonstrating that the mass accretion rate is the primary difference between these categories. Correlated variability occurs predominantly in the FB. Sco X-1 itself is a NS LMXB with an orbital period of 18.9 hours. Previous efforts to echomap Sco X-1 with continuum light have seen that reprocessing is dominated by the accretion disk (Petro et al., 1981), but lack the phase coverage or sensitivity to pick out the companion. Reprocessing on the companion has been detected by Muñoz-Darias et al. (2007) through isolation of the He II 4686 and Bowen blend emission lines, though phase coverage was incomplete and the source was not observed at multiple X-ray states.

1.10 Explanation of terms

Astronomers have a set of terminology that can be difficult for non-astronomers to follow. The unit of measurement for optical and infrared brightness is the magnitude. In general, the apparent magnitude of a star with a photon flux F is $m = -2.5 \log F + m_0$. This is a bit quirky in that brighter objects have lower magnitudes, while fainter ones have higher magnitudes. 2.5 magnitudes is a factor of 10 difference in brightness. Absolute magnitude (M) is defined as the apparent magnitude an object would have at a distance of 10 parsecs. A parsec is the distance at which the distance from the Earth to the Sun (termed an Astronomical Unit) would subtend an angle of 1 arcsecond on the sky and is

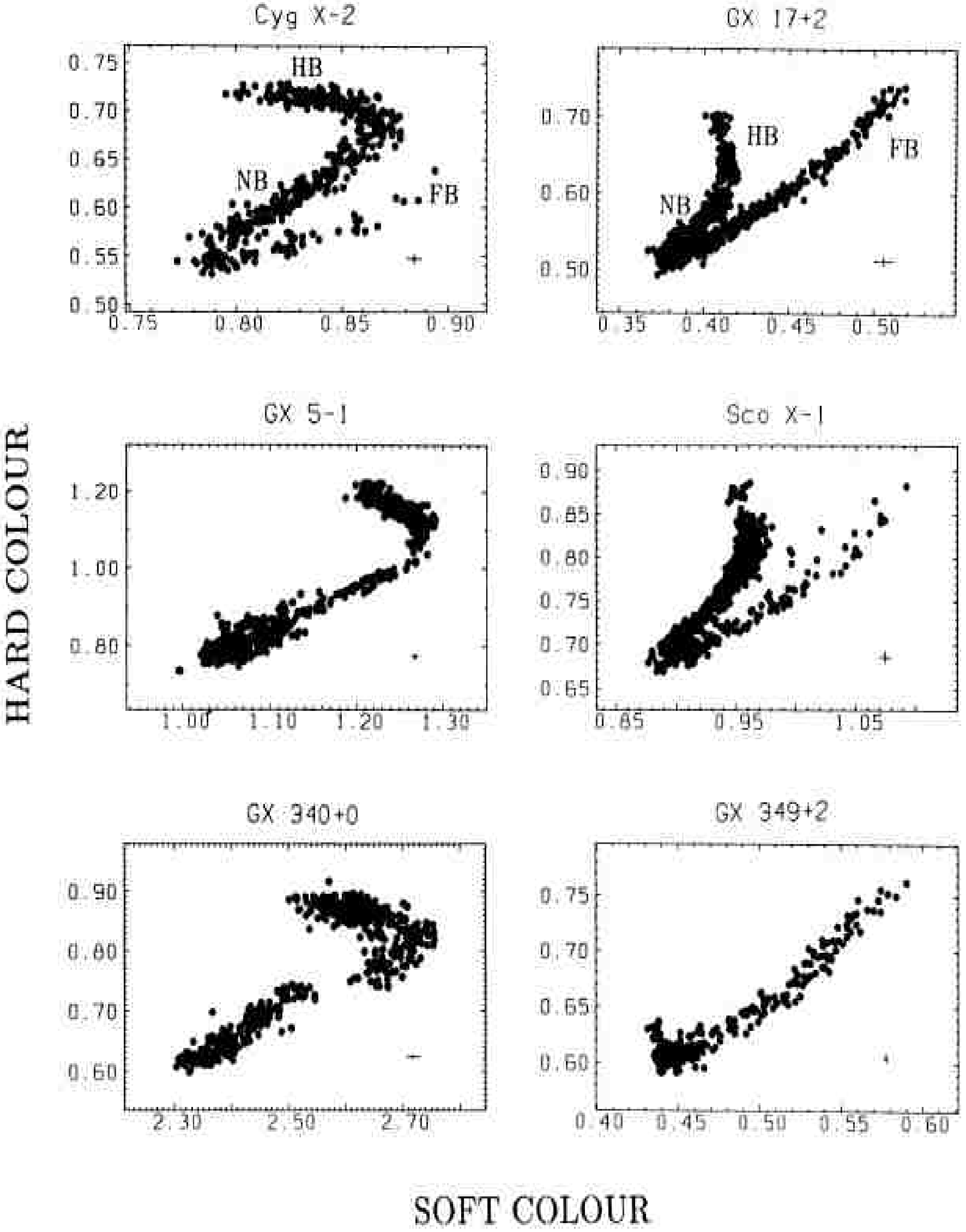

Figure 1.6: Each persistent Z source, with Cyg-like sources on the left-hand column and Sco-like sources on the right. Each branch of the Z is labelled for the first source in each category. Figure reproduced with permission from Church & Bałucińska-Church (2012).

equivalent to 3.26 lightyears. Parsecs (pc) or kiloparsecs (kpc) are the typical unit of distance measurement in the Milky Way. The sun is roughly 8 kpc from the center of the Galaxy. The Milky Way is shaped a bit like 2 fried eggs stuck together; it has a disk $\sim 1\,\mathrm{kpc}$ thick and 30 kpc across, and a bulge in the middle 5 kpc thick.

Stars are grouped in to spectral classes based on their temperature. From hottest to coolest, these classes are O, B, A, F, G, K, and M, which is often remembered by the mnemonic “Oh Be A Fine Girl/Guy, Kiss Me!”. When a number appears after these letters, it simply refines the temperature to a narrower range from 0-9 from hottest to coolest. When Roman numerals appear after the letter, it refers to the evolutionary stage of the star in question, with the Main Sequence using the Roman numeral V. The Sun is a G2V star. The Giant Branch is denoted by the Roman numeral III. Supergiants are designated Ia.

While stars are so far away compared to their size that they can safely be assumed to be a point source, every instrument has a maximum resolution and shapes the incoming wavefront. In general for ground telescopes, the atmosphere has a much larger effect on the shape of the wavefront than the instrument. The final shape of a point source in an instrument is called the Point Spread Function (PSF).

Light is measured in different wavelength regions by using filters. There are many filter sets. The most traditional are perhaps the Johnson UBVRI filter set, where U is ultraviolet, B is blue, V is green, R is red, and I is near-infrared. These are all considered to be optical filters, even though U and I appear black to the human eye. Further in the infrared are the J, H, and K filters. The filter set we use for this work is the Sloan Digital Sky Survey (SDSS) filter set denoted $u'g'r'i'z'$. The centers of these filters are substantially different from the Johnson set, as are the widths and shapes of the filter bandpasses. My variability search is being done in SDSS r', which is centered at 6231 Å. While the energy of optical, UV, and IR light is typically expressed in terms of the wavelength of the photon, the energy of X-ray light is usually expressed in keV. These are equivalent representations in that the wavelength of light corresponds exactly to its energy, with shorter wavelengths being higher in energy.

Therefore I will describe X-ray observations with units of keV, and optical observations in units of Angstroms (Å).

Light coming from a star must travel through dust and gas in the interstellar medium. Dust scatters light, resulting in extinction. Extinction is measured by noting the color difference in light seen by the observer, as the excess in blue light minus the excess in green light, $E(B-V)$. At optical and IR wavelengths, gas and dust scatters more blue light than red. Different compositions of dust will scatter light in different ways. The measure of the amount of light that is lost is denoted in magnitudes as A_λ, where the subscript λ denotes the filter used, with A_V the most frequently quoted. The relationship $\frac{A_V}{E(B-V)} = R_V \sim 3.1$ is widely assumed, but R_V may have a different value depending on the amount and composition of dust in the line of sight of the observer (Cardelli et al., 1989). At X-ray wavelengths, scattering is no longer the dominant effect, being overpowered by photo-electric absorption. Absorption's relationship with photon energy is reversed from that of scattering, and higher energy (bluer) photons pass through Interstellar Medium (ISM) more easily than lower energy (redder) light. This switch happens at a wavelength of 913 Å, which is the longest wavelength of light that ionizes atomic Hydrogen. X-ray absorption is determined by the column density of Hydrogen in the line of sight, given by $N_H = 5.8 \times 10^{21}\,\mathrm{cm}^{-2}\,E(B-V)$ (Bohlin et al., 1978). It is important to note that X-ray absorption below ~ 0.1 keV is dominated by hydrogen in the line of sight, while reddening is due to molecules of dust. Above this point until ~ 2 keV, photoelectric absorption is dominated by helium. In most of the Chandra sensitivity range, absorption is dominated by carbon, nitrogen, and oxygen (a combination usually referred to as CNO, though it is important to note that this is not a chemical formula). The relationship in Bohlin et al. (1978) assumes a solar ratio of hydrogen to CNO and other elements in the line of sight, but this is not always a good assumption.

2. X-ray Observations

2.1 Chandra Galactic Bulge Survey Observations

The Chandra X-ray Observatory (CXO) is a focusing X-ray telescope sensitive to X-ray photons between 0.1 and 10 keV, which relies on a low grazing angle to reflect and focus incident X-ray photons from a cylindrical parabolic mirror. These focused photons then strike the instrument in use. GBS observations consist of 2 ks observations using the AXAF CCD Imaging Spectrometer (ACIS) instrument on the CXO, which is sensitive between 0.2 keV and 10 keV. ACIS consists of 10 X-ray CCDs, while our observations use the I0-I3 CCDs (Garmire, 1997). Observations were limited to photons between 0.3 and 8 keV. In ACIS, incident X-ray photons strike the CCD, promoting many electrons above the Fermi gap numbering in proportion to the energy of the photon. The CCD array measures the location of the photon as it is read out. Because the image is in focus, the position of the photon on the CCD chip measures the direction on the sky it came from. In the case of high X-ray photon flux, two or more photons may be counted as a single event with an energy equal to the sum of the photons. In effect, multiple low energy photons are measured as a single high energy photon. This photon pileup results in a distortion of the spectrum for bright sources.

X-ray observations were collected and analyzed by Peter Jonker and others in Jonker et al. (2011). X-ray sources in the survey area were found using the CXO. Pointings are constructed to avoid overlap with existing surveys of the Galactic center region. Initial observations covered only 3/4 of the proposed survey area, though the rest of the Southern portion of the survey has now been obtained. All X-ray sources are shown in Figure 1.3. In the original observations, 1234 X-rays point sources were identified. An effort was made to screen for duplicate X-ray positions automatically before publishing the source catalog in Jonker et al. (2011), but using more conservative error estimates in Hong et al. (2005), 18 of the 1234 sources in the original catalog were found to be duplicates leaving 1216 unique X-ray sources (Hynes et al., 2012). Including more recent observations of the remaining survey area, the total number of unique X-ray sources in the GBS is 1640. The Chandra X-ray Observatory sources identified in the first batch of X-ray observations are officially named with the prefix “CXOGBS J” and the RA and DEC coordinates, but for ease of use, we refer to these with the prefix “CX” followed by an ID number given in descending order of X-ray brightness, starting with 1. The sources in the second group of Chandra observations are denoted with the prefix “CXB” and numbered in the same way, again starting with 1. This work will only discuss CX sources.

Chandra has a very low background, so even sources with only a few photons observed are significant. Our catalog of X-ray sources includes only those with 3 or more photons observed in a 2 ks observation. For faint sources with so few photons, the X-ray spectrum is impossible to measure with any accuraccy. We do have 89 sources with more than 20 photons, which allows X-ray color to be measured as the ratio of the difference of soft X-rays (0.3 keV - 2.5 keV) to hard X-rays (2.5 keV - 8 keV) divided by the total number of counts, which is shown in Fig. 2.1. If all photons are high energy, hardness is +1, while if all photons are in the low energy band, hardness is -1. The estimation of F_X we have for faint sources is uncertain by at least Poisson statistics $\propto \sqrt{N}$, but have added uncertainties in assuming the shape of the X-ray spectrum of the source and the amount of absorption. To estimate the uncertainty in the photon count for each source, we use the method in Gehrels (1986) that $\sigma_N = 1 + \sqrt{N + 0.75}$. Assuming a powerlaw spectrum with photon index $\Gamma = 2$ and hydrogen column density $N_H = 10^{22}\mathrm{cm}^{-2}$, each photon corresponds to roughly $7.75 \times 10^{-15}\mathrm{ergs\,cm^{-2}\,s^{-1}}$ (Jonker et al., 2011). The powerlaw of $\Gamma = 2$ is assumed because the spectral shape of a BH qLMXB softens as it decreases in luminosity from the low-hard state as the contribution from inverse-Compton scattering decreases, but reaches a plateau at $\Gamma = 2.08 \pm 0.07$ (Plotkin et al., 2013). Inverse-Compton scattering is when a photon interacts with a high energy electron and picks up some of the electron’s energy. For other types of sources, the emission mechanisms are different and different spectral models should be used to estimate a more accurate F_X. For IPs, the X-rays are produced by a curtain of material crashing onto the magnetic pole of a WD and emitting Bremsstrahlung radiation. CVs often have a soft, thermal X-ray spectrum. If there is evidence from other wavelengths that an object belongs to a certain source class, I recalculate the X-ray flux using one of these models with the WebPIMMS tool [1]. For IPs, I use Brehmstrahlung radiation with a characteristic temperature of 25 keV.

For individual sources, we can use reddening maps from Gonzalez et al. (2012) for the X-ray source position to get a better estimate of N_H by using the relationship $N_H = 5.8 \times 10^{21} E(B{-}V)\,\mathrm{atoms\,cm^{-2}\,mag^{-1}}$ in Bohlin et al. (1978) or $N_H = 1.79{\times}10^{21} A_V\,\mathrm{atoms\,cm^{-2}\,mag^{-1}}$ from Predehl & Schmitt (1995). The two relations are within errors of one another since $A_V \approx 3.1\,E(B-V)$. These values are for the particular red clump stars (a position on the H-R diagram whose luminosity and color is more or less independent of metallicity or age) used to measure Bulge reddening in the Gonzalez maps, while the actual X-ray source may be a foreground object rather than in the Galactic Bulge. These relationships therefore do not offer an increase in accuracy in estimated the X-ray flux without some information on the likely absolute magnitude, and therefore distance, of the object in question. It is also important to remember that, as discussed in Chapter 1, variations in the relative abundance of elements causes changes in the relationship between $E(B-V)$ and N_H.

2.2 RXTE Observations of Sco X-1

In order to echomap Sco X-1, we used simultaneous X-ray and optical observations with the Rossi X-ray Timing Explorer (RXTE) and the Argos instrument on the 82" Otto Struve Telescope at the McDonald Observatory. Time with the RXTE satellite was awarded in kiloseconds. Each orbit lasts ~ 100 minutes, of which 1/3 is spent on the other side of the Earth from the target. We were awarded $\sim 130\,\mathrm{ks}$, or 24 orbits, from May 19, 2009 to May 30, 2009.

RXTE excelled at high time resolution X-ray photometry. Because the Argos data was at 1 second resolution, we used 1 second bins for the X-ray photometry. This is adequate

---

[1] http://heasarc.gsfc.nasa.gov/Tools/w3pimms.html

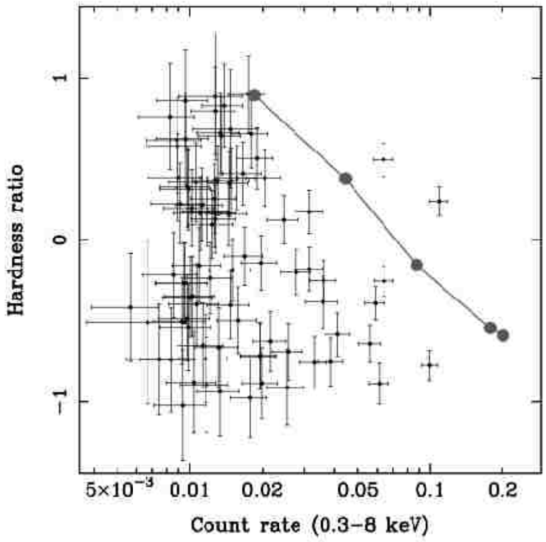

Figure 2.1: The harness-intensity diagram of the 86 sources with more than 20 photons detected in Chandra observations but which are also faint enough to avoid photon pile up in the X-ray detector (Jonker et al., 2011). The gray line shows the effects of N_H on a power law spectrum with $\Gamma = 2$ for a source with a count rate of 0.05 counts s^{-1}. The dots show the effects of increasing N_H from bottom right to top left with values of (0.01, 0.1, 3, 10) $\times 10^{22} cm^{-2}$. Sources with all the photons in the low energy band have a hardness of -1, while those with all photons in the high energy band have hardness of +1.

for the observations, as light travel times are on the order of seconds in the system, while the typical reprocessing time is $\lesssim 0.6$ s (Pedersen et al., 1982). RXTE is set up with 5 Proportional Counter Arrays (PCAs), of which at least 2 should be active throughout the observations. The PCAs were Xe gas chambers in which the X-rays would strike the Xe atoms producing an electron cascade. The spatial pointing is provided by a collimator which screens out X-rays except in the direction of interest, with a FWHM of 1°. Sco X-1 is the brightest persistent X-ray source in the sky other than the Sun, making up $\sim 30\%$ of the total X-ray flux seen on Earth at any given time, except for during X-ray outbursts of other sources. So many X-ray photons would hit the detector if RXTE looked directly at Sco X-1 that the observations would suffer from serious deadtime effects, in which photons continue to strike the instrument before it has become sensitive again. Deadtime corrections are still necessary, and steps to calculate the deadtime correction are described in detail in the XTE data recipes portion of NASA's website. In order to observe Sco X-1, the instrument was pointed so that the source was just outside the field of view, so that the collimator only allowed a portion of the light for Sco X-1 into the intrument. Though the instrument is sensitive to X-rays up to 60 keV, photons of this energy are not reprocessed, but scattered through Compton scattering, and we do not use them for this study.

To extract X-ray lightcurves at the energies 2 to 16 keV, I used the ftools package [2] (Blackburn, 1995). The light curves at 1 second intervals were produced by Dr. Valerie Mikles. I made X-ray lightcurves at a resolution of 0.1 s in order to measure more finely the degree to which X-ray points are correlated with those next to them.

To determine the X-ray state of Sco X-1 in a given observation, I measured the photon flux in 4 energy bands; [2-4] keV, [4-6] keV, [6-10] keV, and [10-16] keV. The ratio of the flux of the two lower energy bands is the "soft color", while the ratio of higher energy bands is the "hard color". The Z-diagram is the path that the source traces on a plot of hard color vs soft color (see Section 1.9). The intensity of the source is also function of state. On the Flaring Branch, intensity increases with both hard color and soft color, which are themselves correlated, as can be seen in Figure 2.2. On the Normal Branch, hard color is only slightly correlated with intensity, while soft color does not change dramatically. On the Horizontal Branch for Sco-like sources, the colors and intensity remain fairly constant. The highest intensity states are on the Flaring Branch. The X-ray state can change on a time scale of minutes to hours. The changes are continuous in that the system does not jump from one position on the Z-diagram to another, but evolves smoothly. Gaps that can be seen in Figure 2.2 are due to interruptions in the observations caused by the occultation of Sco X-1 by the Earth. The evolution on the Z-diagram appears unrelated to the binary orbital phase of the system.

---

[2] http://heasarc.gsfc.nasa.gov/ftools/

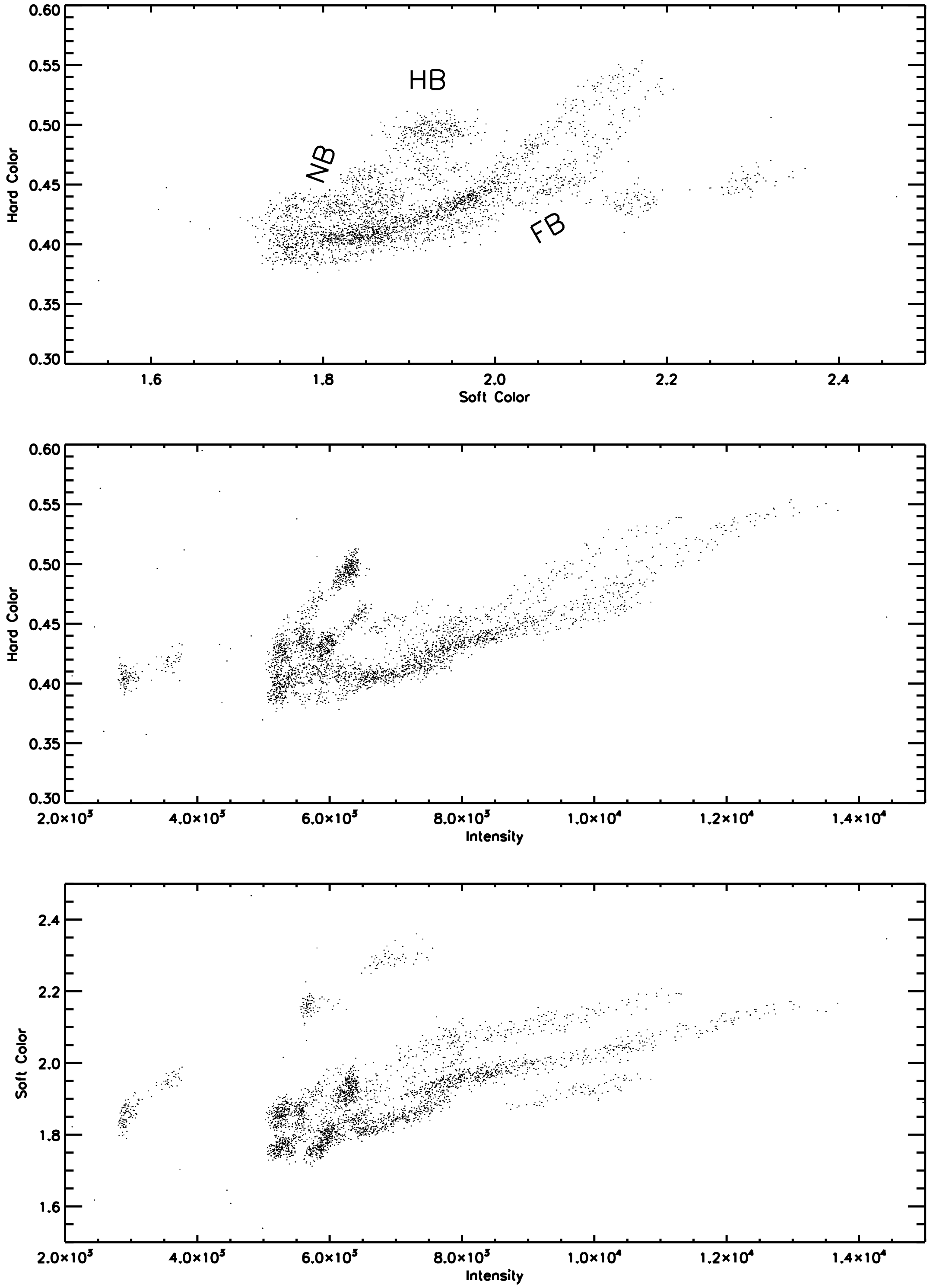

Figure 2.2: In the top figure are the RXTE observations of Sco X-1, in which all 3 branches of the classic Z diagram can be seen. The middle plot shows soft color versus intensity, and the bottom hard color versus intensity.

3. Optical Data

The GBS area has been imaged twice with the Mosaic-II instrument on the Blanco 4.0m telescope at the National Optical Astronomical Observatories' (NOAO) Cerro Tololo International Observatory (CTIO). The first time was in both SDSS r' and i' bands at just a single epoch to plan future spectroscopic observations. Once calibrated, they will give color and magnitude for identified X-ray counterparts. I report here only on the second set of observations which searched for optical variability of possible counterparts. When I refer to r' images, I will be referring to this variability data we collected in r' in 2010.

We used 8 nights in July 2010 with Mosaic-II to measure optical variability in the r' band, reaching magnitudes $16 < r' < 23$. I went to CTIO in Chile with my advisor, Robert Hynes, and an undergraduate, Lauren Gossen, to collect this data, which is described in greater depth in section 3.1.1. I successfully proposed for the 2012A semester to get variability information for stars so bright that they saturate in our Mosaic data with CTIO's YALO 1m telescope. An older version of this proposal was accepted for 2011A, but weather was bad and we did not get enough clear time to get period estimates for variability data. In the 2012A semester, the instrument on the 1.0m experienced some technical problems and our project was moved over to the Tek2K isntrument on the 0.9m on the same mountain. The Tek2K has a significantly smaller field of view than the Y4K CAM on the YALO 1.0m; $13.6' \times 13.6'$ compared to $20' \times 20'$. Since the instrument covered just under half the area we had planned, we were unable to get lightcurves of all the saturated stars in the survey, focusing instead on one corner of the GBS. These observations are further described in section 3.1.2.

I also visited the Las Campanas Observatory in June of 2011 to use the 1.0m Henrietta Swope Telescope with time acquired by collaborator Manuel Torres. This time was used to follow up on individual targets of interest to either confirm or establish periods. Targets were selected based on either optical spectral characteristics or on properties of the Mosaic-II lightcurve such as the detection of an eclipse or an identified ellipsoidal modulation. These observations are described in section 3.1.4.

For the echomapping of Scorpius X-1, I visited the McDonald observatory in May, 2009 with Dr. Robert Hynes and Dr. Valerie Mikles to collect optical data using the Argos instrument on the Struve 82 inch telescope. I will discuss these observations in greater detail in section 3.1.5.

3.1 Observing Strategy

3.1.1 Mosaic-II

We observed with Mosaic-II on the CTIO Blanco 4m telescope from July 8 to July 15, 2010. At this time, we only had received Chandra time for 3/4 of the proposed survey area: all of the strip North of the Galactic Center, and 1/2 of the strip to the south. 1234 X-ray sources were identified in these observations. Since it was unclear whether the remaining southern portion of the survey would ever be done in the X-ray, we restricted our observations to the areas of which we had X-ray observations in hand in order to improve our coverage of the sources that had been observed.

The Mosaic-II instrument has a pixel scale of 0.27 arcsec/pixel. The pixels are $15\,\mu$m in size, with a gain of 2. The Mosaic-II instrument is a mosaic of 8 2048×4096 CCDs with small gaps (≈ 50 pixels) between chips. We therefore dithered our observations between cycles to pick up sources that would fall on a chip gap in one or the other pointing. The instrument reads out in 2.5 minutes using the 8-channel mode. The Field of View (FoV) of the Mosaic Instrument is $41' \times 41'$. A full image is shown in Figure 3.1. We used 45 fields to cover the survey area, with overlap between fields as shown in Figure 3.2. The CCDs remain linear up to $\approx 40,000$ ADU, and saturate at $\sim 60,000$ ADU.

We cycled through each field on average every 2.5 hours. The order in which we observed each field was randomized in order to prevent aliasing the period with our duty cycle. Aliases are simply beat frequencies between the sampling frequency and the intrinsic frequency of variations being observed. For alternate observations of a field, we dithered the telescope position so that sources that fell on chip gaps in one cycle would fall on the CCD in the

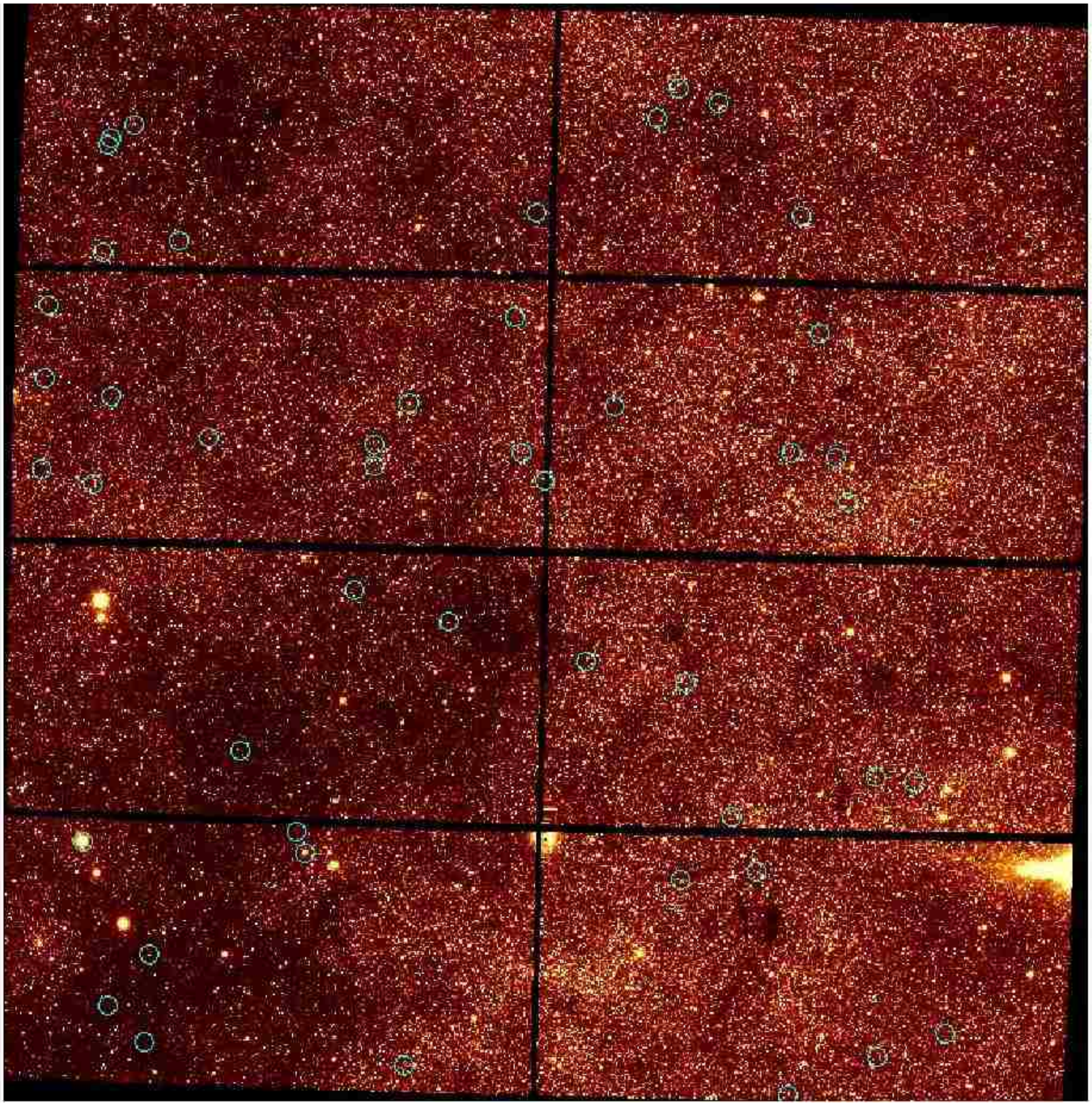

Figure 3.1: A Mosaic field, reprojected into square pixels on the sky. This is just one image, corresponding to one of the outlined squares in Fig. 3.2. The cyan circles are centered on GBS X-ray sources.

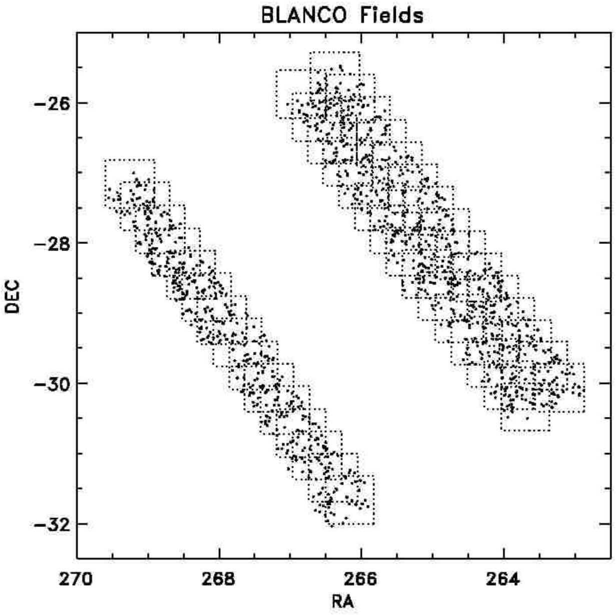

Figure 3.2: Pointings for the July 2010 Mosaic-II run. The dashed lines are the outlines of Mosaic-II fields we used for the optical side of the survey. The dots are X-ray positions in the initial GBS catalog.

next cycle. In the course of 8 nights, we completed 19 cycles though the fields. Because of overlap between fields, sources have at most 38 observations over 8 nights, though a very few sources have as few as 9 observations, which only happens if they are not in an spot where fields overlap and they rest on a chip gap for one of the dither positions. Sources most often have 2-4 observations per night, though some nights for some sources have none, 1, or 5 observations.

3.1.2 SMARTS 0.9m

We carried out these observations from June 1 to June 7, 2012. It is a $2k \times 2k$ pixel CCD, with a pixel scale of 0.401 arcsec/pixel. It is read out by an amplifier at each of the 4 corners of the chip. Each amplifier has a slightly different gain which also depends on gain index selected. We used index 2 to reduce readout time from 53 seconds to 32 seconds. The gain values of the amplifiers are, on average, 2.6 electrons/ADU with this index. The CCD saturates at 65000 ADU. The use of the Tek2K CCD on the SMARTS 0.9m at CTIO was an unplanned adjustment to circumstance. We had originally been granted time with the Y4K CAM on the 1.0m, which with a FOV of 20′ square covers over twice as much area of the sky as the Tek2K CCD, which has a FOV of only 13.6′ square. Our original plan had been to cover all of the X-ray targets that had saturated candidate counterparts in the Mosaic-II data, but because of the smaller field of view we had to limit this search to the NE corner of the survey area. The pointings we used were designed to optimize coverage of the stars saturated in Mosaic-II data in this region, and are displayed in Figure 3.3.

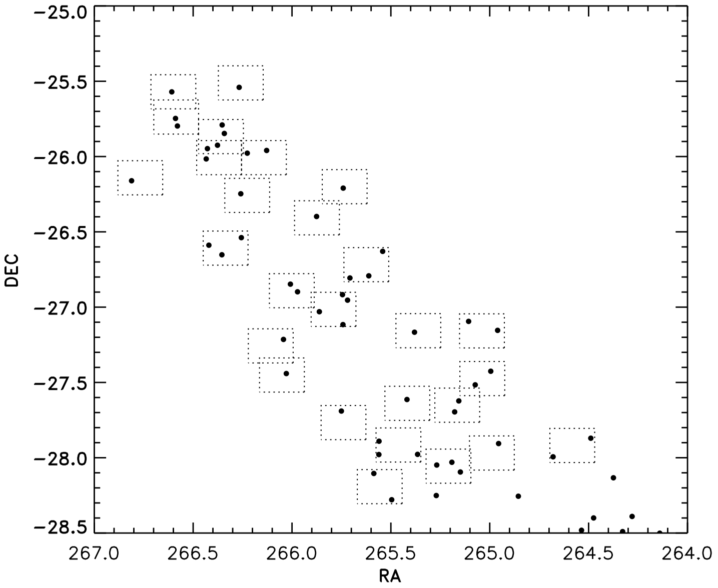

Figure 3.3: Pointings for the June 2012 0.9m run. The dots are X-ray positions in the GBS catalog. Coverage was limited by the small field of view on the instrument.

3.1.3 SMARTS 1.3m

For a handful of sources, we acquired nightly observations with queue observing through the SMARTS consortium. The SMARTS 1.3m telescope operates solely in service mode. The instrument, ANDICAM, has a 6′ FOV. It is a $2k \times 2k$ CCD with $0.15\,\mu$m pixels and a pixel scale of 0.371 arcsec/pixel, has a gain of 2.3 electrons/ADU and remains linear up to 45000 ADU, saturating at 65000 ADU. These brief observations were made twice a night from April 4 to July 19th, 2011 for several objects that showed variability on large timescales.

The objects observed were CX18, CX28, CX351, CX384, CX422, CX487, and CX561. These queue mode observations typically took 2 exposures a night. While this is not enough to determine a short period, for suspected outburst events such as dwarf novae that occur sporadically and last weeks this sampling rate is ideal.

3.1.4 Henrietta Swope Telescope

I spent a week, from June 21 to June 28, 2011, at the Henrietta Swope Telescope at Las Campanas Observatory in Chile with Dr. Valerie Mikles with the objective of monitoring targets of interest identified through spectroscopy by our collaborator Manuel Torres, as well as sources with candidate ellipsoidal variations or eclipsing systems in an effort to confirm suspected short periods from Mosaic-II data. The only instrument on this telescope is the SITe#3 CCD, which is $2k \times 3k$ pixels. For our observations, we used only a $2k \times 2k$ section of the CCD to save readout time. The pixel scale of the CCD is 0.435 arcsec/pixel, with a maximum FOV of $14.8' \times 22.8'$. The Sloan r' filters were not available, and we took these observations in Gunn r filters instead. We observed CX5, CX28, CX37, CX73, CX87, CX93, CX207, CX251, and CX794. We spent 4-5 hours continuously on each source, as well as a few observations on subsequent nights to extend the baseline of observations and further contrain period estimates.

3.1.5 Otto Struve 82-inch Telescope

To make an echo tomogram of Sco X-1, we obtained 12 nights from May 19 to May 30, 2009 with the Argos instrument on the 82-inch telescope at the McDonald Observatory in Texas concurrently with observations from the Rossi X-ray Timing Explorer (RXTE) satellite. I went with Dr. Robert Hynes and Dr. Valerie Mikles to make these observations. The Argos instrument consists of 2 CCDs, one of which is exposed for the science frame and then transfers the charge to the other for read out while another observations begins. This allows constant monitoring of an object with no downtime for readout. In order to read out in 1 s, however, the chip must be small, limited to 510×510 pixels. The pixel scale is

0.334 arcsec/pixel, which means the FOV is $2.8' \times 2.8'$. Each observation period lasted for 45 minutes, since that is the amount of time it took for Sco X-1 to rise and set for the RXTE satellite in its orbit. Optical exposures were 1s long in the BG-40 filter. We could open the dome on 8 of the 12 nights awarded. On the other 4 nights, thunderstorms prevented us from opening the telescope.

3.2 Data Reduction

CCDs are an improvement over photographic plates in many respects, so much so that the inventors of the CCD received the 2009 Nobel Prize in Physics. They operate by having a grid of electrodes held at some electric potential next to a semiconductor. When a photon of an energy greater than the Fermi gap strikes the semiconductor it promotes an electron. The electrons are held in the potential well of one of the electrodes, which constitutes a pixel. At low numbers of electrons, the CCD responds linearly to new photons; twice the photons yields twice the electrons. Once the number of electrons begins to “fill” the potential well of the pixel, however, the response of the CCD weakens and becomes non-linear. Eventually, the potential well of the of the pixel fills and no more electrons are held. These pixels are said to be saturated. If electrons continue to be promoted in a saturated pixel, they will “bleed” into nearby pixels. The CCD is read out through an amplifier by one column at a time as charge is transferred along the row to the edge of the chip, so the electrons bleed on this axis, forming “bleed trails” when enough overflowing electrons saturate pixels on the same row as the saturated star. The bleeding is constrained to the direction of readout because of insulating layers in between rows.

As with all instruments, however, they leave a signature on the data that needs to be removed to have any meaningful analysis. In order to keep a CCD’s readout positive, a pedestal bias voltage is applied during readout. This value often changes with both time and position on the CCD. To account for the time component, it is common practice to continue reading a CCD out beyond the point when all the data has been collected. This gives a few (usually 16 or 32) extra columns of just readout that can be fitted to an nth order polynomial to keep track of changes. These extra columns are called the overscan. To account for position dependence, one can read out the whole CCD without exposing it first. This is called a bias frame.

In general, electrons can be thermally excited above the Fermi gap in the semi-conductor used in CCD's (usually silicon). This "dark current" accumulates with time, making it proportional to exposure time. Some pixels are more easily excited than others, and this current must be measured and subtracted from each data frame. The Mosaic-II instrument, however, is cooled with liquid nitrogen and the dark current is so small ($\leq 2\text{e}^{-}\,\text{pixel}^{-1}\,\text{hr}^{-1}$) that it can be safely neglected for our 120 s exposures.

The light passing through the telescope is also altered by imperfections and dust on the filter and CCD window. Imperfections on the primary mirror do not actually leave any residual on the image at all, since it is exactly out of focus so the effects are spread out evenly across the image. These affects are multiplicative, and are removed by dividing the object frames by a flat field, which is an exposure of an evenly illuminated screen inside the dome of the telescope or of the twilight sky.

At infrared wavelengths, interference patterns can appear in images as monochromatic light from sky emission lines passes through the thin CCD chip. For our observations of standards in the i' band, we took deep images of empty patches of dark sky to measure this fringing, which can be removed from subsequent images by subtracting it out.

CTIO uses a data pipeline to reduce all the object frames from Mosaic-II which makes use of bias frames and flat fields taken during each night (Shaw, 2009). It also uses calibration files available online to correct for cross-talk between CCDs, ghost-pupil images, and patches of bad pixels on the CCD's with a bad pixel mask. It also applies a World Coordinate System (WCS) solution to images and roughly estimates the zero-point magnitude based on USNO-B1.0 stars in the field. Since the CCD is so large, there are optical distortions at the edge of the field of view, which is also corrected for in the pipeline. As such, the final pipeline product is a reprojected image, where the pixels are not the original CCD pixels, but are square on the sky.

I reduced data products from other CTIO and LCO instruments using the CCDRED package in IRAF[1]. First, all images are overscan corrected and trimmed. The residual bias frames are then combined into a master frame, which is subtracted from all other images. If dark current cannot be safely neglected, then this step is replaced by combining and subtracting dark frames from all images, which will also correct for the bias since the bias is applied during readout of the dark frames as well. Second, the bias-corrected flat fields are combined into a master frame. The master flat field is renormalized to an average value of 1 so that the average flux will be unaffected. The data frames are then divided by the master flat, so that differently illuminated sections of the CCD are renormalized. For multi-amplifier CCDs, the entire CCD should be flat fielded at once so that the renormalization is consistent across all parts of the image.

I reduced all of the optical data from Argos on the Otto Struve 82 inch telescope at the McDonald Observatory with IDL rather than in IRAF using programs previously written for the Argos instrument by Dr. Hynes. I used arithmetic functions in IDL to apply dark current corrections and flat field corrections. The chip on Argos is very small so that it can be read out quickly, so only 1 other bright star besides Sco X-1 is visible on the chip.

3.3 Analysis

Each reduced Mosaic image is enormous: over 8500×8650 pixels, varying slightly in size with atmospheric refraction corrections applied by the pipeline. In order to save on computation time, I used the WCS in each image to cut out postage-stamps around each X-ray source. When we started photometry, we used stamps that were 201 × 201 pixels. I found in the course of the project, however, that larger stamps of 401 × 401 pixels or 104" × 104" were necessary to obtain a good subtraction often enough that we began only using these larger

---

[1] IRAF is distributed by the National Optical Astronomy Observatory, which is operated by the Association of Universities for Research in Astronomy (AURA) under cooperative agreement with the National Science Foundation.

stamps. In one case where the stellar field suffered from both heavy extinction of background stars and from many saturated foreground stars, 801×801 pixel stamps were needed to well model atmospheric changes between observations, but this was an isolated occurrance. The WCS extends into gaps between CCD chips, so some of these postage stamps are useless for data analysis in the case that the source lies on the gap in some pointings, in which case they are ignored for photometry. To organize the large amount of data used by several people, I put each source in its own sub-directory with the postage stamp cut-outs of that source. To indicate when a source had been analyzed by someone, we used a Revision Control System to check out a list of sources and assign responsibility for the source. Several undergraduates (Ashley Villar, Monique Gabb, and Austin Baldwin), graduate students Chris Johnson and Andrew Collazi, and Dr. Hynes aided me in performing photometry on selected sources. I personally analyzed 53% of the objects for which photometry was possible and identified the 493 objects that either were saturated, had no counterpart, or appeared in no usable data. To ensure consistency of data quality, I have performed a final check on all results myself, in many cases redoing the photometry to obtain cleaner results for interesting sources.

3.3.1 Photometry

Over the course of the night, the observed brightness of each star changes as the stars rise and set, as the light must travel through changing amounts of air which leads to some extinction of light. The amount of air that light must travel through to reach the telescope is measured by the airmass, which is simply expressed as $a = secz$, where z is the angle between the star and the zenith. This formulation assumes a flat and infinite Earth, and therefore incorrectly approaches a limit of infinity at the horizon, but is fine for the altitude angles at which the telescope operates, which do not extend above an airmass of 3 because of the mechanical limitations of safely operating the Blanco 4m Telescope at the time.

Changes in the weather also change the amount of light seen by each star, as dust and water vapor in the air can reduce the transparency of the atmosphere. Also, the atmosphere can become more or less turbulent as the night progresses and from night to night. Pockets of air turbulence move and refract the starlight in different amounts, scattering the light and causing the familar "twinkling" character of starlight. Over a long exposure, these changes in refraction build up to form a roughly Gaussian distribution of light, called the Point Spread Function (PSF); the spatial Full Width at Half Maximum (FWHM) of the PSF is called the seeing and determines the maximum resolution possible for a given observation. "Good seeing" means the light is more focused on a few pixels, whereas "bad seeing" means the same amount of light from a star is widely distributed across a much larger area. Bad seeing increases noise in an observation and makes it much more difficult to distinguish fainter stars. Fig. 3.4 shows images of the same field from observations with good seeing and bad seeing.

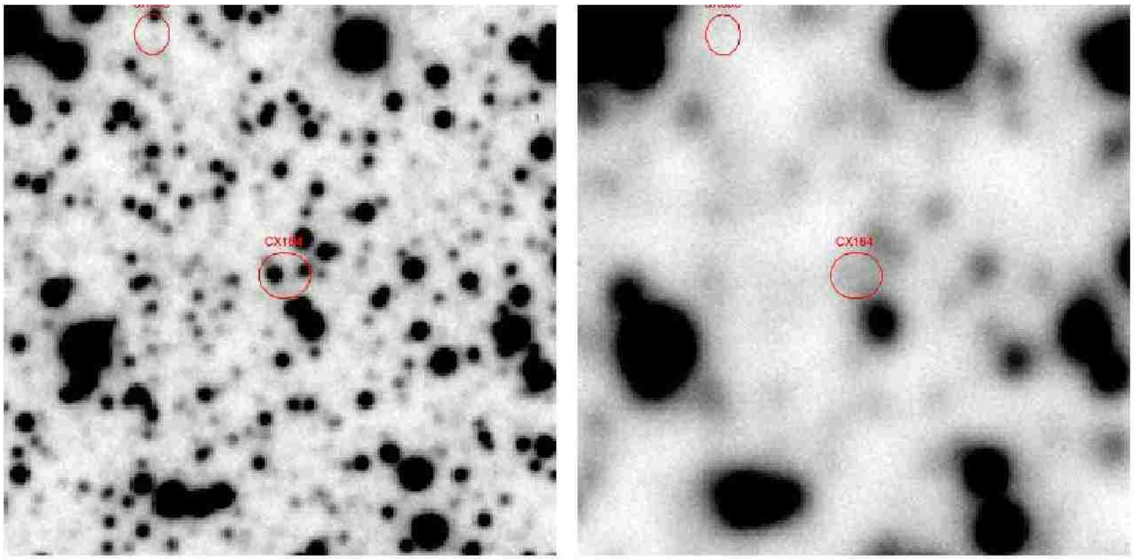

Figure 3.4: Left, the area around one of the X-ray sources in good seeing. Right, an observation of the same field in significantly worse seeing; many previously distinct stars are blended together or altogether lost to the eye as they are swamped by light from the sky and nearby brighter stars.

These changes affect all stars in the field of view equally, and so the ratio of light of stars should remain constant if the brightness of the stars is unchanging. Since magnitudes depend on the log of the flux, dividing one flux by another is equivalent to taking the difference between the magnitudes.

In order to track variability of stars, we use a software package written by Christophe Alard called ISIS, which uses image subtraction to determine changes in source brightness (Alard & Lupton, 1998; Alard, 2000). It makes use of the fact that the vast majority of stars are constant in magnitude to remove most of the coincident stars confused with the variable. It does this by convolving a reference image with a kernel to match each subsequent image. $Ref * Ker = I$ which can be solved as a least-squares problem by solving

$$\sum_i ([R * K](x_i, y_i) - I(x_i, y_i))^2 = 0$$

(Alard & Lupton, 1998). This is not in general linear, but can be made so by expressing the kernel as a summation of basis vectors.

$$K(u, v) = \sum_n a_n K_n(u, v)$$

These basis vectors should peak in the center and fall off, and should allow for complex shapes. Alard uses 3 basis vectors composed of a 2-D Gaussian with a polynomial component.

$$K_n(u, v) = e^{(u^2+v^2)/2\sigma_k^2} u^i v^j$$

The kernel can also be allowed to vary spatially over the image by adding a polynomial dependence to the basis vector coefficeints $a_n = \sum_{i,j} b_{i,j} x^i y^j$ (Alard, 2000). Flux conservation is added as a constraint to the least squares fit in order to get useful photometry as a result (Alard, 2000).

After the convolved reference image is matched to another image, the two are subtracted. The residuals should be due to changes in magnitude of variable stars. Stars of constant brightness should subtract out cleanly. Variables can be easily spotted by adding the square of these residuals, normalized by Poisson noise, as is shown in Fig. 3.5.

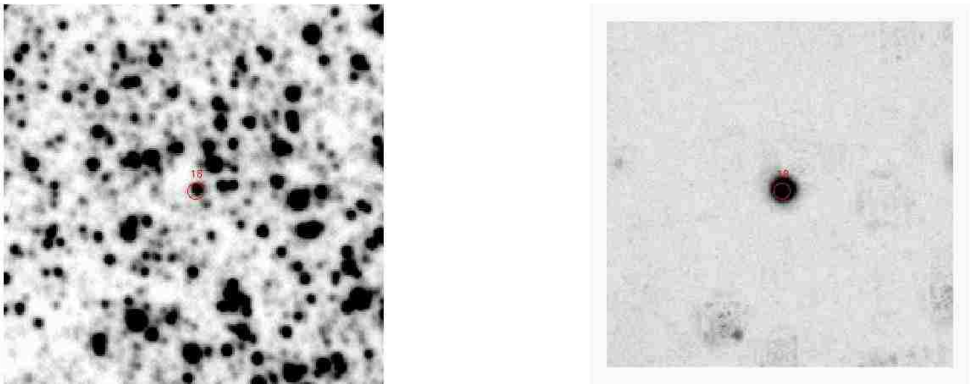

Figure 3.5: Left is the reference image of one of our X-ray sources, CX18 in the catalog. Right is the sum of the subtracted images normalized by the Poisson noise of the counts in the reference image.

Objects can appear to be variable in the aggregate variance image produced by ISIS when they are not for several reasons. First, non-linear or saturated stars a) do not transform with seeing in the same way that the rest of the sky does and b) have a significant amount of light scattered beyond the edge of the calculated PSF. The latter is most often a problem in bad seeing, but can be corrected by either increasing the size of the transformation kernel or by limiting the observations to those with good seeing. Second, cosmic rays and CCD defects can also cause spurious detections of variability. Third, although the data reduction pipeline operated by NOAO attempts to correct for it, cross-talk between CCD chips adds a low amplitude copy of the chip, which is most obvious in the "ghosts" of saturated stars on adjacent chips. These ghosts manifest as marginally higher background in a localized area whose location depends upon the orientation of the CCD and pointing of the telescope.

Once the subtracted images are in hand, photometry is done by fitting the PSF for that position using χ^2 minimization.

$$\chi^2 = \sum_i \frac{(x_i - am_i)^2}{\sigma_i} = \sum \frac{x^2}{\sigma^2} - 2a \sum \frac{mx}{\sigma^2} + a^2 \sum \frac{m^2}{\sigma^2}$$

Where x_i is the value of the subtracted frame at position i, m_i is the value of the PSF at the same point, and a is a scaling factor which yields the count rate. Differentiating with respect to a and setting the derivative equal to zero yields

$$a = \frac{\sum \frac{mx}{\sigma^2}}{\sum \frac{m^2}{\sigma^2}}$$

which gives us the count rate change between the reference image and the current image. Using this scaling, letting $\chi^2 + 1 = \sum \frac{(x-(a+\sigma_a)m)^2}{\sigma^2}$ and subtracting $\chi^2 + 1 - \chi^2$ yields the error in the photometric measurement $\sigma_a = \frac{1}{\sqrt{\sum \frac{m^2}{\sigma^2}}}$. The gain also affects the poisson noise proportionally by $\sqrt{gain}$, but it is easily corrected for by dividing the earlier term by $\sqrt{gain}$.

To save on computation time in running ISIS, I made postage stamp sized images of the area immediately around the X-ray position. I first made stamps 201 × 201 pixels, or 52" × 52". One of the drawbacks to using smaller fields is that there is less information to use for the subtraction, so clusters of saturated stars in the field can have a larger impact. Larger stamps were needed often enough that I generated larger postage stamps of 401×401 pixels, or 104" × 104", for every source. ISIS normally ignores pixels above a critical, user set value for subtraction, but the data pipeline from CTIO "cleans" the images of saturated stars and bleed trails by interpolating across saturated pixels. This makes the image look nicer, but it also means some flagging of saturated objects must be done outside of ISIS. The pipeline produces bad pixel maps, with several different flags including saturation. Since not every field has a high enough density of saturated stars to necessitate masking out saturated objects to obtain a clean subtraction, I found that it was easier and less time consuming to use IDL to raise pixel values on saturated objects back above the critical threshhold for those objects that required it, rather than incorporate the bad pixel masks into ISIS. I estimate this "blacking out" of saturated stars is necessary for $5 - 10\%$ of objects. The PSF fitting that ISIS uses to fit residuals after subtraction results in a count rate difference. In order to convert to magnitudes, or even to express the change in brightness in magnitudes, we must first calculate the number of counts present in the source in the reference image. By default, ISIS searches for bright, relatively isolated stars in the reference image and fits them. It is also possible to include a chosen position, so that photometry can be performed even on non-variable stars.

There are two other methods of estimating the magnitude of the source in the reference image: aperture photometry and PSF fitting. Aperture photometry adds up all the counts within a given radius and subtracts a sky level, usually determined from the mode of an annulus around the star in question. The disadvantage of this method in crowded fields is that there is no way to distinguish between nearby stars. A bright star nearby a dimmer one can dominate the counts inside the aperture. This leads to thinking the star is brighter than it actually is, which makes changes in magnitude appear smaller than they really are. This is not, in general, a large effect. This can be fixed by fitting a model PSF to each star, as we will get ISIS ultimately to do. In the meantime, we can use DAOPHOT II to estimate magnitudes of individual stars (Stetson, 1987). DAOPHOT will only output magnitudes, rather than counts, but because the zero point used is user defined, the two are equivalent.

The zero point accuracy is only as accurate as the magnitudes of the fainter stars in the USNO-B1.0 catalog, which are only good to ~ 0.5 magnitudes. This does not affect the relative magnitude of data points, only the zero point. For the purposes considered here, primarily X-ray to optical flux ratios, this is accurate enough.

3.3.2 Significance of Variability

The first check on whether an object is significantly variable is whether it shows up, shaped like the PSF, in the variance image. These checks are done first by eye. If there appears to be an object in the variance image, then we make a light curve. To check that the variability is significant, we compare the size of the statistical error bars calculated through χ^2 minimization in ISIS to the RMS of the variations in the lightcurve. Sources that show variations unattributable to statistical noise at the 3σ level are considered variable. Sources with a single observation in outburst or in eclipse are considered significantly variable if the observation in question is 4σ above the mean magnitude. With 30 observations per lightcurve and 720 lightcurves, a 3σ limit would result in ~ 58 observations spuriously declared to be outbursts or eclipses, while a 4σ limit results in only ~ 1 spurious outburst or eclipse.

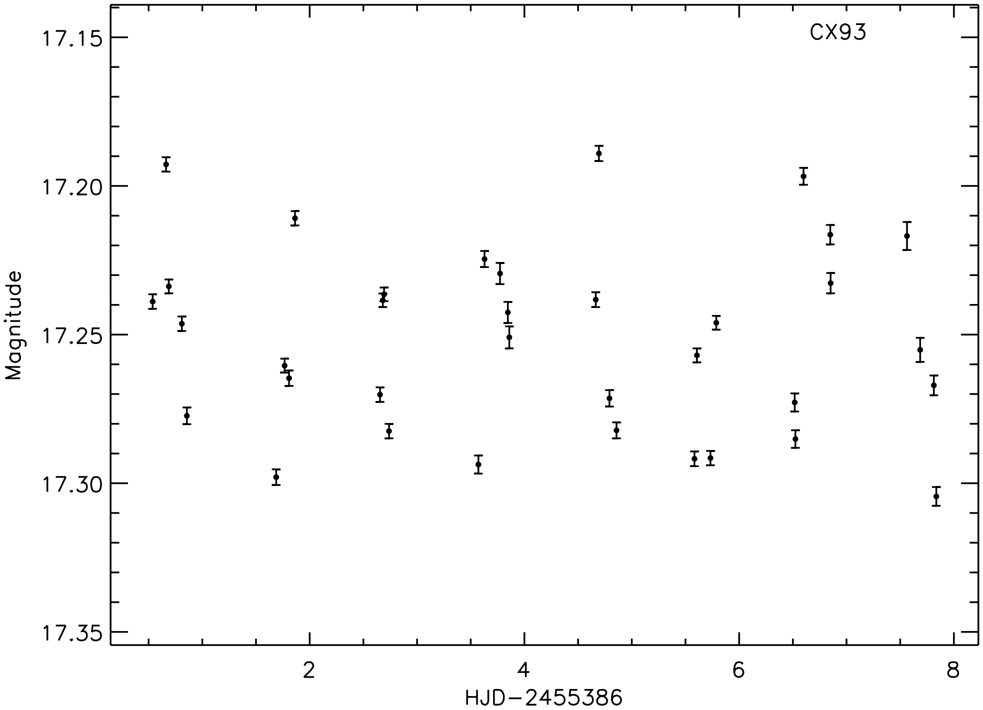

Figure 3.6: Lightcurve of CX93 using Mosaic-II data. No period is obvious to the eye.

3.3.3 Period Determination

To search for the period of a system, we use the Lomb-Scargle statistic in the Starlink PERIOD program[2], which is better for irregularly sampled data than Fourier analysis. In order to test the significance of potential periods, I ran Monte Carlo simulations on the light curve where the dates are matched at random to flux levels. To be considered significant, the candidate period must have a higher power than 99.73% (3σ) of the randomly generated Lomb-Scargle searches at *any* frequency to fairly account for the number of trials used. An example of a periodogram for the lightcurve shown in Figure 3.6 which has a significant peak is shown in Figure 3.7. Ellipsoidal modulations have a period 1/2 that of P_{orb}. The maxima

---

[2] http://www.starlink.rl.ac.uk/

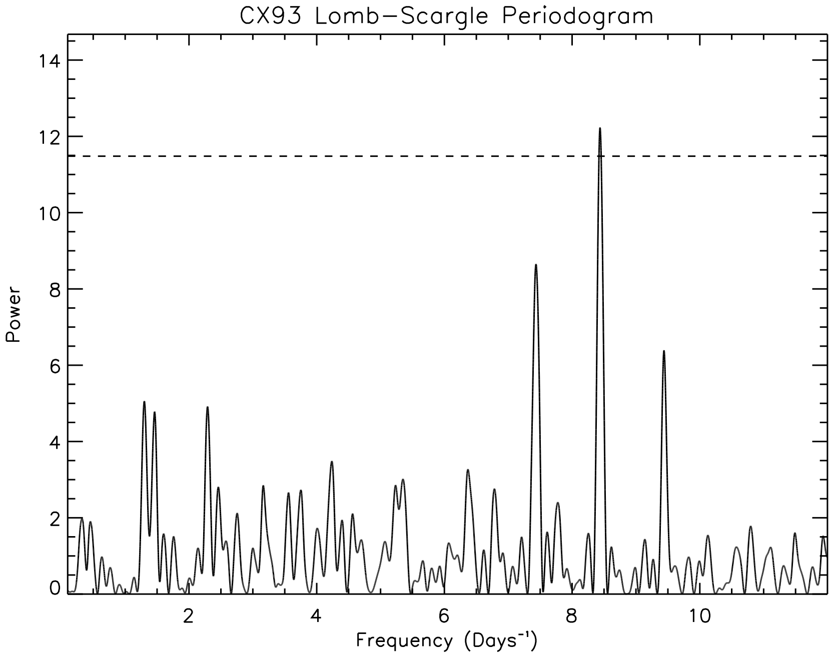

Figure 3.7: The Lomb-Scargle periodogram for CX93. The dotted line is the 3σ significance level. The two peaks on the side of the main peak are the 1 day aliases.

and minima of ellipsoidal variations, however, are often asymmetric with phase (that is, the orientation of the system in the orbital plane relative to the line of sight) because of the presence of a hotspot, and gravity darkening which could be counter-balanced by X-rays heating the side of the companion facing the compact object. Star spots are most likely single peaked, but can show variations of the same character as ellipsoidal modulations. If the period seen in the periodogram is P_{ellip}, then the phase-folded lightcurve should show some bimodality, where the lightcurve seems to split and follow 2 paths until rejoining, then splitting again. An example of this can be seen in the top panel of Figure 3.8. If this is real, then doubling the period given by the periodogram should be the real period, as shown in the bottom panel of Figure 3.8. The example source, CX93, is treated fully inRatti et al. (2013).

In the case of lightcurves easily modeled by either a single sine wave (or 2 with a 2:1 period ratio for the case of asymetric minima and maxima), errors on the period are calculated

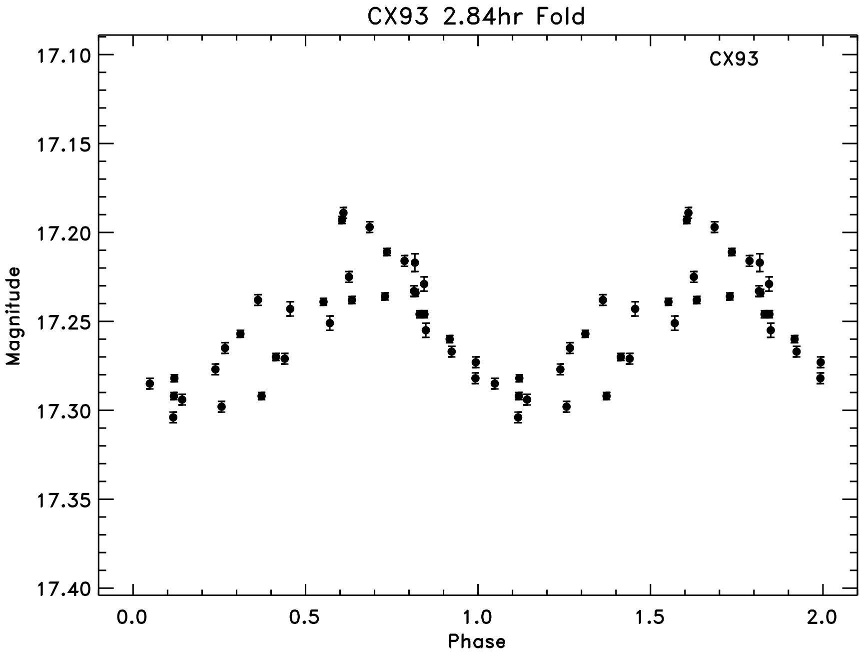

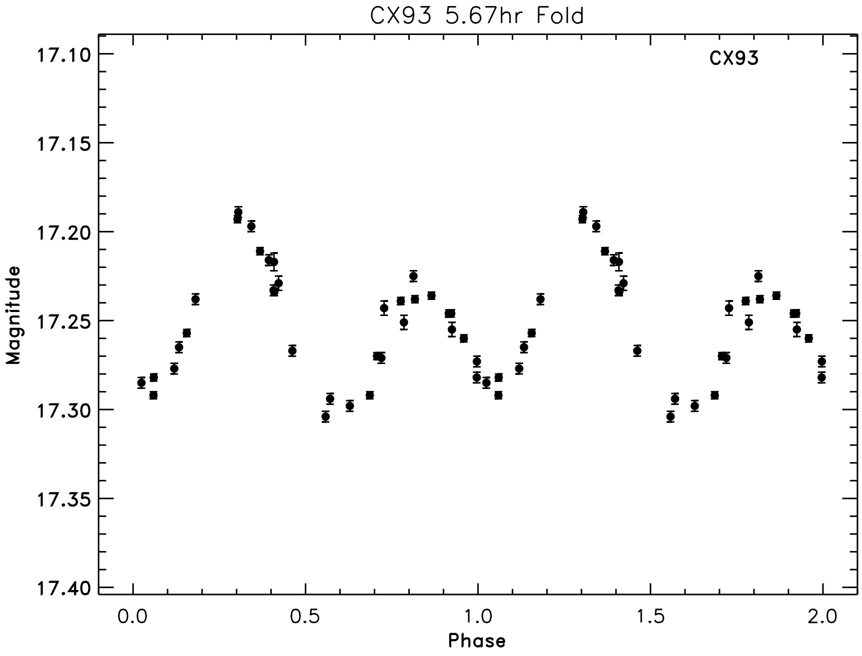

Figure 3.8: Top: Lightcurve folded on the strongest peak in the periodogram CX93. Bottom: Lightcurve folded on twice the period of the strongest peak in Fig. 3.7

through χ^2 analysis. For a Gaussian distribution of errors, the $1 - \sigma$ confidence region of a single variable is when the χ^2 statistic increases by 1.

For more complicated lightcurve morphologies, I use the bootstrapping method to calculate errors on the period. In bootstrapping, one selects a number of points N from the data set with replacement, where N is the number of points in the set, and fits whatever model one is calculating errors for on the newly generated data set. Essentially, all N data points are put into a hat, and one is drawn at a time, placed back in the hat, and repeated N times, resulting in a data set with some repeated points and reduced information. The distribution of the resulting fits is the same as the error distribution of the full data set. This does not rely on a Gaussian distribution of errors as χ^2 fitting does. In my case, I make a new periodogram for each "new" data set and calculate the error in the period based on the spread of the periods found. See (Hynes & Britt, 2012) for an example of this method.

3.4 Spectral Analysis

I have also examined optical/NIR spectra of selected counterparts to GBS sources. This analysis has been published in Britt et al. (2013). Strong emission lines are often an indication of gas being irradiated, as electrons are excited by incident photons bombarding the gas and emit light at characteristic wavelengths as they fall to lower energy orbits. They can also arise when electrons are excited collisionally. In both cases, an emission line object is very likely to be the true counterpart.

A star's spectrum can be extracted in multiple ways, most commonly and in this work by laying a slit across the field to isolate light from stars of interest on one axis on the CCD, then splitting that light into different colors with a diffraction grating or grism. The second axis on the CCD is then composed of different wavelengths of light. Some instruments select stars with optical fibers placed over the star, leading the light to a CCD. These instruments have the advantage of being able to observe multiple targets that are not in a straight line. NTT and VIMOS both use one or more slits to isolate stars of insterest.

I selected 5 emission line objects from our spectroscopic campaigns for more detailed follow-up. These objects are CX5, CX18, CX28, CX37, and CX561. My collaborator Manuel Torres reduced the spectroscopic data. The following text is adapted under copyright agreement from Britt et al. (2013). Data were acquired between July 8th, 2010 and July 11th, 2010 under program 085.D-0441(C) with the New Technology Telescope (NTT) equipped with the ESO Faint Object Spectrograph and Camera (EFOSC2). The observations were performed using grism #13 and a 1" wide slit that provided an instrumental spectral resolution of ~ 17 Å (FWHM) in the $\lambda\lambda = 3700 - 9200$ Å wavelength range. Integration times ranged between 400 s and 900 s. HeAr arc lamp and flat field exposures were taken after each target observation. Additionally, on April 2nd, 2011 two consecutive 875 s spectra of the optical counterpart to CX28 were obtained with the Visible Multi Object Spectrograph (VIMOS; LeFevre et al. 2003) mounted on the ESO Very Large Telescope under program 085.D-0441(A). The MR red grism and a 1" wide slit were used, achieving a spectral resolution of 10 Å FWHM and a wavelength range of $\lambda\lambda = 4600 - 10000$ Å.

The EFOSC2 data set was bias and flat-field corrected with standard IRAF routines. The spectra were extracted with the IRAF KPNOSLIT package. The pixel-to-wavelength calibration was derived from cubic spline fits to HeAr arc lines. The root-mean square deviation of the fit was < 0.1 Å. Checks for the stability of the wavelength calibration were made using the atmospheric [O I] 5577.34 and 6300.3 Å sky lines. In this way we estimated an accuracy in the wavelength calibration of < 0.5 Å. The VIMOS spectra of CX28 were reduced with the VIMOS ESO pipeline version 2.6.2 (Izzo et al. 2004) and extracted using IRAF (see Torres et al. 2013 for details).

4. Variability of Counterparts to GBS Sources

I have examined optical images of every source. 341 sources are saturated or are coincident with a saturated star in Mosaic-II data. 69 of these are brighter than $V = 12$ and are in the Tycho-2 Catalog of Bright Stars (Høg et al., 2000). Hynes et al. (2012) examined these and concluded most were real counterparts to the X-ray source. Of the 341 sources for which photometry is impossible due to the presence of a saturated star in Mosaic-II data, 238 are within the X-ray error circle of the center of the saturated star. Also, 155 stars have no visible counterpart. Some of these are due to heavy foreground extinction, which can be identified by the dearth of stars in the images, while others may become visible after stacking images if they simply have $m_{r'} > 23$. Stacking N good images of equal exposure time will increase the effective signal to noise ratio by, at best, $\sqrt{N}$, though ultimate depth is limited by the quality of flat fielding and by crowding of faint sources, so actual improvements will be by some factor $< \sqrt{N}$. Some of these sources have as many as 20 exposures with seeing $< 1.5''$, which, when stacked, would lead to an effective improvement in sensitivity of, at best, 1.6 magnitudes.

The remaining 723 sources have all been run through ISIS and examined individually. I conducted an automated run on every source in the summer of 2011 to aid in targeting spectroscopic campaigns, but many fields require tailoring parameters in ISIS to obtain clean subtractions.

4.1 Overview of Variability

I define variability as sources having an RMS scatter of at least 3 times the average statistical error, or having one or more data points more than 4 times the statistcal error above or below the mean magnitude. Our sensitivity to variability is quite high (confident detection of variability with an amplitude of hundredths of magnitudes) for sources between $r' = 16$ and $r' = 19$. Sensitivity declines to a tenth of a magnitude at $r' = 22$. At $r' = 23$, we are effectively blind to all but the most dramatic of changes with typical relative photometric errors of 0.2 magnitudes. Errors can also be larger if the target is sufficiently close to much brighter objects than the target.

Of the 1234 X-ray sources from the first three quarters of the Chandra observations, 238 are aligned with counterparts saturated in the Mosaic-II data. A further 98 sources are too near a saturated star or a bleed trail to do photometry on. 155 sources have no visible counterpart in Sloan r' inside the 95% X-ray confidence region. Of the remaining sources, 545 have no counterpart that shows variability over the course of our observations in the 95% confidence region. 7 lie outside regions imaged by Mosaic-II. 16 sources are likely duplicates of the same X-ray source that were not successfully removed when the catalog was made. The remaining 168 sources have likely counterparts that show variability during our observations. The majority of variables show variations for which we were unable to recover a period, which I will refer to as flickering.

Inevitably when examining 1216 unique sources, variables occasionally lie outside the 95% confidence region. Approximately 61 true counterparts should lie just outside the 95% confidence region, which means we should have ≈ 9 variable true counterparts falling outside the error region given the observed rate of variability. This is less than the ~ 25 chance variables just outside the error region that one expects. Sources that show morphology unique to CVs or LMXBs, such as DN outbursts, should be considered the counterpart even if lying outside the listed 95% confidence region. Sources showing more ubiquitous morphologies, such as sinusoidal or ellipsoidal modulations irrespective of period, should be considered to be more likely to be a chance alignment than the true counterpart without other compelling evidence to the contrary. The number of sources we have in each category of variability is shown in more detail in Figure 4.1

The X-ray to optical flux ratio is calculated in Table 4.1 for sources with confirmed counterparts for both absorbed and unabsorbed flux assuming bulge distance using assumptions in Jonker et al. (2011), the extinction law $R_V = 3.1$ found in Cardelli et al. (1989), and the relation between optical extinction and hydrogen column density $N_H = 0.58 \times 10^{22} \times A_V$

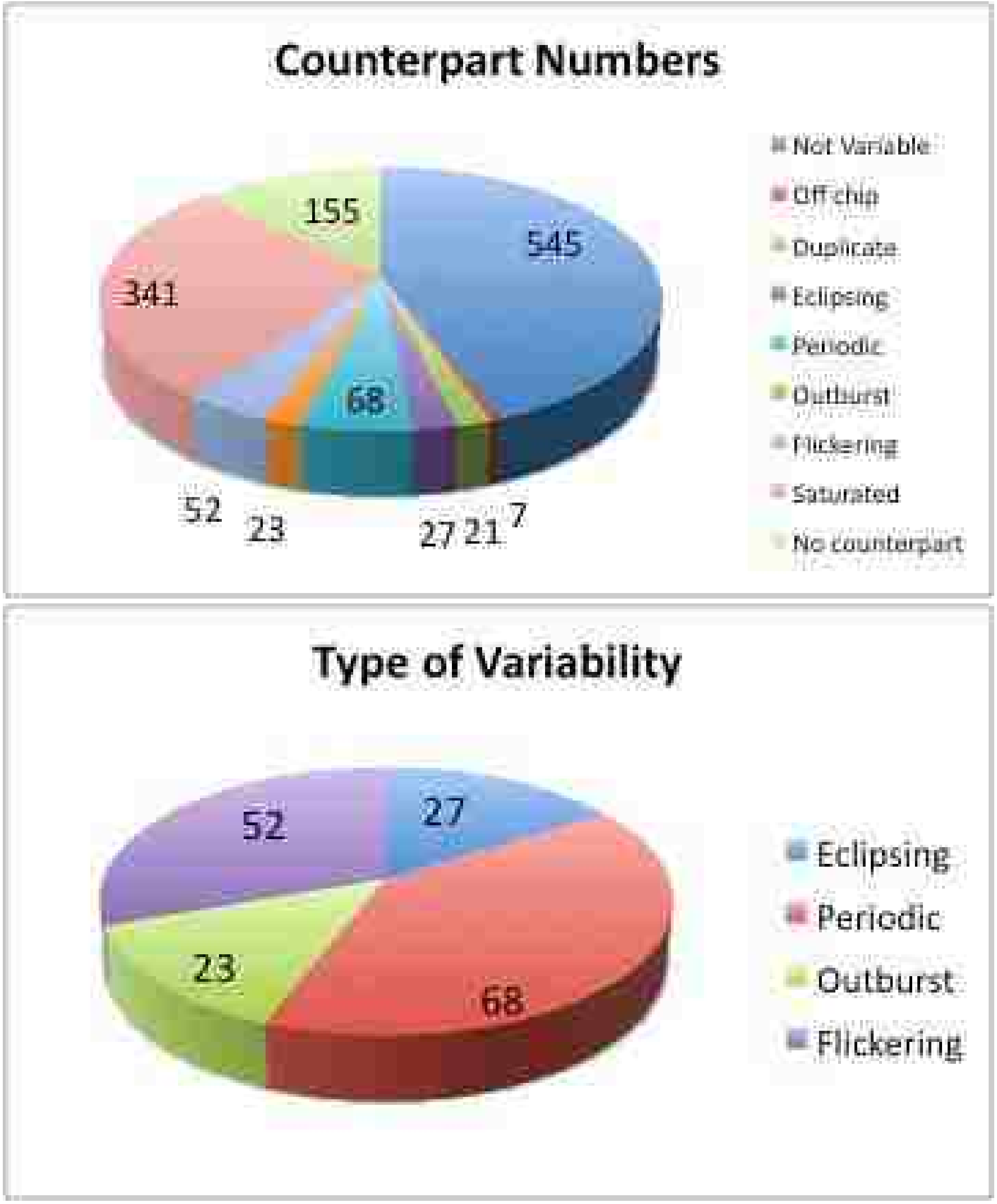

Figure 4.1: The chart above shows the total breakdown of sources in Mosaic-II data. The largest category is non-variables, with sources either saturated or obscured by bleed trails as the second largest. The bottom panel shows the number of variables in each category of variability, those being periodic oscillations (both sinusoidal and ellipsoidal), eclipses, flickering or irregular variability, and outbursts of some form.

from Bohlin et al. (1978). For bulge extinction values, we use the maps from Gonzalez et al. (2012). Many sources are closer than bulge distance, so the absorbed and estimated unabsorbed flux ratios represent approximate upper and lower limits, respectively, to $\frac{F_X}{F_{Opt}}$. We transform these values to the Sloan r' filter using filter properties given in Schlegel et al. (1998). We do not expect to detect sources with an X-ray luminosity below $10^{32}\,\mathrm{ergs\,s^{-1}}$ at Bulge distance, so RS CVns, W UMas, CVs, and BH qLMXBs should tend to have a real value towards the upper end of a source's range possible flux ratios.

A surprising number of sources (545) show no detectable optical variability. For some of these, the true counterpart could be below detection limits, leaving only field stars coincident with the X-ray position. However, there are also 155 sources with no possible counterpart in Sloan $r' < 23$, while in Jonker et al. (2011), it was predicted that the GBS would find a number of 380 sources in Mosaic-II fields without a counterpart. The predicted number is much higher than that observed. Sources with large errors on the X-ray position admit many possibilities as counterparts, but the true counterpart may be below detection limits. There are 291 sources with an estimated error with a radius larger than 3", each of which admits probable chance alignments. The number of non-variables is much greater than the number of sources that admit spurious counterparts, however. This suggests that many of the counterparts are indeed non-variable.

Our discovery efficiency is quite high for eclipsing sources and even small amplitude flickering and periodic sources (Ratti et al., 2013; Britt et al., 2013; Torres et al., 2013). Still, it is difficult to place constraints on the make-up of these non-variables because we have spectroscopically confirmed that some systems that we would expect to show either flickering or ellipsoidal modulations do not, in fact, vary at all [e.g. CX561 (Britt et al., 2013), CX1004 (Torres et al., 2013)].

The sources with variable counterparts are listed in Table 4.1. Sources with the RMS scatter greater than 3 times the statistical error in the measurements are considered to be variable. Sources with at least a single data point more than 4 sigma from the mean magnitude are also considered to be variable. Individual sources of interest will be discussed in Chapter 5.

Table 4.1: Below is listed variability information for every counterpart that showed some variability above background level in the variance image, described in Chapter 3.

CX ID	r' mag	$<$ error $>$	RMS	N	Absorbed $\log \frac{F_X}{F_{opt}}$	$E(B-V)$	$\log \frac{F_X}{F_{opt}}$
2	18.14	0.004	0.027	36	1.9	1.72	0.3
5	18.61	0.005	0.084	28	1.0	2.73	-1.6
11	20.70	0.025	0.164	33	1.6	2.10	-0.4
18	17.36	0.003	0.577	19	0.0	1.45	-1.3
19	19.21	0.007	0.243	20	0.8	1.99	-1.0
21	18.46	0.004	0.371	18	0.5	2.64	-2.0
23	17.96	0.003	0.025	36	0.2	2.06	-1.7
28	16.89	0.002	0.204	28	-0.3	1.47	-1.6
29	16.83	0.001	0.036	19	-0.3	2.75	-2.9
37	19.33	0.009	0.187	33	0.6	1.89	-1.1
39	19.80	0.018	0.413	29	0.8	1.86	-0.9
44	18.68	0.004	0.055	19	0.2	1.48	-1.1
48	17.21	0.002	0.010	32	-0.4	2.06	-2.2
49	20.09	0.024	0.105	18	0.7	1.15	-0.2
54	21.05	0.048	0.207	19	1.1	1.52	-0.2
67	17.92	0.002	0.015	28	-0.2	1.82	-1.8
73	18.62	0.006	0.076	27	0.1	1.98	-1.7
74	15.54	0.001	0.071	17	-1.2	1.43	-2.4
80	16.11	0.001	0.025	9	-0.9	3.19	-3.9

Continued on Next Page

(Table 4.1 continued)

CX ID	r' mag	< error >	RMS	N	Absorbed log $\frac{F_X}{F_{opt}}$	$E(B-V)$	log $\frac{F_X}{F_{opt}}$
81	20.10	0.036	1.503	18	0.7	2.47	-1.6
84	19.02	0.007	0.029	35	0.2	1.98	-1.6
87	23.50	0.248	1.625	22	2.0	1.81	0.3
88	17.42	0.002	0.008	16	-0.5	1.62	-1.9
93	17.25	0.003	0.031	35	-0.5	1.61	-2.0
96	23.49	0.197	0.612	37	2.0	3.34	-1.2
105	17.36	0.002	0.040	19	-0.5	2.96	-3.3
118	17.62	0.003	0.169	34	-0.4	1.98	-2.2
128	20.92	0.044	0.259	18	0.8	1.55	-0.5
161	19.07	0.008	0.083	32	0.0	2.34	-2.1
168	16.71	0.001	0.031	37	-0.9	3.03	-3.7
184	19.00	0.005	0.039	37	-0.0	2.55	-2.4
190	18.23	0.005	0.042	36	-0.4	1.72	-1.9
195	16.27	0.001	0.063	22	-1.2	1.86	-2.8
196	18.08	0.005	0.036	17	-0.4	3.41	-3.7
207	21.12	0.064	0.880	18	0.8	2.07	-1.1
222	16.63	0.001	0.008	26	-1.1	1.91	-2.8
239	19.11	0.018	0.121	67	-0.1	1.68	-1.6
246	17.19	0.002	0.006	36	-0.8	3.68	-4.4
251	16.97	0.001	0.016	17	-0.9	3.31	-4.1
279	18.82	0.010	0.223	18	-0.3	1.40	-1.5
282	19.79	0.016	0.102	24	0.1	1.68	-1.4
291	19.47	0.014	0.085	35	0.0	1.59	-1.4

Continued on Next Page

(Table 4.1 continued)

CX ID	r' mag	$<$ error $>$	RMS	N	Absorbed $\log \frac{F_X}{F_{opt}}$	$E(B-V)$	$\log \frac{F_X}{F_{opt}}$
298	22.72	0.205	0.748	26	1.2	1.44	-0.0
300	16.29	0.001	0.007	20	-1.3	2.08	-3.2
330	17.26	0.002	0.067	18	-0.9	2.07	-2.8
331	18.23	0.005	0.037	33	-0.5	1.71	-2.1
332	17.54	0.002	0.011	24	-0.8	1.86	-2.5
335	17.08	0.002	0.023	12	-1.0	1.59	-2.4
336	17.00	0.002	0.062	19	-1.0	1.77	-2.6
346	15.75	0.001	0.023	25	-1.6	1.71	-3.1
349	23.06	0.117	0.388	17	1.4	2.10	-0.6
354	16.41	0.001	0.089	23	-1.4	1.39	-2.6
361	17.15	0.002	0.023	34	-1.0	1.49	-2.3
368	18.04	0.004	0.088	34	-0.7	1.74	-2.2
376	16.36	0.001	0.013	35	-1.4	1.54	-2.7
377	18.89	0.009	0.060	36	-0.3	2.01	-2.1
399	17.88	0.002	0.015	38	-0.7	2.21	-2.7
411	18.02	0.003	0.026	34	-0.7	1.90	-2.4
420	18.80	0.005	0.041	19	-0.4	2.43	-2.7
426	17.99	0.003	0.320	19	-0.8	1.37	-2.0
437	22.36	0.123	0.798	17	1.0	1.79	-0.6
439	20.70	0.013	0.142	18	0.3	2.15	-1.6
450	17.78	0.003	0.060	26	-0.8	3.19	-3.8
484	17.85	0.003	0.018	33	-0.8	1.88	-2.5
536	16.66	0.001	0.016	14	-1.4	1.80	-3.0

Continued on Next Page

(Table 4.1 continued)

CX ID	r' mag	< error >	RMS	N	Absorbed log $\frac{F_X}{F_{opt}}$	$E(B-V)$	log $\frac{F_X}{F_{opt}}$
585	19.50	0.010	0.511	16	-0.1	3.80	-3.8
645	18.44	0.006	0.632	21	-0.6	2.03	-2.5
691	16.76	0.001	0.006	10	-1.5	1.28	-2.5
730	17.96	0.001	0.021	34	-0.8	4.29	-5.0
740	18.19	0.003	0.013	25	-0.7	3.93	-4.6
741	16.73	0.002	0.017	21	-1.3	4.17	-5.4
744	17.52	0.002	0.042	19	-1.1	2.63	-3.5
748	18.43	0.003	0.012	26	-0.7	3.41	-4.0
750	18.14	0.003	0.114	29	-0.8	3.35	-4.0
755	16.36	0.003	0.112	34	-1.6	1.75	-3.2
774	19.78	0.017	0.102	38	-0.2	2.09	-2.1
792	17.64	0.003	0.012	34	-1.1	1.68	-2.6
794	20.08	0.018	0.496	28	-0.1	1.97	-1.9
800	18.81	0.009	0.060	36	-0.6	1.64	-2.1
816	17.80	0.004	0.022	30	-1.0	1.52	-2.3
818	16.42	0.002	0.010	37	-1.6	1.55	-2.9
819	18.04	0.005	0.025	28	-0.9	1.45	-2.2
820	17.53	0.003	0.015	19	-1.1	1.52	-2.4
837	18.51	0.006	0.020	18	-0.7	2.09	-2.6
838	16.89	0.002	0.008	25	-1.4	1.61	-2.8
847	16.94	0.002	0.011	35	-1.3	1.85	-3.0
853	16.71	0.002	0.051	32	-1.5	1.48	-2.8
855	19.22	0.009	0.038	36	-0.4	1.93	-2.2

Continued on Next Page

(Table 4.1 continued)

CX ID	r' mag	< error >	RMS	N	Absorbed log $\frac{F_X}{F_{opt}}$	$E(B-V)$	log $\frac{F_X}{F_{opt}}$
858	16.36	0.001	0.027	26	-1.6	1.48	-2.9
860	22.68	0.247	1.016	18	0.9	1.30	-0.2
870	20.30	0.030	0.128	36	-0.0	1.58	-1.4
881	17.47	0.002	0.013	36	-1.2	2.49	-3.5
887	20.65	0.030	0.123	23	-0.0	1.53	-1.3
895	16.53	0.002	0.028	34	-1.7	1.47	-3.0
905	20.37	0.022	0.162	12	-0.2	1.08	-1.1
909	17.22	0.002	0.016	28	-1.3	2.33	-3.5
910	16.53	0.001	0.018	19	-1.7	1.36	-2.8
926	18.76	0.004	0.021	18	-0.7	1.86	-2.4
929	17.50	0.002	0.024	17	-1.3	1.12	-2.3
930	20.38	0.019	0.308	17	-0.2	1.14	-1.1
944	17.66	0.003	0.041	18	-1.2	1.61	-2.6
953	16.83	0.001	0.017	17	-1.5	2.27	-3.6
957	18.76	0.009	0.031	36	-0.8	1.59	-2.1
966	18.78	0.006	0.044	24	-0.7	2.22	-2.7
971	20.07	0.012	0.072	12	-0.2	1.69	-1.7
973	18.60	0.006	0.069	36	-0.8	2.11	-2.7
982	21.29	0.047	0.556	37	0.3	1.99	-1.5
985	18.23	0.002	0.031	9	-0.9	2.18	-2.9
990	17.95	0.002	0.018	18	-1.0	4.05	-4.9
995	19.96	0.014	0.193	32	-0.3	1.90	-2.0
997	17.32	0.002	0.020	38	-1.3	2.59	-3.7

Continued on Next Page

(Table 4.1 continued)

CX ID	r' mag	< error >	RMS	N	Absorbed log $\frac{F_X}{F_{opt}}$	$E(B-V)$	log $\frac{F_X}{F_{opt}}$
999	17.32	0.003	0.031	32	-1.3	1.84	-3.0
1008	17.01	0.002	0.025	18	-1.4	2.05	-3.3
1011	16.19	0.001	0.030	17	-1.7	3.15	-4.7
1014	16.72	0.001	0.015	36	-1.5	3.33	-4.7
1019	16.66	0.002	0.056	7	-1.6	1.84	-3.2
1029	17.95	0.004	0.039	19	-1.1	1.28	-2.2
1032	18.01	0.005	0.034	31	-1.1	1.61	-2.5
1045	16.77	0.002	0.019	34	-1.6	1.63	-3.0
1051	18.37	0.006	0.022	19	-0.9	2.09	-2.8
1056	18.74	0.006	0.022	37	-0.8	1.60	-2.2
1060	16.43	0.002	0.014	37	-1.7	1.55	-3.0
1061	18.16	0.003	0.033	34	-1.0	1.66	-2.5
1068	16.92	0.002	0.022	22	-1.5	1.43	-2.8
1071	17.20	0.002	0.036	36	-1.4	1.89	-3.1
1086	18.55	0.004	0.069	70	-0.8	2.11	-2.8
1097	18.05	0.005	0.017	30	-1.0	1.71	-2.6
1099	19.94	0.016	0.057	32	-0.2	2.25	-2.3
1118	17.66	0.003	0.019	15	-1.1	2.82	-3.8
1123	16.74	0.002	0.015	36	-1.6	1.53	-2.9
1140	19.28	0.009	0.033	34	-0.5	2.29	-2.6
1149	16.40	0.001	0.026	15	-1.7	2.07	-3.6
1152	17.63	0.003	0.023	36	-1.2	1.74	-2.8
1153	16.61	0.001	0.014	37	-1.6	1.91	-3.3

Continued on Next Page

(Table 4.1 continued)

CX ID	r' mag	$<$ error $>$	RMS	N	Absorbed $\log \frac{F_X}{F_{opt}}$	$E(B-V)$	$\log \frac{F_X}{F_{opt}}$
1158	18.82	0.006	0.025	32	-0.7	1.95	-2.5
1167	17.80	0.003	0.024	34	-1.1	1.71	-2.7
1179	18.53	0.005	0.034	34	-0.8	2.19	-2.8
1184	17.66	0.003	0.028	18	-1.2	1.55	-2.5
1186	19.36	0.008	0.157	18	-0.5	1.88	-2.2
1187	17.33	0.002	0.019	10	-1.3	1.64	-2.8
1194	16.55	0.001	0.013	34	-1.6	1.72	-3.2
1198	16.29	0.001	0.006	26	-1.7	1.71	-3.3
1205	18.94	0.005	0.030	35	-0.7	1.43	-2.0
1220	16.29	0.001	0.027	17	-1.8	1.35	-2.9
1228	16.71	0.001	0.020	22	-1.6	1.47	-2.9
1232	19.48	0.013	0.085	27	-0.5	1.71	-2.0

4.2 Periods

Our observations have a high rate of period recovery for systems with little to no flickering. As aperiodic fluctuations begin to overtake the periodic, however, we lose the ability to reliably recover periods with the limited sampling we have. To quantify this, I have run Monte Carlo simulations to determine the rate of period recovery for various periods with our average level of sampling at different relative amounts of flickering, the results of which are shown in Figure 4.2. For quiescent LMXB systems in which $\gtrsim \frac{1}{2}$ of the light should come from the donor star rather than the accretion disk, we expect to recover almost all periods between 2 and 23 hours. We do suffer from aliasing around 1 day, which is an expected and unavoidable result of being able to observe only at night. We cannot claim strong evidence of periods longer than 4 days because our baseline of observations only extends 8 days and we cannot, therefore, see a suspected period > 4 days repeat. All periods listed greater than 4 days should be treated as suspected pending other observations. Some systems show a long rise or a single crest or trough. After matching these to the recovered counterparts in OGLE IV data (Udalski et al., 2012), the majority of these systems are long period variables with $P_{orb} > 8$ days. Some are irregular variables with characteristic timescales of days or longer, such as CX332 (Hynes et al., 2013).

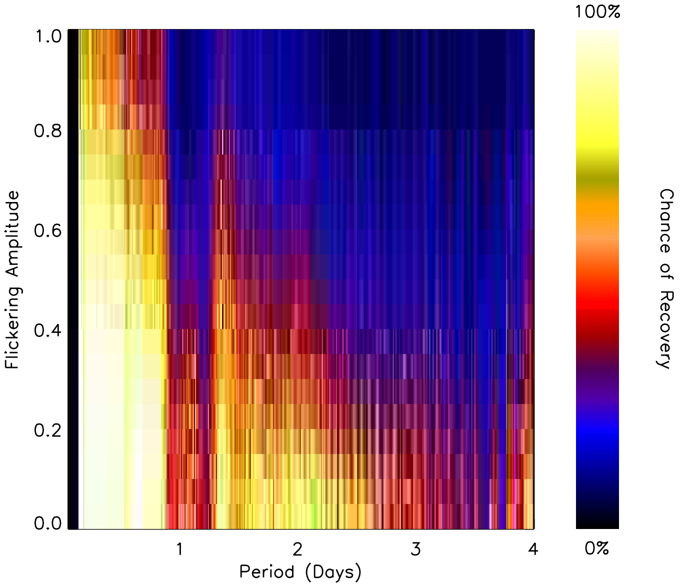

Figure 4.2: This plot shows the likelihood of recovering a given period at different levels of flickering imposed on the underlying periodicity for our Mosaic-II observations. As you can see, it is unlikely that we recover photometric periods below 2 hours, though we maintain better than even chances of recovering periods between 2 hours and 1 day through the RMS of random variations being 80% of the amplitude. Loss of sensitivity due to aliasing around 1 day is apparent. For qLMXBs with periods above 1 day, the donor should comprise a larger fraction of the continuum light because of its larger radius, so random flickering originating in the disk should be smaller amplitude compared to shorter period systems. For RS CVns and W UMas, there should be no intrinsic flickering, with the only noise being photometric error on the order of < 1% for sources brighter than $r' = 19$.

The period distribution, shown in Figure 4.3 is a broad indicator of the types of sources we are finding. As mentioned in Table 1.1, RS CVns tend to have periods of days, W UMas have periods less than a day, while the period of LMXBs depends on the mass and evolutionary stage of the donor. The naive expectation from Kepler's 3rd Law is that the mass of the primary will affect the period of the system, but the Roche Lobe geometry changes as a function of the mass ratio in such a way as to counter this dependence. For main sequence donors, the period is on the scale of hours with $M_2 \approx 0.11\, P_{hr}$, but periods of days are possible for subgiant or giant donors. The fact that most LMXBs known are transient rather than persistent suggests at least some chemical evoltuion of the secondary away from the Zero Age Main Sequence (Lewin & van der Klis, 2006). Of the population of currently known LMXBs, the period distribition peaks around 5-6 hours (Lewin & van der Klis, 2006), though systems with periods > 1 day are certainly known. Non-magnetic CV systems, of which we expect ≈ 46 with optical counterparts in the Mosaic-II area, have a bimodal distribution peaking at 1.5 hours and 3.5 hours for X-ray selected CVs, with a substantial gap in between 2-3 hours that is known as the CV period gap (Gänsicke, 2005). We expect hundreds of RS CVn systems (Jonker et al., 2011), and only 120 LMXBs, so the vast majority of systems with $P_{orb} > 1$ day should be RS CVns rather than LMXBs, though it is likely that a select few LMXBs can be found at these periods. The period distribution for likely counterparts to X-ray sources in the GBS is displayed in Figure 4.3.

As can be seen in the period histogram for GBS counterparts in Mosaic-II data, we have not found 120 systems with ellipsoidal variations with periods below a day. There is a spike in the histogram at period of 5-6 hours, as is expected for LMXBs and CVs. Unfortunately, this spike contains only 7 sources. The sources with periods above 1 day are largely RS CVNs, though there are a few possible LMXBs in this region as well, e.g. CX855. Most RS CVns in the GBS are saturated in Mosaic-II data, as extrapolated from the plot of X-ray versus optical luminosity shown in Figure 4.4 in conjunction with the predictions in Jonker et al. (2011). The fainter tail of the distribution is what we pick up in our Mosaic-II data. We also have contamination from W UMas, which have periods < 1 day and can resemble ellipsoidal variations. W UMas likely comprise a large number of sources with periods below a day, but in some cases they cannot be readily distinguished from ellipsoidal variations without

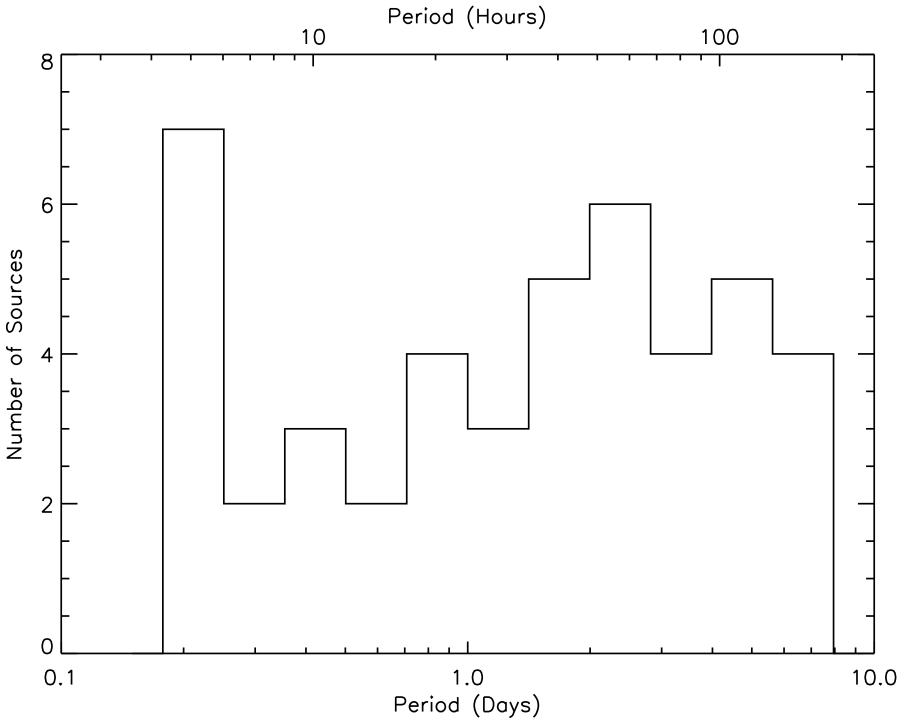

Figure 4.3: The period distribution of likely counterparts to X-ray sources in the GBS. There are only 68sources for which we suspect or confirm periods, compared to the 168sources seen to be variable. A further 23sources are suspected through overlap with OGLE IV fields (Udalski et al., 2012) to be long period variables with periods above 8 days that our observations are not sensitive to. Periods between 4 and 8 days are tentative and require confirmation from observations with a longer baseline.

spectroscopy, especially since BH qLMXBs can have quite low X-ray to optical flux ratios. With the large errors in estimating this ratio, it is not necessarily a reliable diagnostic on its own for differentiating between BH qLMXBs showing elliptical variations and W UMas. This discrepancy is discussed in more depth in Chapter 8.

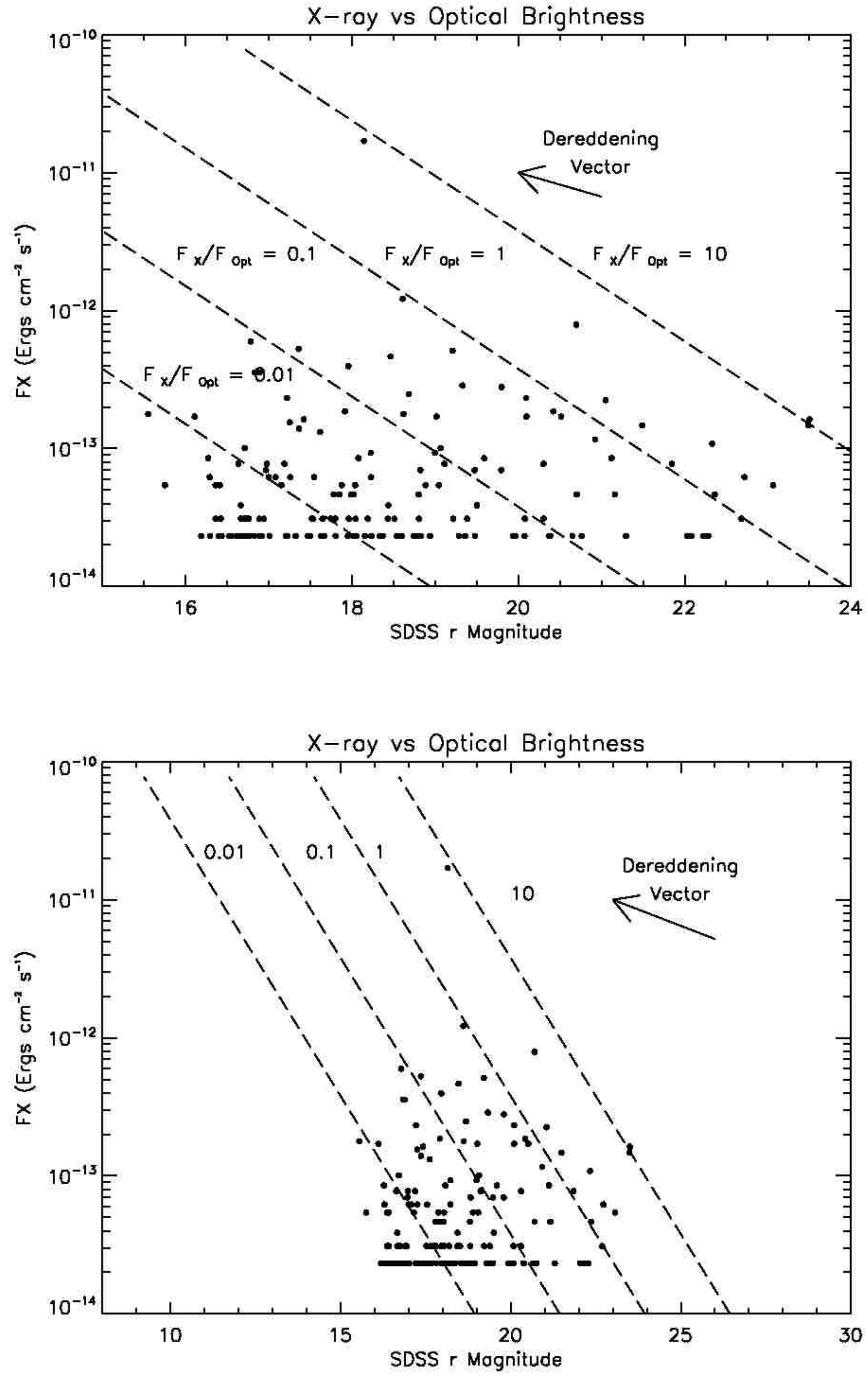

Figure 4.4: Each variable coincident with an X-ray source is plotted as magnitude vs flux. Each optical magnitude carries a systematic uncertainty of 0.5 magnitudes as they were calibrated with the USNO catalog. Statistical errors for the X-ray flux are discussed in Chapter 2, though there are additional systematic uncertainties in the X-ray spectral shape. Uncertainties in extinction affect both X-ray and optical flux, with reddening moving sources in the direction indicated. The same information is plotted above and below, but the scale in the bottom figure has been matched to the population synthesis in Jonker et al. (2011) in order to aid the reader in making comparisons.

5. Emission Line Sources

In this chapter, I discuss objects for which we have optical spectra and/or radio data. 5 of these (CX5, CX18, CX28, CX37, and CX561) were observed with the NTT and VIMOS and are discussed comprehensively in Britt et al. (2013). Much of the text for these 5 sources is reproduced from Britt et al. (2013) with copyright agreement. The others appear in either Torres et al. (2013), Maccarone et al. (2012), or Ratti et al. (2013). All information on spectroscopy or radio observations from these objects is drawn from these papers.

5.1 CX2 = Granat 1734-292

CX2 is explored as a radio source in Maccarone et al. (2012). It is a known Seyfert 1 galaxy at a redshift of 0.0214 (Marti et al., 1998). This object shows optical variability of about 0.2 magnitudes in r' in Mosaic-II observations, shown in Figure 5.1, with a mean magnitude of $r' = 18.4$, giving it an observed X-ray to optical flux ratio of 80, consistent with other AGN.

5.2 CX5 = AX J1740.2-2848

CX5 is also known as AXJ1740.1-2847 and shows an X-ray period of 729s (Sakano et al 2000), suggesting either an IP or an HMXB. In an IP interpretation, this pulse period is the spin of the WD. Sakano et al (2000) fit the X-ray spectrum of CX5 to a power law of photon index $\Gamma = 0.7 \pm 0.6$ with $N_H = 2.5^{+2.9}_{-1.8} \times 10^{22}\,\mathrm{cm}^{-2}$. Kaur et al. (2010) alternatively find $N_H = 1.0 \pm 0.2 \times 10^{22}\,\mathrm{cm}^{-2}$ with $\Gamma = 0.5 \pm 0.1$. Kaur et al. (2010) also report the presence of Fe emission. Its optical spectrum, shown in Figure 5.2, clearly rules out an HMXB and shows He II emission lines, which rules out a qLMXB interpretation. Table 5.1 shows the visible emission and absorption lines for sources with NTT spectra that I analyzed, and includes CX5, CX18, CX28, CX37, and CX561. The ratio of equivalent widths between He II λ 4686 and Hβ is 2.3, which is suggestive of a magnetic CV. Using the value in Kaur et al. (2010) for N_H to calculate extinction and absorption, we find the ratio of X-ray to optical flux is $\frac{F_x}{F_{r'}} \sim 0.4$ which is consistent with an IP, CV, or qLMXB. Assuming a distance of 1

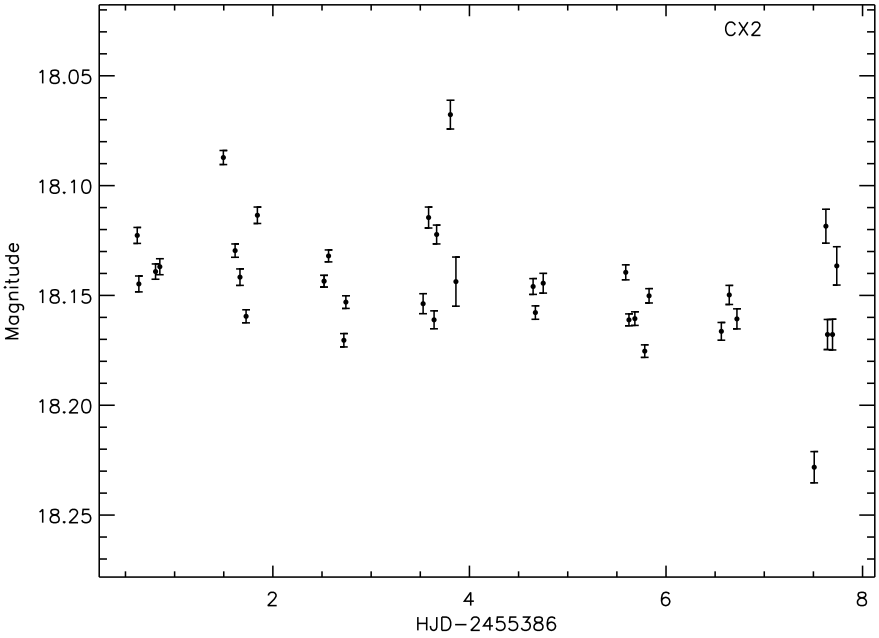

Figure 5.1: Mosaic-II lightcurve of CX2.

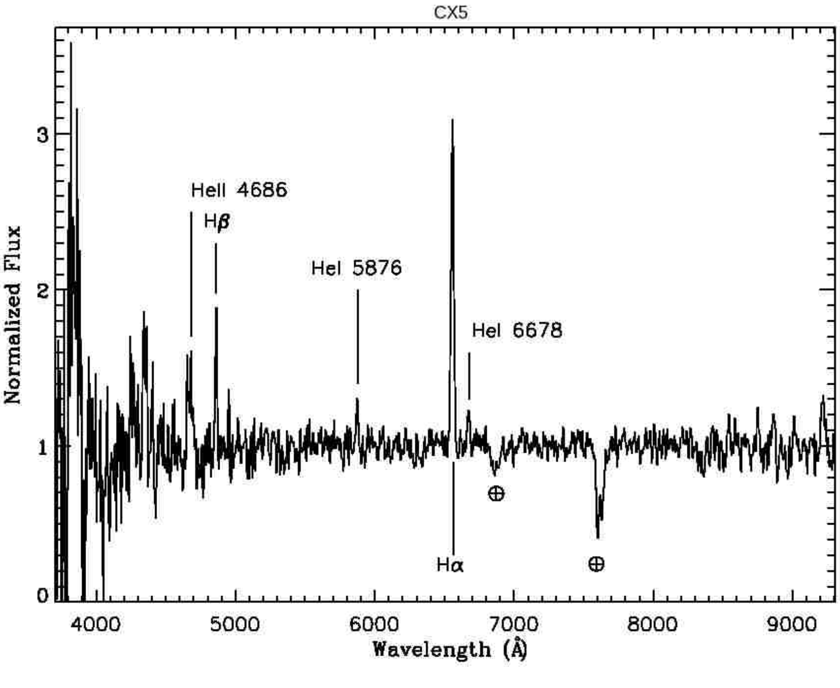

Figure 5.2: The combined and weighted spectra from 2 epochs of observations with the NTT for CX5. He I and He II emission are clearly visible, as is H emission.

kpc yields $L_X = 3 \times 10^{32}\,\mathrm{ergs\,s^{-1}}$, which is within errors of previously reported values for this source.

This source shows variability of 0.3 magnitudes in our Mosaic-II data, shown in Figure 5.3. The Mosaic-II observations for this source do not show a well defined periodicity. We obtained 6 hours of intermittent photometry with the Henrietta Swope Telescope at Las Campanas Observatory from June 22nd, 2011 and turned to this source again on June 27th, 2011. We see evidence of a 125 minute period in the optical (see Fig. 5.4). The Mosaic-II observations do not show evidence of this period. Using $P_{spin} \sim 0.1\,P_{Orb}$ as the apparent peak of the distribution of known IPs (Scaringi et al., 2010), one expects a 729 s pulse period to result in a roughly 2 hour orbital period, lending credibility to identifying the 125 minute period as the orbital period. The previously detected X-ray period of $729\,s$, hard X-ray spectrum with Fe emission, strong He II emission, and possible 125 minute orbital period ($\sim 10 \times P_{spin}$) point to CX5 being an IP when taken together.

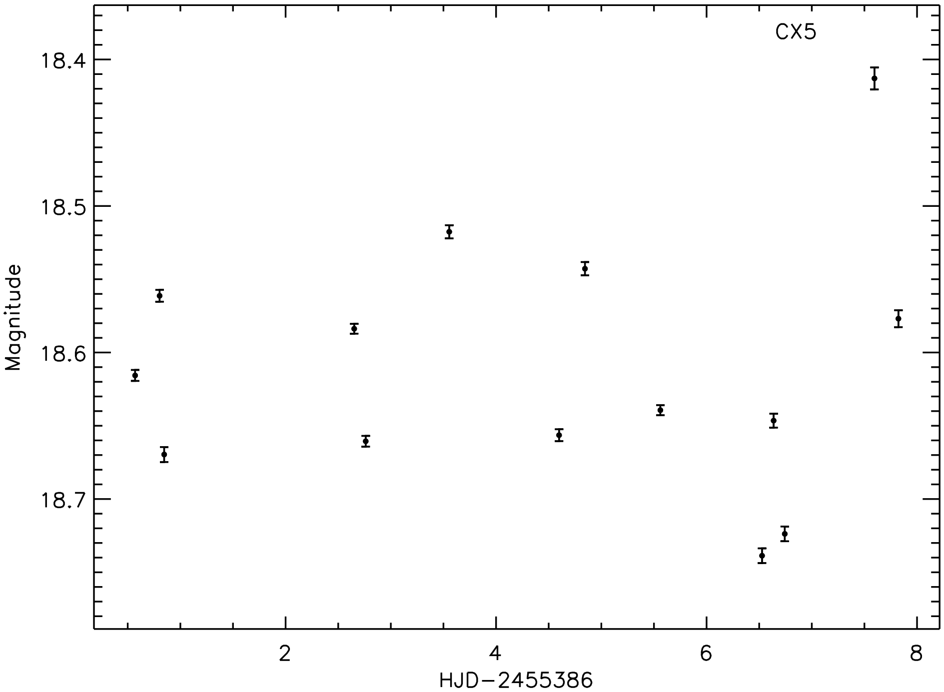

Figure 5.3: Mosaic-II lightcurve of CX5.

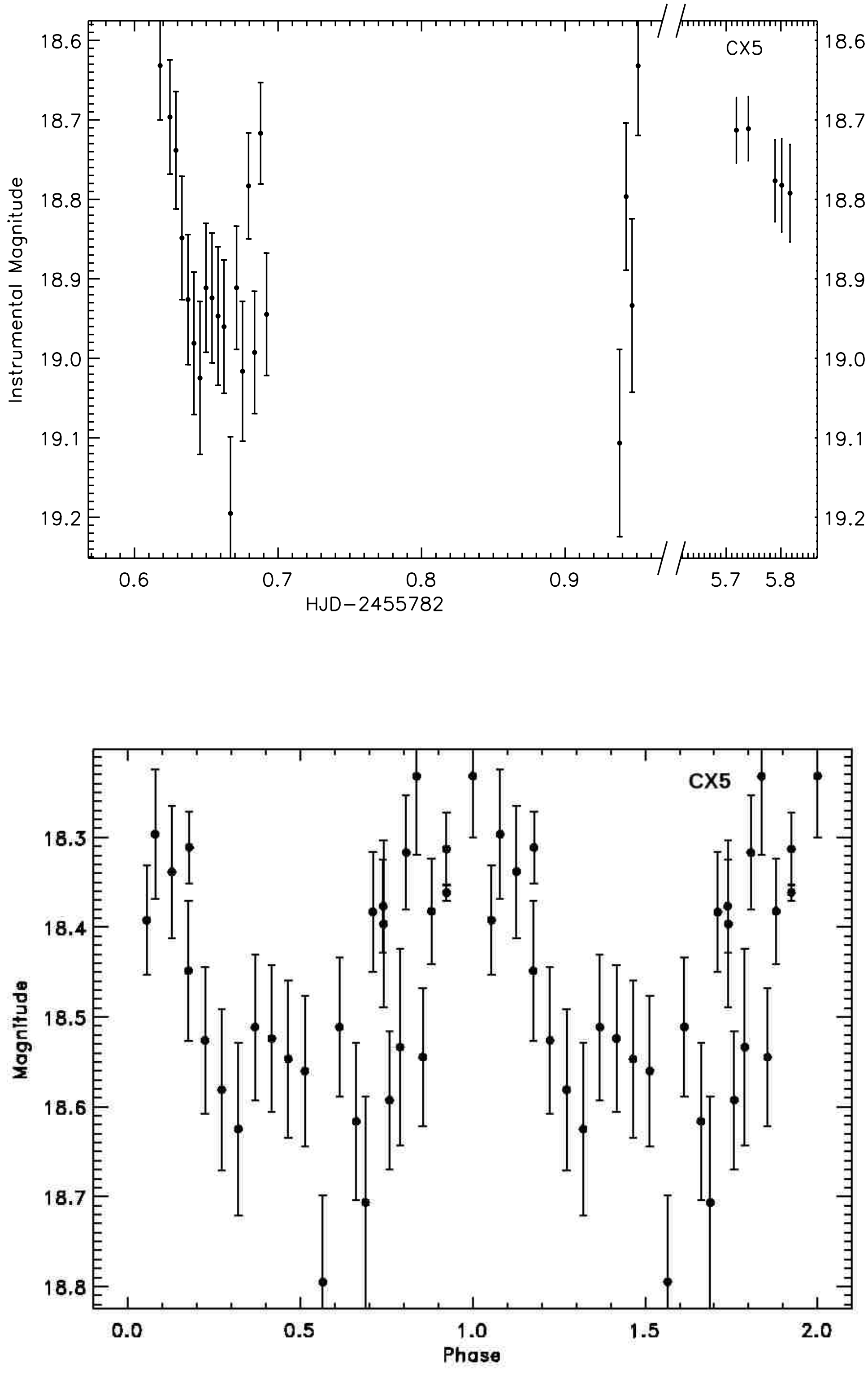

Figure 5.4: Left: Lightcurve of CX5 from the Swope 1.0 meter data taken in the summer of 2011. Right: Swope lightcurve of CX5 folded on a 125 minute period with an arbitrary ephemeris.

Table 5.1: Line properties of sources analyzed in Britt et al. (2013). Three of the five sources have observed spectra at multiple epochs. Line widths are reported for each epoch in which they are present. Two values separated by commas denote a double peaked line; reported values are for each peak. The FWHM of the lines have been deconvolved with the resolution of the instrument, which is 17 Å for NTT spectra and 10 Å for the VIMOS spectrum listed as epoch 2 for CX28.

CX ID	Line	epoch	λ_{Obs} (Å)	Radial Velocity $\mathrm{km\,s^{-1}}$	EW (Å)	FWHM (Å)
5	HeII 4686	1	4682.7	-190 ± 70	-30 ± 4	23
	Hβ	1	4863.9	160 ± 10	-13 ± 1	12
	HeI 5876	1	5879.3	190 ± 20	-4.9 ± 0.3	$< 14^{\dagger}$
	Hα	1	6565.3	112 ± 5	-50 ± 2	13
	HeI 6678	1	6681.1	130 ± 20	-4.9 ± 0.2	9
18	Hδ	1	4096.4	-390 ± 90	-18 ± 3	18
	Hγ	1	4338.8	-110 ± 80	-25 ± 2	19
	HeI 4471	1	4470.3	-80 ± 20	-9 ± 2	$< 11^{\dagger}$
	Hβ	1	4858.8	-160 ± 50	-25 ± 1	21
	HeI 5876	1	5874.4	-60 ± 150	-3 ± 1	19
	Hα	1	6562.1	-30 ± 10	-25 ± 1	21
	HeI 6678	1	6680.2	90 ± 30	-2.6 ± 0.4	$< 11^{\dagger}$
28	Hδ	1	4101.5	-20 ± 10	-15 ± 2	9
	Hγ	1	4340.4	-4 ± 10	-24 ± 2	19
	Bowen Blend	1	4635.6		-12 ± 1	34
	HeII 4686	1	4684.9	-50 ± 20	-22 ± 2	11
		2	4691.8	390 ± 30	-20 ± 2	
	Hβ	1	4858.9	-150 ± 20	-11 ± 1	9
		2	4866.1	290 ± 30	-24 ± 5	12
	HeII 5412	1	5416.1	250 ± 20	-6.9 ± 0.6 1	17
		2	5418.1	360 ± 30	-4.9 ± 0.3	21
	HeI 5876	1	5874.6	-50 ± 20	-1.4 ± 0.6	$< 11^{\dagger}$
		2	5878.1	130 ± 20	-3.5 ± 0.3	11
	Hα	1	6563.2	20 ± 10	-13 ± 0.5	17
		2	6565.9	140 ± 10	-26.2 ± 0.3	16
	HeI 6678	1	6683.3	230 ± 80	-1.9 ± 0.6	7
		2	6682.5	200 ± 20	-2.6 ± 0.2	7
37	Hγ	1	4347.0	450 ± 20	-7.5 ± 0.7	11
	Bowen Blend	1	4626.9		-5.5 ± 0.2	28
	HeII 4686	1	4694.9	590 ± 30	-16 ± 2	14
	Hβ	1	4871.1	600 ± 10	-14 ± 1	9
	Hα	1	6574.4	530 ± 10	-45 ± 2	12
561	Hα	1	6553.4, 6585.5*	$1030 \pm 30, -430 \pm 30^{*}$	$-18 \pm 2,\ -31 \pm 2^{*}$	
		1	6576.6	630 ± 40	-52 ± 5	46
	Ca II 8542	1	8547.8	200 ± 40	4.59 ± 0.3	< 10
	Ca II 8662	1	8670.2	280 ± 40	5.1 ± 0.3	5

---

[a] Line is double peaked, center and EW given for each peak. Line is fit with a single Gaussian below.

[b] Line widths are upper limits

5.3 CX18

This object is noted as a variable star in Terzan & Gosset (1991). The optical spectrum, shown in Figure 5.5, of CX18 shows He I and Balmer emission. In the Mosaic-II data, shown in Figure 5.3, this source brightens by 1.6 magnitudes over the course of 6 days. Follow up data from SMARTS, which can be seen in Fig. 5.7, clearly shows a similar rise of 3 magnitudes followed by an exponential decay and a flat quiescent state after the outburst. In two observations spaced out by several months, we caught two of these outbursts, suggesting a high recurrence rate. This source appears to be a CV undergoing Dwarf Nova (DN) outbursts, which is in agreement with Udalski et al. (2012), who find DN outbursts with a recurrence time around 100 days in OGLE data.

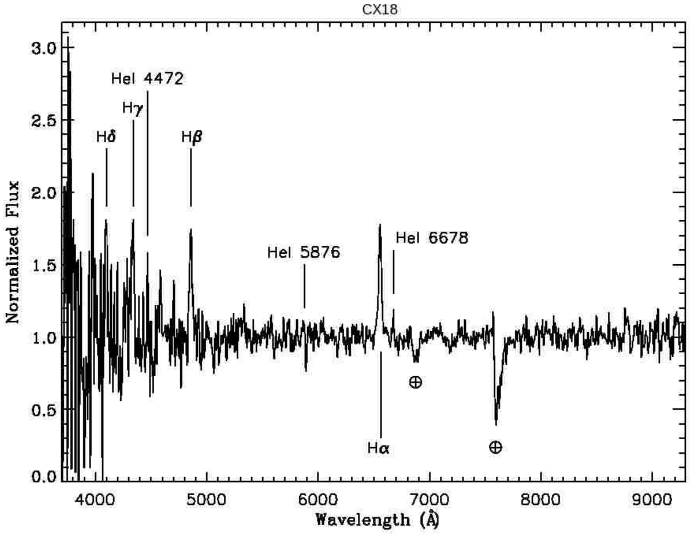

Figure 5.5: The weighted and combined spectrum of 2 epochs of the NTT observations for CX18. He I and H emission is clearly visible.

Using the $E(B-V)$ values from Gonzalez et al. (2012) yields an X-ray to optical flux ratio of order $\frac{1}{10}$, which is consistent with previous observations of the ratio of X-ray to optical light of quiescent DNe (Verbunt et al., 1997). Most DNe are substantially closer than bulge distance, but even assuming that no absorption occurs, the unabsorbed ratio of X-ray to optical flux of order unity is within the range of ordinary CVs. DN outbursts can occur

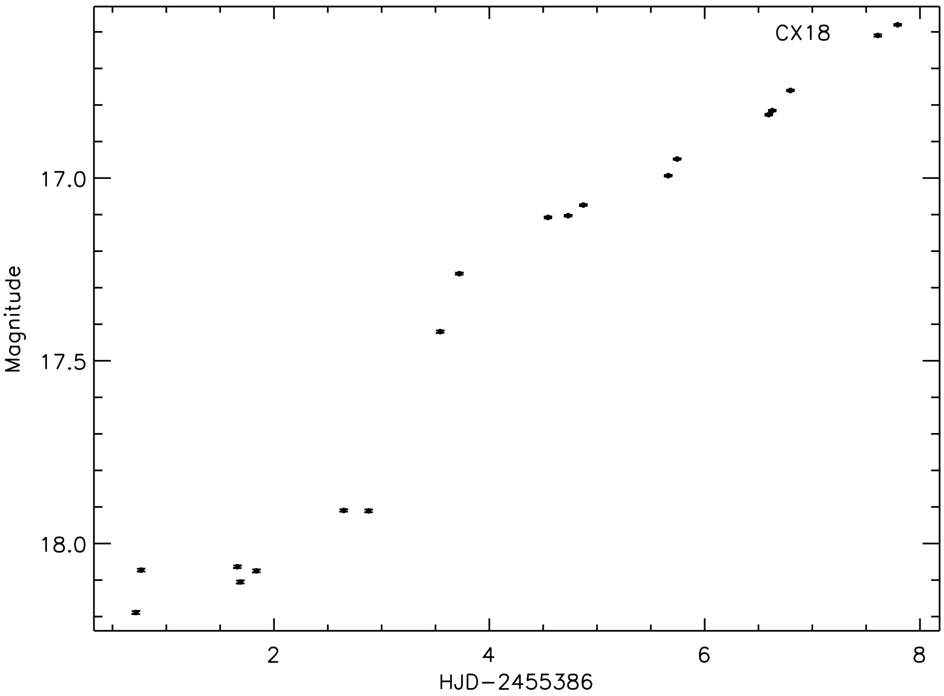

Figure 5.6: Mosaic-II lightcurve of CX18.

in both CVs and in IPs with sufficiently large disks. Many IPs show strong HeII emission in their optical spectra (Edmonds et al., 1999). CX18 does not. The lack of He II lines argues against an IP interpretation, and further indicates that this is a quiescent system at the time of the spectroscopy.

5.4 CX28

The optical spectrum of CX28, shown in Figure 5.8 shows Balmer and He I emission, which makes this a good CV candidate. There is also consistently strong He II emission with $\frac{\mathrm{HeII4686}}{\mathrm{H}\beta} = 2$ in the first epoch of observations and $\frac{\mathrm{HeII4686}}{\mathrm{H}\beta} = 0.8$ in the second, suggesting an IP. X-ray observations described in Jonker et al. (2011) show that the X-ray spectrum of CX28 is hard, $\frac{[2.5-8\,keV]-[0.3-2.5\,keV]}{[0.3-8\,keV]} = 0.5$, which further supports an IP classification, though there are not enough photons in the 2 ks observation for a full spectral fit or for timing analysis. Unabsorbed $\frac{F_X}{F_{r'}} \sim 0.6$ which is consistent with IPs and CVs. This source

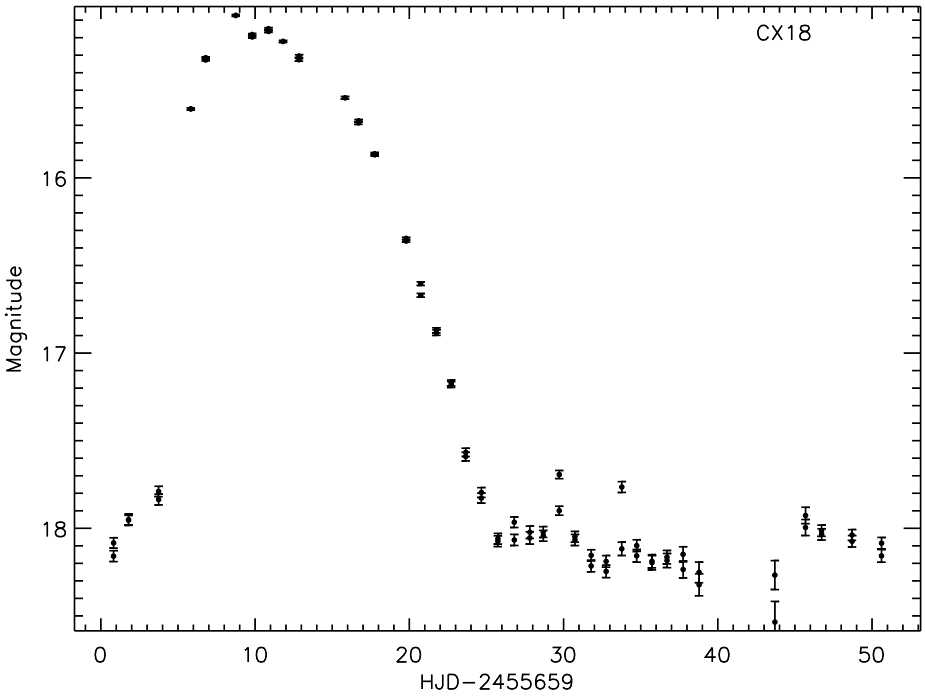

Figure 5.7: Data collected with the SMARTS 1.3m Andicam in the spring of 2011 confirms that CX18 is undergoing dwarf nova outbursts with a fast recurrence time.

cannot be a qLMXB based on the He II emission, and the X-ray strength is too weak for an active LMXB or accretion disk corona source. The strength of the He II emission and hardness of the X-ray spectrum suggest that CX18 is an IP, though there are no observations of the defining IP characteristic of an X-ray spin period. The source varies by 0.7 magnitudes, but is not demonstrably periodic in Mosaic-II data, shown in Figure 5.9. Observations from June 2011 at the Swope telescope, shown in Fig. 5.10 - panel (d), do not exhibit any period on timescales of minutes to an hour. There is some suggestion of a 2.76 hr period, but the observations do not extend long enough to bear this out as we do not cover multiple periods. If this is the real period, flickering on top of the periodic changes could swamp the signal in our Mosaic-II observations. It is worth noting that this falls in the period gap for CVs and could be further evidence for an IP interpretation because the CV period gap is not observed in IPs. The changes in radial velocity (RV) observed between the VIMOS and

NTT observations, shown in Table 5.1, are consistent with velocity variations in either the emitting regions or the motion of the disk around the center of mass of the system.

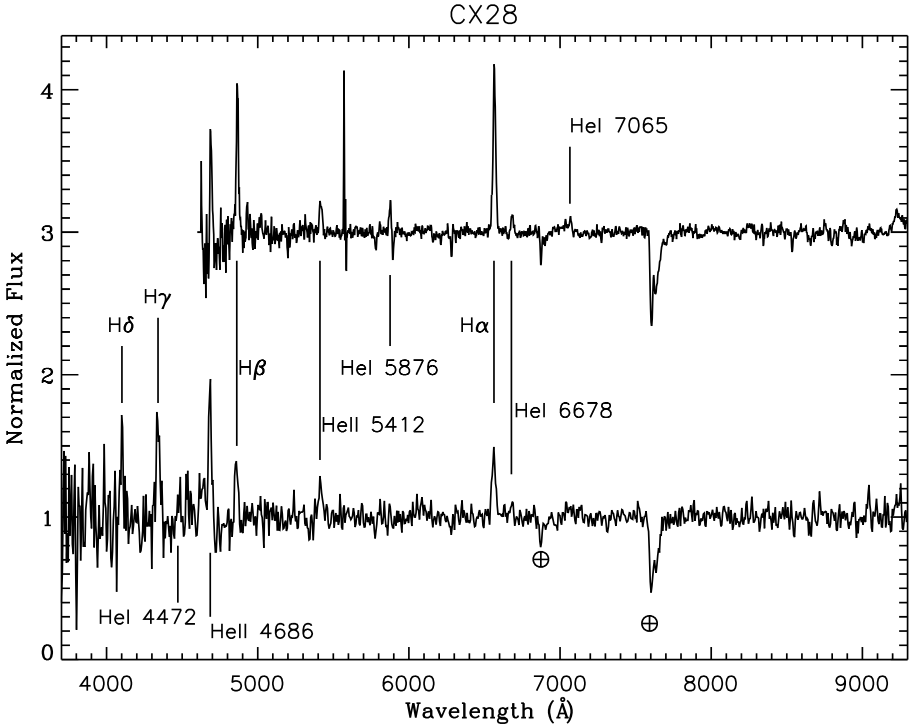

Figure 5.8: The bottom epoch is from NTT observations of CX28, while the top comes from the VIMOS instrument on the VLT. He I and He II emission is clearly present in both observations, as is H emission.

5.5 CX37

The optical spectrum of CX37, shown in Figure 5.11, shows Balmer, He I, and HeII emission. The relative strength of He I to Balmer lines is consistent with a WD primary, while the strong HeII emission ($\frac{\mathrm{HeII4686}}{\mathrm{H}\beta} = 1.1$) rules out a qLMXB (see Table 1.1). Absorbed $\frac{F_X}{F_{r'}} \sim 5$, while adjusting for extinction lowers this value to a minimum of $\frac{1}{16}$ at the bulge, which is consistent with CVs and IPs. There are 37 photons detected in the 2 ks Chandra observation of this source (Jonker et al., 2011), which is enough to reveal that the X-ray spectrum of CX37 is very hard with $\frac{[2.5-8\,keV]-[0.3-2.5\,keV]}{[0.3-8\,keV]} = 0.9$. In the Mosaic-II data, shown in Figure 5.12 CX37 shows non-periodic variability of amplitude 0.15 magnitudes from the mean and

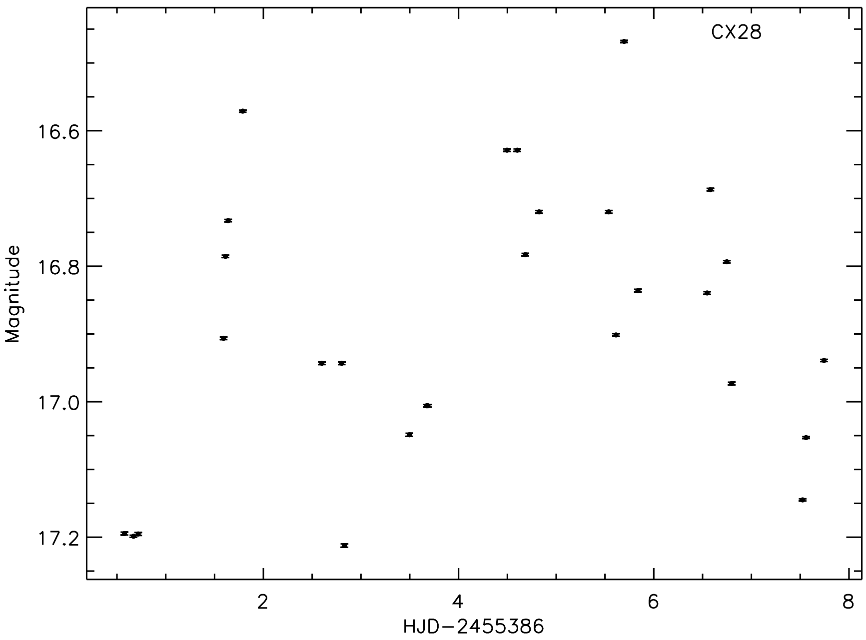

Figure 5.9: Mosaic-II lightcurve of CX28.

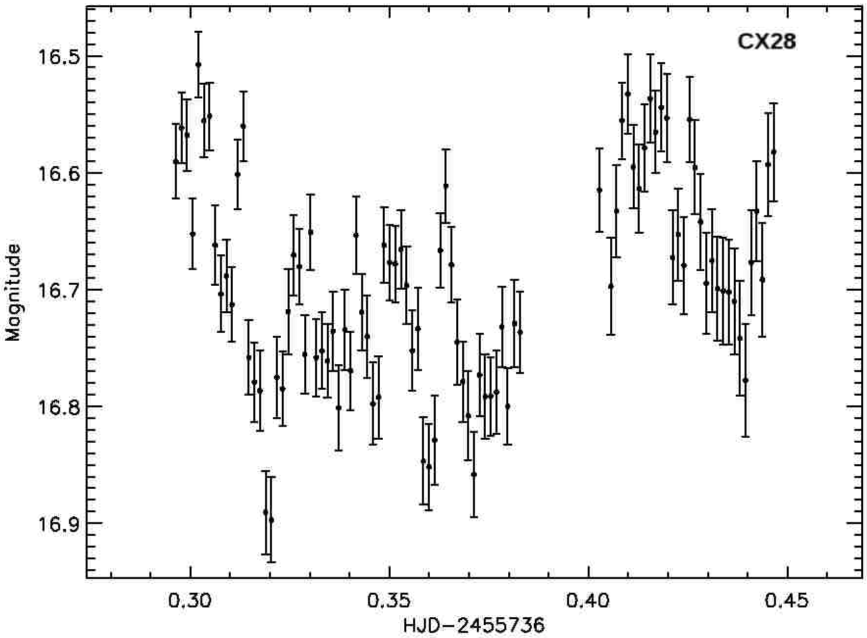

Figure 5.10: CX28 Lightcurve from Henrietta Swope telescope at LCO.

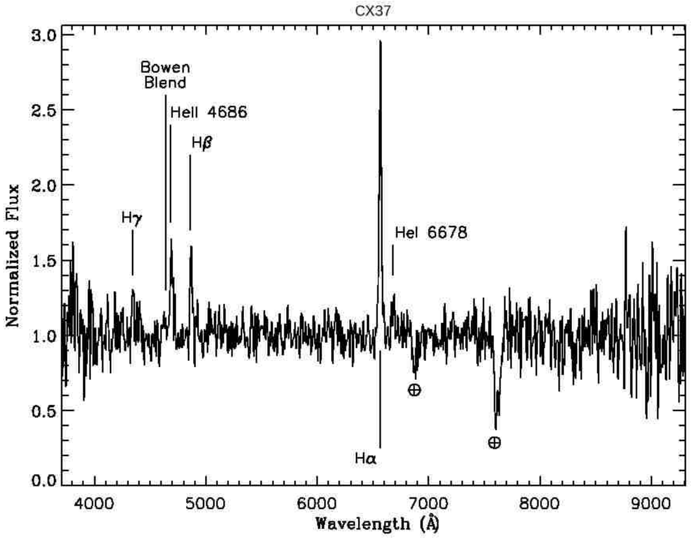

Figure 5.11: The NTT spectrum for CX37. H, He I, and He II are all seen in emission.

evidence of an eclipse at least 0.9 magnitudes deep. The other variations are largely due to flickering, as no significant periodic modulations are recovered from a periodogram. The lowest data point in the Mosaic-II lightcurve is 4.39 times the standard deviation of all the 34 observations, suggesting that it is indeed an eclipse rather than a random fluctuation from flickering. There is a second data point that is 2.64 times the standard deviation below the mean, which is likely a second eclipse. The eclipsing points are 2.7 days apart. Also, catching 2 eclipsing points out of 34 suggests that the eclipse lasts for $\sim 6^{+4}_{-3}\%$ of the period, which is not unusual for CVs (Sulkanen et al., 1981). Since the nearest observation to the eclipse is separated by only 1.25 hours, that suggests a maximum period of $\sim$ 21 hours, assuming the two points are from eclipses at the same phase. In 4.5 hours of observations with the Swope telescope at LCO (not shown), CX37 varies with no periodicity and with no visible eclipse. The LCO observations provide a lower bound to the orbital period, implying that the period is some fraction $\frac{2.7\mathrm{days}}{n}$, $3 \leq n \leq 14$.

Each of the emission lines also exhibit large radial velocities, shown in Table 5.1, from $400-600\mathrm{km\,s^{-1}}$. It is possible to produce offsets this high in short period magnetic systems. The hardness of the X-ray spectrum together with the strong He II emission suggests an IP

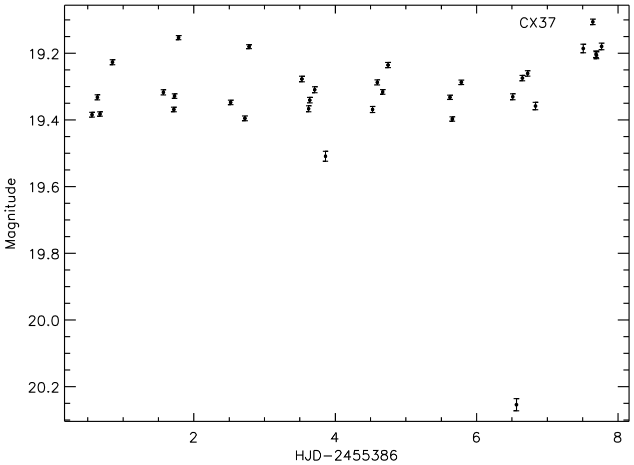

Figure 5.12: Mosaic-II lightcurve of CX37.

classification for CX37, but as with CX28, X-ray observations capable of detecting a spin period are necessary to make this classification definitively.

5.6 CX39

CX39 is covered in depth in Torres et al. (2013), and shows an outburst of 1.2 magnitudes which has already begun at the start of observations, and returns to a steady state by the fourth night of observations, as shown in Figure 5.13. Though they usually are brighter and last longer, there are some small amplitude DNe which last only a few days (Shears et al., 2006), and it is possible that this is such a DN. Using the magnitude out of outburst, absorbed $\frac{F_X}{F_{opt}} = 8$, which is consistent with a CV with some extinction; with Bulge reddening, $\frac{F_X}{F_{opt}} = \frac{1}{8}$. The optical spectrum described in Torres et al. (2013) show large emission lines in Hα and He I, confirming that this is a CV.

5.7 CX44

CX44 appears in depth in Torres et al. (2013). The optical counterpart has a Sloan r' magnitude of 18.55, which shows aperiodic flickering with an amplitude of 0.1 magnitudes, shown in Figure 5.14. The X-ray to optical flux ratio, uncorrected for extinction, is ≈ 1, which is consistent with some of the higher accretion rate quiescent CVs and qLMXBs. In

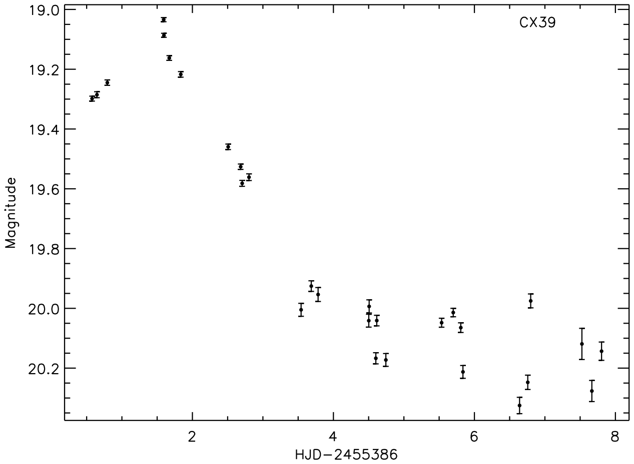

Figure 5.13: Mosaic-II lightcurve of CX39.

the optical spectrum, He I 5876 is in emission while He I 6678 is on a chip gap. The strong He I emission indicates that this is a CV and not a qLMXB, though we cannot rule out an IP.

5.8 CX49

CX49 appears in Maccarone et al. (2012) and has absorbed $\frac{F_X}{F_{opt}} = 7$, which is consistent with magnetic CVs, qLMXBs, AGN, and CVs. CX49 is highly variable, changing 0.4 magnitudes over the course of our observations. There is no significant periodicity to the variations, which occur on a timescale of hours to days and are shown in Figure 5.15. The large amplitude flickering is suggestive of a strong contribution to continuum light by an accretion disk, which argues against a quiescent system. The radio observations and discussion in Maccarone et al. (2012) suggest that this is an AGN, though that categorization is insecure.

5.9 CX70

CX70 is discussed in depth in Torres et al. (2013) and has a counterpart that shows some flickering, shown in Figure 5.16. We recover a suspected period of 0.2332 days, or 5.6 hours, but with a False Alarm Probability of 8% it is not a secure detection. The folded lightcurve is presented in Figure 5.17. The brightness of the counterpart changes by up to 0.2 magnitudes

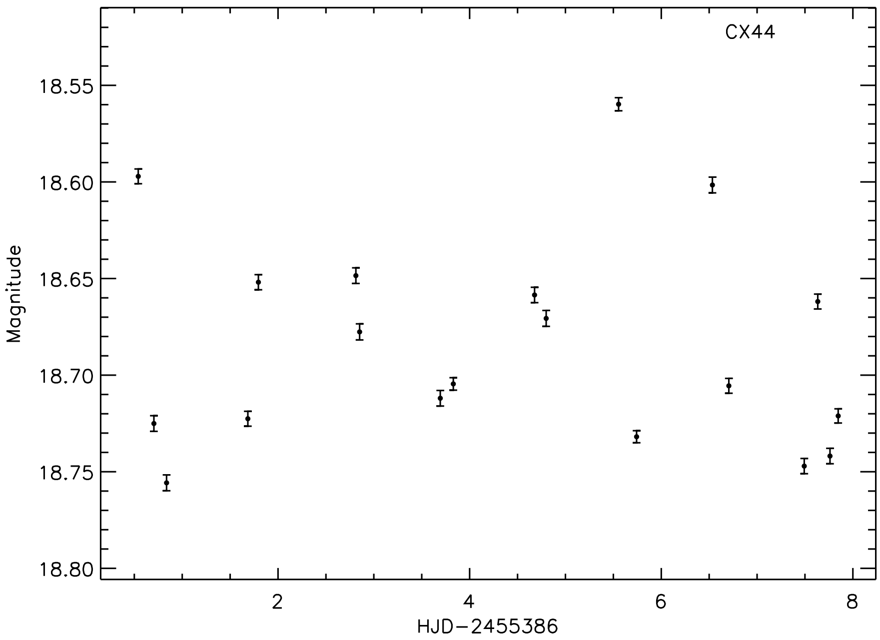

Figure 5.14: Mosaic-II lightcurve of CX44.

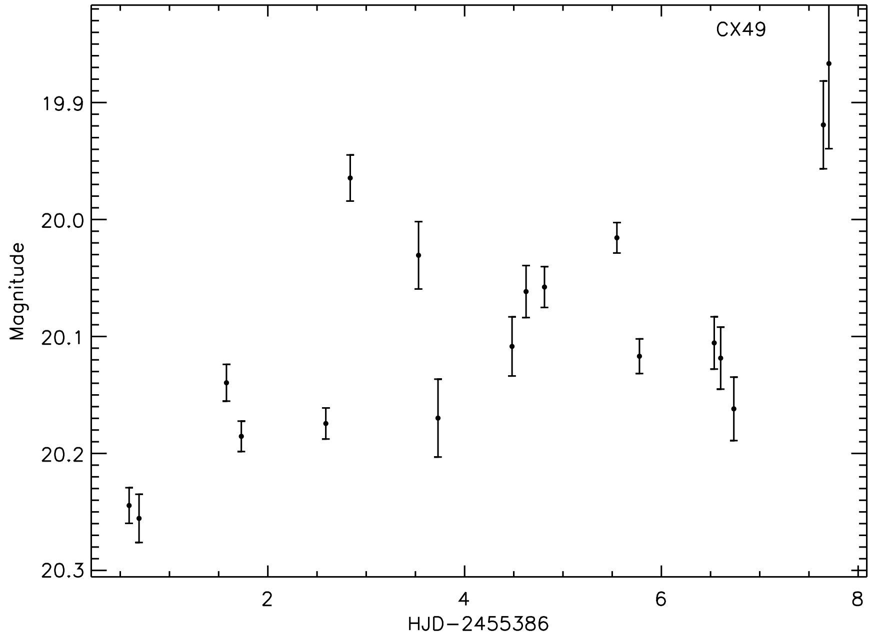

Figure 5.15: Mosaic-II lightcurve of CX49.

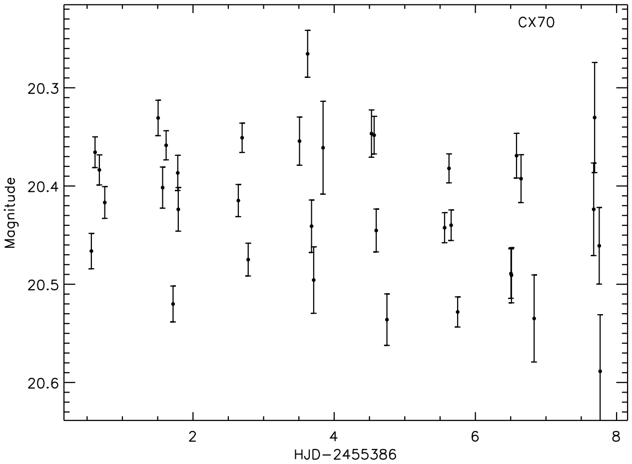

Figure 5.16: Mosaic-II lightcurve of CX70.

on a timescale of hours, which is consistent with CVs, magnetic CVs, and qLMXBs, as would be the period if it were real. Absorbed $\frac{F_X}{F_{opt}} = 8$, which is consistent with CVs, qLMXBs, and magnetic CVs. The presence of some flickering could be attributable to an accretion disk. The optical spectrum lacks strong He I or He II emission, while the Ca II triplet is visible in absorption, signifying a quiescent system. This is a strong candidate for a new qLMXB system.

5.10 CX93

This source is covered in detail in Ratti et al. (2013), where it is classified as a CV based on dynamic mass determinations. CX93 was observed with both the Mosaic-II instrument on the Blanco 4m Telescope at CTIO and with the 1m Henrietta Swope Telescope at LCO. The orbital period of CX93 was determined using the Mosaic-II lightcurve. The Swope data are used only to verify Mosaic-II results, as the time between observations was too large compared to the relative errors in period and ephemeris in the two observation runs to reliably phase them relative to each other. An initial period of 0.12 d was found with the Mosaic-II data using the Lomb-Scargle periodogram. The high dispersion in a fold on this period indicated that this was a harmonic of the true period. Folding on twice this period

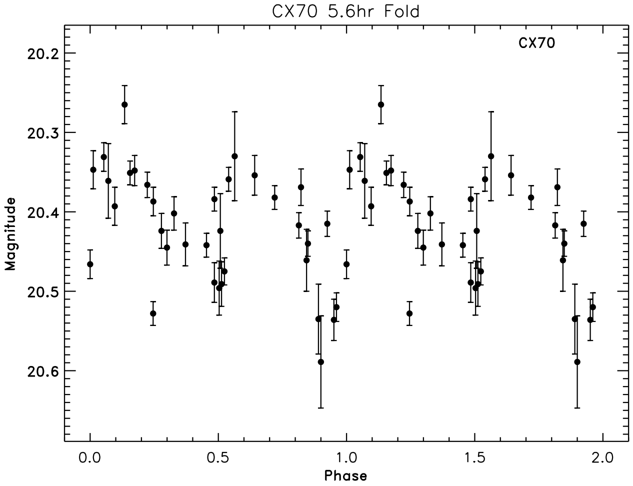

Figure 5.17: Lightcurve of CX70 folded on a 5.6 hour period. This period has a FAP of 8%, and requires further observations to confirm. The statistical errors and small amounts of apparent flickering could mask a real period.

yielded an asymmetric double-humped lightcurve, shown in Figure 5.18, top panel. A fit with 2 sine waves with periods at a 2:1 ratio was motivated by interpreting the asymmetric peaks as the combination of ellipsoidal modulations with the presence of a hotspot (accretion impact point) on the disk. Fitting 2 sine waves with this period ratio and allowing the other parameters to wander gave a best fit of $P = 0.23710(5)$. Error bars were estimated with χ^2 fitting after adding a systematic error to the Mosaic-II data to account for flickering in the source. The size of this systematic error was determined by normalizing the best fit χ^2 to the number of degrees of freedom. The Swope data provide a less constrained $P = 0.23(1)\,\mathrm{d}$, consistent with the Mosaic-II result.

The character of the source's counterpart changed somewhat in the year between LCO observations and Mosaic-II observations in that the maxima in LCO lightcurve are equal. This means that the LCO lightcurve is more purely due to ellipsoidal modulations, which predict equal maxima, and that the presence of a hotspot at some phase offset has greatly diminished. The data quality of the observations with the Blanco 4m telescope is much higher, and these data were used to constrain the inclination angle of the system with

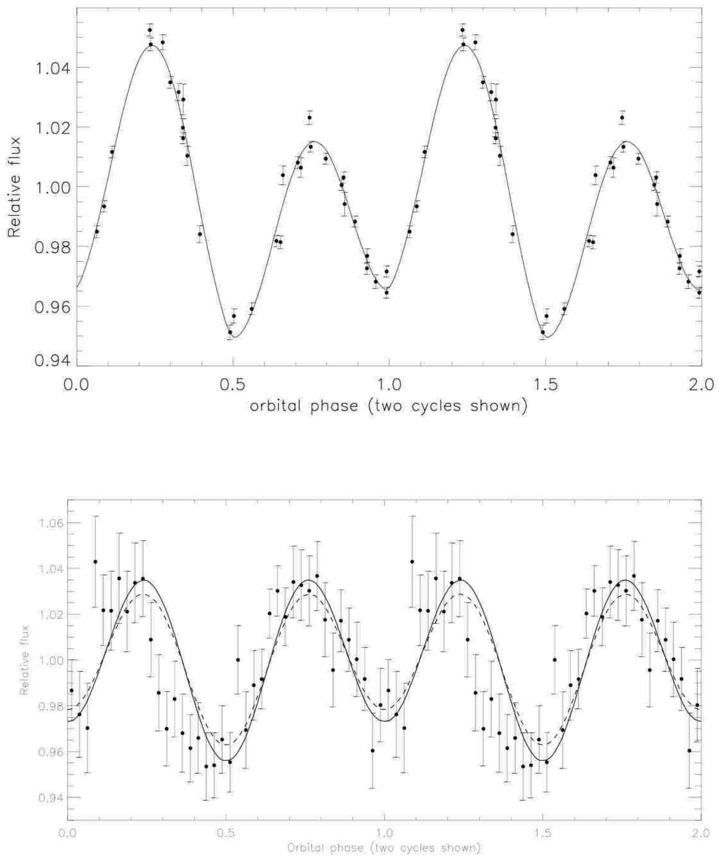

Figure 5.18: This folded lightcurve of CX93 is presented as it appears in Ratti et al. (2013). Top panel: Mosaic-II lightcurve. The solid line represents the best fit model assuming ellipsoidal variations plus a single bright spot. Bottom panel: LCO lightcurve, fitted with a pure ellipsoidal modulation model for an inclination of $i = 32.3°$ (dashed line) and $i = 36.2°$ (solid line). The observations are binned for clarity, but fitting was done on unbinned data.

the XRBinary code developed by E.L. Robinson*. I was not the one who performed this analysis as it draws not only from the Mosaic-II data, but also from spectroscopy obtained by collaborators who performed this analysis which appears in Ratti et al. (2013).

5.11 CX128

CX128 is discussed in depth in Torres et al. (2013). The source is variable, with aperiodic flickering of amplitude 0.4 magnitudes, as shown in Figure 5.19. This suggests that the accretion disk dominates over the light from the donor. Absorbed $\frac{F_X}{F_{r'}} = 6$, which becomes $\frac{F_X}{F_{r'}} = \frac{1}{3}$ for bulge reddening of $E(B-V) = 1.48$. Both of these numbers are consistent with

---

*http://pisces.as.utexas.edu/robinson/XRbinary.pdf

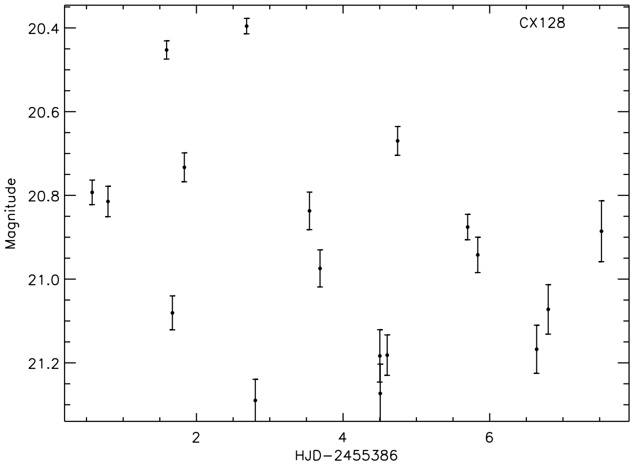

Figure 5.19: Mosaic-II lightcurve of CX128.

qLMXBs or IPs, while the X-ray to optical flux ratio for high reddening is consistent with CVs as well. The optical spectrum shows strong Balmer emission at Hα and Hβ which is single peaked with a FWHM of $\sim 1400\,\mathrm{km\,s^{-1}}$. He I appears in double-peaked emission at $\lambda\lambda$5876, 6678, and 7065, which confirms the CV nature of this source. He II is not detected, which argues against this being an IP.

5.12 CX142

CX142 is covered in depth in Torres et al. (2013), who identify the counterpart with optical spectroscopy. There is weak evidence of aperiodic variability for the optical counterpart of CX142, shown in Figure 5.20, which has a mean Sloan r' magnitude of 22.3. The RMS scatter of the observations is 0.18 magnitudes, which is twice the average statistical error in the observations of 0.09 magnitudes. The observations cover a range of 0.5 magnitudes, but the source is at the faint edge of what the Blanco observations can detect. Absorbed $\frac{F_X}{F_{r'}} = 20$, which is consistent with a UXCB, qLMXB, or magnetic CV or CV with some extinction. The optical spectrum of this source shows strong Balmer emission with low FWHM, which rules out UCXBs, and He I emission which rules out qLMXBs. He II is undetected. This is likely a CV suffering extinction.

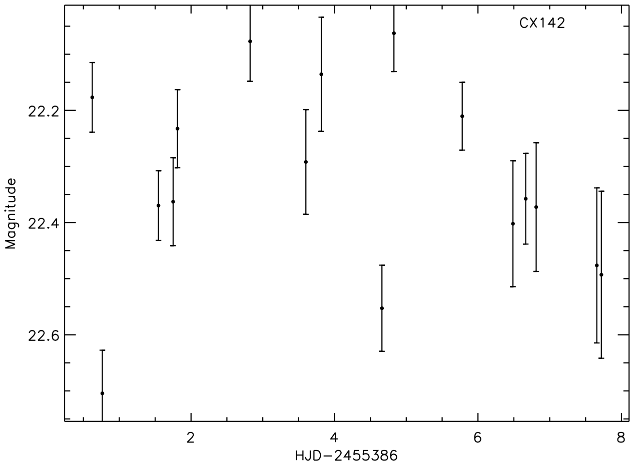

Figure 5.20: Mosaic-II lightcurve of CX142.

5.13 CX154

The optical counterpart of CX154, identified through spectroscopy in Torres et al. (2013), has an estimated Sloan r' magnitude of 21.7. It is not photometrically variable, as shown in Figure 5.21. Using $E(B-V) = 1.83$ for a bulge source, $\frac{F_X}{F_{r'}} = \frac{1}{4}$ with an upper limit of $\frac{F_X}{F_{r'}} = 12$ for a source suffering no extinction, which is consistent with qLMXBs, magnetic CVs and CVs, but is too high for the X-rays to be generated by coronal emission from active stars or RS CVns. The counterpart is so faint that some low level flickering could escape significant detection in the noise. Hα, though weak, is observed in both available epochs of spectroscopy for this source, though He I is detected in only one of these.

5.14 CX207

This source is covered in depth along with optical/NIR spectroscopy in Torres et al. (2013). CX207 has an eclipse of at least 2 magnitudes shown in Figure 5.22 indicating a large temperature difference between components. We also observe aperiodic photometric variability of amplitude 0.3 magnitudes indicating a large contribution to continuum light from an accretion disk. The mean magnitude out of eclipse is $r' = 20.7$, which yields an absorbed $\frac{F_X}{F_{r'}} = 4$, while using $E(B-V) = 2.07$ from the Gonzalez et al. (2012) reddening map gives

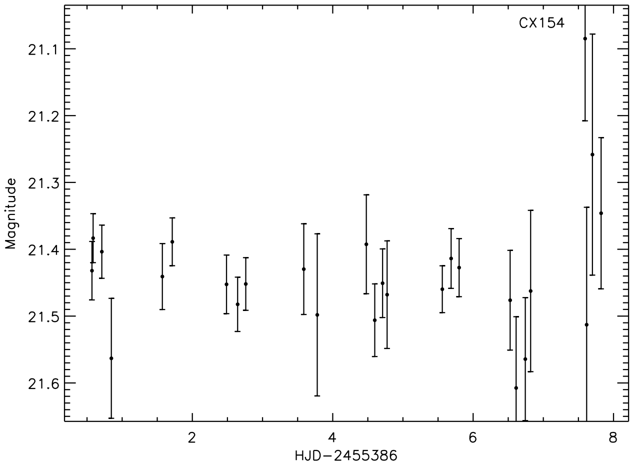

Figure 5.21: Mosaic-II lightcurve of CX154.

$\frac{F_X}{F_{r'}} = \frac{1}{20}$. The source is likely not at bulge distance, however, as it would have $M_{r'} = 0.5$ which is too intrinsically bright for either CVs, magnetic or otherwise, or qLMXBs.

The optical spectrum from VIMOS for CX207 shows broad single-peaked Hα emission, with a FWHM of $1600\,\mathrm{km\,s^{-1}}$ and fairly high RV offset of $> 350\,\mathrm{km\,s^{-1}}$. The broad, single peaked Hα line is consistent with nova-like CVs, as well as some NS and BH LMXBs. The X-ray to optical flux ratio is lower than an LMXB in outburst, however, and He I is not typically present in spectra of qLMXBs.

5.15 CX377

CX377 is covered in depth in Torres et al. (2013). The optical counterpart to CX377 is variable with a mean Sloan r' magnitude of 18.85. There is no significant periodicity to this variability, which has an RMS scatter of 0.05 magnitudes about the mean, with an amplitude of 0.1 magnitudes, as shown in Figure 5.23. This short time-scale flickering implies a strong contribution from an accretion disk to the continuum light. Uncorrected $\frac{F_X}{F_{r'}} = 0.4$, while using $E(B-V) = 2.01$ for bulge distance extinction yields $\frac{F_X}{F_{r'}} = \frac{1}{200}$. The latter is likely an underestimate, as it would imply $M_{r'} = -1.3$ which is too bright to be consistent with either CVs or qLMXBs with Main Sequence donors. Without accounting for extinction, at

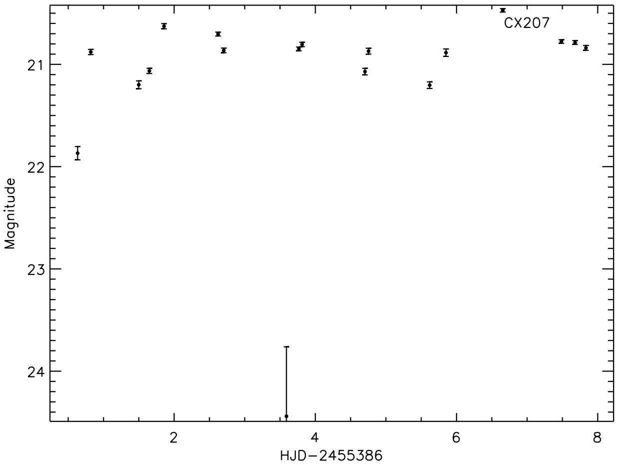

Figure 5.22: Mosaic-II lightcurve of CX207.

a distance of 1kpc $M_{r'} = 8.8$, which would be consistent with qLMXBs, magnetic CVs and CVs. In the optical spectrum, Hα is double peaked in emission, while He I is weak or not present. This is a candidate qLMXB.

5.16 CX446

This source is covered in depth, along with spectroscopy, in Torres et al. (2013). CX446 also shows an eclipse with a depth of 0.6 magnitudes, shown in Figure 5.24, marking it as a high inclination system. We can find no significant period in the Mosaic-II observations of this source, though there appear to be two eclipses separated by 4.84 days. The counterpart has a Sloan r' magnitude of 21.3, which gives an absorbed $\frac{F_X}{F_{r'}} = 4$, while using the bulge $E(B-V) = 2.01$, $\frac{F_X}{F_{r'}} = \frac{1}{20}$. Either is consistent with magnetic CVs, though the source would have to be closer than bulge distance if a CV, favoring the higher end of this range. Either is also consistent with qLMXBs, as BH qLMXBs are fainter in the X-ray than NS qLMXBs. At bulge distance, $L_X = 4 \times 10^{32}\,\mathrm{ergs\,s^{-1}}$, which is more consistent with NS qLMXBs, while at a distance of 1 kpc, $L_X = 3 \times 10^{30}\,\mathrm{ergs\,s^{-1}}$ which is consistent with BH qLMXBs and CVs. The optical spectrum shows only Hα in emission with a single peak and with a very broad FWHM of $\sim 2200\,\mathrm{km\,s^{-1}}$. Because of the eclipses, we know this to be a high inclination

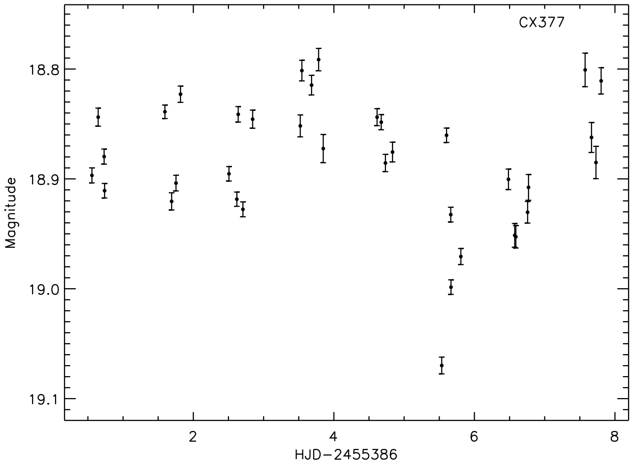

Figure 5.23: Mosaic-II lightcurve of CX377.

system. The broad Hα profile and lack of He I in emission favor a qLMXB over a CV. If this is confirmed to be a BH qLMXB through dynamic mass estimates, it would be the first eclipsing BH system in the Galaxy, and the first dynamically confirmed galactic BH binary discovered in quiescence.

5.17 CX561

This source is one of those covered in Britt et al. (2013). The approximate r' magnitude of CX561 is 20.2. The only feature in this spectrum is $H\alpha$, as can be seen in Figure 5.25. As shown in Fig. 5.26 and Table 5.1, the Hα emission line is split with peaks of unequal heights, suggesting significant contribution from a hotspot on the disk. The separation between the peaks is $1420\,\mathrm{km\,s^{-1}}$, which is high, but not high enough to securely rule out a CV interpretation (Szkody et al., 2002; Szkody & Henden, 2005; Warner, 2003). The center of the line profile is at 6576.5 Å, which suggests a velocity along our line of sight of 630 km s^{-1}. It is possible to produce these speeds for low inclination and short period magnetic or nova-like WD systems if observed at the right phase. Natal kicks routinely produce LMXBs with systemic velocities on this order. There is no evidence of HeI or HeII lines in the spectrum, but the signal to noise ratio is so low that a typical amount of HeI for a CV could

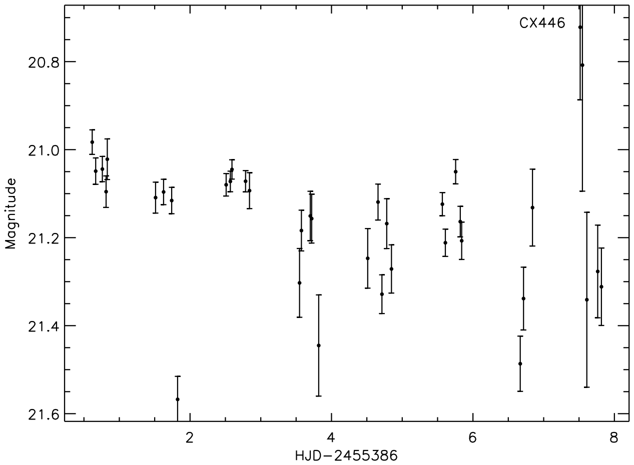

Figure 5.24: Mosaic-II lightcurve of CX446.

be present and buried in the noise. We are able, however, to detect absorption lines from the donor at Ca II λλ8542 and Ca II λλ8662. The relative equivalent widths of these lines is consistent with early K stars, which would imply the presence of an absorption line at λλ6495 as well, but the signal to noise ratio at this part of the spectrum is high enough that it is unsurprising that we do not detect it.

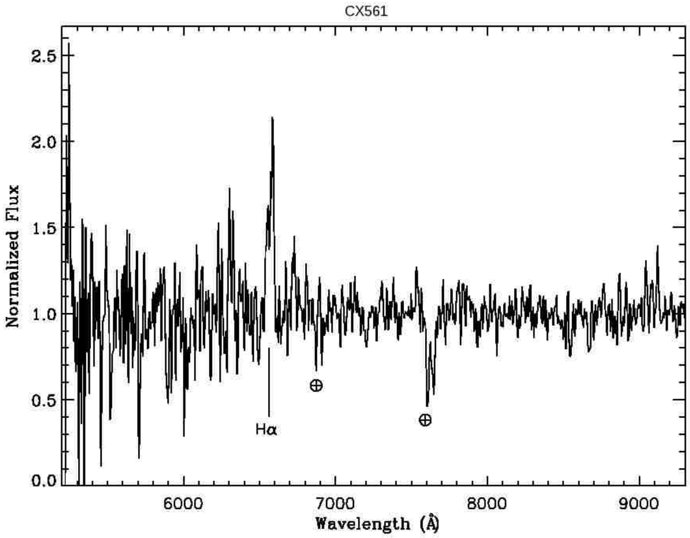

Figure 5.25: The NTT spectrum for CX561. H emission is the only significant emission feature, but 2 Ca II absorption lines from the donor can be seen as well. Because donor absorption lines can be seen, this is a quiescent system.

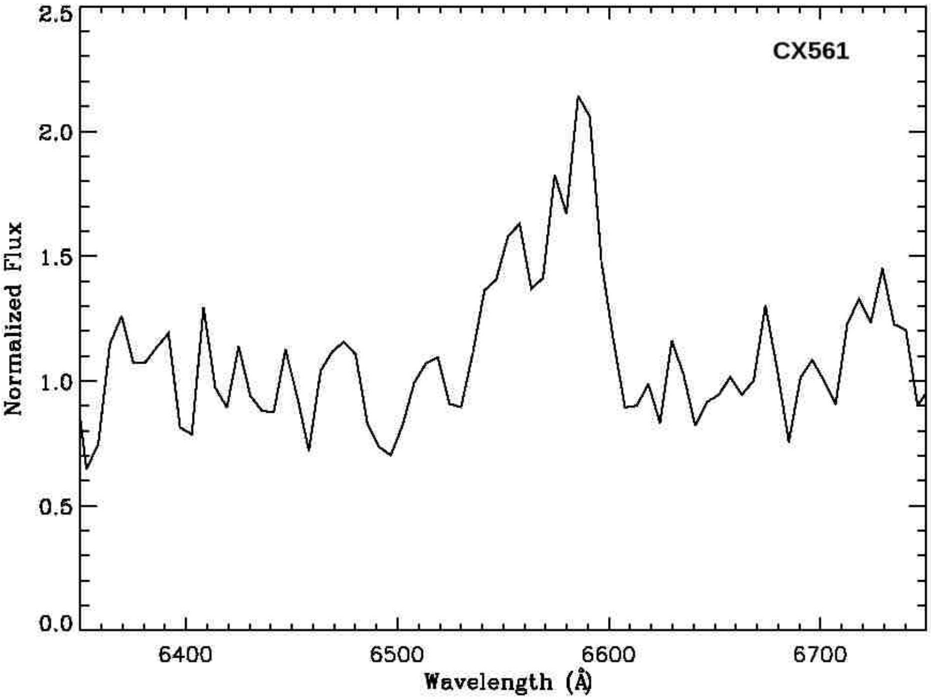

Figure 5.26: Zoom in on the double peaked Hα line in the NTT spectrum of CX561. The peaks are separated by 30 Å or 1420 $\mathrm{km\,s^{-1}}$, which implies a disk velocity of 710 $\mathrm{km\,s^{-1}}$

We have only 5 counts in the Chandra data for this source, so we cannot know the shape of the spectrum, but using assumptions in Jonker et al (2011) we find that $\frac{F_X}{F_{r'}}$ lies in the range of $\frac{1}{50} - 1$, depending on how much of the dust in the line of sight it lies behind. This is consistent with both CVs and qLMXBs. The double peaked Hα line rules out a coronally active star, and $H\alpha$ is not redshifted enough to suggest an AGN as X-ray faint as CX561 is. Its absolute magnitude at a distance of 1 kpc would be consistent with quiescent CVs and qLMXBs depending on the donor star, and its absolute magnitude at a distance of 8 kpc is $M_{r'} \approx 1$ which is consistent with the brightest qLMXBs. At bulge distance, $L_X = 6 \times 10^{32}\,\mathrm{ergs\,s^{-1}}$ which is consistent with both NS and BH qLMXBs, while $L_X = 5 \times 10^{30}\,\mathrm{ergs\,s^{-1}}$ for a distance of 1 kpc, which is consistent with BH qLMXBs and CVs. If the system is distant, the X-ray to optical flux ratio is a bit low for a NS primary, but this cannot be ruled out for 2 reasons. First, the uncertainty in the ratio is quite high.

With only 5 photons in the X-ray and no spectral information, and without photometric standards in the optical or an exact extinction measurement, this value could be off by an order of magnitude when uncertainties from all of these factors are considered. Also, if this is indeed a qLMXB with a NS primary, it has not undergone recent outbursts and could display different properties in quiescence than those systems that have been followed into quiescence from an active state.

CX561 showed no significant optical variability in the Mosaic-II data, as shown in Figure 5.27. There is, however, an eclipsing binary with r' magnitude 17.2 ± 0.5 with a 12.5 day period next to the emission line object. It is marked in the finder chart in Fig. 5.28 with a white circle. It is this nearby variable that has been mistakenly identified as the counterpart by Udalski et al. (2012). The fact that it shows donor emission lines means that a substantial fraction of the light must come from the donor star rather than the disk, yet it shows no ellipsoidal modulations. This implies a low inclination system. The high FWHM of Hα combined with a low inclination suggests a very high mass for the accretor, which is why this object is such a strong candidate BH qLMXB.

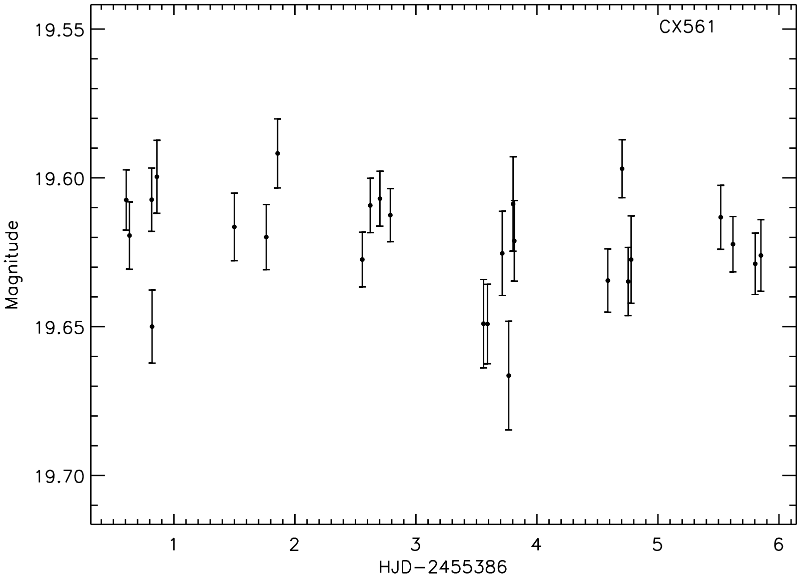

Figure 5.27: Mosaic-II lightcurve of CX561.

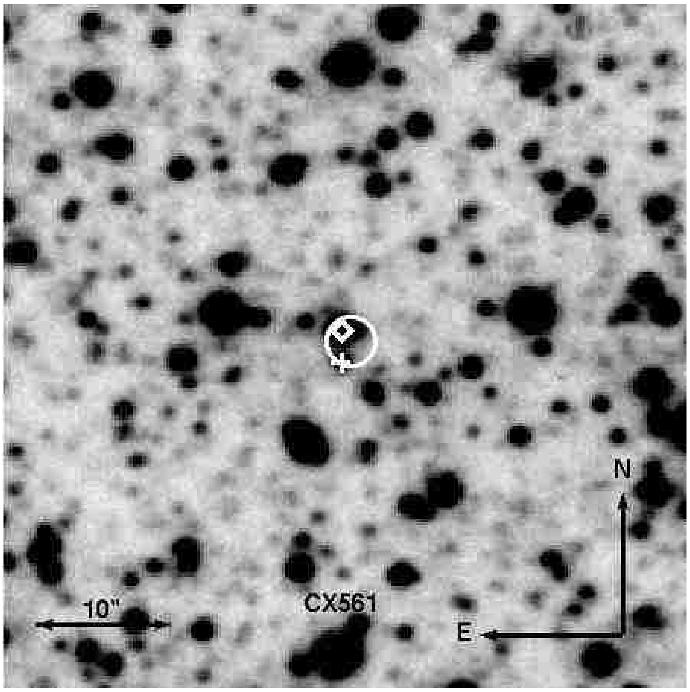

Figure 5.28: Finder charts for CX561. The 3-sigma X-ray position is plotted with a white oval, while the optical companion is marked with a white cross, with a nearby eclipsing binary system marked with a white diamond. North is up and East is left.

5.18 CX781

CX781 is covered in depth by Torres et al. (2013). The optical counterpart of CX781 dips by 0.25 magnitudes before returning to full brightness of 17.8 magnitudes, as shown in Figure 5.29. It is unclear whether this behavior is periodic because our baseline does not extend far enough to see it repeat. There is also flickering of order 0.05 magnitude amplitude on top of the underlying morphology. The flickering argues in favor of the presence of an accretion disk. If this behavior is periodic, the period would be either 6.90 ± 0.31 days for a single humped modulation or 13.9 ± 0.62 days for a double humped modulation. The optical spectrum shows narrow Hα emission as well as some He I emission. This is consistent with CVs.

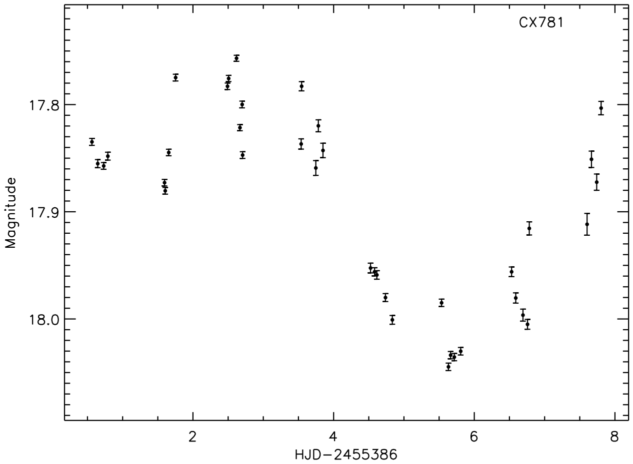

Figure 5.29: Mosaic-II lightcurve of CX781.

5.19 CX794

This source is covered in depth along with optical/NIR spectroscopy in Torres et al. (2013). We observe 2 eclipses on successive nights in Mosaic-II data for CX794, of depth 1.8 magnitudes and 1.3 magnitudes, respectively. The unfolded lightcurve is shown in Figure 5.30 We find a period of 0.1179 days, or 2.8 hours, with another peak in the Lomb-Scargle periodogram at 0.1052 days which is the one day alias of 0.1179 days, adding weight to the 0.1 day period suggested for this object in Udalski et al. (2012). The lightcurve folded on both periods is shown in Figure 5.31. This is in the period gap for CVs. The eclipse is very well defined, with a hump before the eclipse in phase. This is consistent with CVs at high inclination with a hotspot on the accretion disk from the stream impact point. The magnitude while not in eclipse is $r' = 19.9$, which yields an X-ray to optical flux ratio of 0.7 without extinction corrections. Using the bulge $E(B-V)$ of 1.97, $\frac{F_X}{F_{r'}} = \frac{1}{100}$. This is consistent with qLMXBs or CVs. The optical spectrum shows Hα in emission as well as He I. This is consistent with a CV.

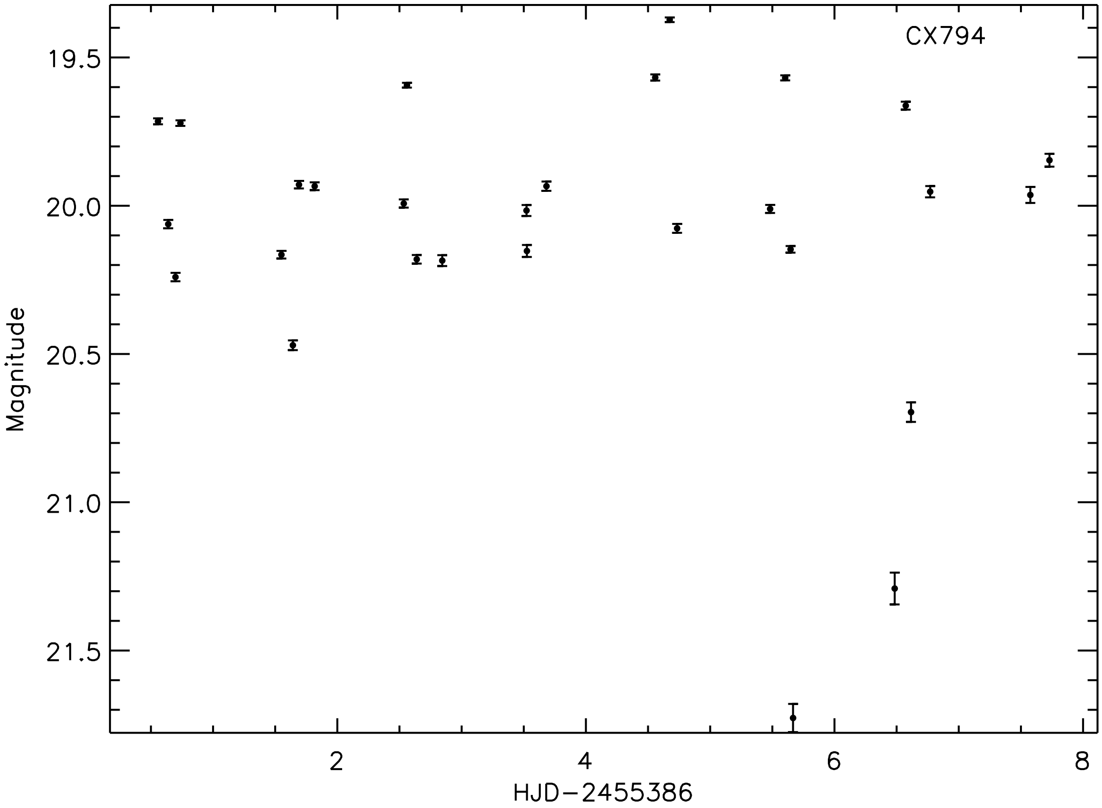

Figure 5.30: Mosaic-II lightcurve of CX794.

5.20 CX1011

This object is discussed in depth along with optical/NIR spectroscopy in Torres et al. (2013). This source is near the saturation limit in the Mosaic-II data with a Sloan r' magnitude of 15.93. There are 28 observations which do not saturate, which are shown in Figure 5.32. The optical counterpart shows low amplitude aperiodic flickering of 0.05 magnitudes between maximum and minimum. The RMS of the flickering is 0.01 magnitudes. This variability is not significantly correlated with the seeing, which suggests it is real and not a product of non-linear CCD response. Absorbed, $\frac{F_X}{F_{r'}} = \frac{1}{60}$, which is consistent with CVs and BH qLMXBs. Using $E(B-V) = 3.15$ for Bulge sources, $\frac{F_X}{F_{r'}} = 10^{-4.8}$ which would suggest coronal X-ray emission but the optical spectrum rules this out. The optical spectrum shows

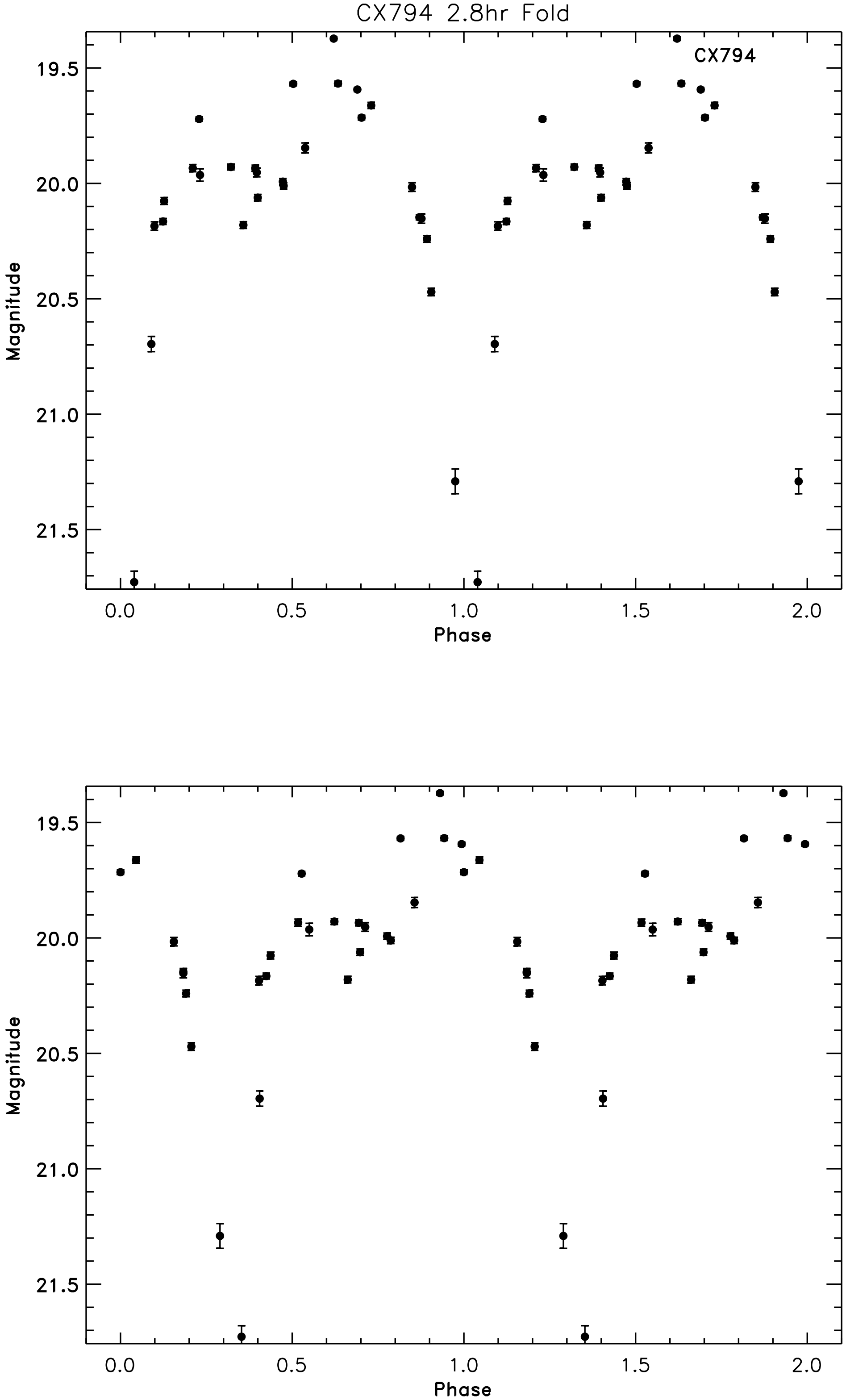

Figure 5.31: Left: Mosaic-II lightcurve of CX794 folded on a period of 0.1179 days. Right: The same data folded on the OGLE IV period of 0.1052 days.

narrow Hα emission, with interstellar absorption at Na D $\lambda\lambda$5780 with EW 0.4 Å. There is no indication of photospheric absorption lines, while He II $\lambda\lambda$4686 and the Bowen Blend are in emission, arguing for either a magnetic CV or nova-like variable at a distance substantially closer than the Bulge, in front of most of the dust in that line of sight.

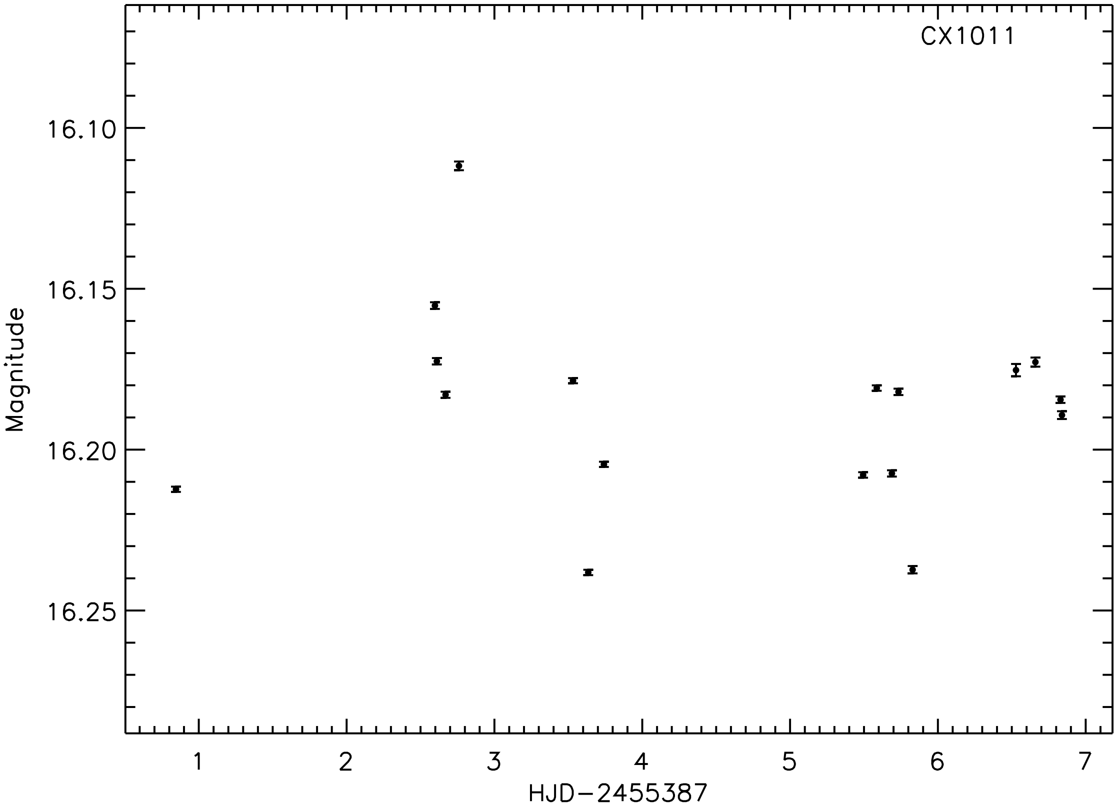

Figure 5.32: Mosaic-II lightcurve of CX1011.

6. Selected Sources

In this chapter, I will discuss in greater detail sources that show interesting behavior, such as eclipses, outbursts, ellipsoidal modulations, periods less than a day, or aperiodic flickering above 0.1 magnitudes. Many of these are likely CVs or qLMXBs, though W UMas can also strongly resemble ellipsoidal variations because of the breadth of their eclipses and they have periods less than a day. Even by using $\frac{F_X}{F_{opt}}$ to discriminate, this list will doubtless include some W UMas. Spectroscopy is needed to fully distinguish between source types, and is a part of the larger GBS strategy, but it is mostly outside the scope of this work which is primarily focused on photometry. I make no attempt to discuss possible interpretations for every variable counterpart to sources in the GBS catalog individually, though the data for all variable sources can be found in Table 4.1 and in Appendix A.

6.1 CX11

This object has an X-ray to optical flux ratio of 40, uncorrected for extinction, and shows dramatic, aperiodic variations shown in Figure 6.1. At Bulge distance, $L_X \approx 10^{34}\,\mathrm{ergs\,s^{-1}}$ and $\frac{F_X}{F_{opt}} = 0.4$ with Bulge reddening. $\frac{F_X}{F_{opt}}$ is high enough to rule out a quiescent CV, which are not typically luminous enough in the X-ray to be detected at this strength in the Galactic Bulge and thus could not suffer the full amount of extinction predicted by the Gonzalez (2012) maps, though it is consistent with a closer magnetic CV with moderate extinction or a NS qLMXB in the Bulge.

The variability is irregular, coming in dips and small outbursts, each on the order of $0.2 - 0.4$ magnitudes, and lasting on the order of several hours as points within a night are strongly correlated.

6.2 CX19

CX19 is an eclipsing object, as shown in Figure 6.2, in addition to having a fairly high X-ray to optical flux ratio. It also shows large amplitude aperiodic variability, up to 0.4 magnitudes. The eclipse is deep, at almost a magnitude, implying a substantial temperature difference

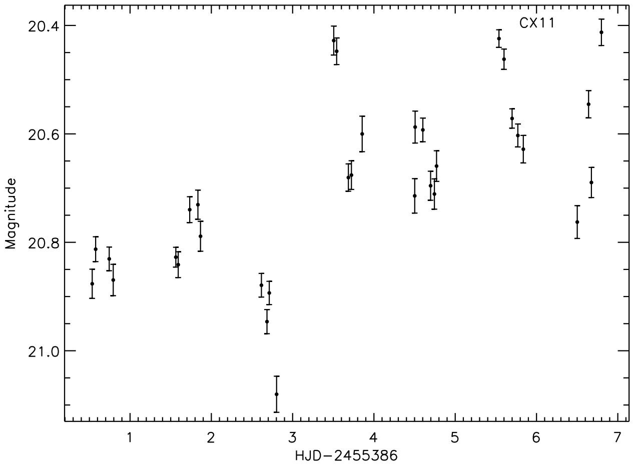

Figure 6.1: Mosaic-II lightcurve of CX11.

between bodies. The eclipse lasts no more than 3 hours, and there is only 1 observation in eclipse out of 20. Assuming a roughly uniform sampling of the phase (which is not true for periods very near integer multiples of 1 day), this implies the eclipse lasts for $5^{+5}_{-4}\%$ of the phase. The upper end of this range is consistent with CVs and qLMXBs. By assuming the eclipse lasts 5% of the orbital phase and takes the full 3 hours consistent with observations, we place an upper limit on the orbital period of 3 days. It is very likely a binary with a compact object.

6.3 CX21

CX21 is widely variable, on timescales of hours, showing a change in brightness of over 1 magnitude shown in Figure 6.3. There is no periodicity to these changes. Absorbed $\frac{F_X}{F_{opt}} = 3$, which, given the large uncertainty in extinction, is consistent with both magnetic and non-magnetic CVs and qLMXBs. $L_X \approx 3 \times 10^{33}\,\mathrm{ergs\,s^{-1}}$ at the Bulge. The high amplitude flickering suggests a large contribution to the continuum light from the accreting material compared to the donor star, which argues against a quiescent system. The lightcurve is also similar to other confirmed IPs in our survey such as CX5. A magnetic CV is a more likely classification than a qLMXB or CV, though without the detection of an X-ray pulse period

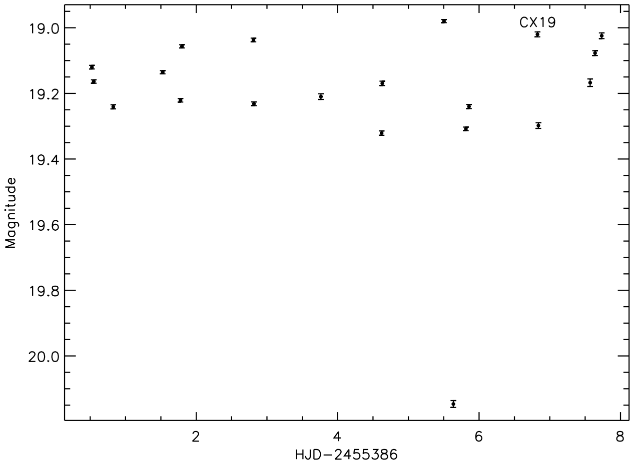

Figure 6.2: Mosaic-II lightcurve of CX19.

or optical spectroscopy no solid determination can be made. We can safely rule out an RS CVn, W UMa, active star, or AGN.

6.4 CX29

CX29 shows smooth variations which both rise and fall, as shown in Figure 6.4. There is a crest and a trough and our data are consistent with a period of $\sim$ 10.2 days, but this is highly speculative. There is a small flare, ≈ 0.1 magnitudes in amplitude, which lasts for several hours on the fifth night of observations. Absorbed $\frac{F_X}{F_{opt}} = \frac{1}{2}$, which is consistent with qCVs, IPs, and qLMXBs. With errors, it is also consistent with active M dwarfs since most the light they emit is in the infrared and $\frac{F_X}{F_{opt}} >> \frac{F_X}{F_{bol}}$. At the bulge, $L_X \approx 2.4 \times 10^{33}\,\mathrm{ergs\,s^{-1}}$. If this were an M dwarf, with an absolute magnitude of $M_{r'} \approx 15$, then the distance would be $23 \pm 7\,\mathrm{pc}$ which would imply $L_X \approx 2 \times 10^{28}\,\mathrm{ergs\,s^{-1}}$ which is consistent with M dwarfs. It is possible that this is a flare star, with the complex multi-day variations arising from a combination of star spots as the star rotates with $P_{spin} > 8$ days. CX161 is a likely flare star, discussed later in this chapter, which shows smooth sinusoidal variations on multi-day period with a larger flare. Each star spot contributes a sine wave to the lightcurve.

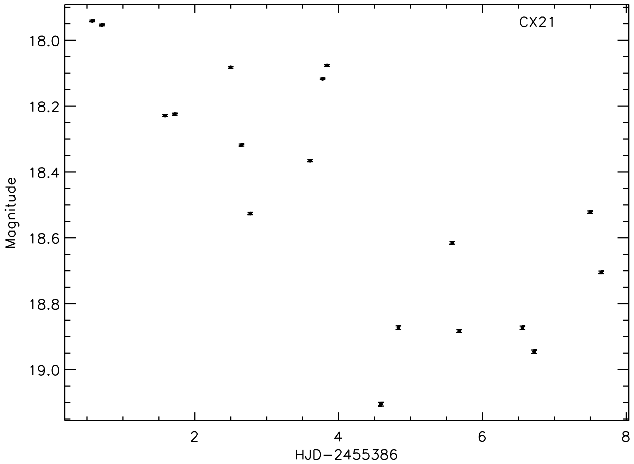

Figure 6.3: Mosaic-II lightcurve of CX21.

Differences among star spots in phase and brightness, and even small differences in period by latitude due to differential rotation, can lead to more complex lightcurve morphologies.

6.5 CX54

CX54 is faint, at $r' = 21$, and $\frac{F_X}{F_{opt}} = 13$ which is consistent with AGN and, with extinction, NS qLMXBs, CVs and IPs. There is an outburst over 0.5 magnitudes in brightness on the last night of observations, shown in Figure 6.5. This is also the night with the worst seeing. There is only one good observation on this night, so it is impossible to determine how long the outburst lasts. Observations on the night 7 are also somewhat brighter than the steady level of the other nights. The outburst could begin on night 7 and continue well beyond night 8, as a DN would, or it could last for any where from hours to minutes. Further observations are needed to classify this object, but a dramatic change in luminosity on a short time scale points to this optical star being the true counterpart to the X-ray source.

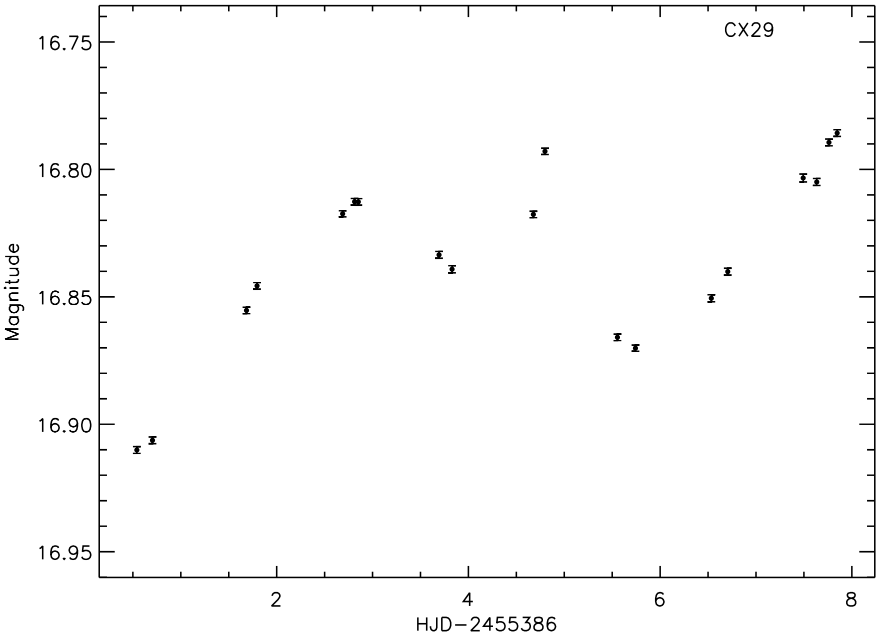

Figure 6.4: Mosaic-II lightcurve of CX29.

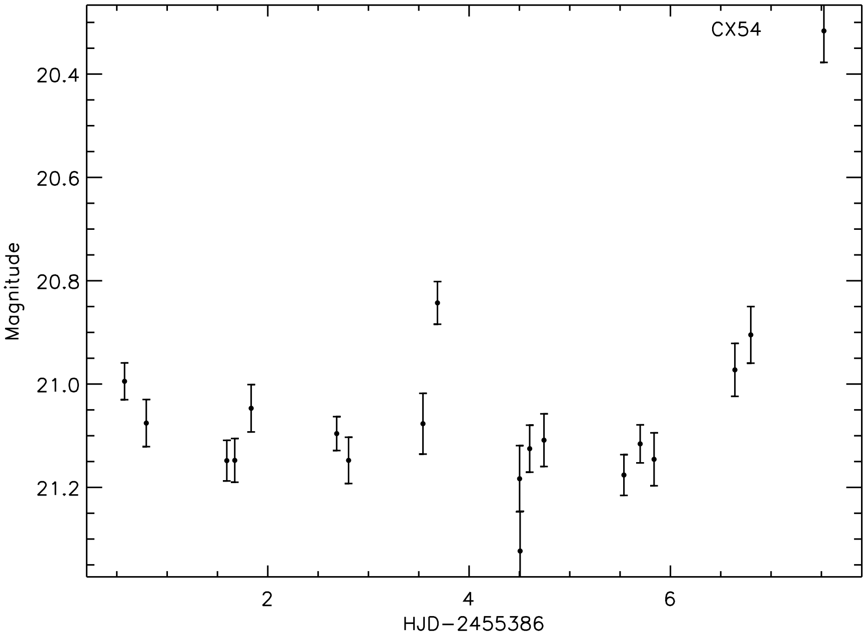

Figure 6.5: Mosaic-II lightcurve of CX54.

6.6 CX67

CX67 has a suspected period of 5.67 days. The Mosaic-II lightcurve is shown in Figure 6.6. Absorbed $\frac{F_X}{F_{opt}} = 0.7$ which is consistent with CVs, IPs, qLMXBs, and M dwarfs. It is too X-ray bright to be an RS CVn. It is possible that this is a longer period binary with a compact object and a subgiant donor, such as V404 Cyg (Hynes et al., 2009). If this is the case, $\frac{F_X}{F_{opt}}$ should be lower for quiescent systems than for systems with a MS donor because the optical contribution from the larger counterpart is much higher.

6.7 CX74

CX74 has a counterpart on the edge of the saturation limit, and we can only use data from nights with poor seeing. It varies from $r' = 15.60$ to $r' = 15.48$ within 6 hours, and has a maximum change of 0.17 magnitudes, as shown in Figure 6.7. The absorbed X-ray to optical flux ratio is 0.08, which is consistent with qLMXBs, CVs, W UMas, or RS CVns. We do not recover a period for this source, which argues against sources like RS CVns or W UMas with very clear, smooth modulations and no flickering, especially for a source this bright with very good signal to noise. While we lost $\frac{1}{2}$ our data to non-linearity or saturation, we still have 17 data points with a baseline of 6 days, which should be adequate to pick up most periods between 2 hours and 3 days. The changes in brightness do not correlate with seeing. There is a possible period at 1.22 days, but it has a False Alarm Probability of 6.6%. It is possible that there is some flickering intrinsic to the source that is obscuring the true period, but the presence of such flickering would also argue against the source being an RS CVn or W UMa.

6.8 CX81

CX81 shows an outburst of 3.5 magnitudes and lasts at least a few days, as shown in Figure 6.8, which is typical of DNe. Absorbed $\frac{F_X}{F_{opt}} = 5$, which is consistent with CVs with reddening. This source is very likely a CV undergoing DNe outbursts.

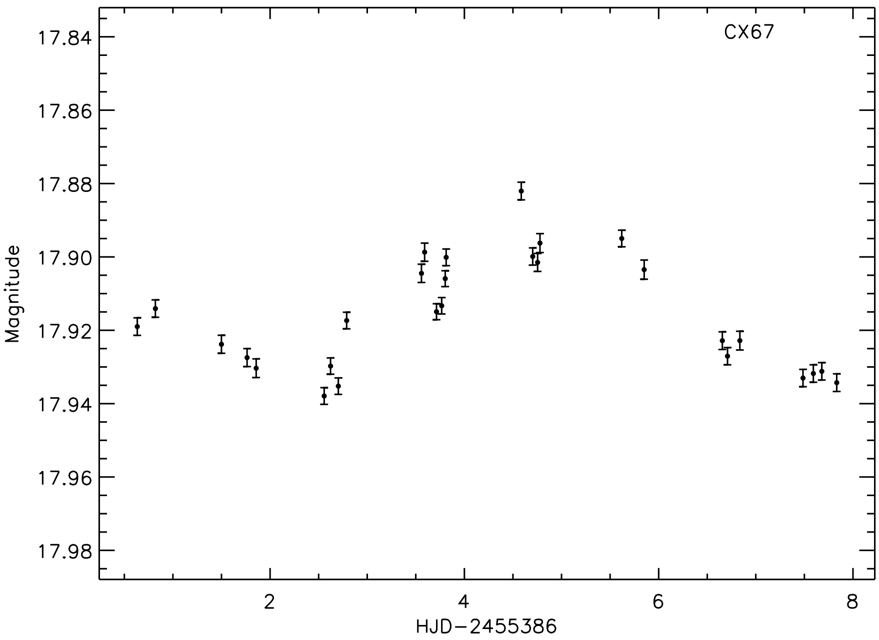

Figure 6.6: Mosaic-II lightcurve of CX67.

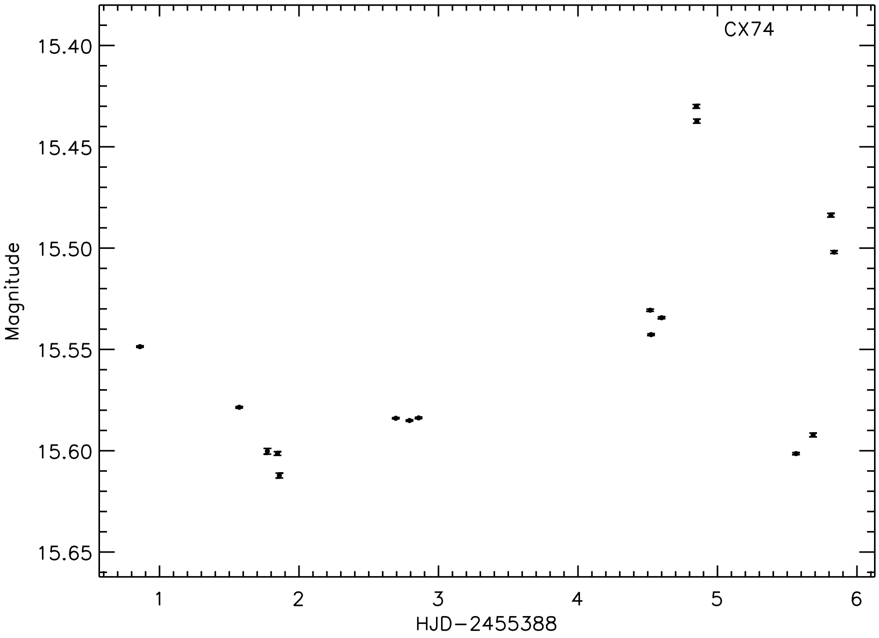

Figure 6.7: Mosaic-II lightcurve of CX74.

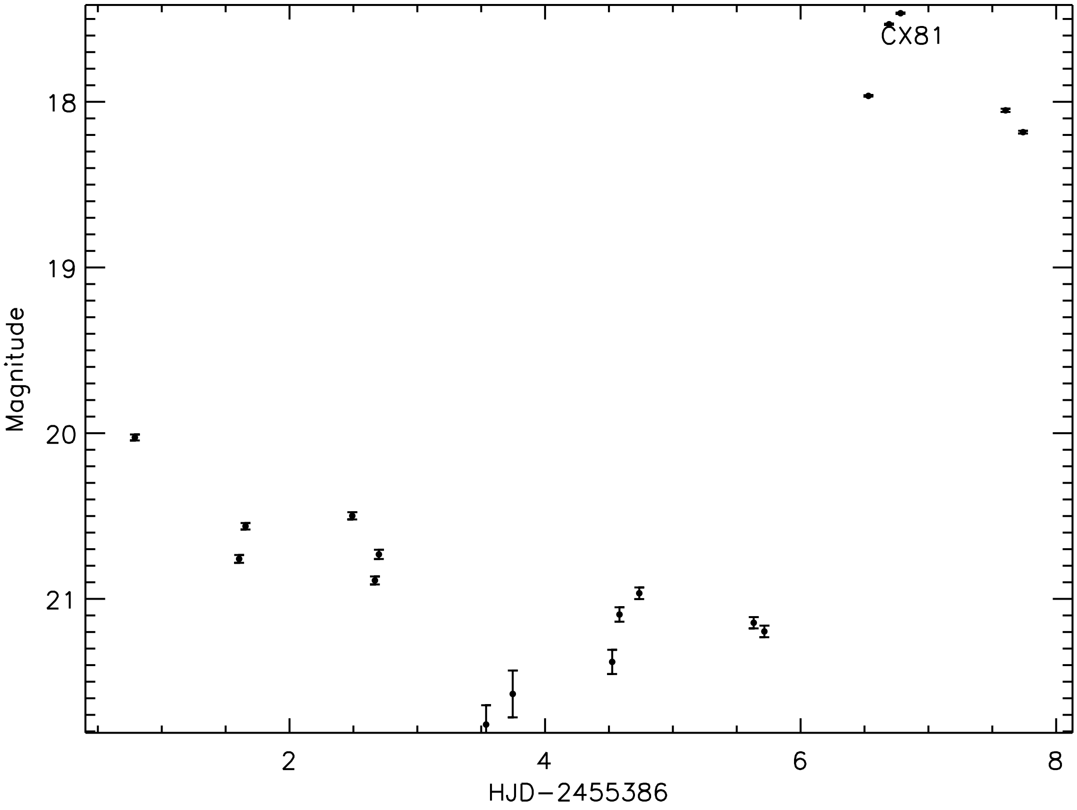

Figure 6.8: Mosaic-II lightcurve of CX81.

6.9 CX83

CX83 is not significantly variable except for an eclipse on the 5th night of observations shown in Figure 6.9. This eclipse is 0.2 magnitudes in depth and lasts no more than 2 hours. Only 1 observation out of 26 points is in eclipse which lasts only $4 \pm 4\%$ of the phase. From these constraints, we place an upper limit on the orbital period of 2 days. Absorbed $\frac{F_X}{F_{opt}} = 7$, which drops to 0.02 with reddening at the Bulge distance, which is a range consistent with both CVs, magnetic CVs and qLMXBs.

6.10 CX84

CX84 has a suspected period of 4.67 days shown in Figure 6.10, and an absorbed $\frac{F_X}{F_{opt}} = 2$. Similarly to CX67, this object is unlikely to be an RS CVn based on the high X-ray to

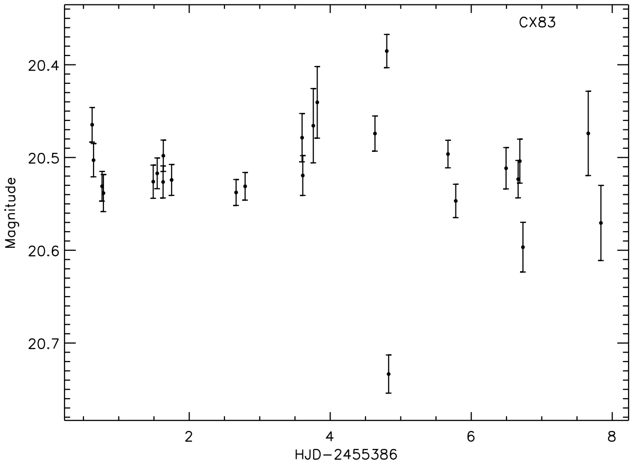

Figure 6.9: Mosaic-II lightcurve of CX83.

optical flux ratio, but it could be a qLMXB or CV with a subgiant donor or an active M dwarf with starspots. The amplitude of the variations is 0.1 magnitudes which is consistent with both ellipsoidal variations from accreting binaries and with starspots on an active M dwarf which can be very large.

6.11 CX87

CX87 starts at close to $r' = 20.4$ at the beginning of our observations, and declines over the next few days to the limiting magnitude of our observations at $r' \approx 23$ as shown in Figure 6.11. This decline of 2-3 magnitudes over a few days is consistent with a DN outburst. Measured from the magnitude when not in outburst, $\frac{F_X}{F_{opt}} = 100$, which is too high for a CV. The faint magnitude in the optical and low density of stars in the field is consistent with some extinction. $E(B-V) = 1.81$ in this field, making $\frac{F_X}{F_{opt}} = 2$ at Bulge distance, while $L_X = \approx 1.3 \times 10^{33}\,\mathrm{ergs\,s^{-1}}$ at the Bulge. This is brighter than is consistent with a CV, suggesting it would have to be closer, which means it likely can't suffer enough extinction to be consistent with a CV. DN have been observed rarely in IPs. It is possible that this is such a system at a distance of 2-3 kpc, which would give L_X and $\frac{F_X}{F_{opt}}$ consistent with IPs.

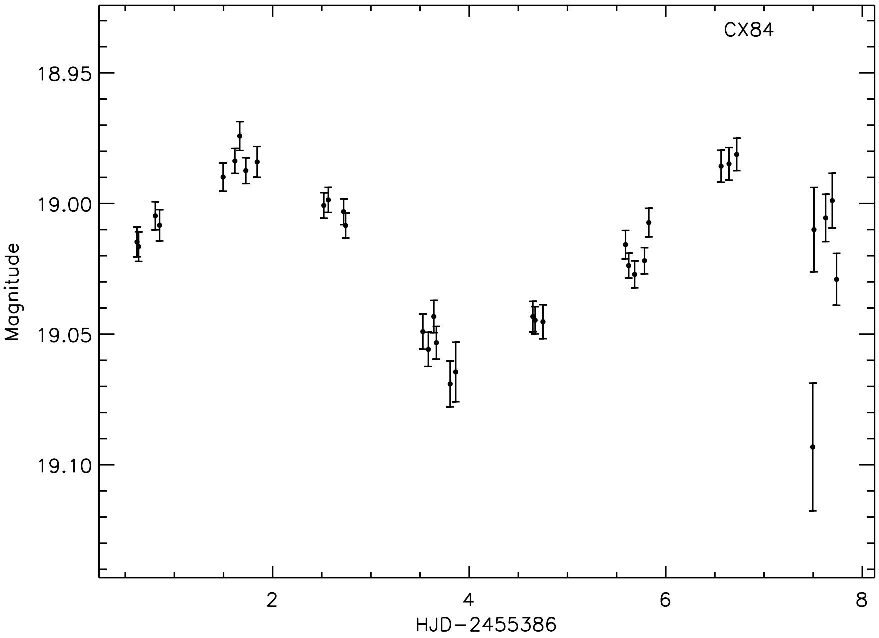

Figure 6.10: Mosaic-II lightcurve of CX84.

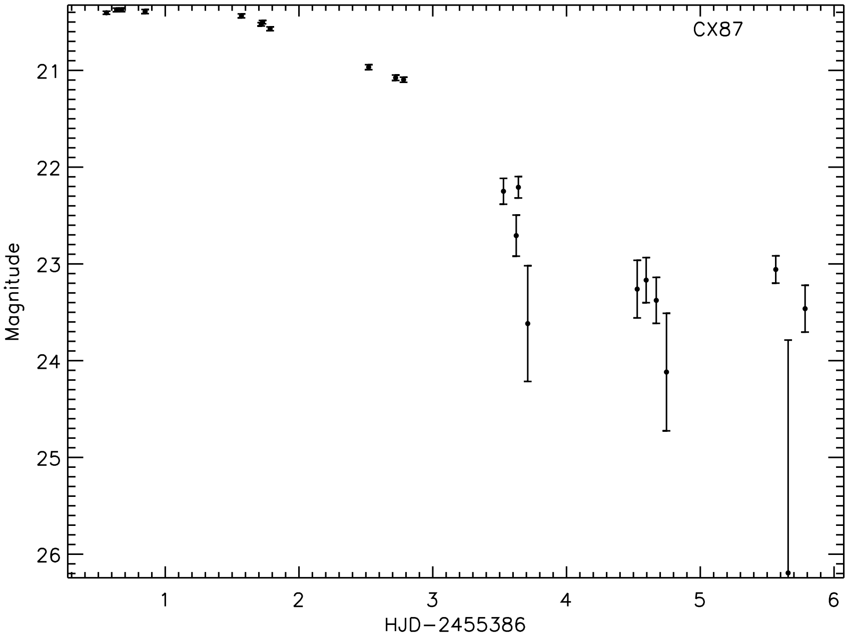

Figure 6.11: Mosaic-II lightcurve of CX87.

6.12 CX96

CX96 is very faint optically and there are observations when the counterpart drops below the limiting magnitude of our observations. The Mosaic-II lightcurve is shown in Figure 6.12. This variability is not simply due to changes in seeing, as it is securely detected in the worst seeing observations and vanishes in some observations with the best seeing conditions. Roughly $\frac{1}{4}$ of observations are below the limiting magnitude, suggesting either relatively broad eclipses or that the drops in magnitude are due to flickering. Absorbed $\frac{F_X}{F_{opt}} = 100$ which is among the highest in the GBS. It is possible that this is a UCXB, which are optically very faint. It is predicted in Jonker et al. (2011) that 32 UCXBs will be detected with optical counterparts in the GBS area. $L_X \simeq 10^{33}\,\mathrm{ergs\,s^{-1}}$ at the Bulge. This is too faint for an active LMXB, but is consistent with NS qLMXBs. Extinction in this field, however, is also very high. For Bulge reddening, $\frac{F_X}{F_{opt}} \approx \frac{1}{16}$. This range is consistent with qLMXBs.

6.13 CX118

CX118 shows dramatic flickering of 0.6 magnitudes shown in Figure 6.13. There is no detectable period to these variations, which occur on a timescale of hours. Absorbed $\frac{F_X}{F_{opt}} = 0.4$ which is consistent with IPs, CVs, and qLMXBs. The dramatic aperiodic changes in continuum light are similar in character to IPs in the survey identified in Britt et al. (2013). Quiescent CVs can flicker as well. Without additional information from spectroscopy, however, secure classification is impossible. If CX118 is an IP, one expects to see strong H, He I, and He II emission in its spectrum.

6.14 CX161

CX161 has a secure period of 3.32 days and shows a flare of 0.3 magnitudes that fades back to the quiescent level before the next observation 2.3 hours later, as shown in Figure 6.14. Absorbed $\frac{F_X}{F_{opt}} = 1$, which could be consistent with a flaring M dwarf between uncertainties in reddening, flux levels, and the fact that most of the light is emitted in the IR rather than

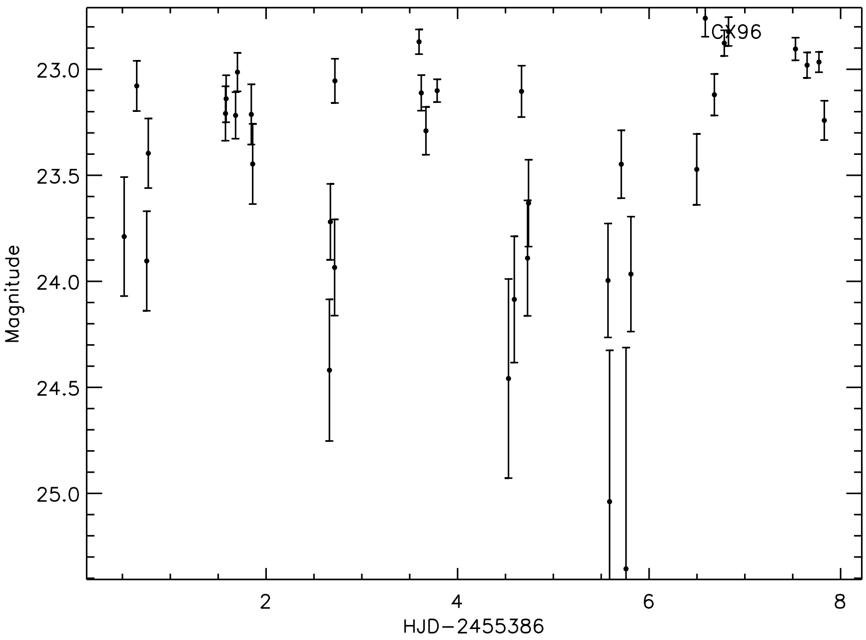

Figure 6.12: Mosaic-II lightcurve of CX96.

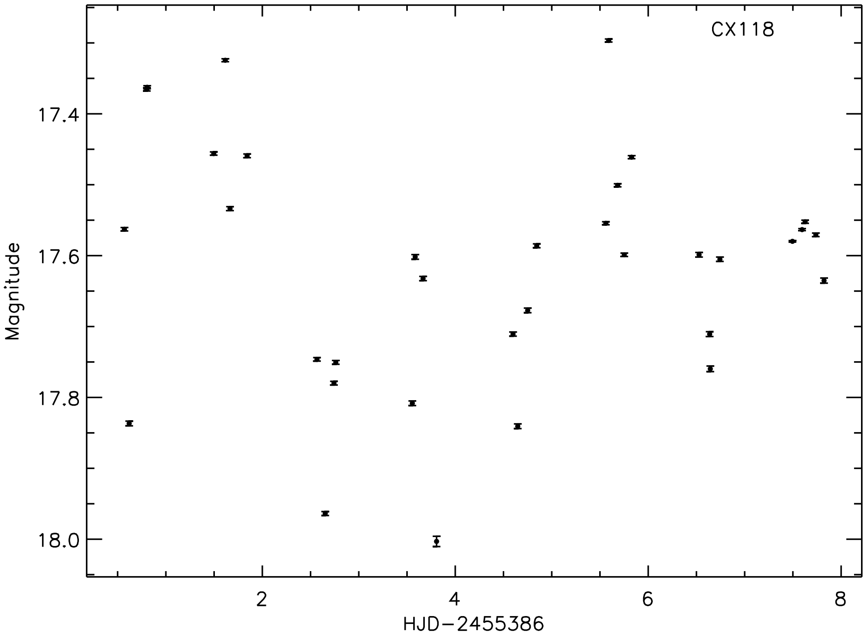

Figure 6.13: Mosaic-II lightcurve of CX118.

at optical wavelengths so that $F_{opt} << F_{Bol}$. The short timescale and magnitude of the flare is typical of active stars, while the period is attributable to stellar rotation and star spots.

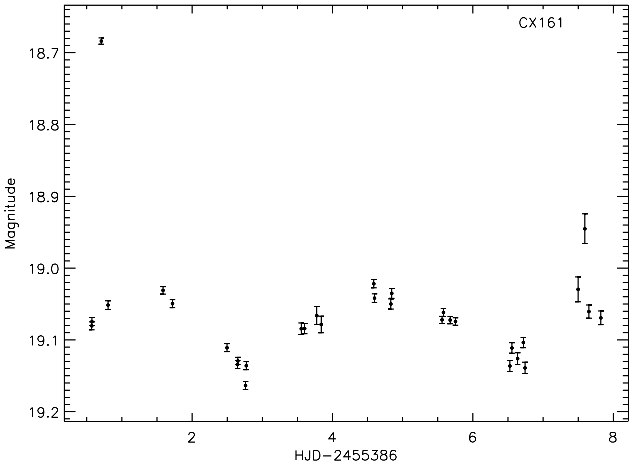

Figure 6.14: Mosaic-II lightcurve of CX161.

6.15 CX168

CX168 shows smooth variations with a possible period of 3.8 days as shown in Figure 6.15, but there is also some flickering superposed on these variations and a brightening of 0.1 magnitudes lasting at least a few hours on night 8. Absorbed $\frac{F_X}{F_{opt}} = 0.1$, which is consistent with CVs, qLMXBs, as well as RS CVns and active M dwarfs with some extinction. We do not expect to see the latter of these at Bulge distance, and the absolute magnitude of this object if it were in the Galactic Bulge is $M_{r'} = -6.1$ which too bright for CVs or qLMXBs. In addition, with Bulge reddening, $\frac{F_X}{F_{opt}} \approx 10^{-4}$ which is too low for compact objects. The true X-ray to optical flux ratio is therefore likely towards the high end of that range with the distance of the source substantially closer than the Bulge. In addition to the outburst on night 8, there is a small dip of 0.07 magnitudes on night 6 that lasts less than 2 hours. It is an isolated event, and if the 3.8 day period is the orbital period of a binary, then it is too brief to be an eclipse.

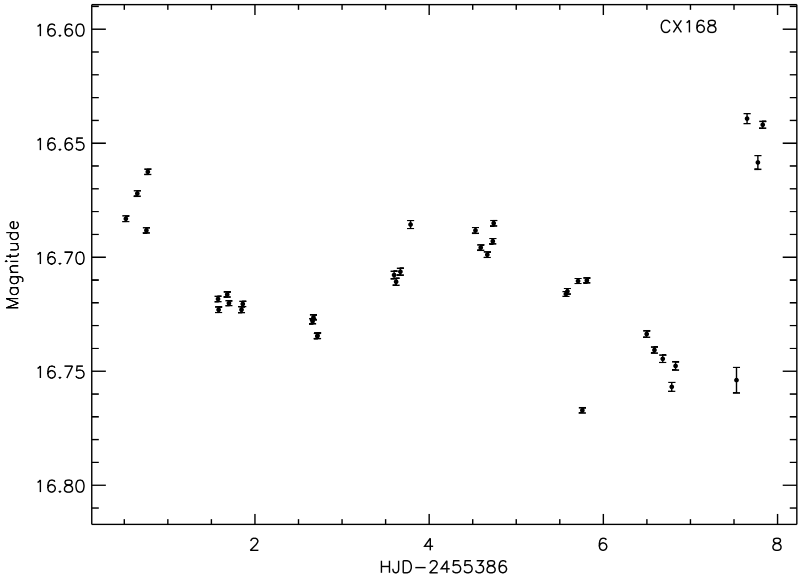

Figure 6.15: Mosaic-II lightcurve of CX168.

6.16 CX184

CX184 has a photometric period of 0.811 days, or 19.5 hours. The unfolded lightcurve is shown in Figure 6.16, while the folded lightcurve is shown in Figure 6.17. Absorbed $\frac{F_X}{F_{opt}} = 1$, which is consistent with qLMXBs, CVs, or M dwarfs. The variations are sinusoidal, and have an amplitude of 0.1 magnitudes. It is also possible that they are ellipsoidal variations with roughly equal minima. The higher X-ray to optical flux ratio in combination with a possible orbital period below a day makes this a candidate qLMXB, though spectroscopic follow up is necessary to differentiate it from a CV or fast rotating active M dwarf.

6.17 CX251

CX251 is very steady except for a single eclipse at least 0.07 magnitudes deep, shown in Figure 6.18. The eclipse duration is not well constrained as the last observation in night 2 is the only point in eclipse, so many different depths and durations are consistent with the data. Absorbed $\frac{F_X}{F_{opt}} = \frac{1}{10}$ which is consistent with qLMXBs and CVs.

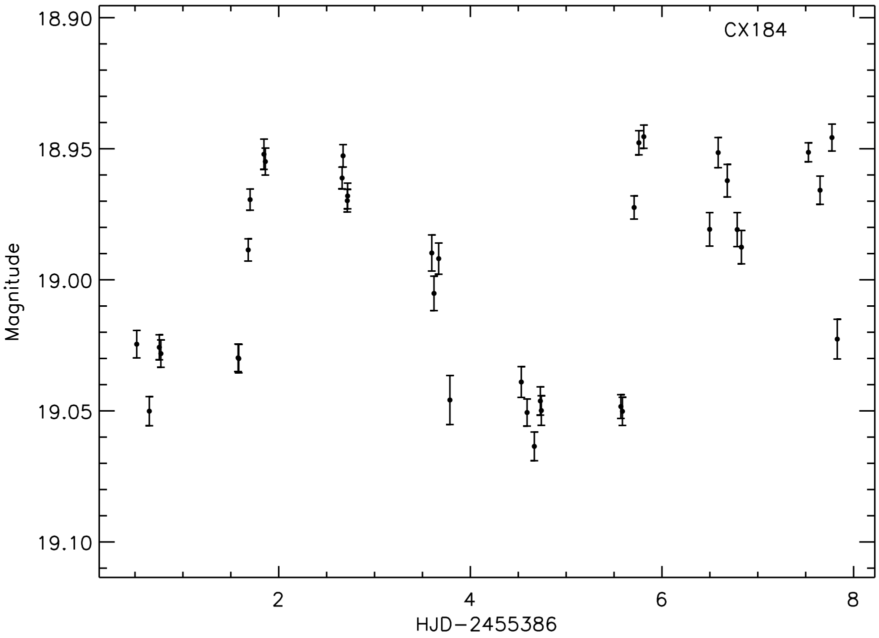

Figure 6.16: Mosaic-II lightcurve of CX184.

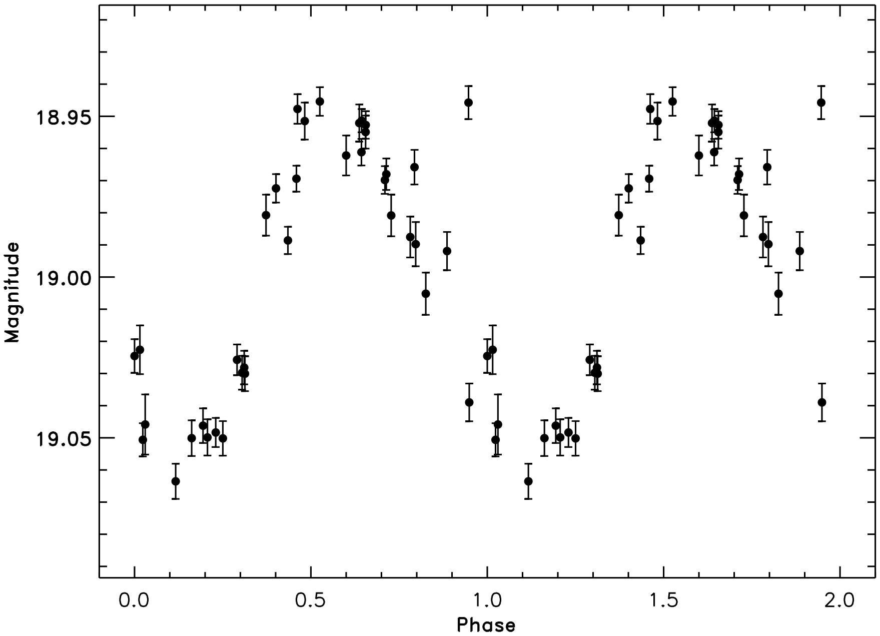

Figure 6.17: Mosaic-II lightcurve of CX184 folded on a 19.5 hour orbital period.

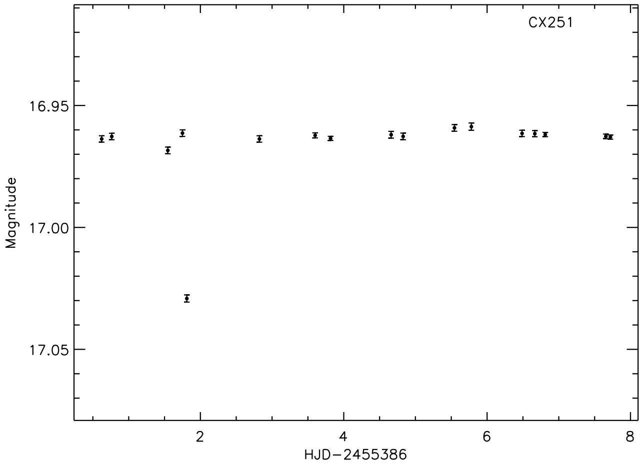

Figure 6.18: Mosaic-II lightcurve of CX251.

6.18 CX279

We recovered no significant period for CX279 as determined by Monte Carlo simulations with the Lomb-Scargle statistic. This source appears to be eclipsing, shown in Figure 6.19, and the eclipses are reasonably broad, taking 4 out of 18 observations, implying they last for $22 \pm 11\%$ of the phase. Absorbed $\frac{F_X}{F_{opt}} = 0.6$ which is consistent with qLMXBs, CVs and IPs.

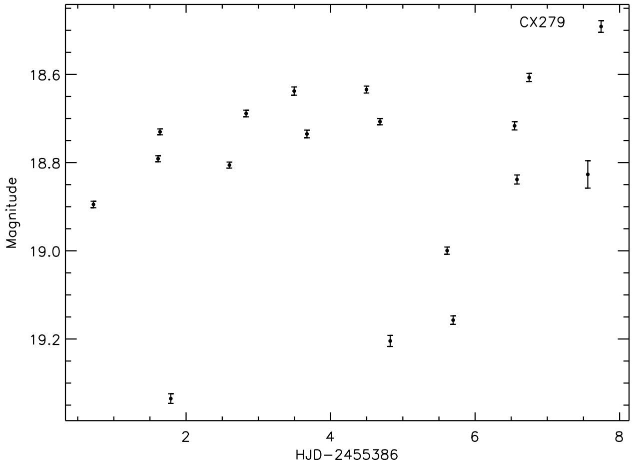

Figure 6.19: Mosaic-II lightcurve of CX279.

6.19 CX282

CX282 peaks and luminosity at $r' = 19.7$ before declining over the next 6 days to $r' = 20.0$, shown in Figure 6.20. The large amplitude change could be due to a long period (> 16 days). Absorbed $\frac{F_X}{F_{opt}} = 2$, which is consistent with CVs, qLMXBs, and active M dwarfs but not with RS CVns. The smooth changes on a multi-day timescale rules out magnetic CVs.

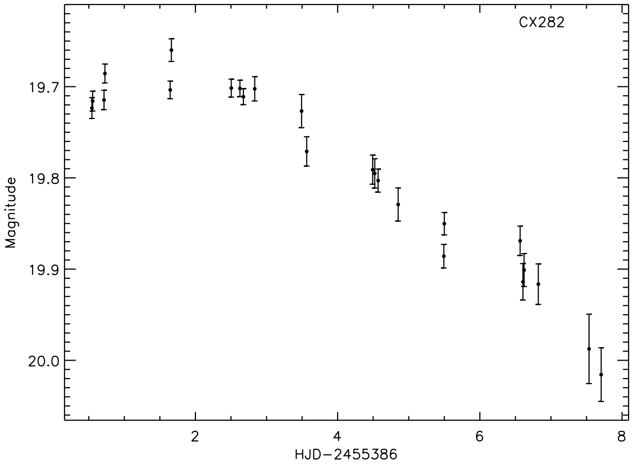

Figure 6.20: Mosaic-II lightcurve of CX282.

6.20 CX291

CX291 has a single point in eclipse in the first night of observations, with a depth of 0.5 magnitudes, shown in Figure 6.21. There is no variability apart from this eclipse. As with CX251, the only observation in eclipse comes at the end of the night, leaving its duration unconstrained. The absorbed X-ray to optical flux ratio is 1, which is consistent with CVs or qLMXBs.

6.21 CX298

CX298 drops from $r' = 21.4$ on the first night of observations to the limiting magnitude of $r' = 23$ by night 4, where it remains steady as shown in Figure 6.22. This large, steady decline could be the end of a DN outburst. If measured from the quiescent state, absorbed $\frac{F_X}{F_{opt}} = 20$,

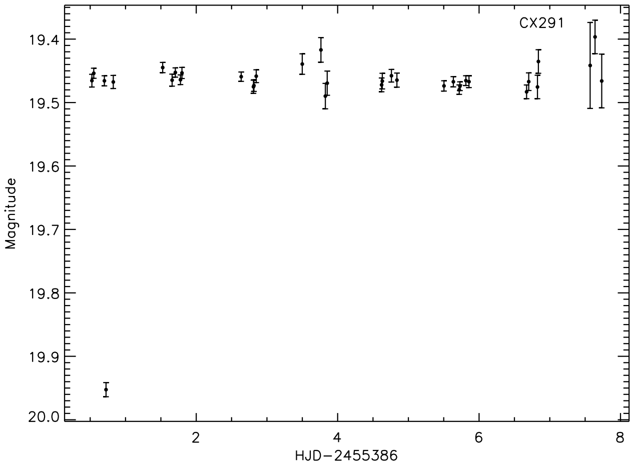

Figure 6.21: Mosaic-II lightcurve of CX291.

though it could be lower with reddening. At the bulge, $\frac{F_X}{F_{opt}} = 1$, which is consistent with qLMXBs, IPs, or CVs. If it is a CV undergoing DNe outbursts, however, then the distance should be substantially closer than the Bulge as their X-ray luminosity is below what we are likely to detect at that distance. With a moderate amount of extinction, however, this ratio of X-ray to optical light is consistent with a CV undergoing DNe outbursts. This is a similar source to CX87, which also appears to be the end of a DN outburst with a very high X-ray to optical flux ratio, fading to or below our limiting magnitude.

6.22 CX330

CX330 shows large amplitude aperiodic flickering covering a range of 0.3 magnitudes shown in Figure 6.23. This object also appears in OGLE IV data (Udalski et al., 2012) as an irregular variable. The X-ray to optical flux ratio is fairly low at 0.1 before correcting for extinction. The brightness varies on a timescale of hours. It is consistent with a magnetic CV, CV, or qLMXB.

6.23 CX349

CX349 shows dramatic variability with an amplitude of over 1 magnitude, shown in Figure 6.24, as well as a very high X-ray to optical flux ratio. Absorbed $\frac{F_X}{F_{opt}} = 24$ which is consistent

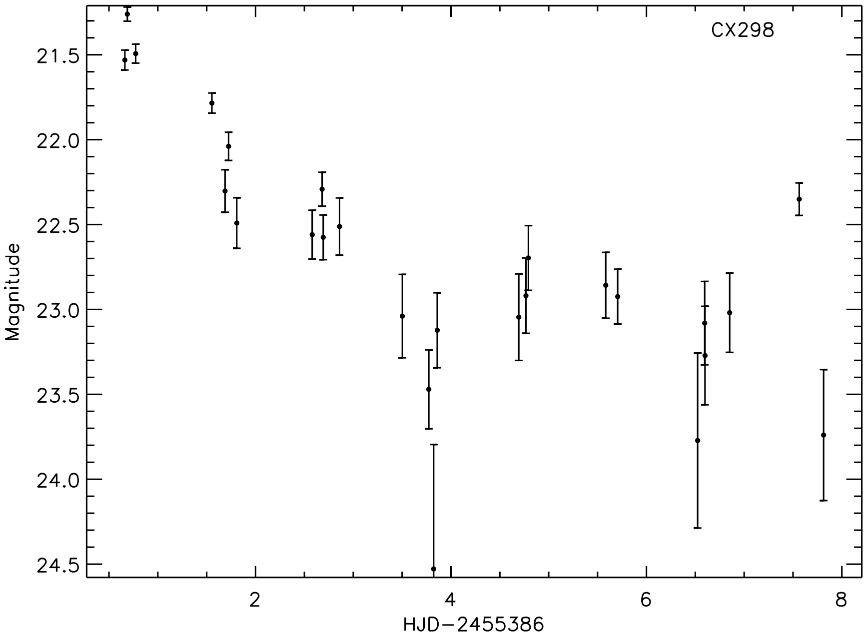

Figure 6.22: Mosaic-II lightcurve of CX298.

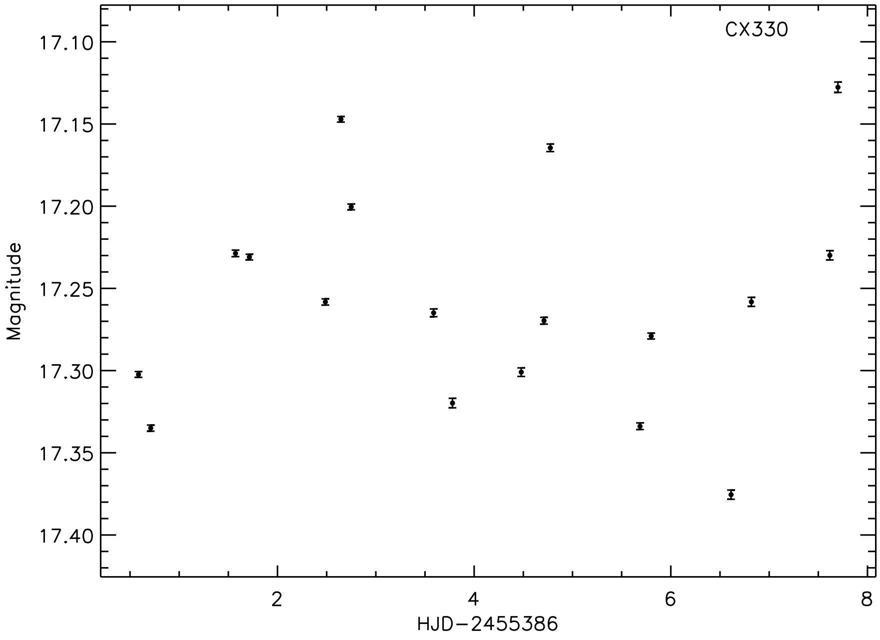

Figure 6.23: Mosaic-II lightcurve of CX330.

with ADC sources, UCXB, or with substantial reddening a magnetic CV or NS qLMXB. The lack of strong orbital modulation argues against an ADC source. At Bulge reddening, $\frac{F_X}{F_{opt}} = \frac{1}{4}$ which is consistent with NS qLMXBs and IPs. $L_X = 4 \times 10^{32}\,\mathrm{ergs\,s^{-1}}$ at the Bulge, which is also consistent with NS qLMXBs and IPs.

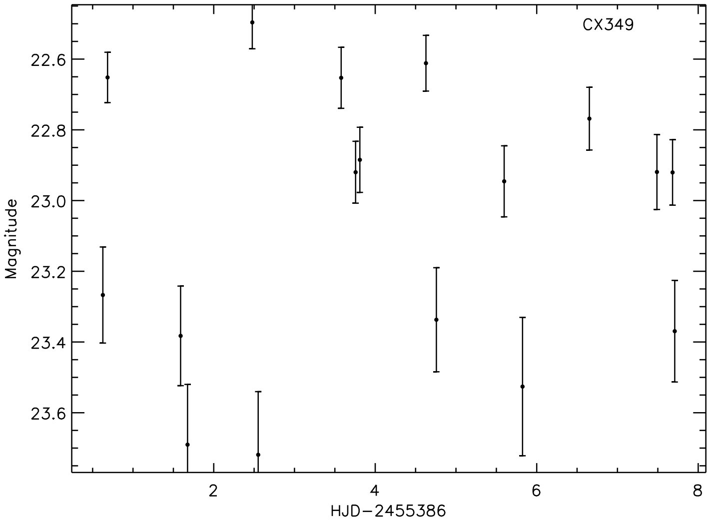

Figure 6.24: Mosaic-II lightcurve of CX349.

6.24 CX368

This source shows a dip of 0.2 magnitudes before holding steady at the peak brightness, as shown in Figure 6.25. The dip lasts for at least 3 days, though it begins before the start of our observations. The magnitude of the counterpart is $r' = 17.96$ which is consistent with a giant star at the Bulge distance. This object appears in the 2MASS catalog at $J = 14.185$ and $K = 12.692$. For Bulge reddening, $E(J-K) = 0.91, A_K = 0.63$. This implies $M_K = -2.46$ which is also consistent with a RGB star. In Symbiotic Binaries, X-rays are produced when winds from a Giant star accrete onto a WD or NS. We have already identified a possible Carbon star Symbiotic XRB in CX332 (Hynes et al., 2013), which are much more rare than ordinary symbiotics. Absorbed $\frac{F_X}{F_{opt}} = 0.2$, which is consistent with CVs or qLMXBs, which cannot be ruled out. At Bulge reddening, $\frac{F_X}{F_{opt}} = 0.006$ which is also consistent with a Symbiotic Binary. At Bulge distance, $L_X \simeq 10^{32}\,\mathrm{ergs\,s^{-1}}$, which is also consistent with Symbiotic X-ray Binaries.

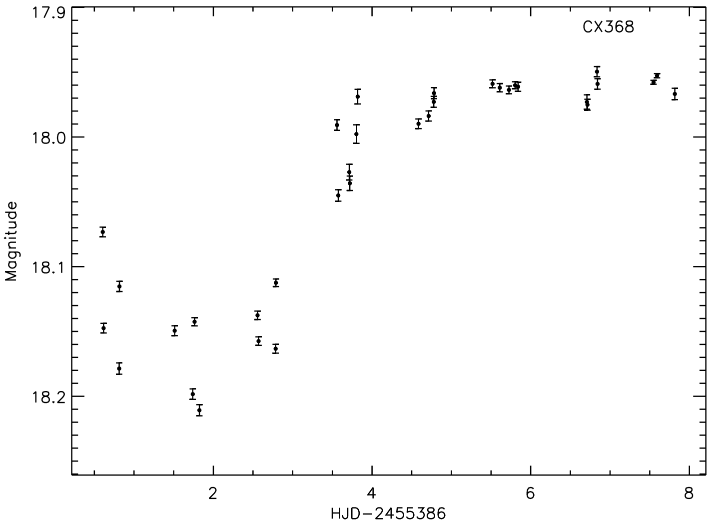

Figure 6.25: Mosaic-II lightcurve of CX368.

6.25 CX420

CX420 shows a period of 1.45 days. The Mosaic-II lightcurve is shown in Figure 6.26, while the folded lightcurve is displayed in Figure 6.27. It has an absorbed $\frac{F_X}{F_{opt}} = 0.4$ which is consistent with qLMXBs, CVs, and active M dwarfs. With the bulge reddening in this line of sight, $\frac{F_X}{F_{opt}} = 0.002$ is consistent with RS CVns as well, but RS CVns are too faint in the X-ray to be detected at Bulge distance. There is also some indication of flickering, which would also rule out an RS CVn or M dwarf. Long period qLMXBs or CVs indicate an evolved companion, which should have lower X-ray to optical flux ratios than those with MS donors due to the brighter donor. This object is consistent with such an object.

6.26 CX426

CX426 shows a steady decline of 0.9 magnitudes over the course of observations, shown in Figure 6.28. This is consistent with a DN outburst. The X-ray to optical flux ratio is 0.3 using the faintest observations from Mosaic-II data. This data is therefore consistent with

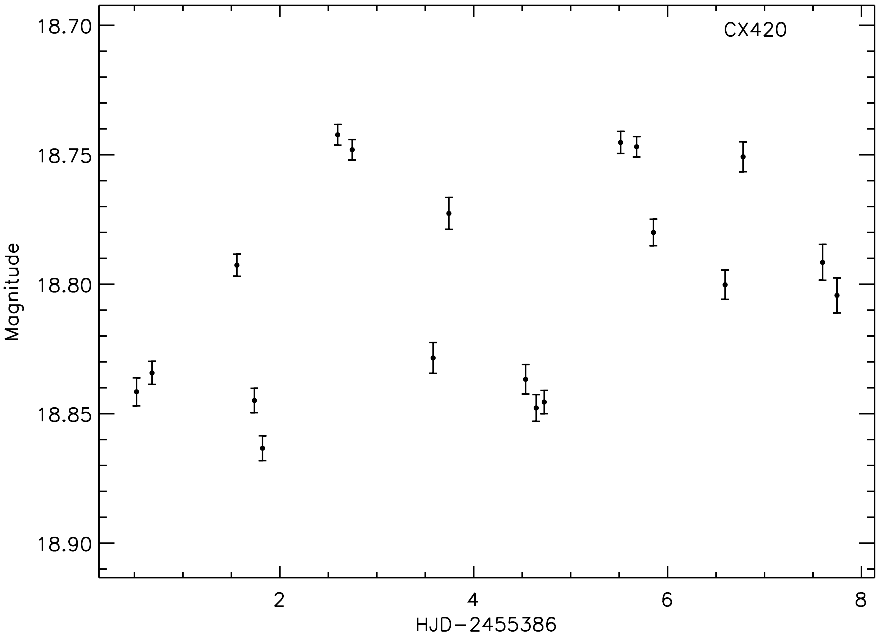

Figure 6.26: Mosaic-II lightcurve of CX420.

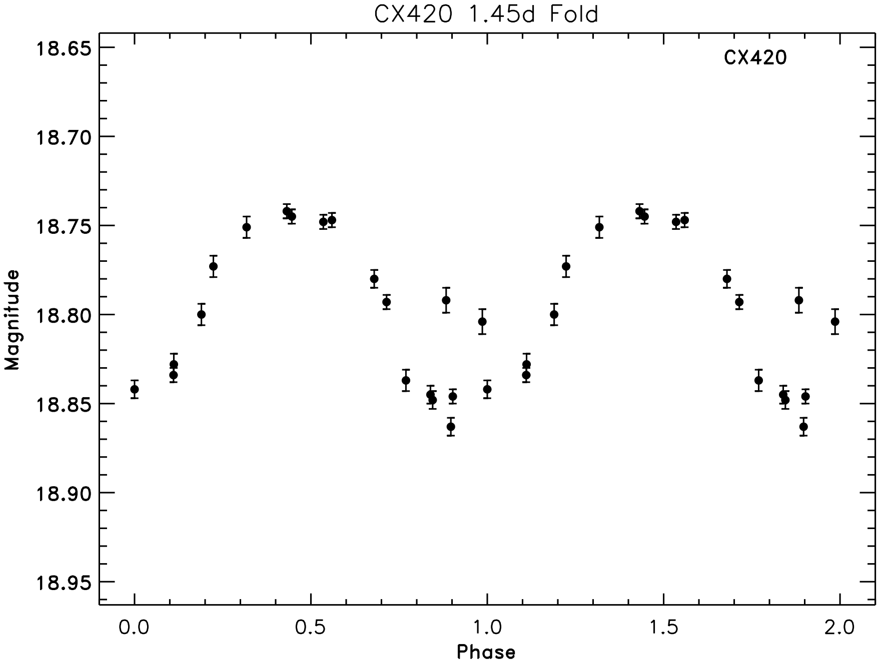

Figure 6.27: Mosaic-II lightcurve of CX420 folded on a 1.45 day orbital period.

a CV undergoing DNe outburst. There is some flickering around a best fit line as well with an amplitude $0.1-0.2$ magnitudes which is much higher than expected from simple photon noise or instrumental errors as well, which argues in favor of a CV interpretation as ordinary long period variables should not flicker.

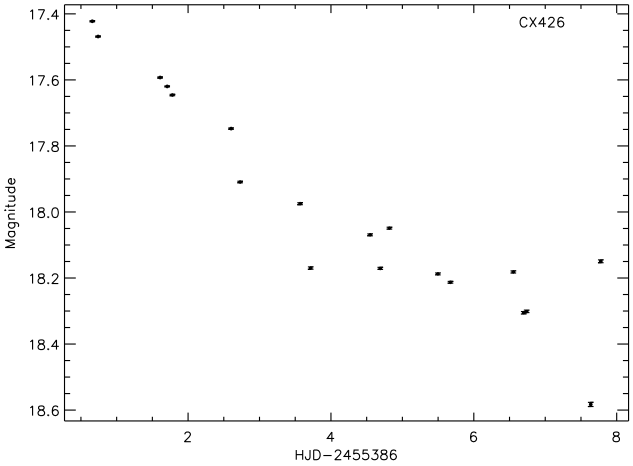

Figure 6.28: Mosaic-II lightcurve of CX426.

6.27 CX437

CX437 shows 2 eclipses of at least a magnitude, shown in Figure 6.29. The counterpart is very faint, $r' \approx 22.1$, and the eclipses drop below the limiting magnitude of our observations. There are 2 eclipses seen in 17 observations, suggesting an eclipse duration of $12^{+8}_{-7}\%$ of the orbital phase, which is typical of CVs and qLMXBs. The eclipses last no more than 5 hours, which places an upper limit on the orbital period of 2 days. Absorbed $\frac{F_X}{F_{opt}} = 10$ which is consistent with either qLMXBs or CVs with moderate extinction. Spectroscopic follow up is needed to differentiate between the CV and qLMXB possibilities.

6.28 CX476

CX476 starts out near $r' = 21$ before dropping below the limiting magnitude after a few days, shown in shown in Figure 6.30. This appears to be a CV undergoing DNe outbursts.

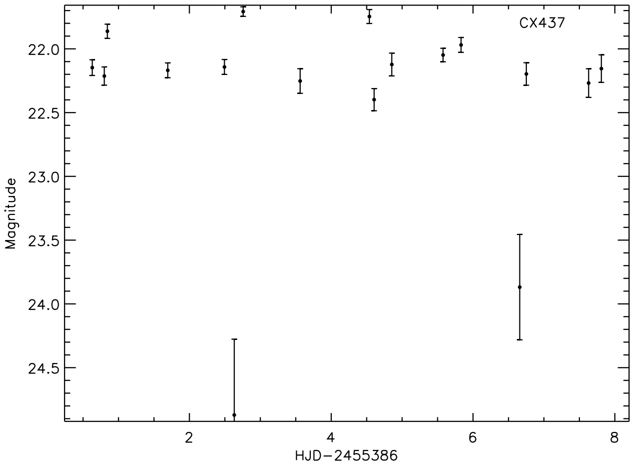

Figure 6.29: Mosaic-II lightcurve of CX437.

Absorbed $\frac{F_X}{F_{opt}} = 20$ which is a little high for a CV, but with some extinction and uncertainties in both X-ray and optical fluxes, it is consistent.

6.29 CX585

CX585 shows large scale aperiodic variability, changing over 2 magnitudes in brightness on a timescale of hours, as shown in Figure 6.31. One data point is a full magnitude below all of the others, but the scatter is so high among the others that it is not unlikely to be a result of random flickering rather than an eclipse. Absorbed $\frac{F_X}{F_{opt}} = 0.6$ which is consistent with magnetic CVs, CVs, and qLMXBs. The large amount of aperiodic variability is consistent with confirmed IPs in the survey, but spectroscopy is needed to further support any classification. If this system is an IP, it should have strong H, He I, and He II emission in its optical spectrum.

6.30 CX645

CX645 shows large scale aperiodic variability, changing over a magnitude in brightness on a timescale of days as shown in Figure 6.32. One data point 1.7 magnitudes below the nearest observation 5.5 hours later appears to be an eclipse. Absorbed $\frac{F_X}{F_{opt}} = \frac{1}{4}$, while with Bulge

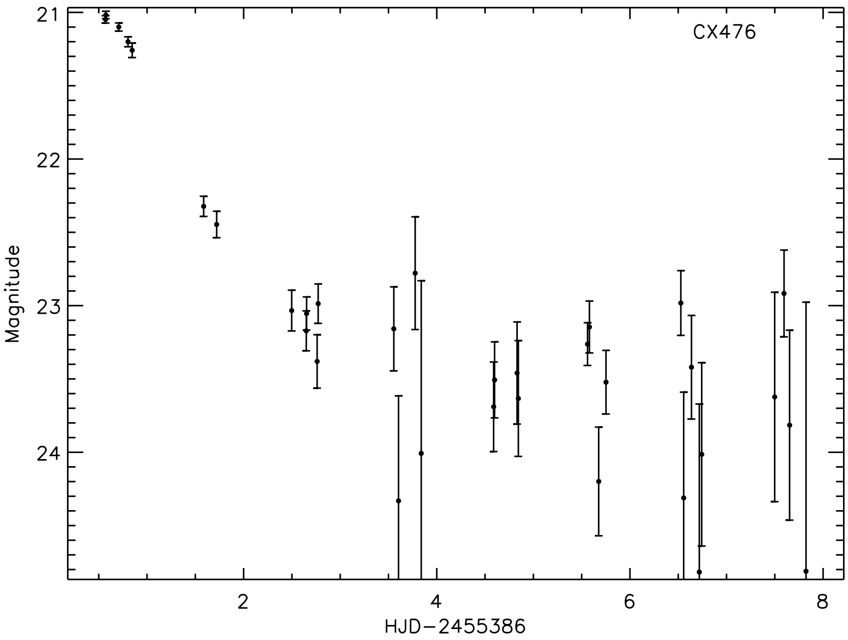

Figure 6.30: Mosaic-II lightcurve of CX476.

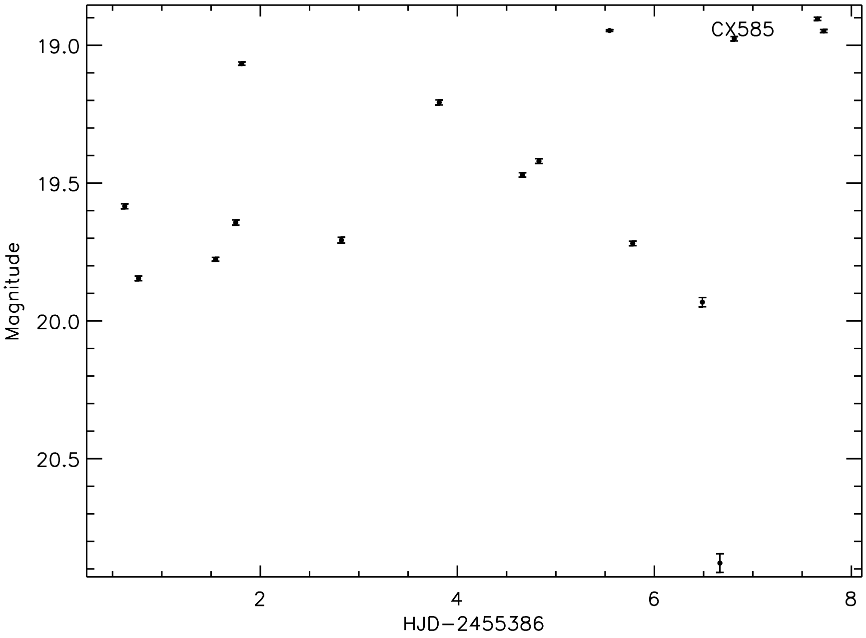

Figure 6.31: Mosaic-II lightcurve of CX585.

distance reddening, unabsorbed $\frac{F_X}{F_{opt}} = 0.003$. This is consistent with a nearby magnetic CV, CV, or qLMXB. Spectroscopy is needed to further support any classification.

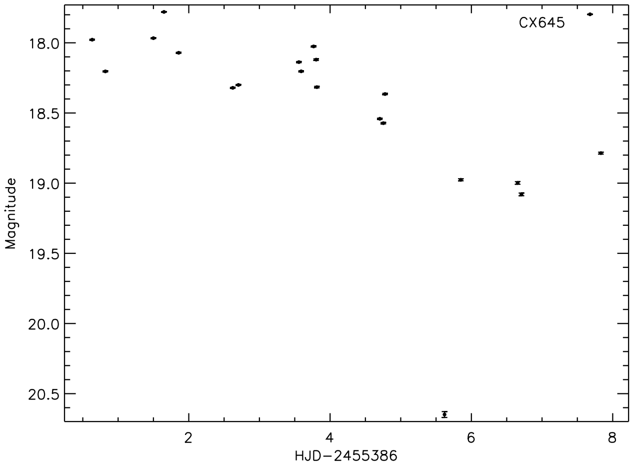

Figure 6.32: Mosaic-II lightcurve of CX645.

6.31 CX705

CX705 shows eclipses in 7 out of 38 observations shown in Figure 6.33, implying that it lasts for $18 \pm 7\%$ of the phase. We recover no significant period, due either to flickering or a period very near 1 day or an integer fraction of 1 day. It is faint in the X-ray for this optical brightness, with absorbed $\frac{F_X}{F_{opt}} = 0.05$. This is consistent with CVs or BH qLMXBs. This drops to $\frac{1}{1000}$ at Bulge reddening, but this is not consistent with either CVs or qLMXBs, while the flickering and eclipses are not consistent with other source types with low X-ray to optical flux ratios. This object is therefore more likely a CV or BH qLMXB substantially closer than Bulge distance.

6.32 CX718

CX718 shows an eclipse 0.4 magnitudes deep, shown in Figure 6.34. Unfortunately, this object is very close to a star that saturates in good seeing, so we only have 7 usable observations of it. Absorbed $\frac{F_X}{F_{opt}} = 0.6$, which is consistent with CVs, IPs, and qLMXBs. Optical spectroscopy is needed to distinguish between these cases.

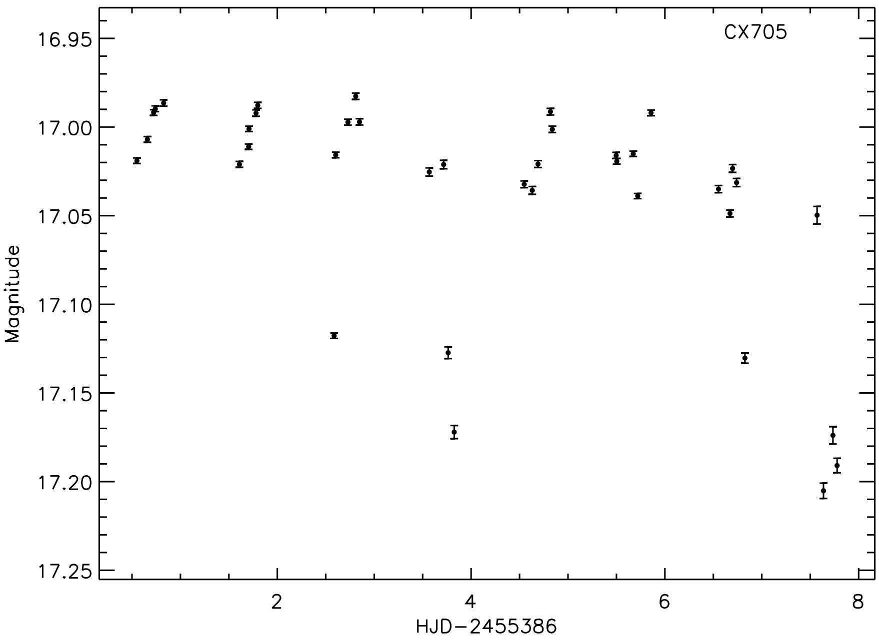

Figure 6.33: Mosaic-II lightcurve of CX705.

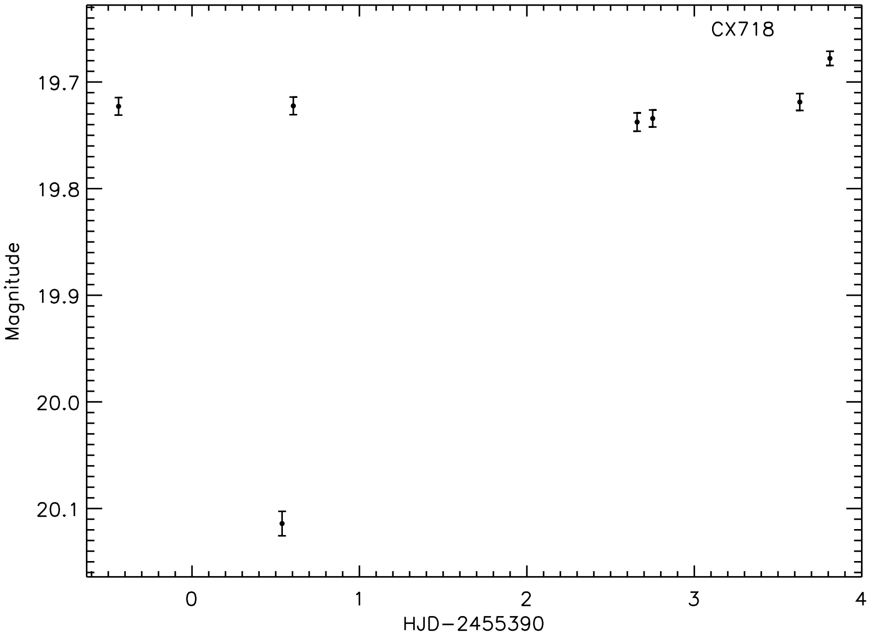

Figure 6.34: Mosaic-II lightcurve of CX718.

6.33 CX740

CX740 shows modulations of 0.06 magnitudes, shown in Figure 6.35, and with a period of 0.765 days, and is shown in Figure 6.36. Absorbed $\frac{F_X}{F_{opt}} = \frac{1}{6}$, though extinction in this line of sight is quite high and at Bulge distance this drops to 2×10^{-5}. This range is consistent with qLMXBs, CVs, or active M dwarfs which have been observed to rotate this quickly. The changes could also be ellipsoidal with a period of 1.53 days, but this is so close to an integer fraction of a day that we cannot distinguish between the periods because of gaps in phase coverage. The lower values of the X-ray to optical flux ratio are favored by larger distances, but it is unlikely that we would detect a W UMa system much further than several hundred parsecs because they are not luminous enough in the X-ray to be detected at the Bulge in our short X-ray exposures, and W UMas are unlikely to have a period as long as 1.5 days anyway. CX740 is a candidate qLMXB or CV based on the possibilty of ellipsoidal variations, but some active M dwarfs have rotation periods below a day as well, and we cannot rule this possibility out either wihout spectroscopy, which should quickly differentiate between these cases.

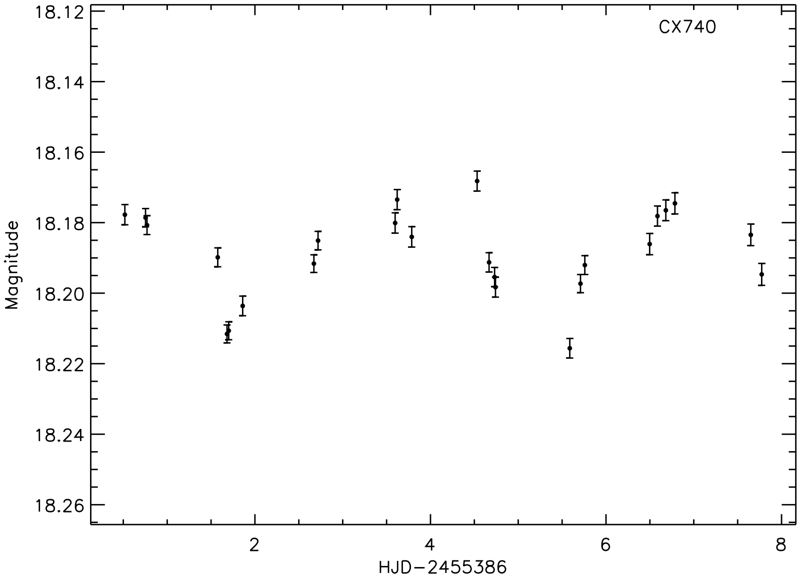

Figure 6.35: Mosaic-II lightcurve of CX740.

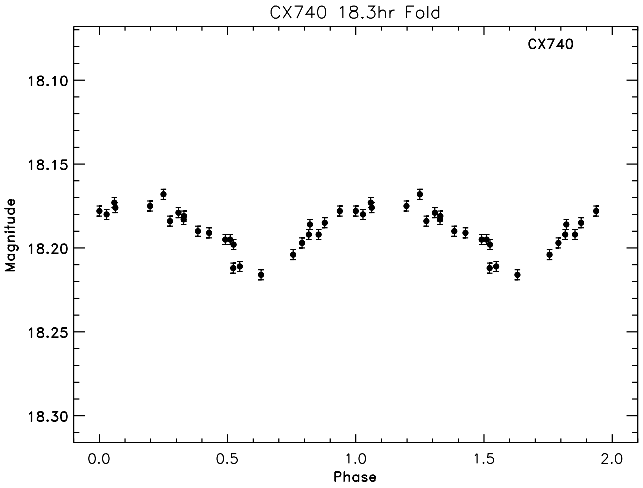

Figure 6.36: Mosaic-II lightcurve of CX740 folded on an 18.3 hour period.

6.34 CX750

There are 2 variable stars within the X-ray error circle for CX750. Both show what appear to be ellipsoidal variations, one also shows an eclipse. One is possibly a field W UMa, with $P_{orb} = 1.12 \pm 0.03$ days an a mean magnitude of $r' = 19.4$ which would imply an X-ray brightness, given typical values for W UMa stars, of $\sim 10^{-15}\,\mathrm{ergs\,cm^{-2}\,s^{-1}}$ which is well below the X-ray detection limit. The other object has a period of 0.468 ± 0.005 days, or 11.24 hours, with an eclipse 0.25 magnitudes deeper at phase $\phi = 0$ than at phase $\phi = 0.5$, which is consistent with qLMXBs and CVs, as is the observed absorbed X-ray to optical flux ratio of $\frac{1}{8}$. The Mosaic-II lightcurve is shown in Figure 6.37, and the folded lightcurve is shown in Figure 6.38. The period is consistent with W UMas, but the asymmetry in the eclipse depths means that the temperatures of the two bodies are different which is not the case for a W UMa in which the two stars share a common envelope. Indeed, the dip at $\phi = 0.5$ is not inconsistent with a minima from ellipsoidal variations without an eclipse, while the eclipse at $\phi = 1$ is incompatible with ellipsoidal modulations, which means this is unlikely to be a W UMa. This object is a candidate eclipsing qLMXB, and spectroscopic follow-up is necessary to differentiate between a CV and qLMXB.

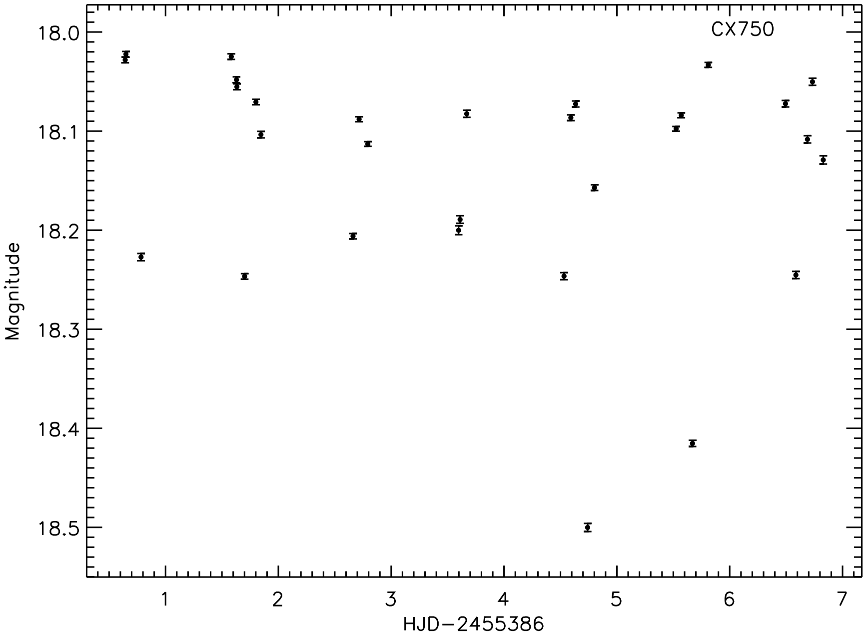

Figure 6.37: Mosaic-II lightcurve of CX750.

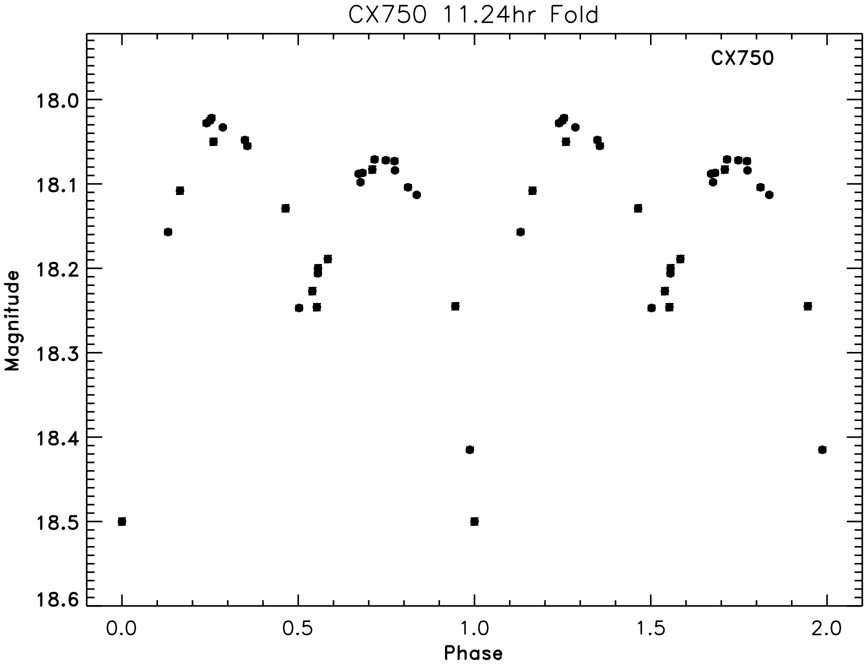

Figure 6.38: Lightcurve of one of the possible counterparts to CX750 folded on an 11.24 hour period.

6.35 CX774

There are 2 variable stars within the X-ray error circle for CX774 as well. One undergoes a smooth decline of 0.04 magnitudes over the 8 days of our observations. The other shows ellipsoidal modulations with a period of 0.362 days, or 8.72 hours. The original lightcurve is shown in Figure 6.39 , and the folded lightcurve is shown in Figure 6.40. The variable showing ellipsoidal variations has a magnitude of $r' = 19.8$, which means it likely below the X-ray detection limit if it were a W UMa star. If this is a W UMa, then the other object showing the slow decline is likely the true counterpart. The X-ray source could realistically be either variable, but the one with the short period is certainly a close binary, and if it is the X-ray source then a candidate qLMXB or CV. If it is one of these types of sources, then follow up spectroscopy should show strong H emission for both qLMXBs and CVs, and strong He I emission for CVs.

6.36 CX820

CX820 shows smooth sinusoidal variations on a period of 2.242 days and an amplitude of only 0.02 magnitudes, shown in Figure 6.41. The folded lightcurve is displayed in Figure 6.42. Absorbed $\frac{F_X}{F_{opt}} = 0.1$ which is consistent with RS CVns, active M stars, and BH qLMXBs and CVs. The small amplitude of variation and multiday period is suggestive of an RS CVn. This object is primarily of note as a demonstration of how well the photometry methods work even for very small amplitude changes.

6.37 CX853

CX853, shown in Figure 6.43, has a period of 0.893 days, which agrees with the period found in OGLE IV data in Udalski et al. (2012), who also classify it as an eclipsing source. The folded lightcurve is shown in Figure 6.44. Orbital modulations on this period are single humped, and we cannot differentiate between this period and a period of 1.79 days, which is too long for W UMas, though it could be a spotted star or CV or qLMXB. Absorbed

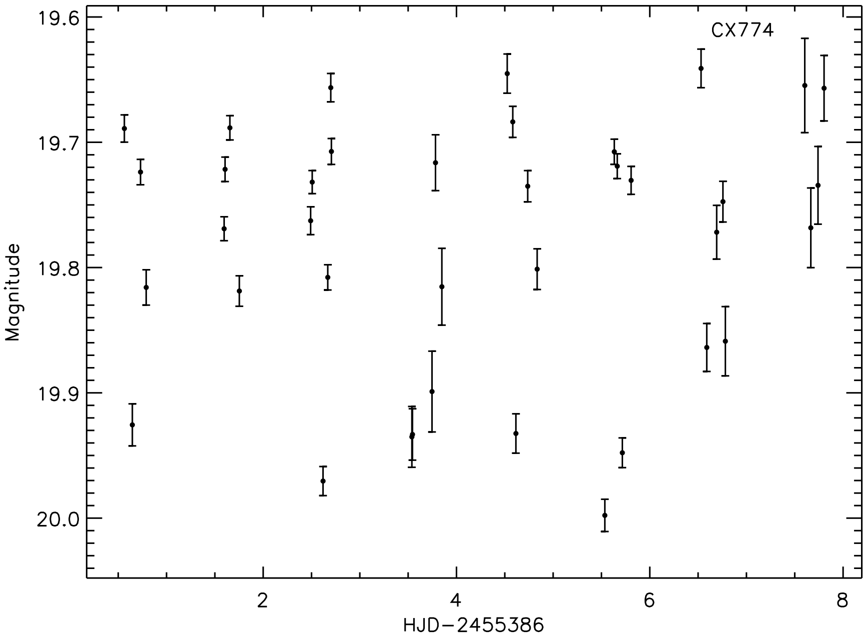

Figure 6.39: Mosaic-II lightcurve of CX774.

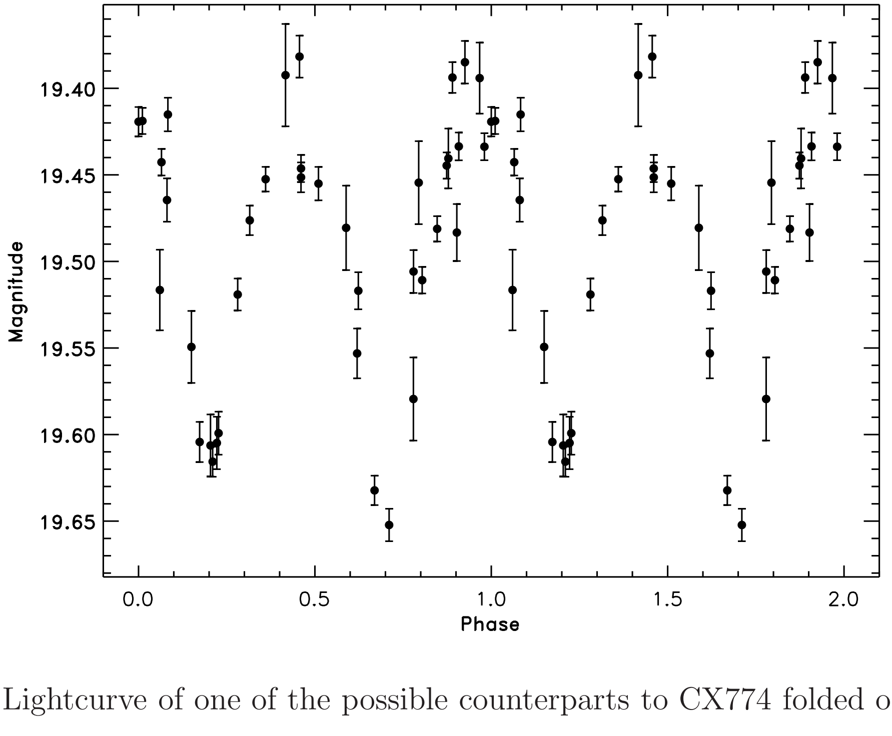

Figure 6.40: Lightcurve of one of the possible counterparts to CX774 folded on a 8.72 hour period.

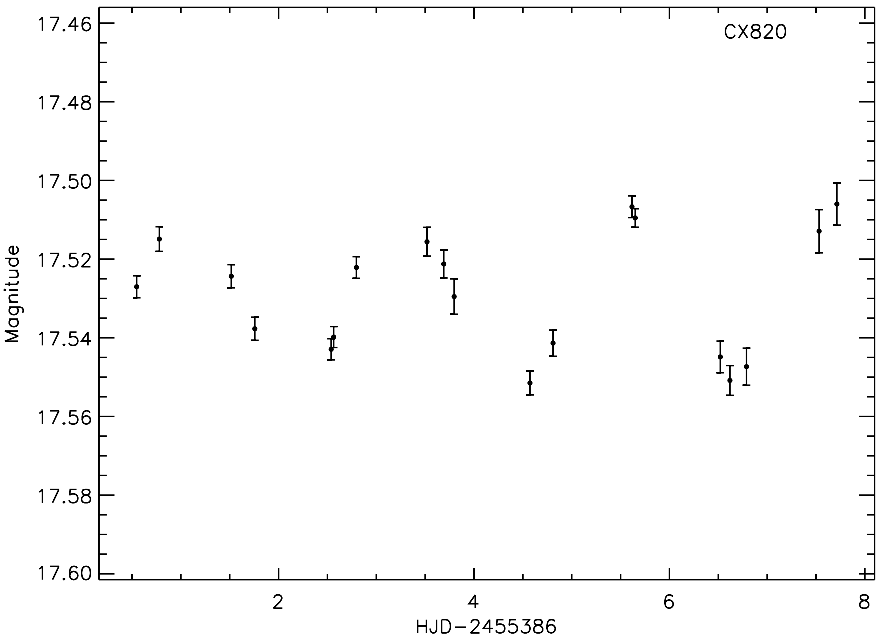

Figure 6.41: Mosaic-II lightcurve of CX820.

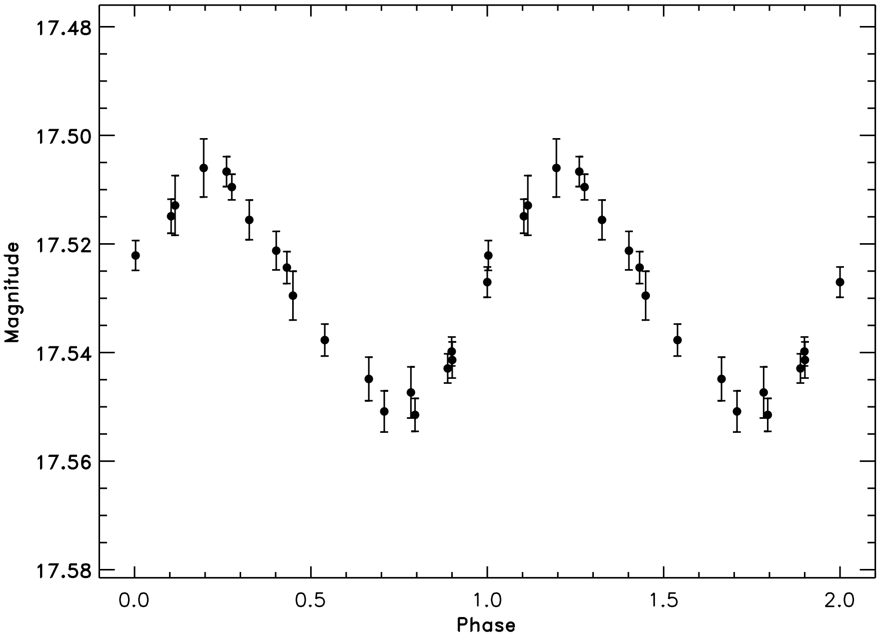

Figure 6.42: Lightcurve of CX820 folded on a 2.242 day period.

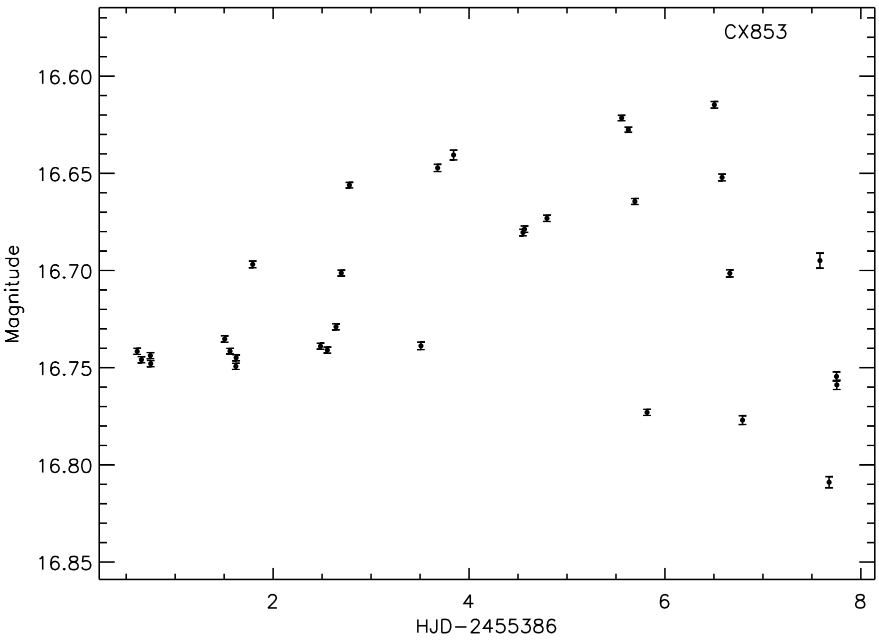

Figure 6.43: Mosaic-II lightcurve of CX853.

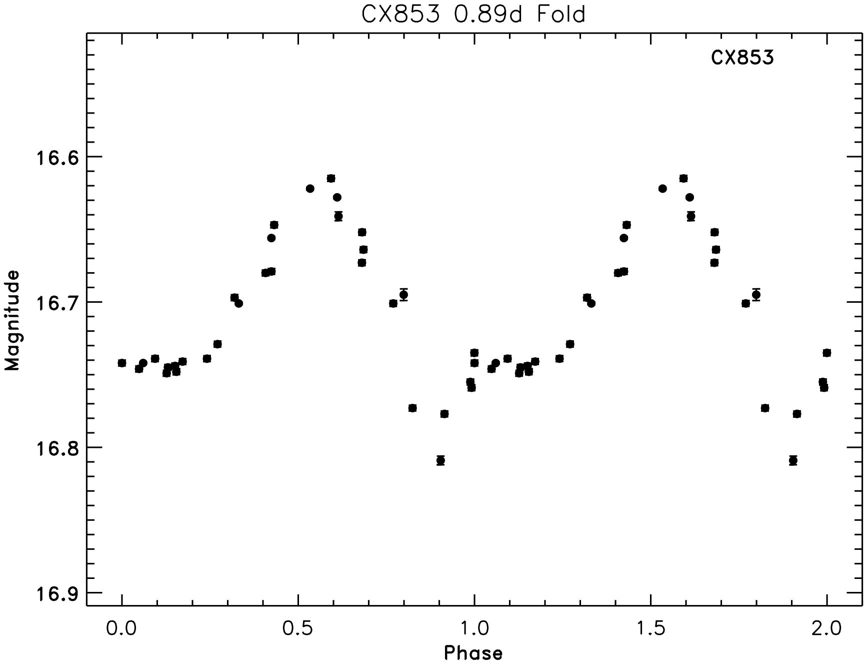

Figure 6.44: Mosaic-II lightcurve of CX853 folded on a period of 0.89 days.

$\frac{F_X}{F_{opt}} = 0.03$ which is consistent with a CV or BH qLMXB, though small amounts of reddening tend to favor an RS CVn.

6.38 CX855

CX855, shown in Figure 6.45, has an orbital period of 1.82 days and a shallow, brief eclipse. The rise and fall are asymmetric, so the lightcurve is not very well fit by a sine wave. The folded lightcurve is shown in Figure 6.46. All of the observations on night 8 are slightly higher than other observations at the same phase, suggesting some intrinsic brightening of the source. Absorbed $\frac{F_X}{F_{opt}} = 0.4$, which is consistent with qLMXBs and CVs. Phase resolved spectroscopy is needed to determine the mass of the primary, which could be either a WD, NS, or BH accretor.

6.39 CX860

CX860 shows an outburst of at least 2.2 magnitudes shown in Figure 6.47, from $r' = 23$ to at least $r' = 20.8$. The counterpart is rising in brightness on night 7 of observations and is falling again on night 8. The outburst peaks during the day between these observations. An outburst lasting only 2-3 days is fast for a DN, though it is not without precedent. The dramatic increase in luminosity is certainly consistent with a DN outburst. Absorbed $\frac{F_X}{F_{opt}} = 10$, which is consistent with CVs undergoing DNe outburst, especially once reddening is taken into consideration. This appears to be a CV undergoing a DN outburst.

6.40 CX887

CX887 shows large amplitude variability on a timescale of hours, as shown in Figure 6.48. No period was recovered. Absorbed $\frac{F_X}{F_{opt}} = 1$ which is consistent with qLMXBs, CVs, and magnetic CVs. Spectroscopy is needed to classify this object more firmly.

6.41 CX895

CX895, shown in Figure 6.49, shows a possible period of 0.432 ± 0.05 days, or 10.4 hours, with a FAP of 1.2% with ellipsoidal modulations, shown in Figure 6.50. There is some flickering

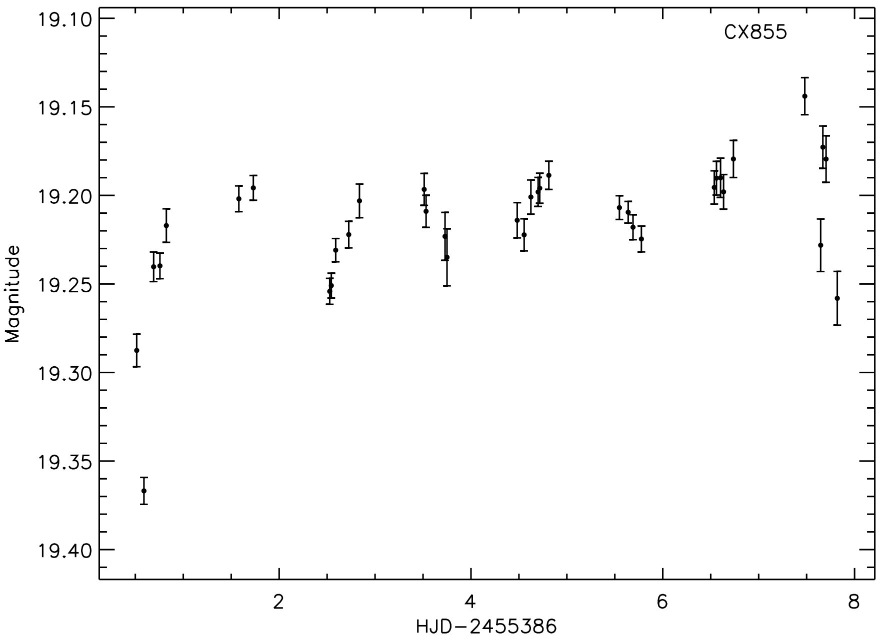

Figure 6.45: Mosaic-II lightcurve of CX855.

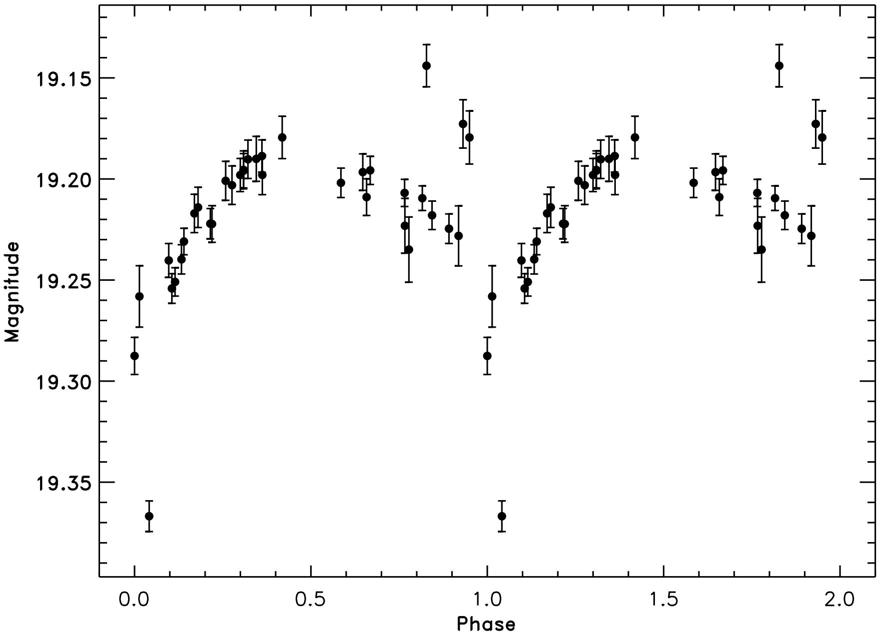

Figure 6.46: Lightcurve of CX855 folded on a 1.8 day period.

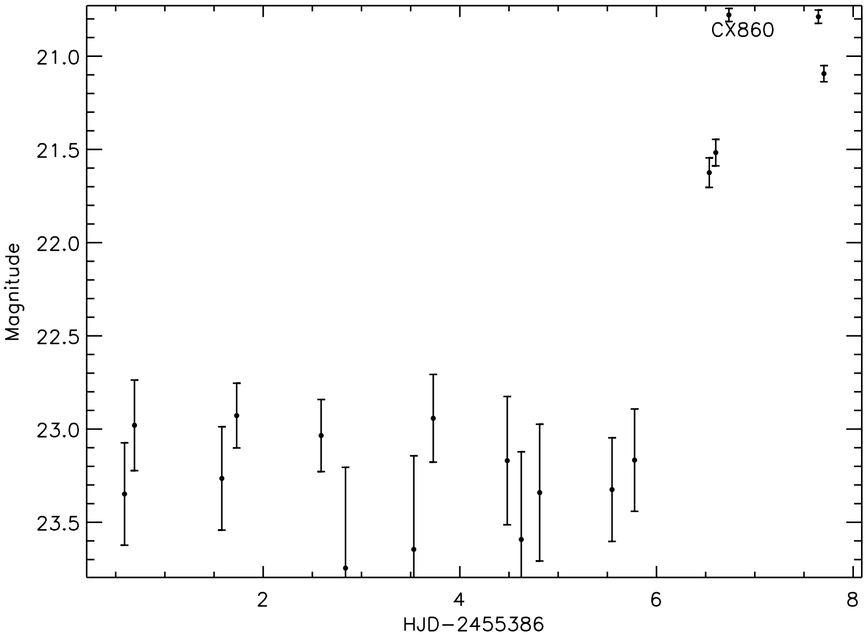

Figure 6.47: Mosaic-II lightcurve of CX860.

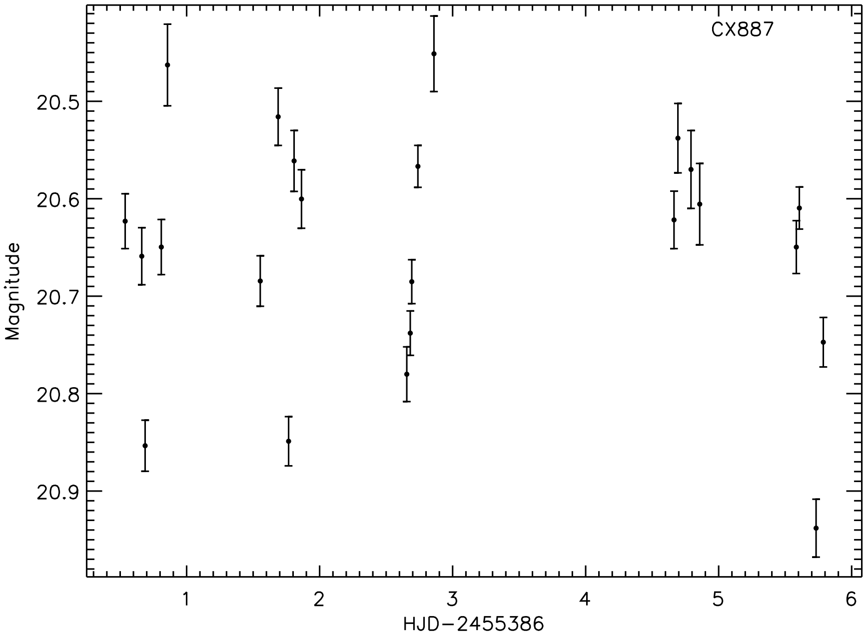

Figure 6.48: Mosaic-II lightcurve of CX887.

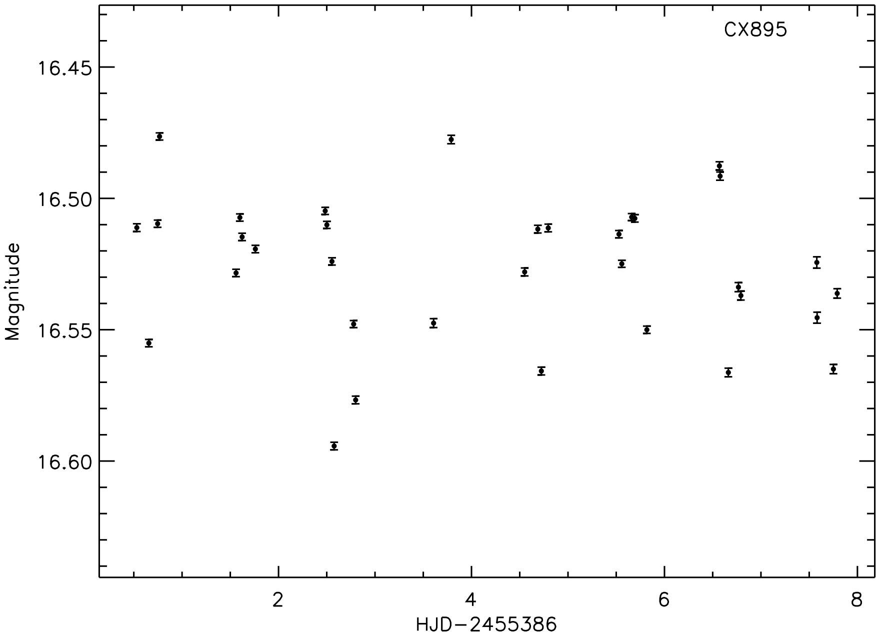

Figure 6.49: Mosaic-II lightcurve of CX895.

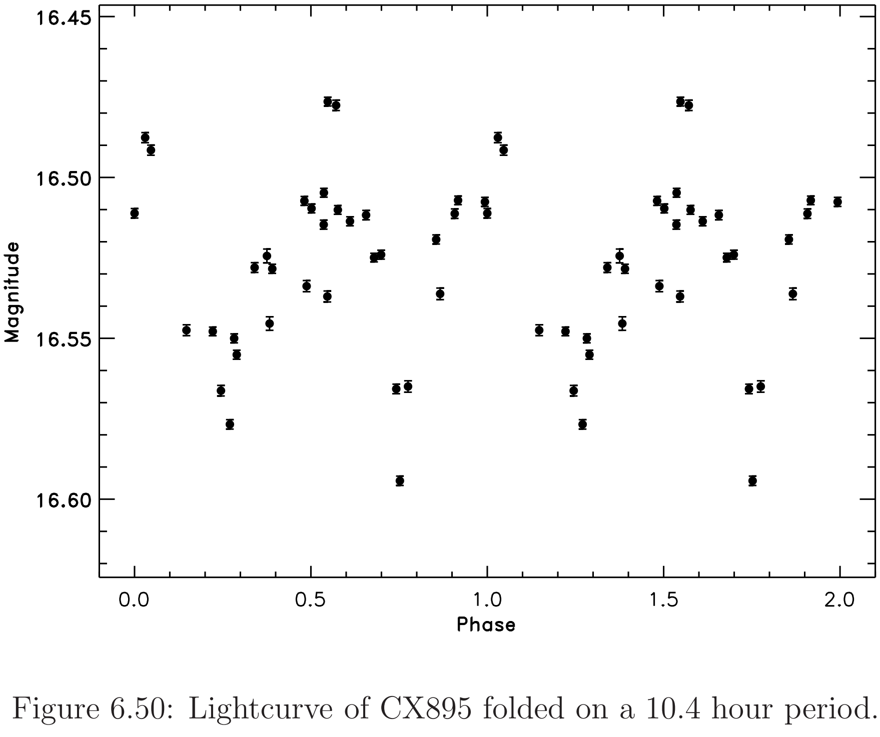

Figure 6.50: Lightcurve of CX895 folded on a 10.4 hour period.

in the lightcurve on the order of 0.03 magnitudes, which argues strongly against this being a W UMa. This source is very optically bright, near the non-linear regime, and the relative photometric errors are generally much less than the observed dispersion. If the period is false, then so is the eclipse, as it is not substantially deeper than some of the observations offset by 0.5 phase. This period was found with Phase Dispersion Minimization rather than the Lomb-Scargle statistic. Absorbed $\frac{F_X}{F_{opt}} = \frac{1}{40}$, which is too low for a NS qLMXB or IP, but could be a CV or BH qLMXB.

6.42 CX905

CX905 shows variations of up to 0.4 magnitudes within a few hours, as shown in Figure 6.51. There are only 12 good observations for this source, and we are unable to recover a significant period, if there is one to be found. Absorbed $\frac{F_X}{F_{opt}} = 1$, which is consistent with qLMXBs, CVs, and magnetic CVs.

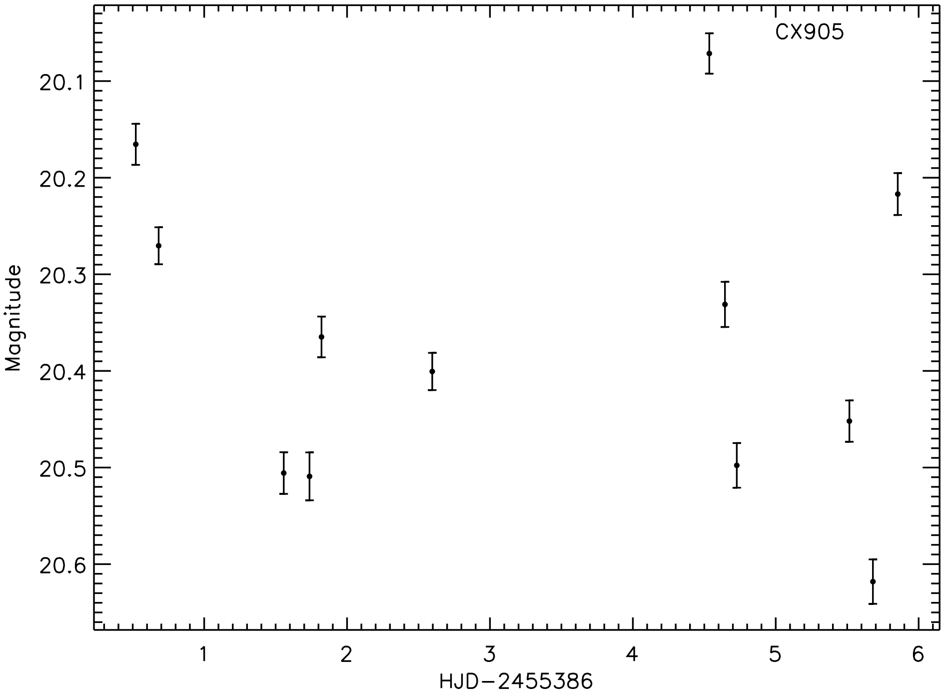

Figure 6.51: Mosaic-II lightcurve of CX905.

6.43 CX930

CX930 has a variable star outside the X-ray confidence region showing broad eclipses with a period of 0.547 days, shown in Figure 6.52. This appears to be a W UMa in the field. It is faint enough that we do not anticipate being able to detect a W UMa in the X-ray with that optical brightness, and it is unlikely to be the true counterpart of the X-ray position due to the size of the position offset.

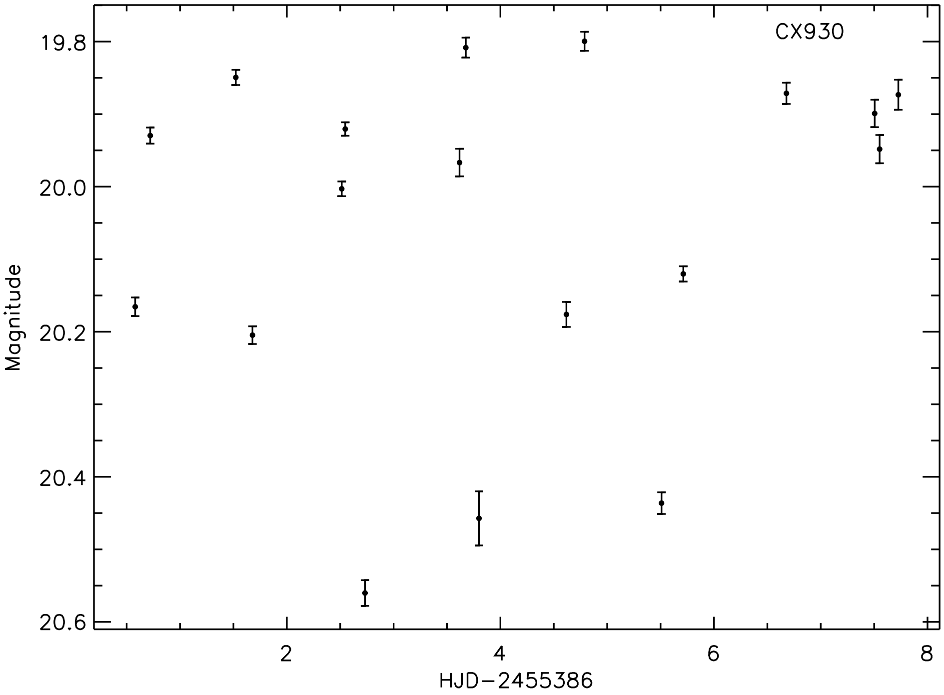

Figure 6.52: Mosaic-II lightcurve of CX930.

6.44 CX957

CX957 shows no variability except for 3 points in eclipse out of 36, shown in Figure 6.53. The eclipse is brief, lasting no more than 2 hours as the observations before and after those in eclipse are back to the steady state. We can place an upper limit on the orbital period of 1 day. The eclipses are at least 0.13 magnitudes deep. Absorbed $\frac{F_X}{F_{opt}} = 0.2$ which is consistent with qLMXBs and CVs.

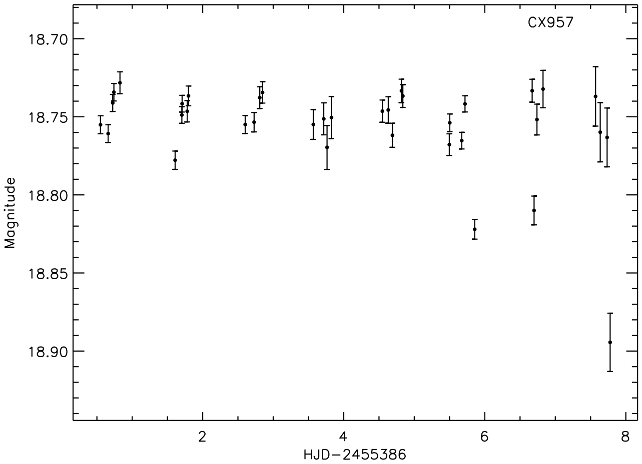

Figure 6.53: Mosaic-II lightcurve of CX957.

6.45 CX973

CX973 shows smooth variations over several days shown in Figure 6.54, which could be a double humped lightcurve with a period of roughly $\sim$ 11 days. The first hump is 0.1 magnitudes in amplitude, while the second is 0.15 magnitudes above that. We observe only 1 minima. Absorbed $\frac{F_X}{F_{opt}} = 0.2$ which is consistent with qLMXBs and CVs, while at Bulge reddening, $\frac{F_X}{F_{opt}} = 0.002$. $L_X = 2 \times 10^{32}\,\mathrm{ergs\,s^{-1}}$ at the Bulge, which is consistent with qLMXBs. The possible long period and low X-ray to optical flux ratio at the Bulge could be indicative of a qLMXB with a giant companion. At the Bulge, $M_{r'} = -1.7$ which is consistent with an giant star.

6.46 CX982

CX982 is somewhat unique. There is an outburst of 1.3 magnitudes starting on night 6 of observations, but on night 7 it drops 2 magnitudes from the peak of the outburst within 1.5 hours. It returns to its peak brightness at the next observation 36 minutes later. The full lightcurve is shown in Figure 6.55. There is nothing wrong with the images showing it back to or below its quiescent brightness, and there are 3 observations of it at low level within the apparent outburst. If it were not for these 3 points, it would appear to be a fairly typical DN

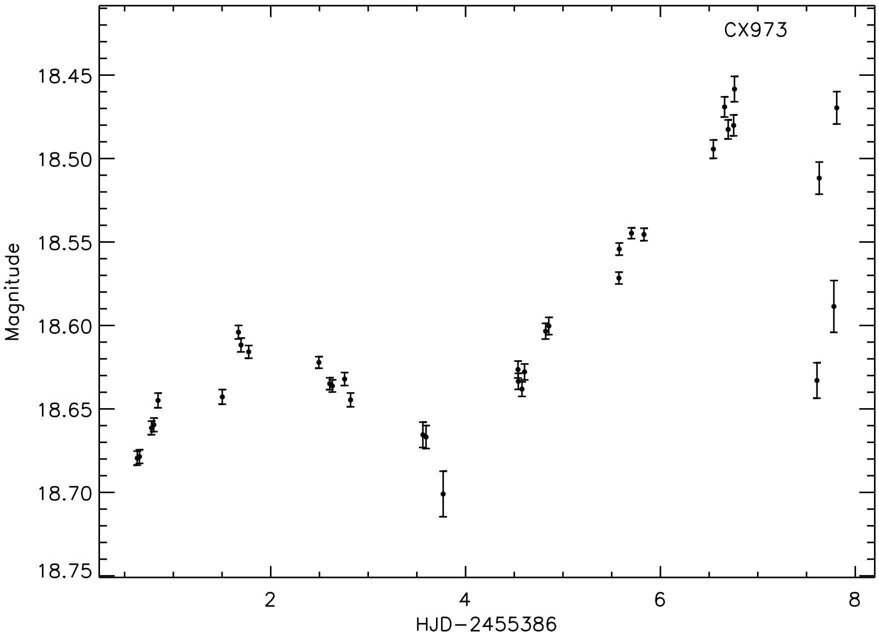

Figure 6.54: Mosaic-II lightcurve of CX973.

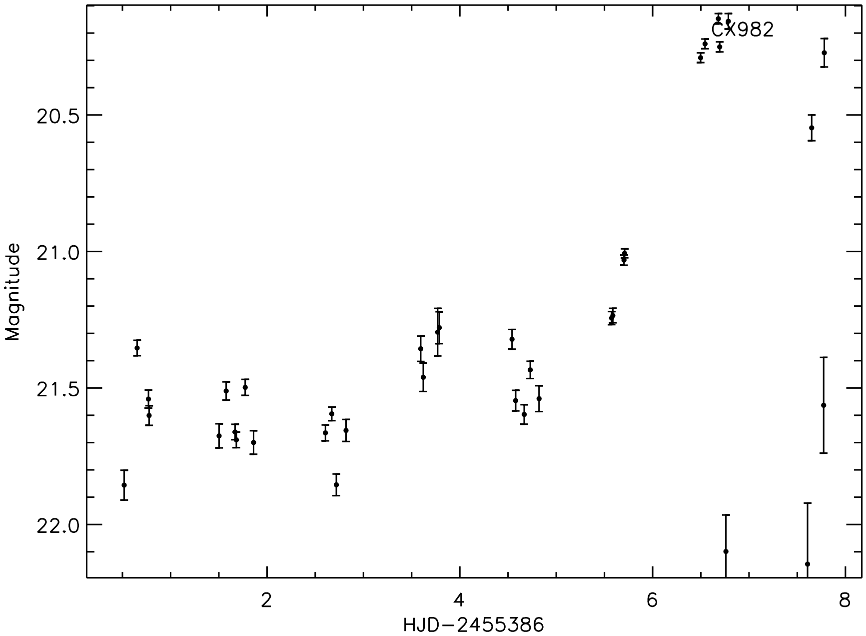

Figure 6.55: Mosaic-II lightcurve of CX982.

outburst. It is possible that this is a high inclination system and the donor star blocks the rapidly accreting disk in these points, which would explain the sudden drops and increases in observed luminosity.

6.47 CX995

CX995 also has two variables inside the X-ray confidence region, both with periods below a day. The reference image and variance image are shown in Figure 6.56. The one closer to the center of the confidence region shows an eclipse ~ 1 magnitude deep, with no significant period, shown in Figure 6.57. The eclipse lasts over two observations separated by 20 minutes. The eclipse comes at the start of the night's observations, so there is no way to be sure exactly how deep the eclipse is or how long it lasts. The lower limit for the eclipse duration can be found if we assume that we see the eclipse at its full depth; it should last 1.3 hours. It is also possible that the first data point is taken as the source goes into eclipse, in which case the eclipse could be substantially shorter.

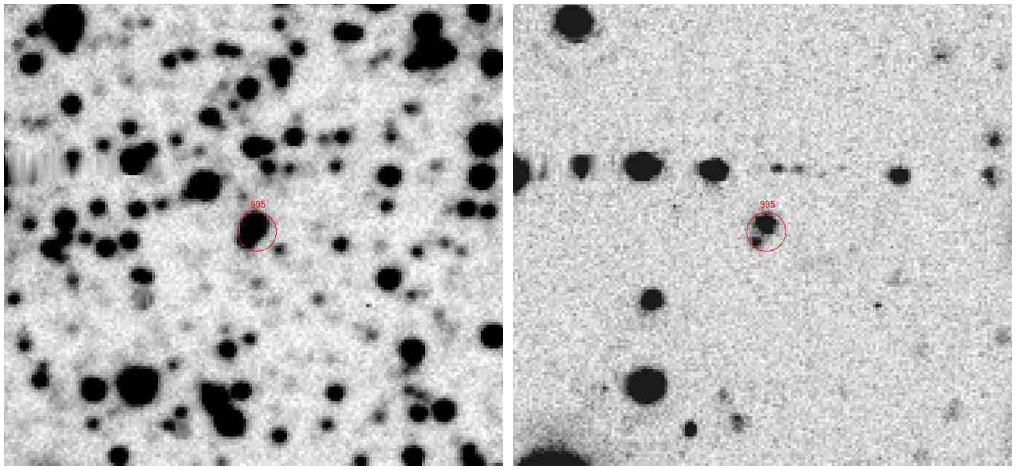

Figure 6.56: Left: Finder chart for CX995 with X-ray position plotted in red. Right: Variance map of Mosaic-II images of this field.

The second variable in the X-ray confidence region has a period of either 0.4517 days or 0.9034 days, depending upon whether the variations are ellipsoidal or sinusoidal. The 0.4517 day fold is shown in Figure 6.58. Our observations cannot adequately distinguish between the two in this case. Some M dwarfs have rotation periods that fast. The first variable is marginally more likely to be the counterpart based on the proximity to the center of the X-ray position, while the second could be a fast rotating M dwarf or W UMa with broad eclipses of equal depth.

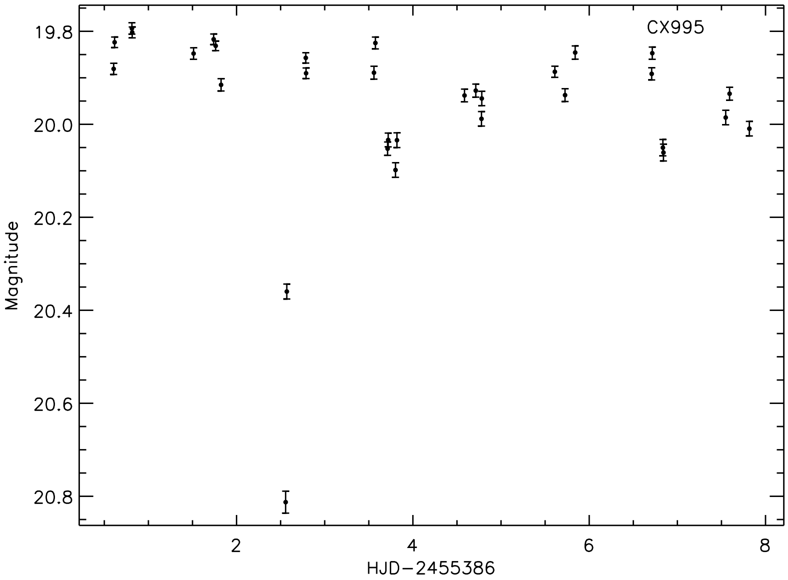

Figure 6.57: Mosaic-II lightcurve of CX995-a.

The closer counterpart has an absorbed X-ray to optical flux ratio of 0.6, which is consistent with CVs, qLMXBs, and magnetic CVs. The second variable would have an absorbed flux ratio of 0.1, which is consistent within reddening errors with W UMas and RS CVns. Spectroscopy is needed to distinguish between possibilities, as well as to confirm which of these two variables is the true counterpart to the X-ray source.

6.48 CX997

CX997 has a period of 1.468 days and an amplitude of only a few percent, shown in Figure 6.59, with absorbed $\frac{F_X}{F_{opt}} = \frac{1}{20}$, consistent with RS CVns, CVs, and qLMXBs. The counterpart is at the bright end of what our observations can measure at $r' = 17.32$. There is some flickering present which argues against an RS CVn interpretation.

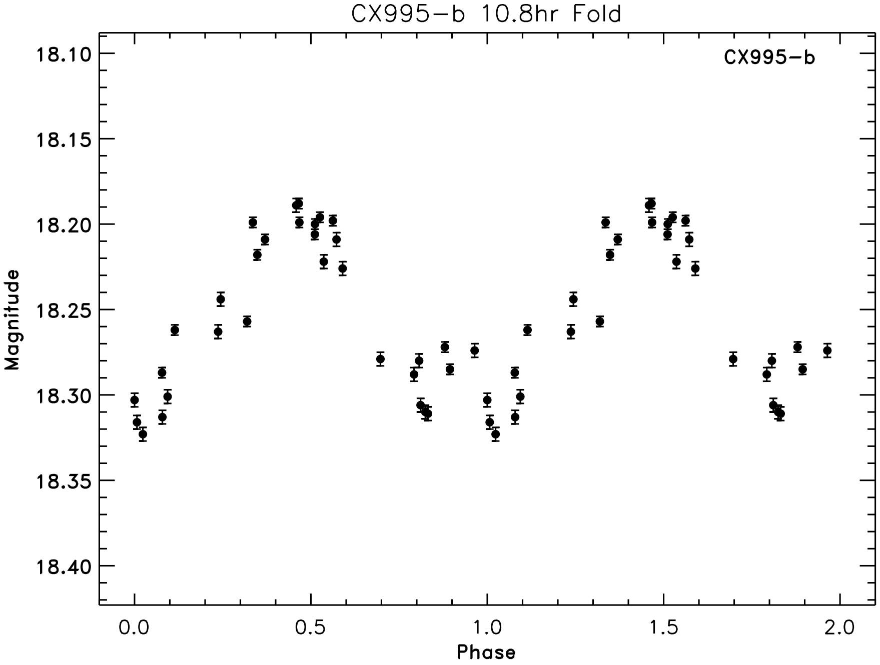

Figure 6.58: Lightcurve of the second possible counterpart to CX995 folded on a 0.45 day period.

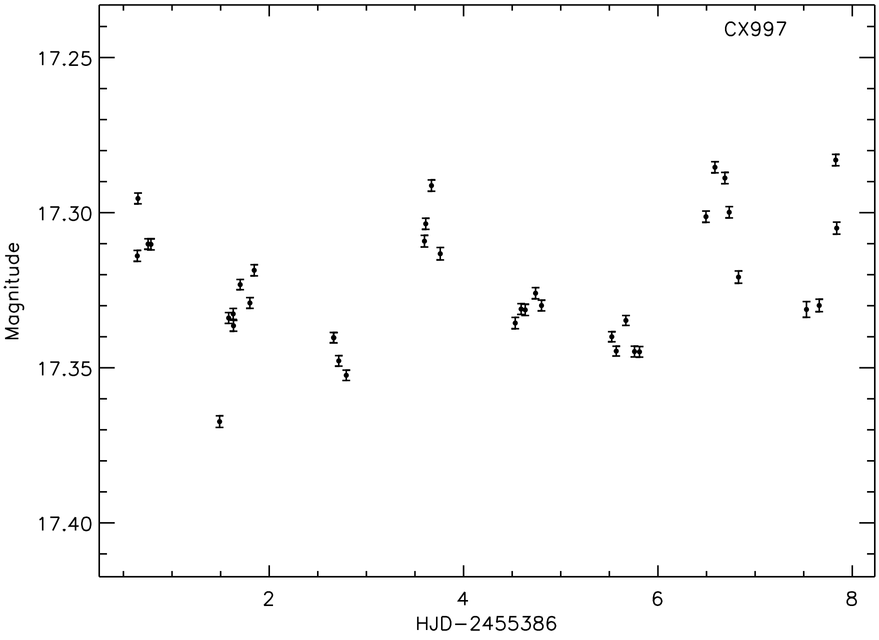

Figure 6.59: Mosaic-II lightcurve of CX997.

6.49 CX1051

CX1051 has a brief eclipse 0.1 magnitudes deep, lasting no more than 2 hours, shown in Figure 6.60. Only 1 observation out of 19 is in eclipse. If we assume the eclipse lasts the full 2 hours possible and lasts only the 5% of the orbit indicated by seeing $\frac{1}{19}$ observations in eclipse, this places an upper limit of 40 hours on the orbital period. Absorbed $\frac{F_X}{F_{opt}} = \frac{1}{7}$, which is consistent with qLMXBs and CVs.

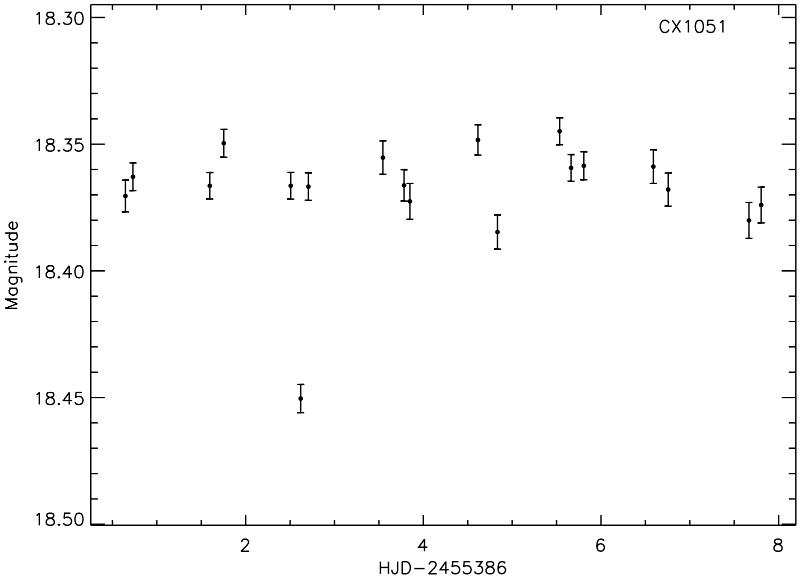

Figure 6.60: Mosaic-II lightcurve of CX1051.

6.50 CX1060

CX1060, shown in Figure 6.61, has periodic modulations with a fundamental period of 1.161 days, and an amplitude of only 0.05 magnitudes. There is more scatter around the peak on this period than in the rest of the lightcurve. Doubling the period to 2.322 days produces a somewhat cleaner lightcurve, but is not a significantly better fit. Each fold is shown in Figure 6.62. Absorbed $\frac{F_X}{F_{opt}} = 0.02$ which is consistent with an RS CVn, CV, or BH qLMXB, but the high amount of dispersion is inconsistent with an RS CVn which should not show flickering. This object is therefore a candidate CV or BH qLMXB.

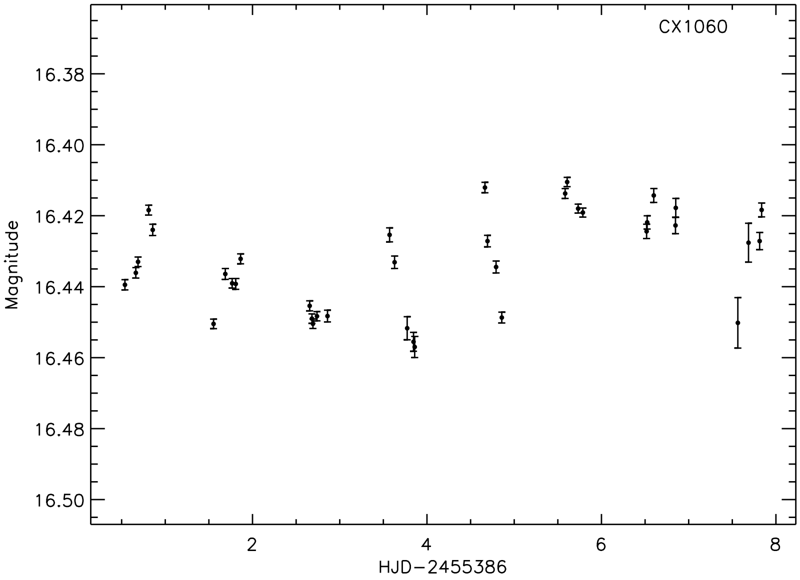

Figure 6.61: Mosaic-II lightcurve of CX1060.

6.51 CX1086

CX1086 shows what appears to be an eclipse with a depth of 0.26 magnitudes and FWHM duration of 2 days, shown in Figure 6.63. It could also be half of ellipsoidal modulations or a result of a combination of star spots on an RS CVn. Absorbed $\frac{F_X}{F_{opt}} = \frac{1}{6}$, which is consistent with CVs or qLMXBs. An eclipse this broad or ellipsoidal modulations lasting this long would imply a giant donor. At the Bulge, $E(B-V) = 2.11$ in this line of sight, which would imply $M_{r'} = -1.77$, consistent with giant stars. $\frac{F_X}{F_{opt}} = 0.002$ at the Bulge, which is also consistent with qLMXBs with giant donors or with RS CVns. Without a longer baseline of observations, however, we cannot confirm that this behavior is periodic.

6.52 CX1186

CX1186 brightens by 0.5 magnitudes from the start of observations, before holding at a mean magnitude of 19.25 and flickering up to 0.1 magnitudes, as shown in Figure 6.64. Flickering is present as the source brightens, as well. Absorbed $\frac{F_X}{F_{opt}} = \frac{1}{3}$, which is consistent with qLMXBs or CVs.

CX1060 1.161d Fold

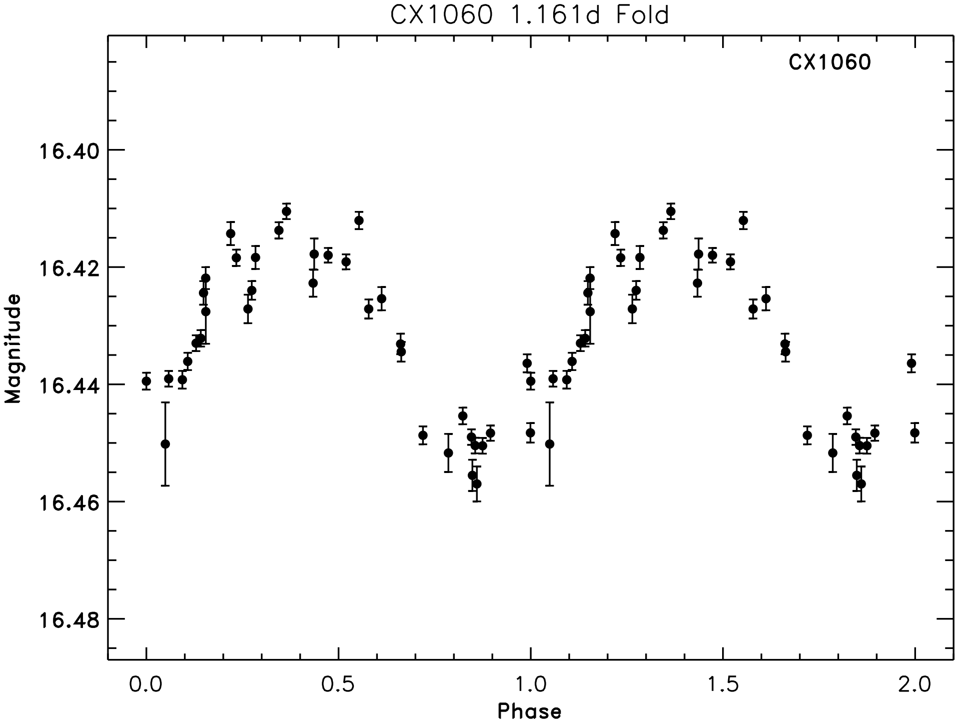

CX1060 2.32days Fold

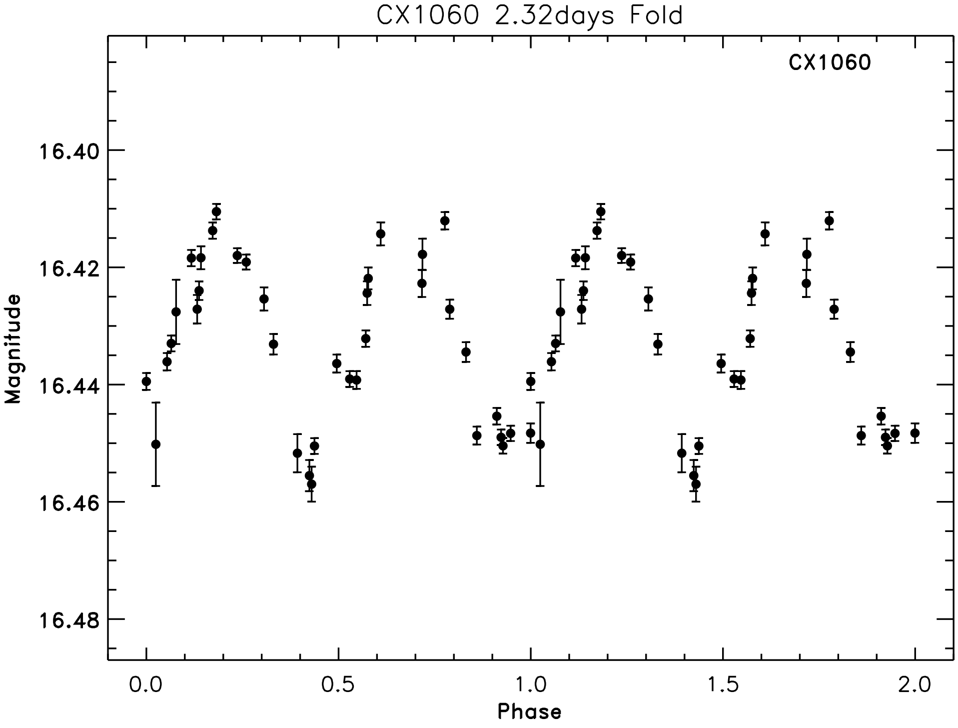

Figure 6.62: Above, Lightcurve of one possible counterpart to CX1060 folded on a 1.161 day period. Below, the same object plotted with twice the period.

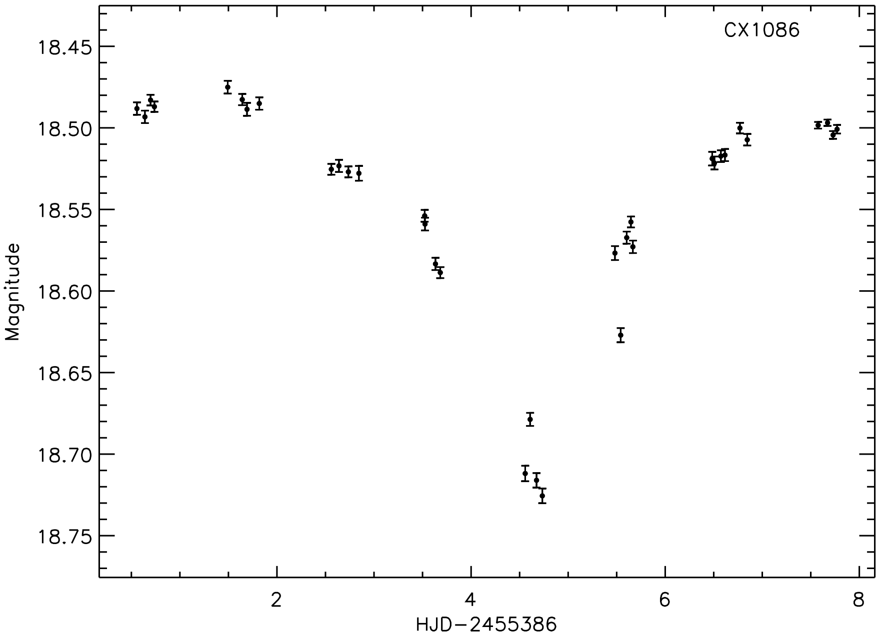

Figure 6.63: Mosaic-II lightcurve of CX1086.

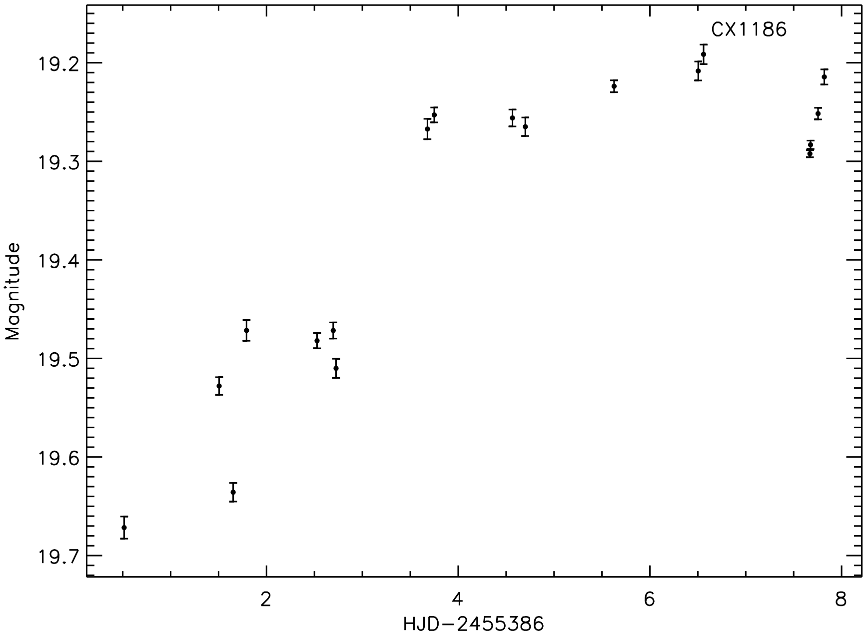

Figure 6.64: Mosaic-II lightcurve of CX1186.

6.53 CX1194

CX1194, shown in Figure 6.65, has a significant period of 1.94 days, which is of note because it is so close to an integer of 1 day, and is strongly aliased by our nightly sampling rate. This aliasing is apparent in the folded lightcurve in the form of large gaps at near $\phi = 0.4$ and $\phi = 0.9$ seen in Figure 6.66. The gaps in phase coverage make it difficult to determine the exact amplitude of the variations, but they are on the order of 0.06 magnitudes. Absorbed $\frac{F_X}{F_{opt}} = \frac{1}{40}$, which is consistent with RS CVns. This object is likely an RS CVn.

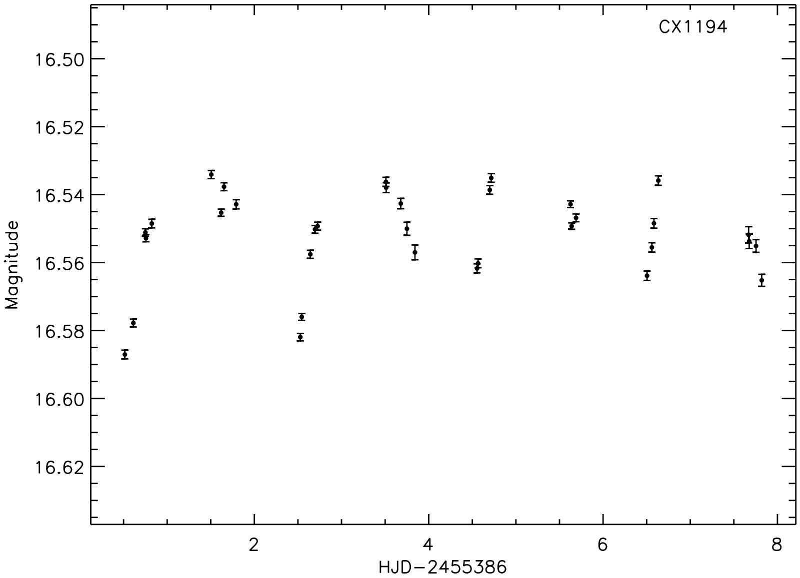

Figure 6.65: Mosaic-II lightcurve of CX1194.

6.54 CX1220

CX1220 has a counterpart that is very near the non-linear regime of the CCD response at $r' = 16.29$, and some observations in good seeing conditions were removed for being in this regime. This source shows a brief outburst of 0.1 magnitudes and a rise and decline of 0.06 magnitudes over several days, shown in Figure 6.67. This could be a flare star or an RS CVn. Absorbed $\frac{F_X}{F_{opt}} = \frac{1}{50}$ which is consistent with RS CVns and active stars.

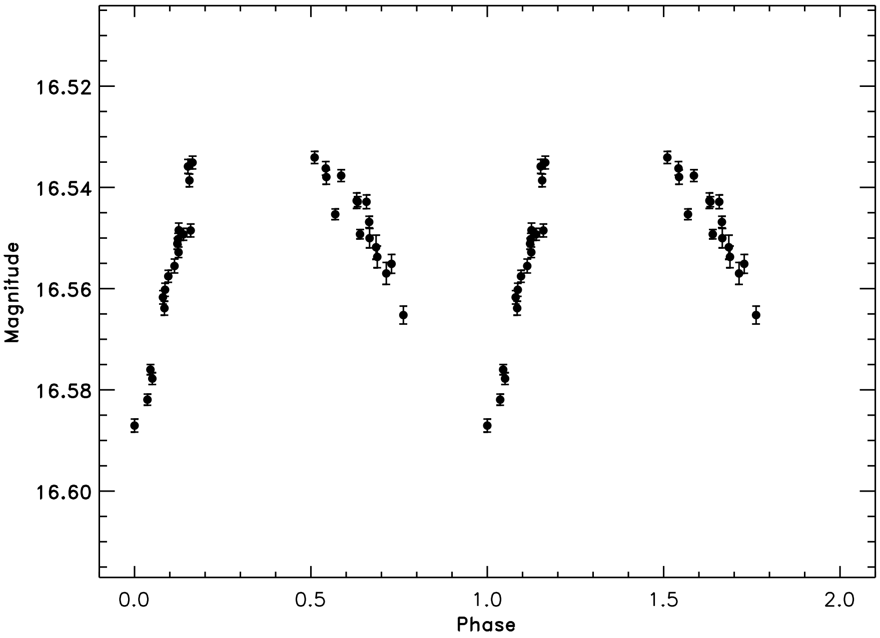

Figure 6.66: Lightcurve of one possible counterpart to CX1194 folded on a 1.94 day period.

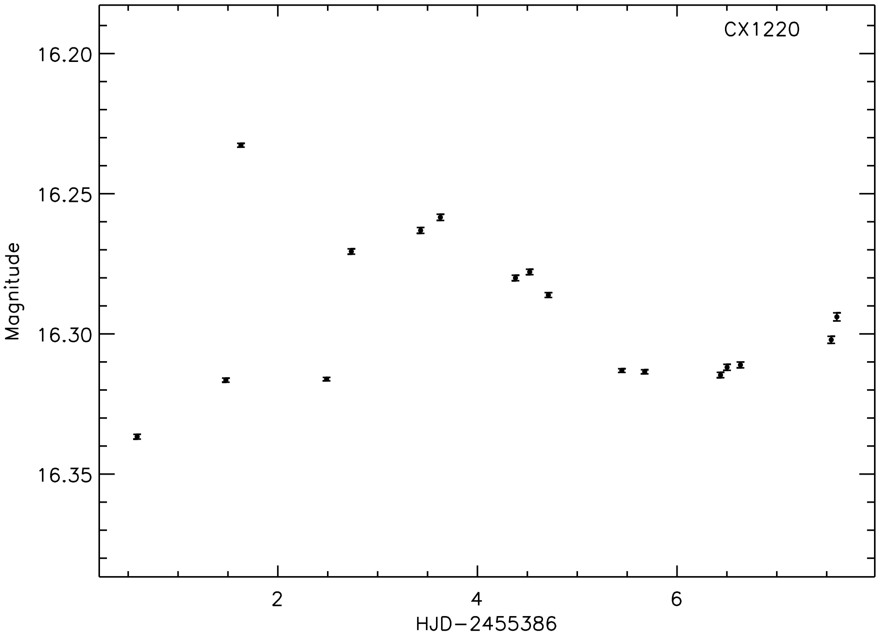

Figure 6.67: Mosaic-II lightcurve of CX1220.

6.55 CX1232

CX1232, shown in Figure 6.68, has a strong peak in the Lomb-Scargle statistic at a period of 0.3179 days, or 7.63 hours, with an amplitude of 0.24 magnitudes. The true period could be twice this if the modulations are ellipsoidal, though the fit provided by doubling the period is no better. The folded lightcurve is shown in Figure 6.69. Absorbed $\frac{F_X}{F_{opt}} = 0.4$ which is consistent with CVs and qLMXBs. The period, amplitude of oscillations, and X-ray to optical flux ratio are certainly suggestive of a compact binary, but spectroscopy is needed to securely classify this object.

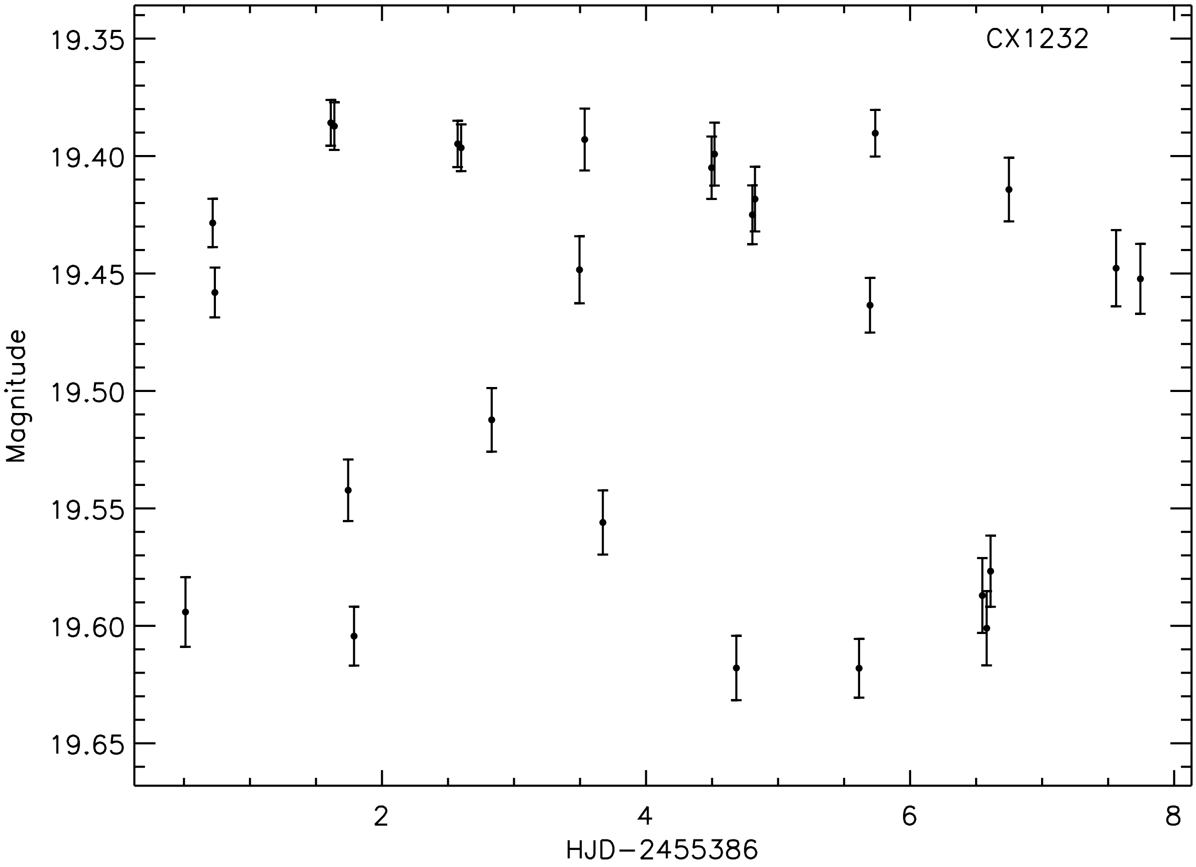

Figure 6.68: Mosaic-II lightcurve of CX1232.

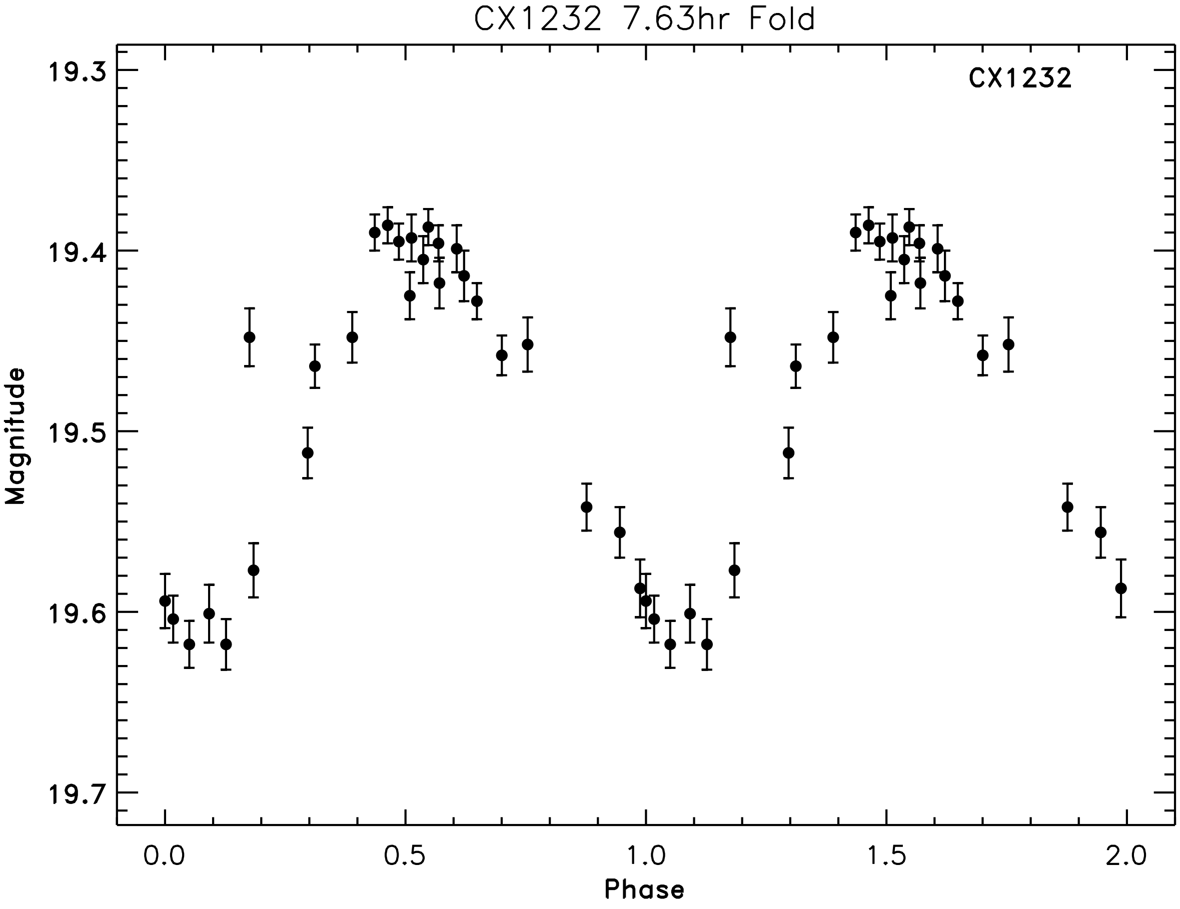

Figure 6.69: Lightcurve of one possible counterpart to CX1232 folded on a 7.63 hour period.

7. Echomapping Scorpius X-1

When X-rays are reprocessed into optical emission, the geometry of the system forms a transfer function (TF) that is convolved with both the reprocessing properties of the material in the system to form the Response Function (RF) and with the X-ray signal to produce the optical signal (Ilovaisky et al., 1980). We measure the optical response to the X-ray signal with the discrete cross-correlation function (CCF) (Edelson & Krolik, 1988)

$$CCF(\tau) = F_X \star F_{Opt} = \sum \left(\frac{(F_X(t-\tau) - \langle F_X \rangle)(F_{Opt}(t) - \langle F_{Opt} \rangle)}{normalization} \right)$$

The X-ray flux is autocorrelated as well; a high-flux observation tends to be surrounded by other high-flux observations. Because the X-ray signal is not a delta function, the CCF between the X-ray and optical lightcurves is not a direct measurement of the Transfer Function; rather, it is convolved with the auto-correlation of the X-ray signal.

7.1 Data preparation

To perform photometry, I used a program written by Dr. Hynes which read in each image and cross-correlate later images with a reference image in order to track Sco X-1 and the comparison star as they moved on the small Argos chip. This program also carried out differential aperture photometry in IDL.

In analyzing the data, I broke each section of lightcurve up into 832 s chunks such that there are 4 evenly sized "kiloseconds" in each X-ray observation. 832 s is chosen because it is $\frac{1}{4}$ of the observation window. This cuts off the very edges of the X-ray observations, where the count rate falls dramatically as the source moves out of view. I will refer to each of these 832 s chunks as a ks for the sake of simplicity.

With each lightcurve, I passed the optical data through a high-pass filter to remove effects from long term variations of the source in an attempt to isolate the $0.01 - 1$ Hz timescale of the variability which would show cross correlation between the X-ray and optical. I used 0.004 Hz as the cutoff frequency for this filter.

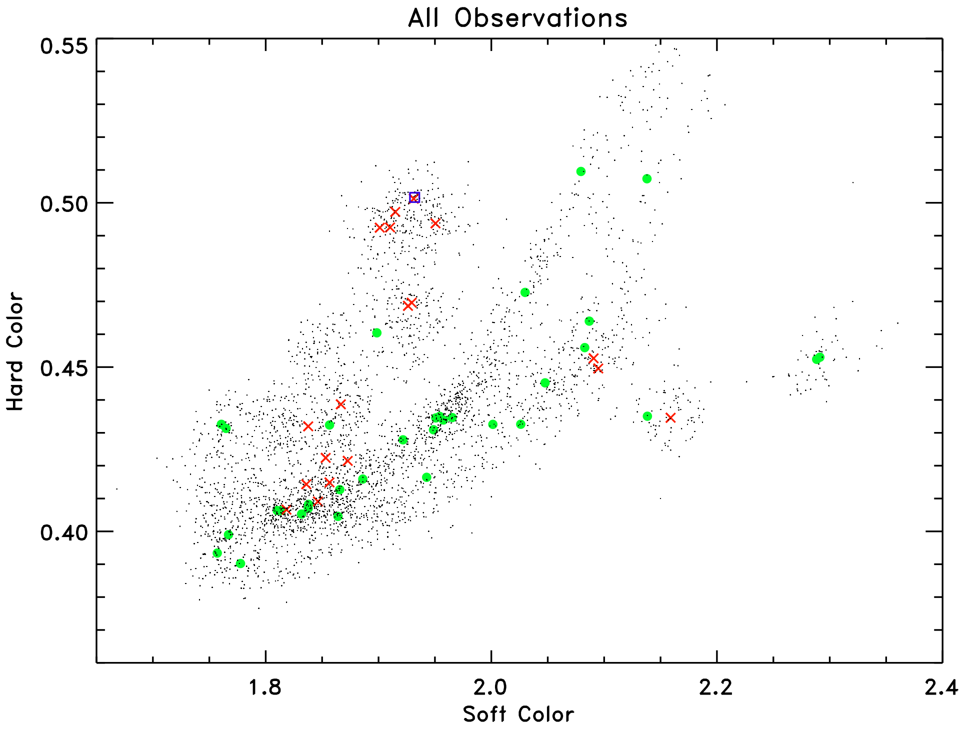

Figure 7.1: A plot of hard X-ray color versus soft X-ray color of our observations. Correlations were checked on 832s chunks of data, the average X-ray colors of which are used to plot the presence of correlation in green circles, no correlation in red Xs, and anti-correlation in blue squares.

7.2 Cross Correlation Functions

I then calculated the CCF between X-ray and optical for each period of observations. Observations which show correlations are plotted as a function of X-ray state in Figure 7.1. Those which show correlations were binned by orbital phase in order to attempt to recreate an analog of the model transfer function shown in Figure 1.5. In the left image in Fig. 7.2, we can clearly see the accretion disk's contribution to the CCF peaking at a value of $\tau = 2 - 4\,\mathrm{s}$ independent of phase. The effects of subtracting out the average of all phases to try and remove the contribution of the accretion disk and leave the companion star can be seen on the right of Fig. 7.2. We cannot claim to significantly see the companion star move with phase in the CCFs. The CCF should consist of a contribution from the accretion disk and the companion star. Most of the reprocessing occurs on the disk, with some contributions near $\tau = 0$ but larger contributions from the outer disk, which is $\sim 10^6\,\mathrm{km}$ in radius (Kallman et al., 1998). For an inclination angle of $\sim 45°$ (Fomalont et al. (2001) calculate that $i = 44° \pm 6°$ for Sco X-1), reprocessing on the outer edge of the accretion disk on the opposite side of the primary from the Earth should take $\frac{(\sqrt{2}+1)10^6\mathrm{km}}{3\times10^5\,\mathrm{km\,s^{-1}}} \approx 6\,\mathrm{s}$. The time it takes light to reach us from the near side of the disk is $\frac{(\sqrt{2}-1)10^6\mathrm{km}}{3\times10^5\,\mathrm{km\,s^{-1}}} \approx 1\,\mathrm{s}$, so the peak of the CCF from the disk should be $\approx 3-4\,\mathrm{s}$. The companion star moves with phase, but light travel times should average $\sim 10\,\mathrm{s}$.

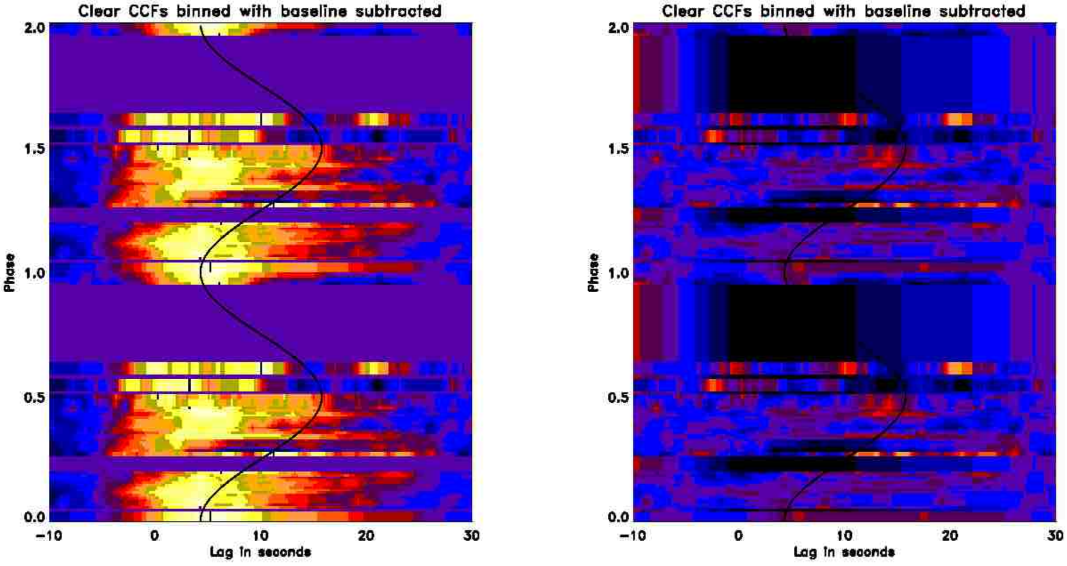

Figure 7.2: Sco X-1 CCFs as a function of phase. Left is all the CCFs for data in the Flaring Branch, binned by phase. The accretion disk dominates reprocessing. Right, I have subtracted out the average CCF across all phases to remove the disk. The black line you see is a track of the COM of a companion at $a = c \times 10\,\mathrm{s}$ with an inclination angle of $i = 38°$ as the lower end of the range in Fomalont et al. (2001). This black line is NOT a fit to the data, just a guide to what *should* be there if the companion is visible.

7.3 Maximum Entropy Techniques

The Response Function for a delta-function X-ray pulse is called the Transmission Function (TF), such that $TF * ACF_X = CCF_{X,Opt}$. By measuring the X-ray ACF and the CCF between X-ray and optical lightcurves at a given phase, in principle we have the information we need to construct the TF. To do this, I tried at first to do a direct deconvolution using

Fast Fourier Transforms in IDL.

$$\widehat{TF} \times \widehat{ACF} = \widehat{CCF} \Rightarrow TF = \frac{\widehat{\widehat{CCF}}}{\widehat{ACF}}$$

This method is very sensitive to noise, however. The amount of light reprocessed from the secondary is only a few percent of the total reprocessed, with the rest coming from the accretion disk.

I also tried smoothing out the TF using Maximum Entropy methods, in which one models the TF to recreate the CCF using the X-ray ACF as the starting point by not only minimizing χ^2 but also using a smoothing constraint with an adjustable weight (Skilling & Bryan, 1984). To do these calculations, I used the MEMECHO program (Horne, 1994). Ideally, one expects a constant contribution from the accretion disk peaking at 3-4 seconds for Sco-X-1 with a smaller second peak which will move with phase, as shown in Figure 1.5. By adjusting the entropy constraint to be higher or lower, I could artifically produce an unphysical TF with 3 or more peaks, which leads me to believe that the TFs with 2 peaks, although physically motivated, are not reliable and are instead an artifact of noise. Indeed, these secondary peaks are not seen to change coherently in position with phase as is expected if they originated with the companion star.

7.4 Possible Sighting of the Companion

There is a possibility that the companion star is revealed in one of our observations in the raw CCF; it is a second peak at 7 seconds of lag, where the companion is expected to be, 5 seconds after the first peak, which is where the accretion disk is expected, and more than twice as large as the second largest deviation from a model of a Gaussian with a linear polynomial in the data. It is 2.62 times the rms deviation around this model to the CCF. If I fit the rest of the CCF with the exception of the region $5 < \tau < 10\,\mathrm{s}$, then this jumps to 4 times the standard deviation. The section of lightcurve the CCF is for, along with the CCF and the best fit Gaussian+line, is shown in 7.3. The secondary peak in the CCF is narrower than the first, which could mean that the second peak is a result of noise.

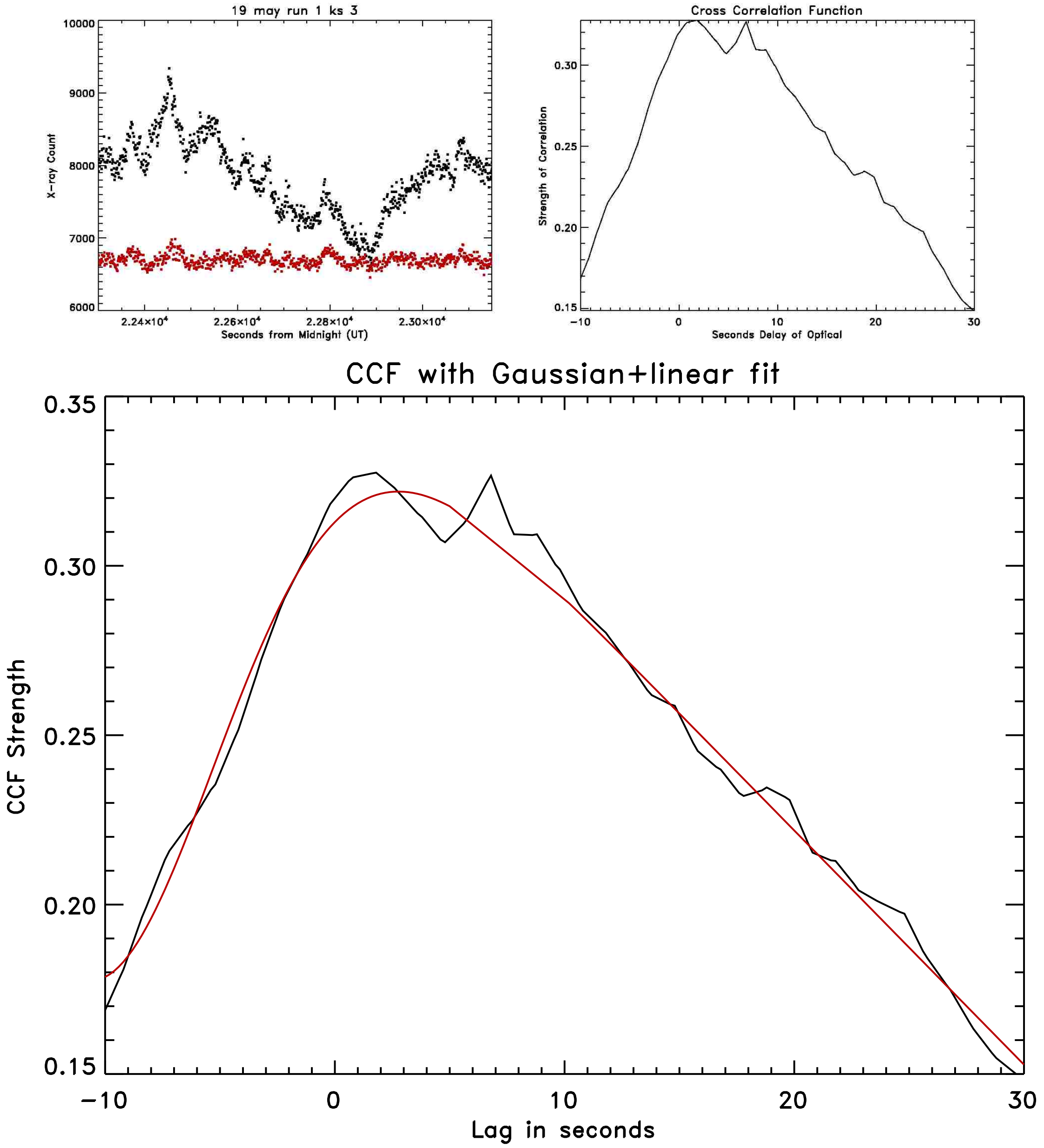

Figure 7.3: One observations shows good evidence for reprocessing on the secondary of Sco X-1. Left: Optical (red) and X-ray (black) lightcurves the third kilosecond of the first orbit of May19, 2009. The optical lightcurve has been scaled to fit on the X-ray lightcurve plot. Right: The CCF for these lightcurves. The broad peak at $\tau = 1 - 2\,\mathrm{s}$ is consistent with reprocessing on the accretion disk, while the second peak at $\tau = 7\,\mathrm{s}$ is consistent with the expected position of the companion star. Bottom: The CCF (black) fit with a model of a Gaussian plus a linear polynomial (red).

8. Conclusions

The total number of GBS X-ray sources closely matches the number predicted by population synthesis models in Jonker et al. (2011). That population synthesis also predicted that ≈ 380 sources in the region covered by Mosaic-II would not have an optical counterpart in our variability survey. We found 155 sources without any visible star inside the X-ray error circle in Sloan r', while a further 545 objects had at least one star inside the error circle which was not seen to vary. It is certain that many of these non-variable stars are not the optical counterpart to the X-ray source, but rather are field stars. The crowding in our fields in the Bulge region is, on average, high enough that coincident alignments are expected, especially for sources observed in the X-ray at a large off-axis angle. Some X-ray sources observed far off-axis and with few counts have confidence regions 10" across, with tens of candidate counterparts. It is therefore possible that the expected remaining sources without optical counterparts could be "hiding" in the group of non-variables, leaving ≈ 330 sources with truly non-variable counterparts. Some of these have been identified through spectroscopy to be interacting binaries, e.g. CX561 and CX1004.

We identify 27 sources as having a confirmed or suspected period between 1 day and 8 days. These are likely a mix of mostly RS CVns and active M dwarfs with star spots, though there are likely some qLMXBs or CVs as well. Some systems, e.g. CX855, more clearly contain a compact object of some sort, while others are more ambiguous. While future spectroscopic observations can distinguish between these options, we can already place constraints on the population of LMXBs in the Milky Way. We further identify 18 sources as having firm periods below a day. Some of these are W UMas, some are CVs, and some are qLMXBs.

8.1 RS CVns

RS CVns are much more common than LMXBs. They are comparatively well studied, and there are far fewer uncertainties in estimates of their population compared to qLMXBs. Jonker et al. (2011) predicted ≈ 447 RS CVns in the GBS area covered by Mosaic-II, all with optical counterparts as they are relatively optically bright and X-ray faint. They also show no detectable intrinsic aperiodic variations, but instead a smooth lightcurve that is a combination of variations on the same period produced by star spots which the Lomb-Scargle statistic is excellent at finding. As an estimated upper limit, we can assume that all 341 sources for which photometry is impossible are RS CVns, which is unlikely as quiescent BH LMXBs can have very faint X-ray luminosities and therefore optically bright counterparts if they are detected in X-rays, as do W UMas. We can further assume that every object with a period above a day, totalling 27 sources, is an RS CVn. If we finally assume that all 23 sources that might show long period variability are RS CVns, then we have at most 391 RS CVns in the GBS area. This serves as a hard upper limit on the number of RS CVns with $F_X > 2.3 \times 10^{-14}\,\mathrm{ergs\,cm^{-2}\,s^{-1}}$ over the 9 square degree area of the Mosaic-II survey in the direction of the Galactic Bulge. Realistically, some of those objects brighter than $r' = 16$ which saturate in Mosaic-II observations are also nearby W UMas, of which 120 are predicted to be detected in the X-ray in the region covered by the variability survey, as well as active single stars, massive stars, and Algols (Hynes et al., 2012). Based on Monte Carlo simulations with noise on the scale of relative photometric errors, I estimate that we have recovered periods for $\sim 70\%$ of unsaturated RS CVns with periods less than 8 days and suspected long period variables, which implies that 40 RS CVns are unsaturated. Using the population estimates in Jonker et al. (2011), most RS CVns should indeed be saturated in our Mosaic-II data. We have observed somewhat fewer RS CVns in the Mosaic-II region than the 447 expected, though the exact amount less remains somewhat uncertain from these data.

8.2 W UMas

A similar estimate with W UMas with periods below a day shows that, since there is no instrinsic flickering in W UMa systems on a scale that we can detect as there is in CVs and qLMXBs, we expect to recover nearly all of the periods for W UMas which do not saturate. Assuming that the spike in the period histogram at 5-7 hours is due entirely to either CVs or qLMXBs and that W UMas are responsible for all other detected periods below a day, I estimate that we observe ~ 12 unsaturated W UMa systems.

Using the population estimates in Jonker et al. (2011), I expect W UMas and RS CVns to saturate in our data in roughly equal proportions. W UMas are slightly less luminous than RS CVns in X-rays and so will be detected slightly closer to Earth, but they also have slightly fainter absolute magnitudes so that these effects tend to cancel one another. Assuming the proportion of RS CVns and W UMas in our Mosaic-II data set holds true for saturated sources, and that sources on chip gaps and bleed trails are evenly distributed among all source types, I predict that we have ~ 100 W UMas in our Mosaic-II fields and ~ 350 RS CVns. This is likely an overestimate because some of the sources with detected periods in these ranges are CVs or qLMXBs, rather than RS CVns or W UMas. These numbers are in reasonably good agreement with predictions.

8.3 CVs and LMXBs

IPs are expected to show dramatic flickering, and can easily have periods below what we can confidently detect. We have 83 sources which flicker without a large outburst or periodicity. Assuming the predicted proportion of IPs in the sources lost to bleed trails and chip gaps, we would have 98 IPs in the Mosaic-II fields. This is somewhat below the estimated 113 IPs with visible optical counterparts predicted in Jonker et al. (2011), but is in fair agreement. While some IPs could saturate in our data, most will not because they are faint enough in the optical compared to their X-ray luminosity. Some of these flickering objects are likely non-magnetic CVs as well, and not IPs. The initial estimate of visible IPs in the survey area is sensitive to the optical magnitude we reach. We have difficulty securely detecting most variability fainter than $r' = 22$, so a larger proportion of IPs may be hiding among the sources with non-variable or non-detected counterparts than in that prediction.

CVs and qLMXBs can also show some degree of flickering, though CVs and LMXBs in quiescence can show very smooth lightcurves, for example in the case of CX93. Most of these systems, though not all, should have a period below a day, concentrated around a few to several hours (Gänsicke, 2005), where indeed we see a spike in our period histogram. Under the assumption that qLMXBs show clear ellipsoidal modulations, we can place a hard limit of 5 sources that could be qLMXBs in our optical data set, as one of the 6 sources showing ellipsoidal modulations, CX93, is confirmed as a CV. This is dramatically lower than the predicted number of 90 qLMXBs the Mosaic-II region in Jonker et al. (2011), by over an order of magnitude. Some qLMXBs are doubtless flickering without a recovered period, but there are only ~ 100 of these, which is not enough to cover 45 expected CVs and 120 expected IPs in addition to 90 expected qLMXBs. Among the candidate qLMXBs we have found are CX70, which lacks He I in its optical spectrum but shows dramatic variability on a timescale of hours, CX446, which shows eclipses with a broad Hα emission line, and CX561, which shows no variability but has very broad double peaked Hα emission and no He I in its spectrum.

8.4 Missing qLMXBs

Where are the qLMXBs in the GBS? While the above estimate does not take different different lightcurve morphology, such as in CX855, into account, those cases cannot make up the difference between the observed number of qLMXB candidates and the predictions of the population synthesis used. There are 5 possibilities:

- The initial estimate in Jonker et al. (2011) may have overestimated the X-ray luminosity of qLMXBs. We know that BH qLMXBs are fainter, as discussed in Chapter 1, though this could account for only $\sim 10\%$ of the problem since only $\sim 10\%$ of qLMXBs should contain a BH primary. If quiescent LMXBs that have not undergone a recent outburst are fainter than the known population of LMXBs followed into quiescence from outburst, they might not have been detected in the X-ray.

- The qLMXBs with optical counterparts may be too faint to notice flickering or variability. A source with modulations like CX93 would be invisible as a variable at $r' = 22$

because the photometric errors are on par with the amplitude of the variability. Such an object would likely not show up in the ISIS results.

- Some qLMXBs could be intrinsically nonvariable, showing no flickering or ellipsoidal modulations. A candidate BH qLMXB based on spectroscopy, CX561, shows no variability despite being at $r' = 20$. CX1004 is a spectroscopically confirmed UCXB or AM CVn with $P_{orb} = 48\,\mathrm{minutes}$ which showed no photometric variability in our Mosaic-II data. If this is the case, a new survey approach focused on spectroscopy will be necessary to find qLMXB systems.

- qLMXBs may flicker too much to recover periods reliably. This cannot resolve the problem for several reasons. First, as shown through Monte Carlo simulations in Figure 4.2, we can reliably find periods below 1 day even with intrinsic flickering up to 50%. Second, IPs in the survey should be flickering, and are observed in roughly the expected numbers. While a few qLMXBs are certainly hiding in this population, there are not enough flickering sources to account for *both* the expected populations of IPs and qLMXBs. Solving our missing qLMXB problem by brushing them beneath the rug of flickering sources simply turns it into a missing IP problem. Because we expect IPs to flicker more than qLMXBs, this seems at best a partial solution.

- The final possibility is that the missing qLMXBs simply *are not there to be found*. Population synthesis estimates of LMXBs in the Galaxy carry large uncertainties of orders of magnitude. ~ 10 qLMXBs may simply be the actual size of the population rather than ~ 100. Objects like the BH LMXB A0620-00 have been observed to go into outburst twice in the last century, and their duty cycle is not in question. Many additional sources with longer recurrence times are predicted, however. If this last possibility is correct, this would mean that this population of qLMXBs waiting to go into outburst simply does not exist. Our current sample of LMXBs known from outbursts over 50 years of X-ray astronomy would then represent a sizeable portion of the Galactic LMXB population.

It is this last possibility that has the widest reaching implications. The ratio of quiescent LMXBs to active LMXBs in Globular Clusters has been observed to be ≈ 10 (Heinke et al., 2003), though these studies may underestimate the number of qLMXBs by half (Heinke et al., 2005). The Galactic Bulge may not produce qLMXBs with the same duty cycle as in Globular Clusters, however, because those in Globular Clusters are formed by different predominant mechanisms than in the Bulge. It is perhaps worth noting that we observe 2 active LMXBs in the GBS (CX1, CX3), which would imply ~ 20 qLMXBs in the Mosaic-II data if Bulge LMXBs have the same quiescent to active proportions as those in Globular Clusters.

The prediction actually used in Jonker et al. (2011) relied upon X-ray binary formation rates and lifetimes. The estimates of Jonker et al. (2011) used a formation rate of 10^{-5} NS binaries formed per year (Portegies Zwart et al., 1997; Kiel & Hurley, 2006). Using a typical lifetime for LMXB systems of 1 Gyr yields 10^4 LMXB systems in the Galaxy (Jonker et al., 2011), which combined with 140 active LMXBs at a given time, yields a ratio of quiescent to active LMXBs of 70. Pfahl et al. (2003) predict $\approx 10^3 - 10^5$ LMXBs by assuming many LMXBs are descendants of Intermediate Mass X-ray Binaries, with the major driver of the different population sizes being a substantial dependence on the structure of the Common Envelope. The population estimate in Jonker et al. (2011) fits in the center of this range. The period distrubution predicted by Pfahl et al. (2003) for the median CE parameter peaks around $\log P_{orb}(\text{days}) = 0.25$, which, referring to Figure 4.2, we are only likely to recover with flickering of 20% of the amplitude of orbital variability or less.

The favored population model of Kiel & Hurley (2006), however, predicts a somewhat lower number of 1900 LMXBs, both active and quiescent, with a ratio between the two closer to 13. The primary differences between the models in Kiel & Hurley (2006) and Pfahl et al. (2003) are an updated model for the CE, an inclusion of the helium star's mass-loss from wind after the CE phase, metallicity of the binary, and the inclusion of tidal forces in the code. The resulting population of LMXBs would lead to ~ 17 qLMXBs with optical counterparts in the GBS region surveyed with the Mosaic-II instrument by using the same luminosity and extinction assumptions as in Jonker et al. (2011), which is quite possible, although we have not identified even this many possible qLMXBs based on the photometry or existing spetroscopy. A quiescent to active LMXB ratio of 10-20 would suggest that the duty cycles for LMXBs in the Galaxy are similar to those observed in Globular Clusters, with many fewer transient sources waiting to undergo a period of outburst than predicted by the more generous models.

8.5 Echomapping Sco X-1

The lack of reprocessing of X-rays in the NB and HB of Sco X-1 is significant. Reprocessing can only occur when the photons are absorbed rather than scattered. At energies above $\sim 10\,\mathrm{keV}$, Compton scattering dominates over photoelectric absorption. This means that X-ray states with more hard color than soft color, as we define them, should have more scattering of X-rays than reprocessing. However, there is no X-ray state at which the flux from high energy photons above $10\,\mathrm{keV}$ is actually higher than the number of lower energy photons. The X-ray luminosity of Sco X-1 increases only slightly as it moves up the NB, while the proportion of high energy photons increases, as can be seen in Figure 2.2. We would therefore expect the noise to be greater on the NB and HB, though this does not explain a total shutdown of reprocessing.

Another possibility is that the portion of the accretion disk which provides most of the reprocessing is gone on the NB and HB. According to some models (Lin et al., 2009), the inner disk radius does greatly increase when Sco X-1 leaves the FB. But is this enough to explain the lack of reprocessing? The typical light travel time for reprocessing we observe is $\tau \sim 3\,\mathrm{s}$. Taken as an average over all paths of travel, this means the inner disk radius would have to be greater than $\sim 10^6\,\mathrm{km}$, which is fully half the disk radius estimated by model fitting by Kallman et al. (1998). No models predict the inner disk radius being that large.

Bałucińska-Church et al. (2010) use kHz QPOs in Cyg-like Z-sources to estimate that the inner disk radius is on the order of $\sim 20 - 40\,\mathrm{km}$ on the HB. Most of the reprocessing signal appears to come from the outer accretion disk which has a larger area.

The last possibility is that something is blocking the X-rays from reaching reprocessing sites on the disk. Bałucińska-Church et al. (2010) estimate that the disk height at the inner disk edge for the Cyg-like Z-source GX5-1 should be thick, on the order of the inner disk radius, at the hard apex point on the Z-diagram under the assumption of a radiatively supported disk which reaches equilibrium at the apex and disrupts the inner disk. Sco-like Z-sources, however, cannot be modeled in the same way as Cyg-like sources (Lin et al., 2009; Bałucińska-Church et al., 2010; Church & Bałucińska-Church, 2012), with the primary difference being the large amount of flaring in Sco-like sources, which could be due to a combination of unstable nuclear burning on the surface of the NS along with increasing mass accretion rate.

8.6 Summary of Results

We have examined optical variability of X-ray sources on both long and short timescales. We have identified 168 variable counterparts to GBS sources, including 68 periodic sources. The GBS contains between 16 and ~ 90 CVs with optical counterparts, between 6 and ~ 52 IPs, and on the order of 10 qLMXBs, with 4 strong candidates (CX: 70, 96, 446, 561) and many that are ambiguous between IPs, CVs, and qLMXBs, especially between the latter 2. We have placed a limit on the number of qLMXBs in the GBS that can be found by ellipsoidal modulations. Optical variability is a powerful tool, but it has limitations. There could be many true counterparts in the group of 545 sources without a variable inside the X-ray error circle, such as CX561. We have also constrained the reprocessing geometry of Sco X-1 by demonstrating that reprocessing on the outer disk is cut off in the Normal Branch and Horizontal Branch of the Z-diagram and by placing limits on the presence of the companion star in CCFs.

References

Alard, C. 2000, A&AS, 144, 363

Alard, C., & Lupton, R. H. 1998, ApJ, 503, 325

Bailyn, C. D., Jain, R. K., Coppi, P., & Orosz, J. A. 1998, ApJ, 499, 367

Bałucińska-Church, M., Gibiec, A., Jackson, N. K., & Church, M. J. 2010, A&A, 512, A9

Blaauw, A. 1961, BAN, 15, 265

Blackburn, J. K. 1995, in Astronomical Society of the Pacific Conference Series, Vol. 77, Astronomical Data Analysis Software and Systems IV, ed. R. A. Shaw, H. E. Payne, & J. J. E. Hayes, 367

Bohlin, R. C., Savage, B. D., & Drake, J. F. 1978, ApJ, 224, 132

Britt, C. T., Torres, M. A. P., Hynes, R. I., et al. 2013, ApJ, 769, 120

Cardelli, J. A., Clayton, G. C., & Mathis, J. S. 1989, ApJ, 345, 245

Casares, J., Charles, P. A., Jones, D. H. P., Rutten, R. G. M., & Callanan, P. J. 1991, MNRAS, 250, 712

Church, M. J., & Bałucińska-Church, M. 2012, MmSAI, 83, 170

Church, M. J., Halai, G. S., & Bałucińska-Church, M. 2006, A&A, 460, 233

Demorest, P. B., Pennucci, T., Ransom, S. M., Roberts, M. S. E., & Hessels, J. W. T. 2010, Nature, 467, 1081

Dempsey, R. C., Linsky, J. L., Fleming, T. A., & Schmitt, J. H. M. M. 1997, ApJ, 478, 358

Echevarria, J. 1988, MNRAS, 233, 513

Edelson, R. A., & Krolik, J. H. 1988, ApJ, 333, 646

Edmonds, P. D., Grindlay, J. E., Cool, A., et al. 1999, ApJ, 516, 250

Farr, W. 2012, in X-ray Binaries. Celebrating 50 Years Since the Discovery of Sco X-1

Farr, W. M., Sravan, N., Cantrell, A., et al. 2011, ApJ, 741, 103

Fomalont, E. B., Geldzahler, B. J., & Bradshaw, C. F. 2001, ApJ, 558, 283

Frank, J., King, A., & Raine, D. J. 2002, Accretion Power in Astrophysics: Third Edition

Gänsicke, B. T. 2005, in Astronomical Society of the Pacific Conference Series, Vol. 330, The Astrophysics of Cataclysmic Variables and Related Objects, ed. J.-M. Hameury & J.-P. Lasota, 3

Garmire, G. P. 1997, in Bulletin of the American Astronomical Society, Vol. 29, American Astronomical Society Meeting Abstracts #190, 823

Gehrels, N. 1986, ApJ, 303, 336

Gonzalez, O. A., Rejkuba, M., Zoccali, M., et al. 2012, A&A, 543, A13

Grimm, H.-J., Gilfanov, M., & Sunyaev, R. 2003, MNRAS, 339, 793

Grindlay, J. E. 1999, in Astronomical Society of the Pacific Conference Series, Vol. 157, Annapolis Workshop on Magnetic Cataclysmic Variables, ed. C. Hellier & K. Mukai, 377

Grindlay, J. E. 2006, Advances in Space Research, 38, 2923

Grindlay, J. E., Hong, J., Zhao, P., et al. 2005, ApJ, 635, 920

Güdel, M. 2004, A&ARv, 12, 71

Hands, A. D. P., Warwick, R. S., Watson, M. G., & Helfand, D. J. 2004, MNRAS, 351, 31

Hasinger, G., Priedhorsky, W. C., & Middleditch, J. 1989, ApJ, 337, 843

Heinke, C. O., Grindlay, J. E., & Edmonds, P. D. 2005, ApJ, 622, 556

Heinke, C. O., Grindlay, J. E., Lugger, P. M., et al. 2003, ApJ, 598, 501

Hjellming, R. M., Stewart, R. T., White, G. L., et al. 1990, ApJ, 365, 681

Høg, E., Fabricius, C., Makarov, V. V., et al. 2000, A&A, 355, L27

Homan, J., van der Klis, M., Wijnands, R., et al. 2007, ApJ, 656, 420

Hong, J., van den Berg, M., Grindlay, J. E., Servillat, M., & Zhao, P. 2012, ApJ, 746, 165

Hong, J., van den Berg, M., Schlegel, E. M., et al. 2005, ApJ, 635, 907

Horne, K. 1994, in Astronomical Society of the Pacific Conference Series, Vol. 69, Reverberation Mapping of the Broad-Line Region in Active Galactic Nuclei, ed. P. M. Gondhalekar, K. Horne, & B. M. Peterson, 23–25

Hynes, R. I., Brien, K. O., Mullally, F., & Ashcraft, T. 2009, MNRAS, 399, 281

Hynes, R. I., & Britt, C. T. 2012, ApJ, 755, 66

Hynes, R. I., Robinson, E. L., & Jeffery, E. 2004, ApJL, 608, L101

Hynes, R. I., Wright, N. J., Maccarone, T. J., et al. 2012, ApJ, 761, 162

Hynes, R. I., Torres, M. A. P., Heinke, C. O., et al. 2013, ApJ

Ilovaisky, S. A., Chevalier, C., White, N. E., et al. 1980, MNRAS, 191, 81

Ivanova, N., Belczynski, K., Fregeau, J. M., & Rasio, F. A. 2005, MNRAS, 358, 572

Ivanova, N., & Taam, R. E. 2003, ApJ, 599, 516

Janka, H.-T. 2013, ArXiv e-prints, arXiv:1306.0007

Jonker, P. G., Bassa, C. G., Nelemans, G., et al. 2011, ApJS, 194, 18

Kallman, T., Boroson, B., & Vrtilek, S. D. 1998, ApJ, 502, 441

Kalogera, V. 1999, ApJ, 521, 723

Kaur, R., Wijnands, R., Paul, B., Patruno, A., & Degenaar, N. 2010, MNRAS, 402, 2388

Kennea, J. A., Krimm, H. A., & Holland, S. T. 2012, The Astronomer's Telegram, 4149, 1

Kiel, P. D., & Hurley, J. R. 2006, MNRAS, 369, 1152

Krivonos, R., Tsygankov, S., Lutovinov, A., et al. 2012, A&A, 545, A27

Kupfer, T., Groot, P. J., Levitan, D., et al. 2013, MNRAS, 432, 2048

Lasota, J.-P. 2001, NewAR, 45, 449

Lattimer, J. M., & Prakash, M. 2001, ApJ, 550, 426

—. 2007, PhR, 442, 109

Lewin, W. H. G., & van der Klis, M. 2006, Compact Stellar X-ray Sources

Lin, D., Remillard, R. A., & Homan, J. 2009, ApJ, 696, 1257

Lin, D., Remillard, R. A., Homan, J., & Barret, D. 2012, ApJ, 756, 34

Maccarone, T. J., Torres, M. A. P., Britt, C. T., et al. 2012, MNRAS, 426, 3057

Marsh, T. R., Robinson, E. L., & Wood, J. H. 1994, MNRAS, 266, 137

Marti, J., Mirabel, I. F., Chaty, S., & Rodriguez, L. F. 1998, A&A, 330, 72

Mauerhan, J. C., Muno, M. P., Morris, M. R., et al. 2009, ApJ, 703, 30

Menou, K., Esin, A. A., Narayan, R., et al. 1999, ApJ, 520, 276

Muñoz-Darias, T., Martínez-Pais, I. G., Casares, J., et al. 2007, MNRAS, 379, 1637

Muno, M. P., Baganoff, F. K., Bautz, M. W., et al. 2003, ApJ, 599, 465

Narayan, R., & McClintock, J. E. 2005, ApJ, 623, 1017

Nelemans, G. 2005, in Astronomical Society of the Pacific Conference Series, Vol. 330, The Astrophysics of Cataclysmic Variables and Related Objects, ed. J.-M. Hameury & J.-P. Lasota, 27

Nelemans, G., & Jonker, P. G. 2010, NewAR, 54, 87

Nelemans, G., Jonker, P. G., & Steeghs, D. 2006, MNRAS, 370, 255

Nowak, M. A., Heinz, S., & Begelman, M. C. 2002, ApJ, 573, 778

Nowak, M. A., Wilms, J., Heindl, W. A., et al. 2001, MNRAS, 320, 316

O'Brien, K., Horne, K., Hynes, R. I., et al. 2002, MNRAS, 334, 426

Orosz, J. A., & Bailyn, C. D. 1997, ApJ, 477, 876

Orosz, J. A., McClintock, J. E., Narayan, R., et al. 2007, Nature, 449, 872

Özel, F. 2006, Nature, 441, 1115

Özel, F., Baym, G., & Güver, T. 2010a, Phys. Rev. D, 82, 101301

Özel, F., Güver, T., & Psaltis, D. 2009, ApJ, 693, 1775

Özel, F., Psaltis, D., Narayan, R., & McClintock, J. E. 2010b, ApJ, 725, 1918

Özel, F., Psaltis, D., Narayan, R., & Santos Villarreal, A. 2012, ApJ, 757, 55

Paczyński, B. 1971, ARA&A, 9, 183

Paczynski, B. 1976, in IAU Symposium, Vol. 73, Structure and Evolution of Close Binary Systems, ed. P. Eggleton, S. Mitton, & J. Whelan, 75

Patterson, J. 1994, PASP, 106, 209

Pedersen, H., Lub, J., Inoue, H., et al. 1982, ApJ, 263, 325

Petro, L. D., Bradt, H. V., Kelley, R. L., Horne, K., & Gomer, R. 1981, ApJL, 251, L7

Pfahl, E., Rappaport, S., & Podsiadlowski, P. 2003, ApJ, 597, 1036

Plotkin, R. M., Gallo, E., & Jonker, P. G. 2013, ArXiv e-prints, arXiv:1306.1570

Portegies Zwart, S. F., Verbunt, F., & Ergma, E. 1997, A&A, 321, 207

Predehl, P., & Schmitt, J. H. M. M. 1995, A&A, 293, 889

Ratti, E. M., van Grunsven, T. F. J., Jonker, P. G., et al. 2013, MNRAS, 428, 3543

Remillard, R. A., & McClintock, J. E. 2006, ARA&A, 44, 49

Repetto, S., Davies, M. B., & Sigurdsson, S. 2012, MNRAS, 425, 2799

Scaringi, S., Bird, A. J., Norton, A. J., et al. 2010, MNRAS, 401, 2207

Schlegel, D. J., Finkbeiner, D. P., & Davis, M. 1998, ApJ, 500, 525

Schmitt, J. H. M. M., Fleming, T. A., & Giampapa, M. S. 1995, ApJ, 450, 392

Shara, M. M., Hinkley, S., Zurek, D. R., Knigge, C., & Dieball, A. 2005, AJ, 130, 1829

Shaw, R. A. 2009, NOAO Data Handbook

Shears, J., Boyd, D., & Poyner, G. 2006, Journal of the British Astronomical Association, 116, 244

Silber, A. D. 1992, PhD thesis, Massachusetts Institute of Technology.

Skilling, J., & Bryan, R. K. 1984, MNRAS, 211, 111

Stetson, P. B. 1987, PASP, 99, 191

Strader, J., Chomiuk, L., Maccarone, T. J., Miller-Jones, J. C. A., & Seth, A. C. 2012, Nature, 490, 71

Sugizaki, M., Mitsuda, K., Kaneda, H., et al. 2001, ApJS, 134, 77

Sulkanen, M. E., Brasure, L. W., & Patterson, J. 1981, ApJ, 244, 579

Szkody, P., Gänsicke, B. T., Sion, E. M., & Howell, S. B. 2002, ApJ, 574, 950

Szkody, P., & Henden, A. 2005, Journal of the American Association of Variable Star Observers (JAAVSO), 34, 11

Taam, R. E., & Sandquist, E. L. 2000, ARA&A, 38, 113

Tauris, T. M., & van den Heuvel, E. P. J. 2006, Formation and evolution of compact stellar X-ray sources, ed. W. H. G. Lewin & M. van der Klis, 623–665

Terzan, A., & Gosset, E. 1991, A&AS, 90, 451

Torres, M. A. P., Jonker, P. G., Bassa, C. G., et al. 2013, ApJ, In Preparation

Udalski, A., Kowalczyk, K., Soszyński, I., et al. 2012, AcA, 62, 133

van der Sluys, M. 2006, PhD thesis, Utrecht University.

Verbunt, F., Bunk, W. H., Ritter, H., & Pfeffermann, E. 1997, A&A, 327, 602

Véron-Cetty, M. P., & Véron, P. 2000, A&ARv, 10, 81

Warner, B. 2003, Cataclysmic Variable Stars

Zurita, C., Casares, J., & Shahbaz, T. 2003, ApJ, 582, 369

Appendix A: Mosaic-II Lightcurves of Optical Counterparts

In this appendix are those sources with identified counterparts, either variable and identified though photometry, or nonvariable and confirmed through spectroscopy or other observations in other wavelengths. Together with those sources in Chapters 5 and 6, these sources represent a complete catalog of the photometry of known counterparts of X-ray sources to GBS sources for magnitudes $16 < r' < 23$.

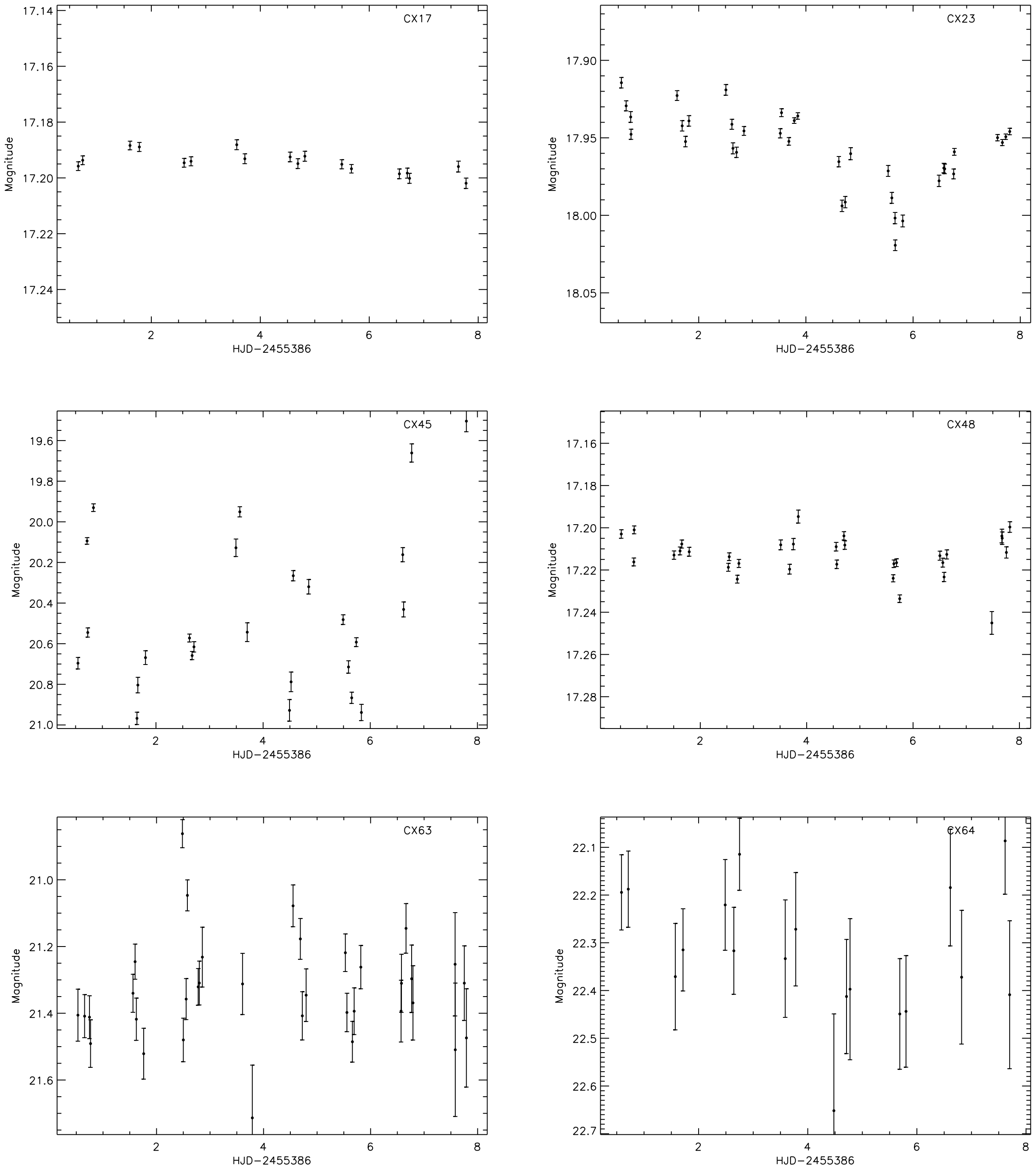

Figure A.1: CX17, CX23, CX45, CX48, CX63, CX64 Lightcurves

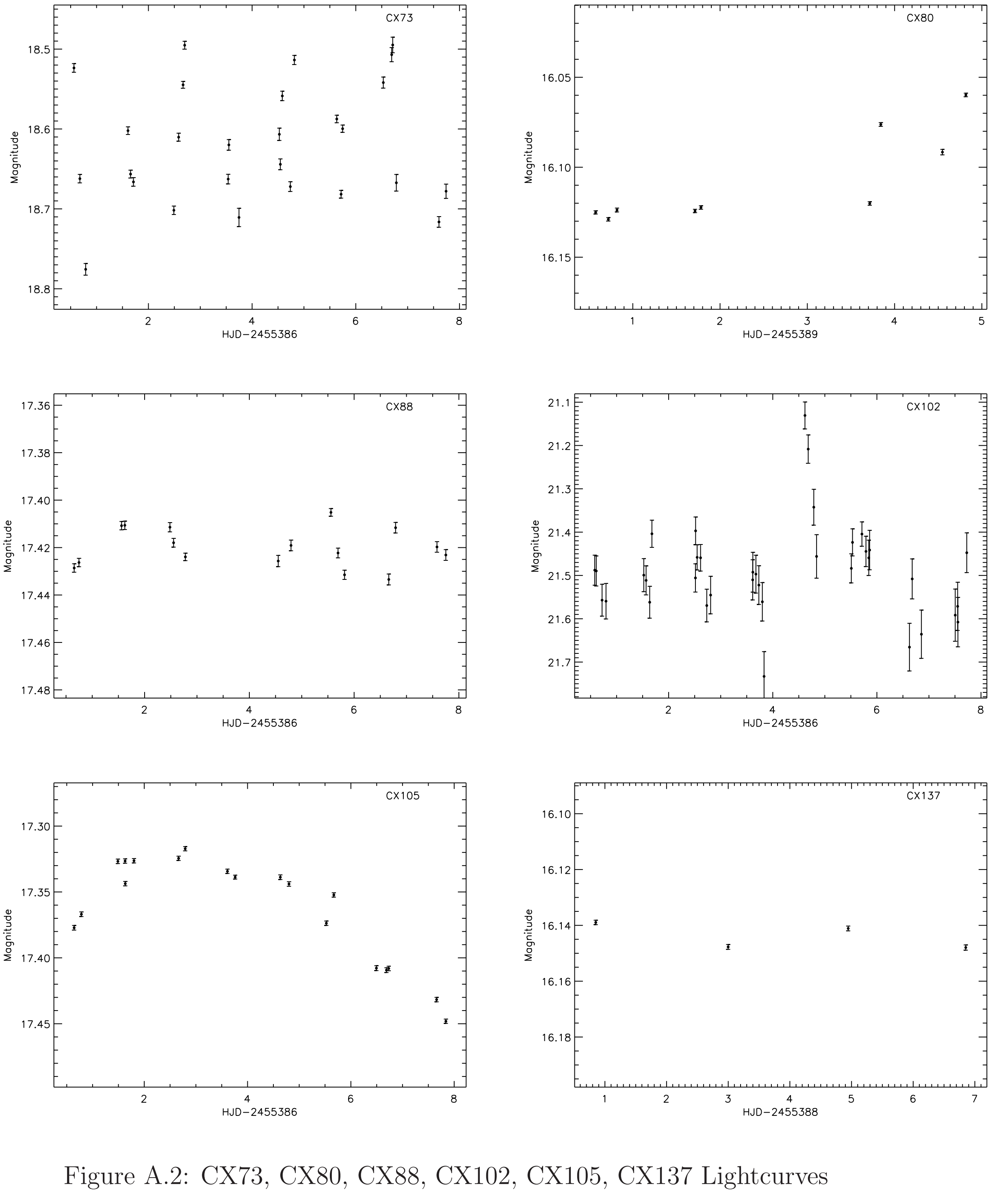

Figure A.2: CX73, CX80, CX88, CX102, CX105, CX137 Lightcurves

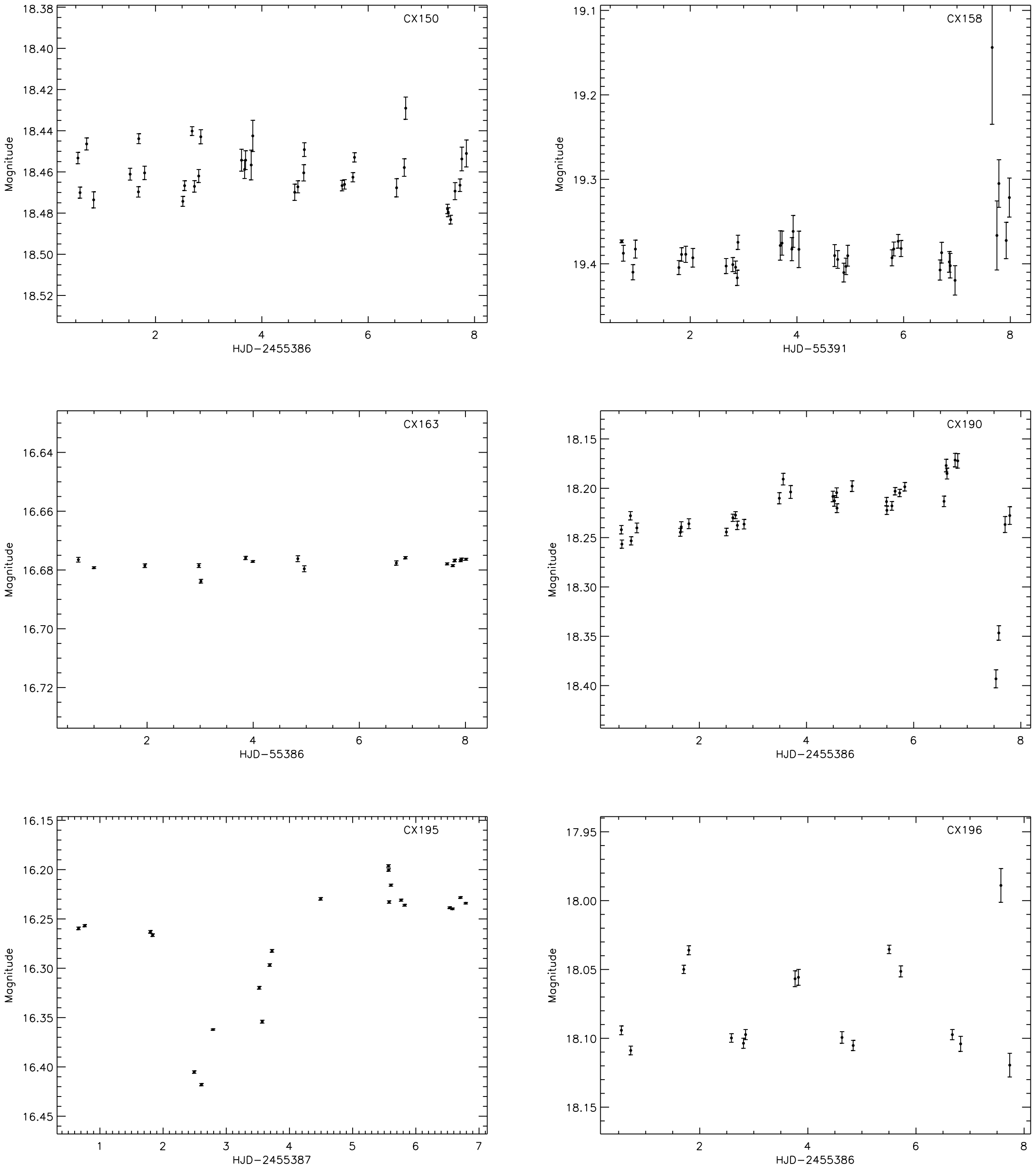

Figure A.3: CX150, CX158, CX163, CX190, CX195, CX196 Lightcurves

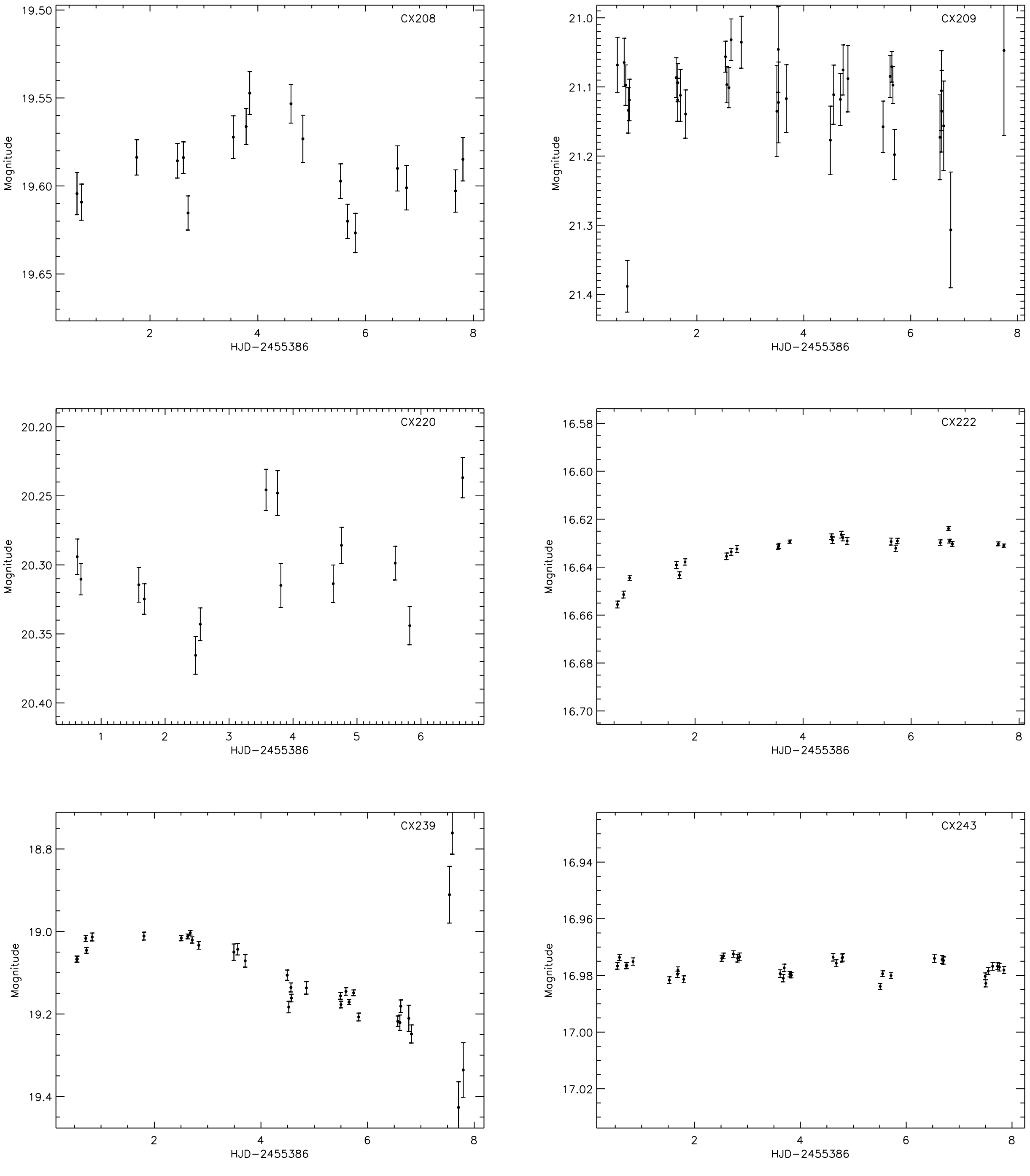

Figure A.4: CX208, CX209, CX220, CX222, CX239, CX243 Lightcurves

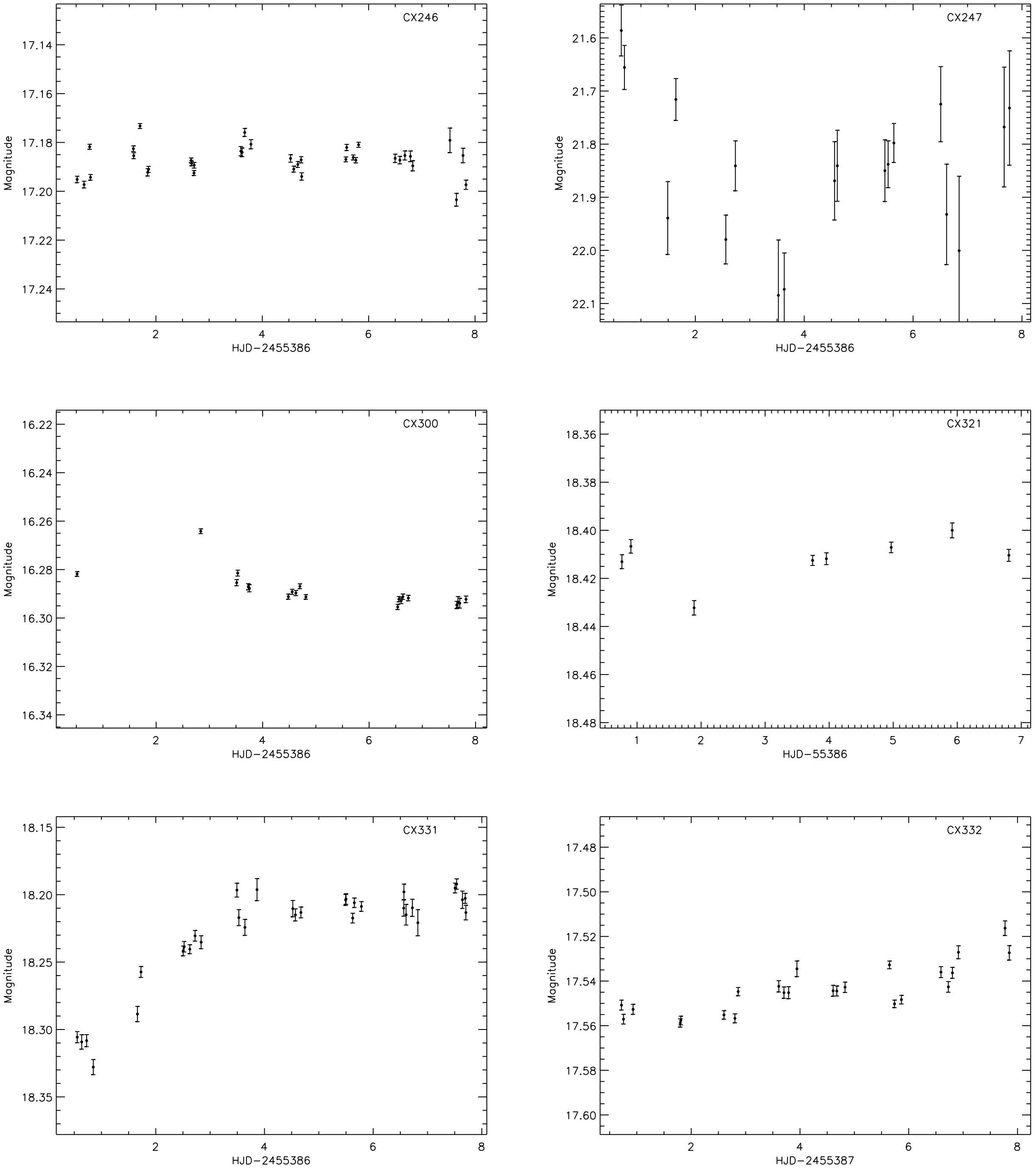

Figure A.5: CX246, CX247, CX300, CX321, CX331, CX332 Lightcurves

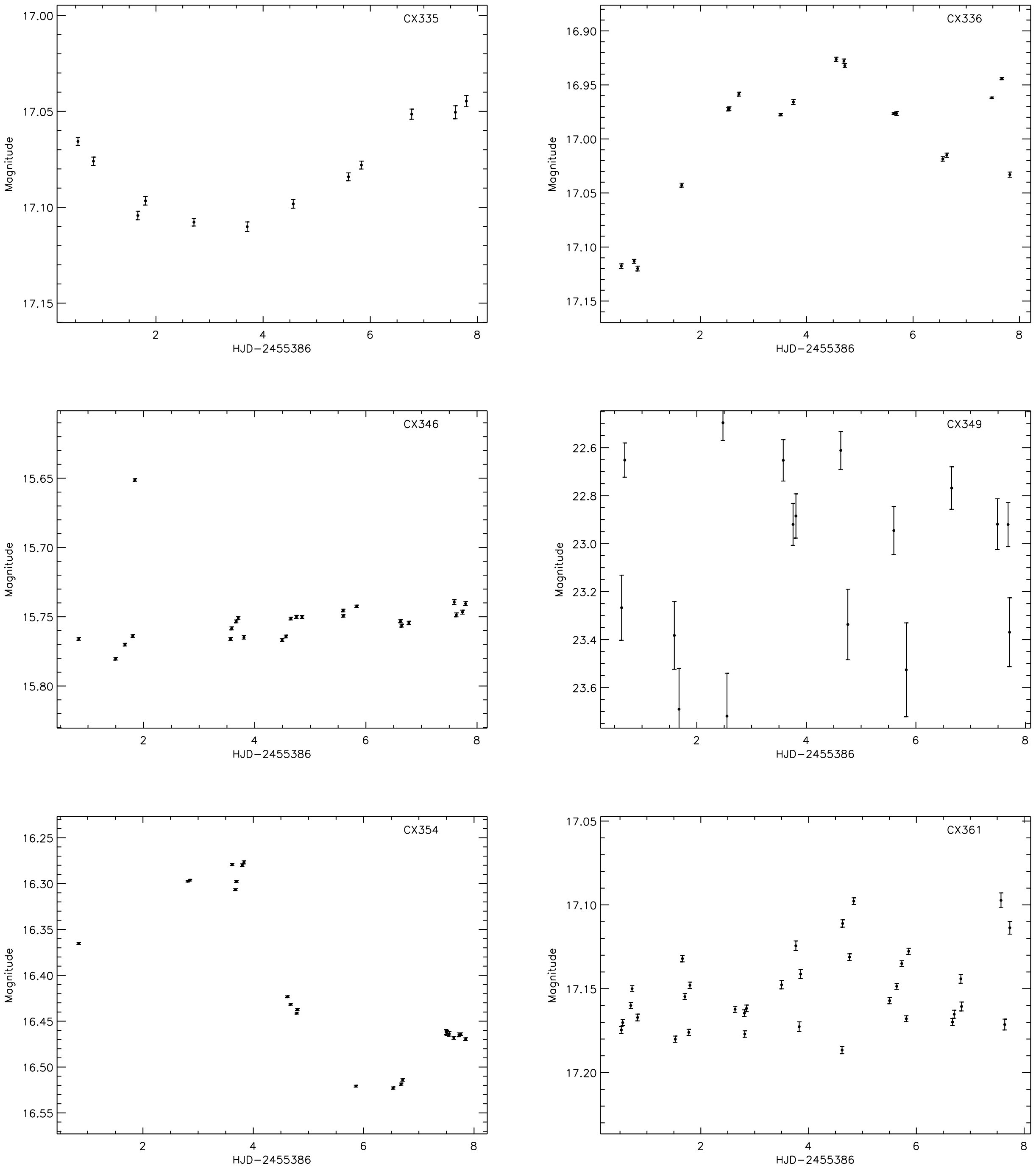

Figure A.6: CX335, CX336, CX346, CX349, CX354, CX361 Lightcurves

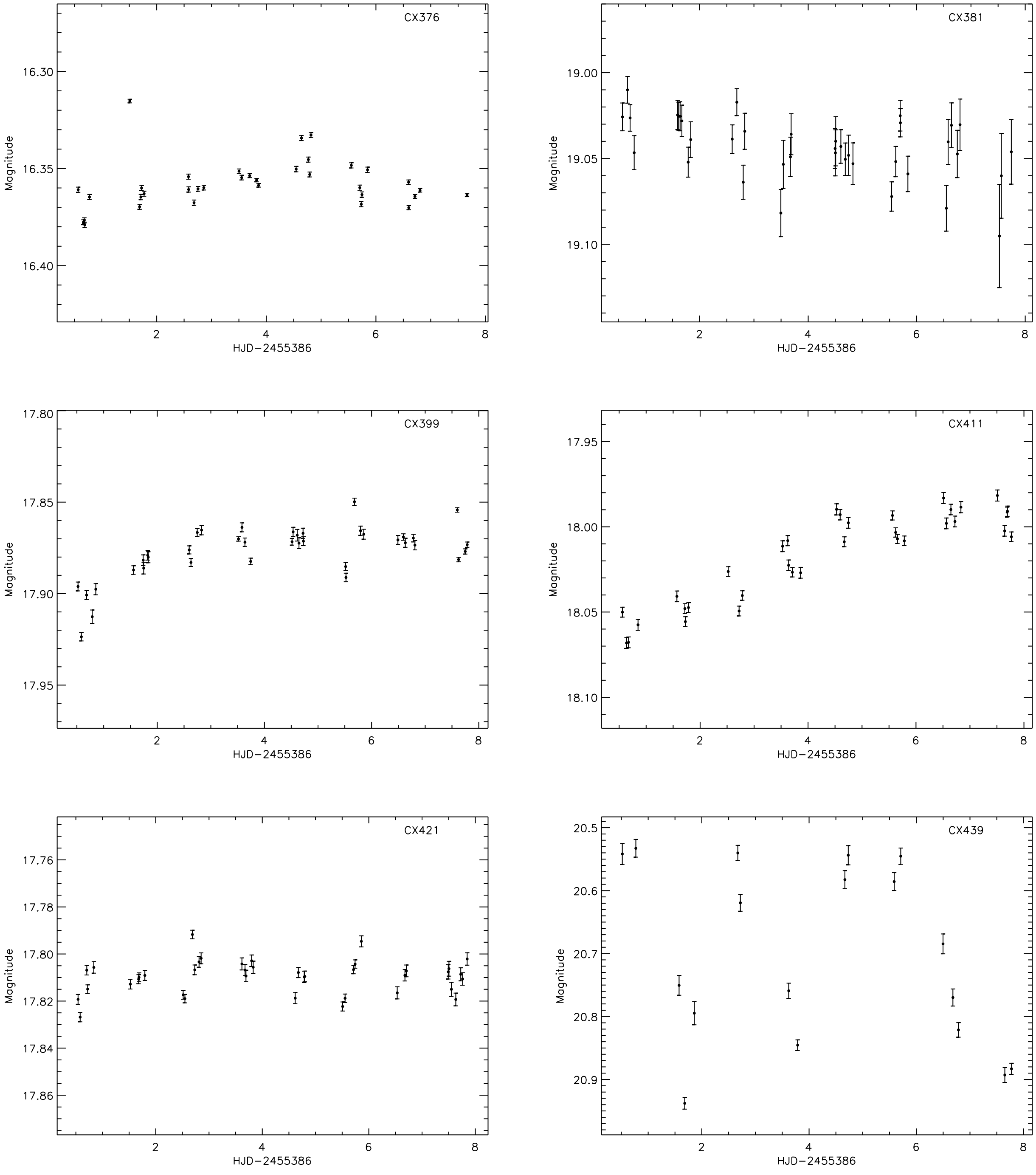

Figure A.7: CX376, CX381, CX399, CX411, CX421, CX439 Lightcurves

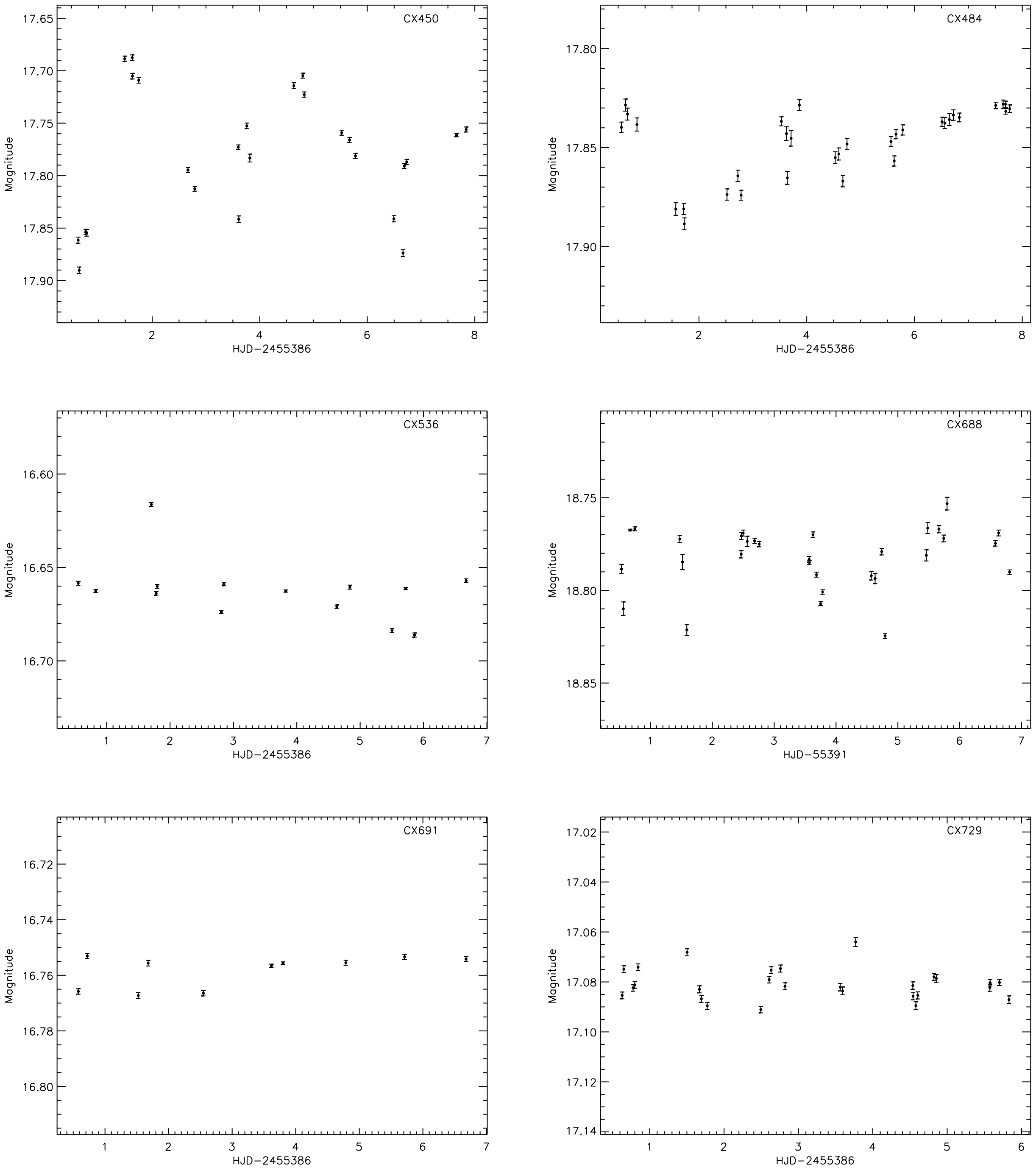

Figure A.8: CX450, CX484, CX536, CX688, CX691, CX729 Lightcurves

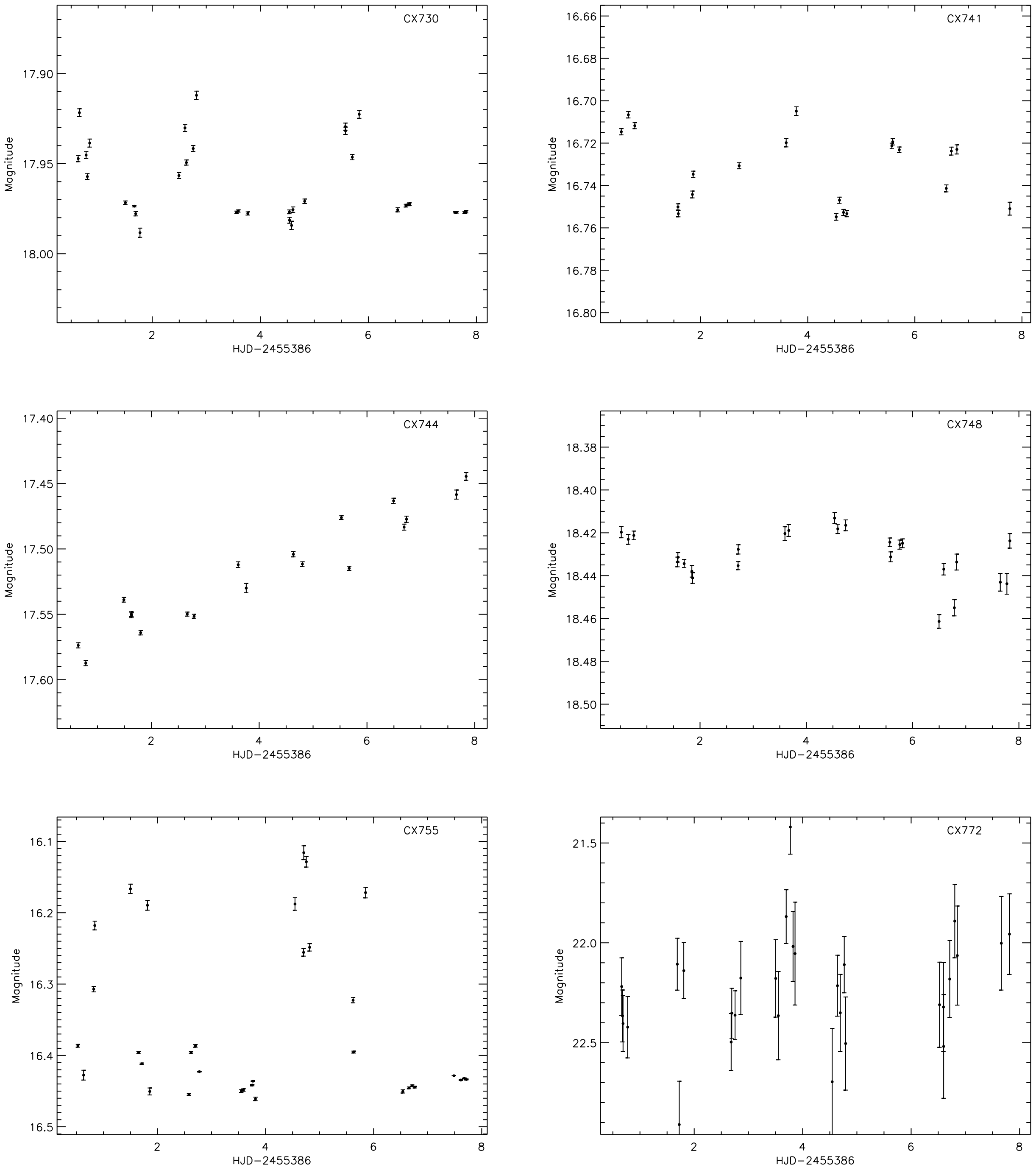

Figure A.9: CX730, CX741, CX744, CX748, CX755, CX772 Lightcurves

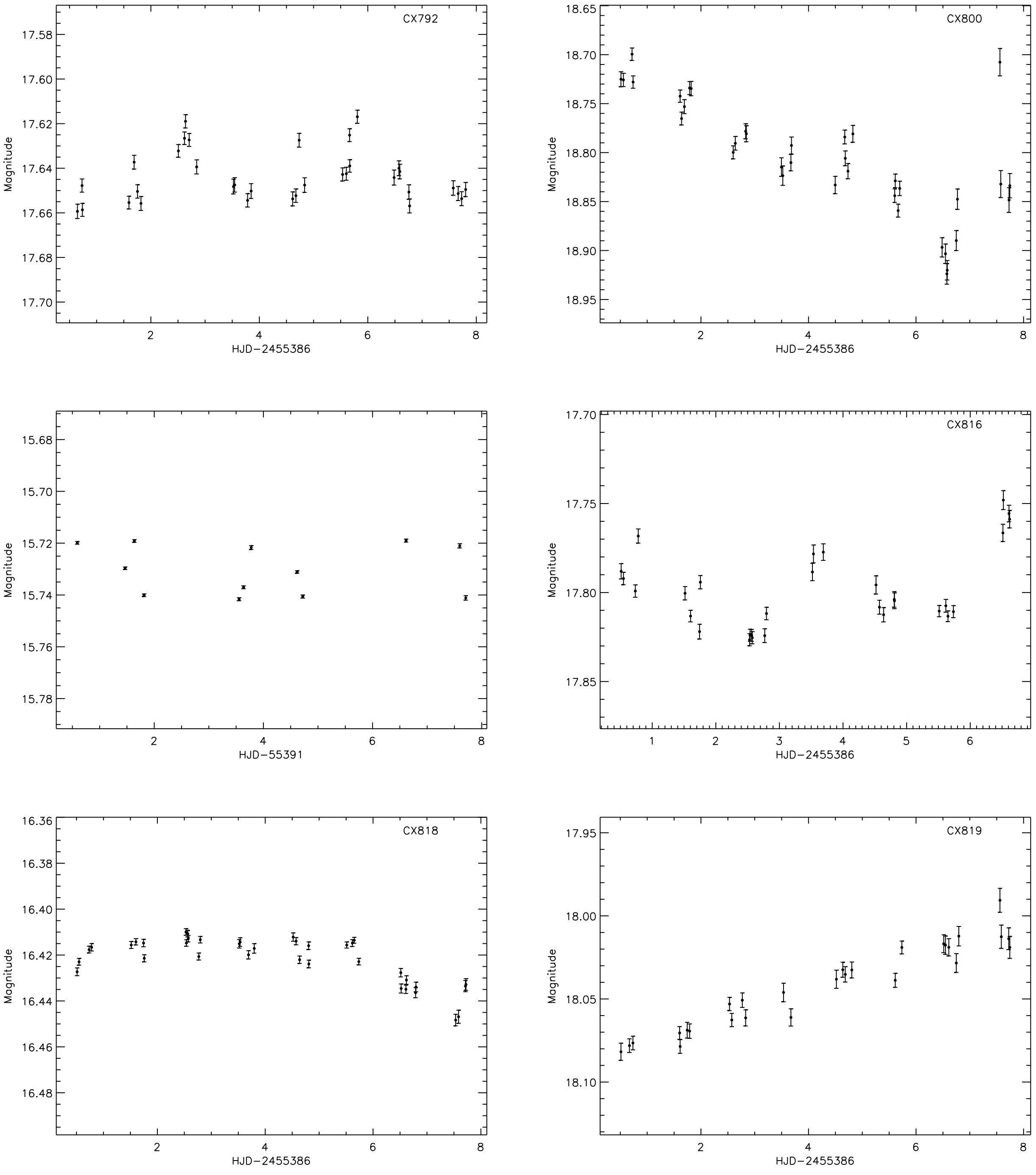

Figure A.10: CX792, CX800, CX812, CX816, CX818, CX819 Lightcurves

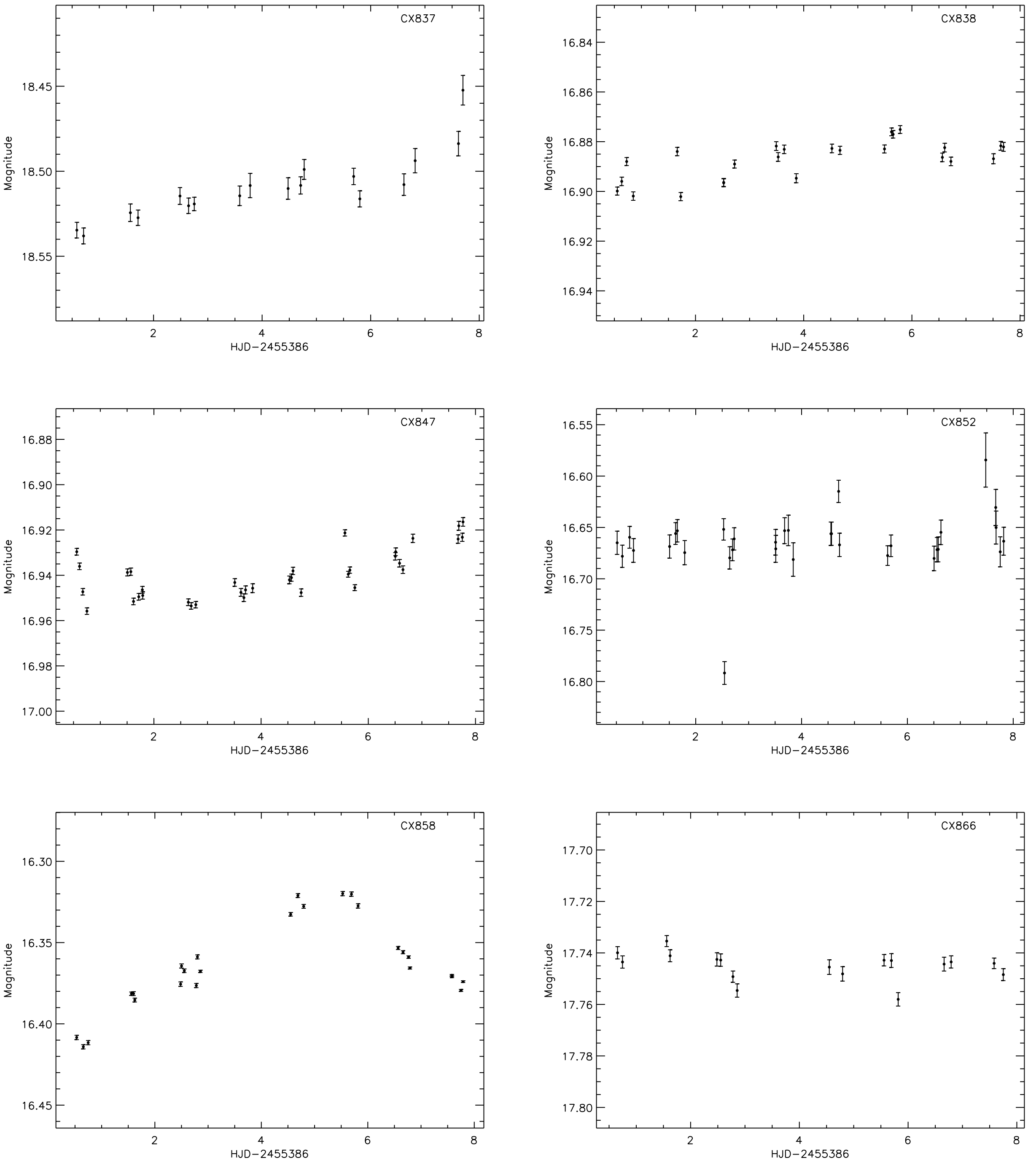

Figure A.11: CX837, CX838, CX847, CX852, CX858, CX866 Lightcurves

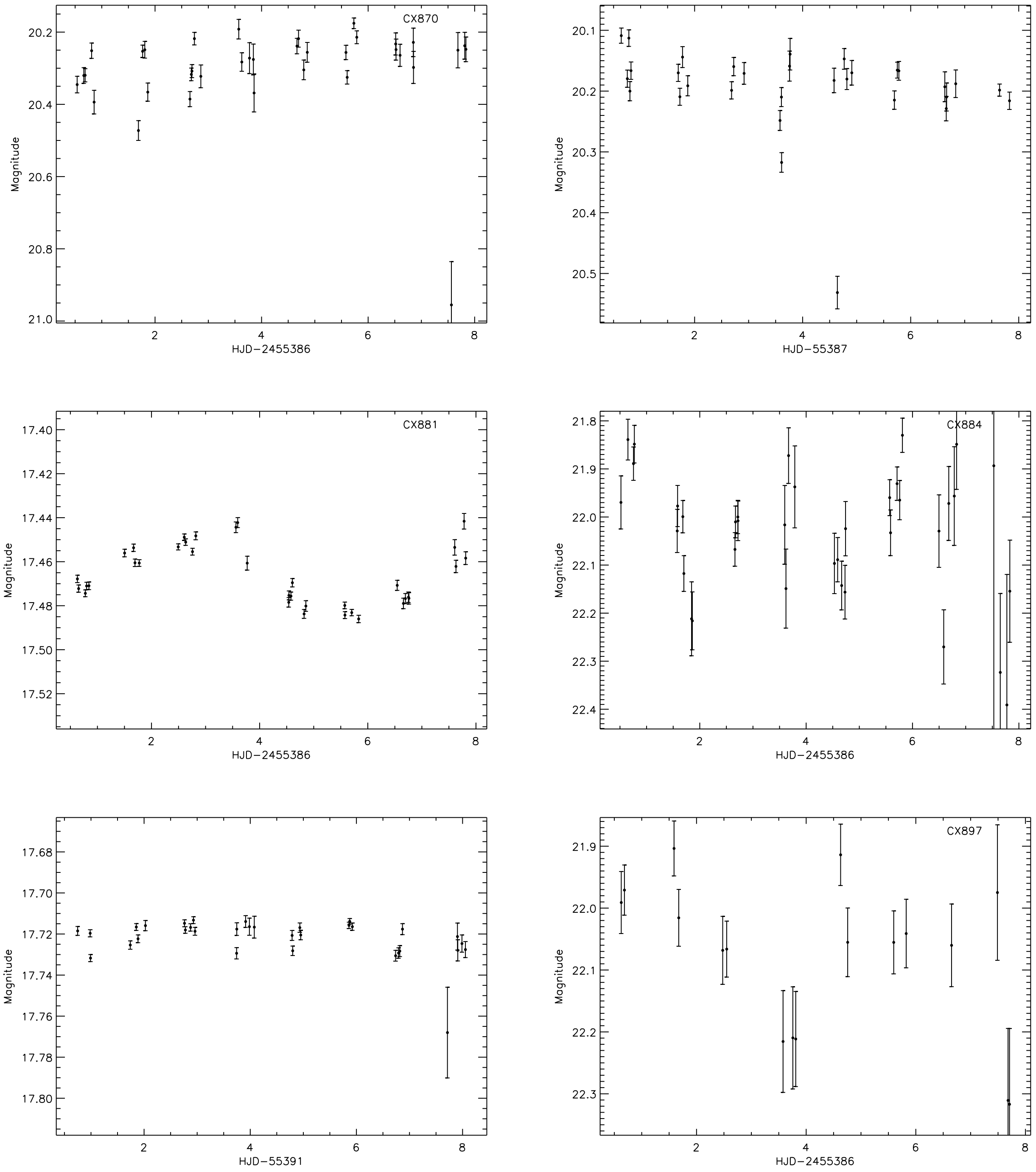

Figure A.12: CX870, CX873, CX881, CX884, CX894, CX897 Lightcurves

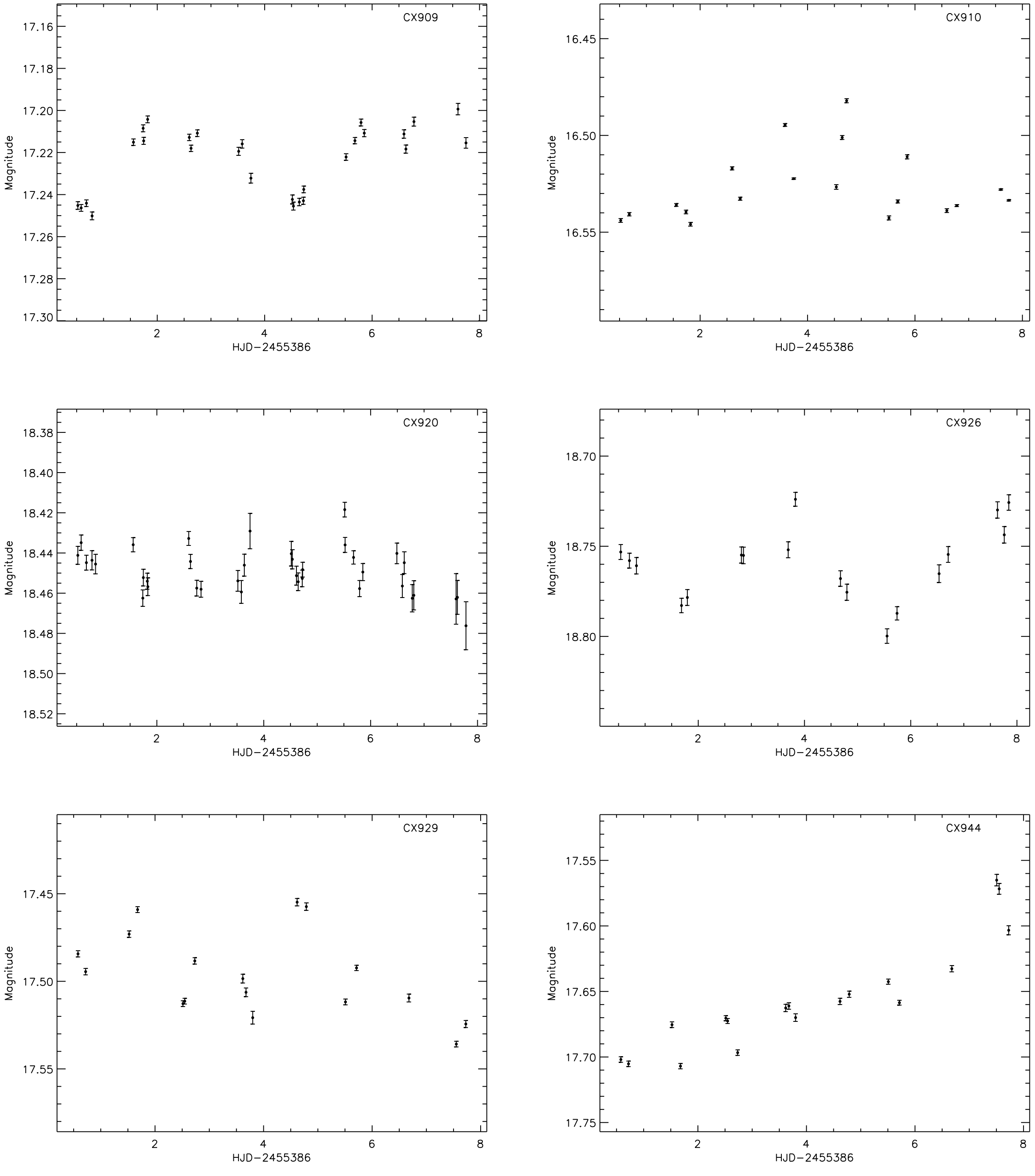

Figure A.13: CX909, CX910, CX920, CX926, CX929, CX944 Lightcurves

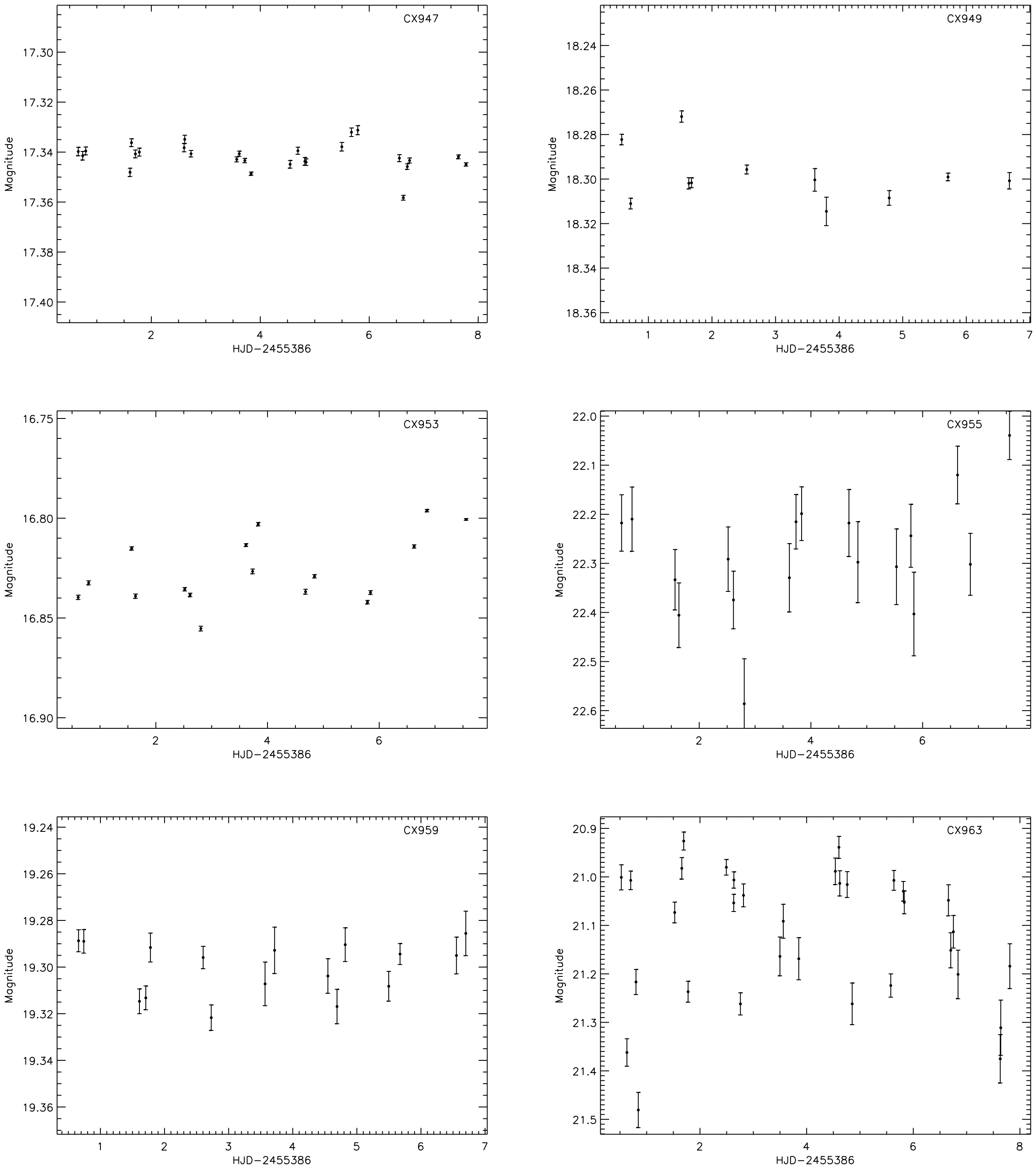

Figure A.14: CX947, CX949, CX953, CX955, CX959, CX963 Lightcurves

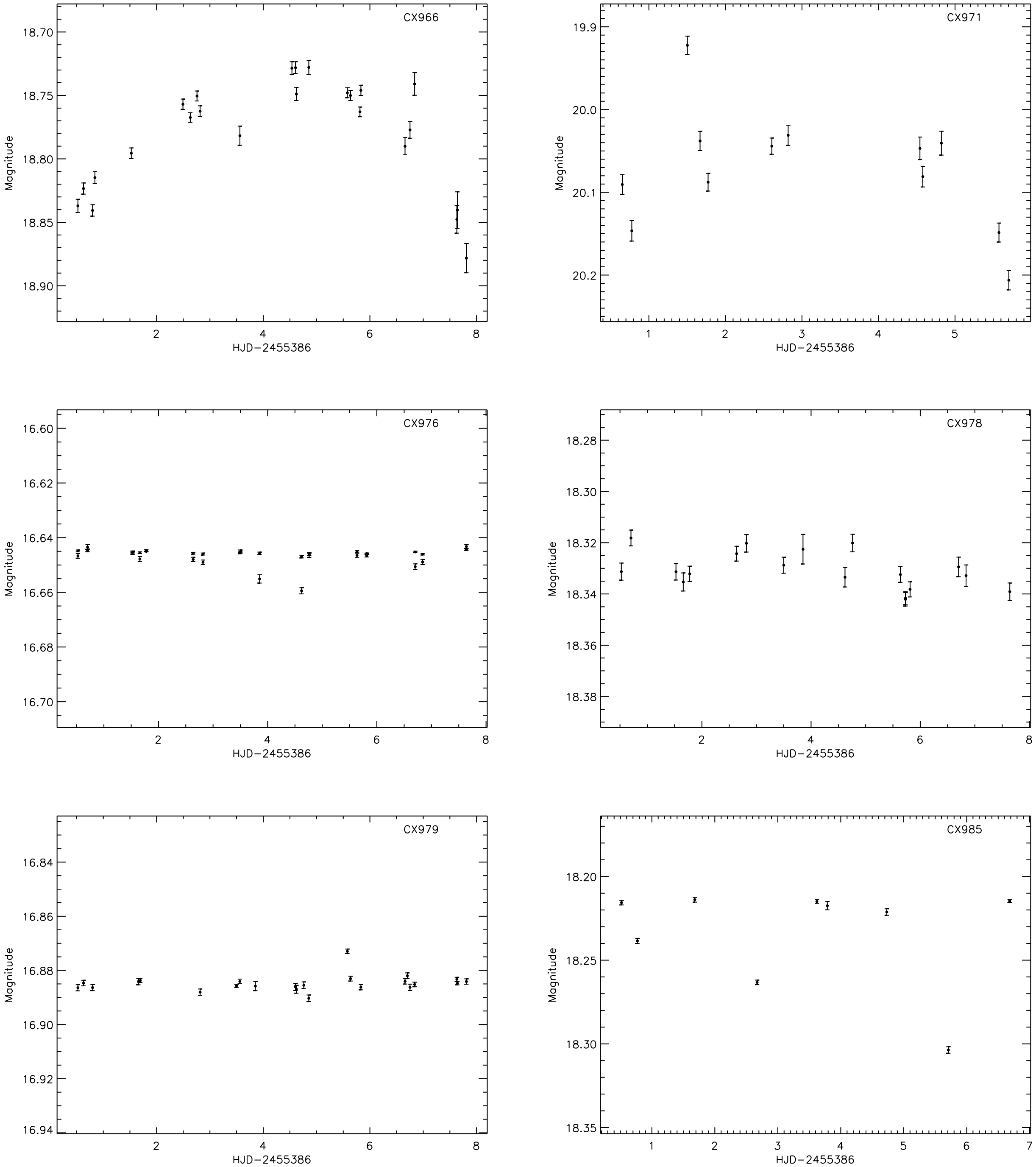

Figure A.15: CX966, CX971, CX976, CX978, CX979, CX985 Lightcurves

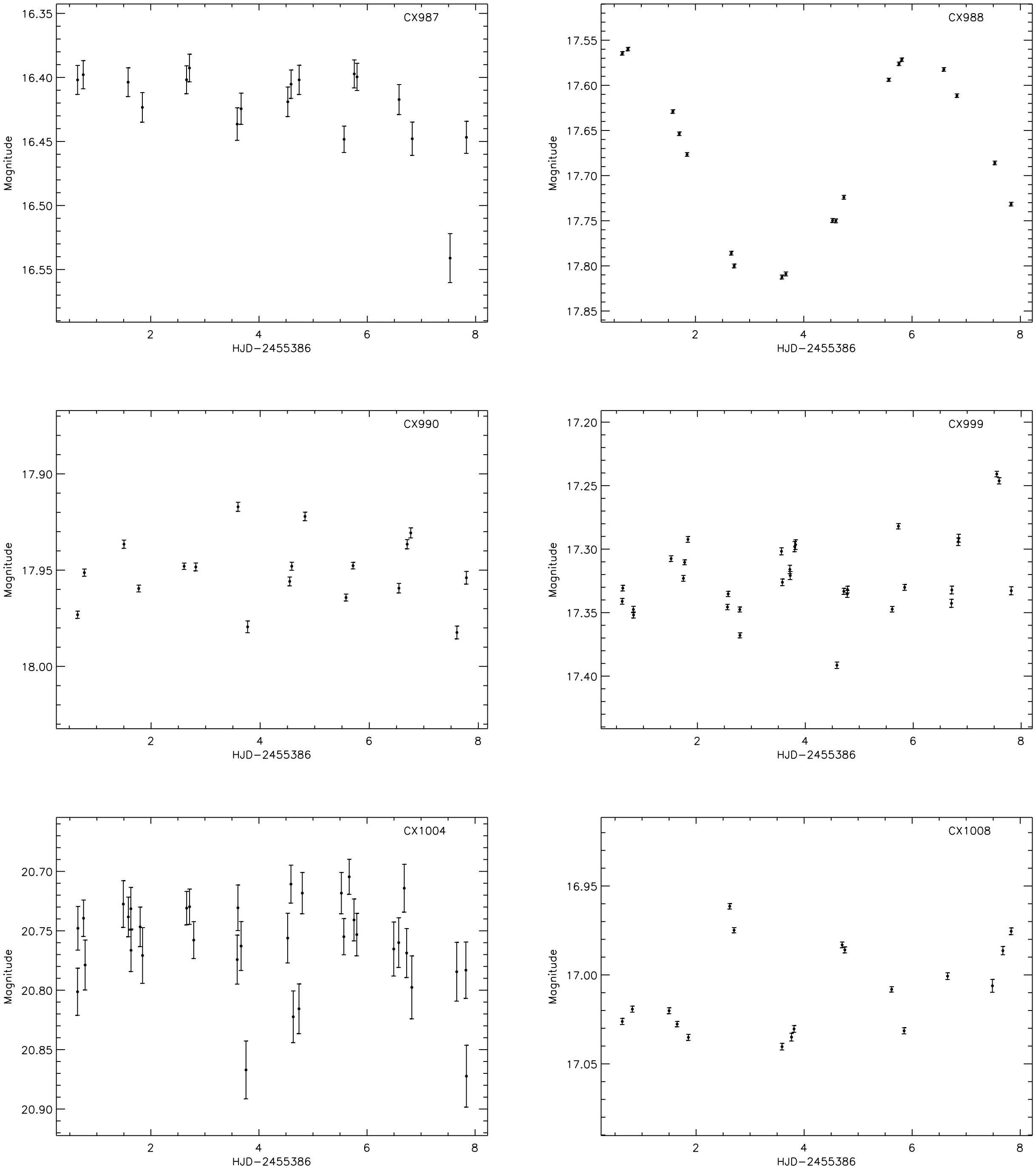

Figure A.16: CX987, CX988, CX990, CX999, CX1004, CX1008 Lightcurves

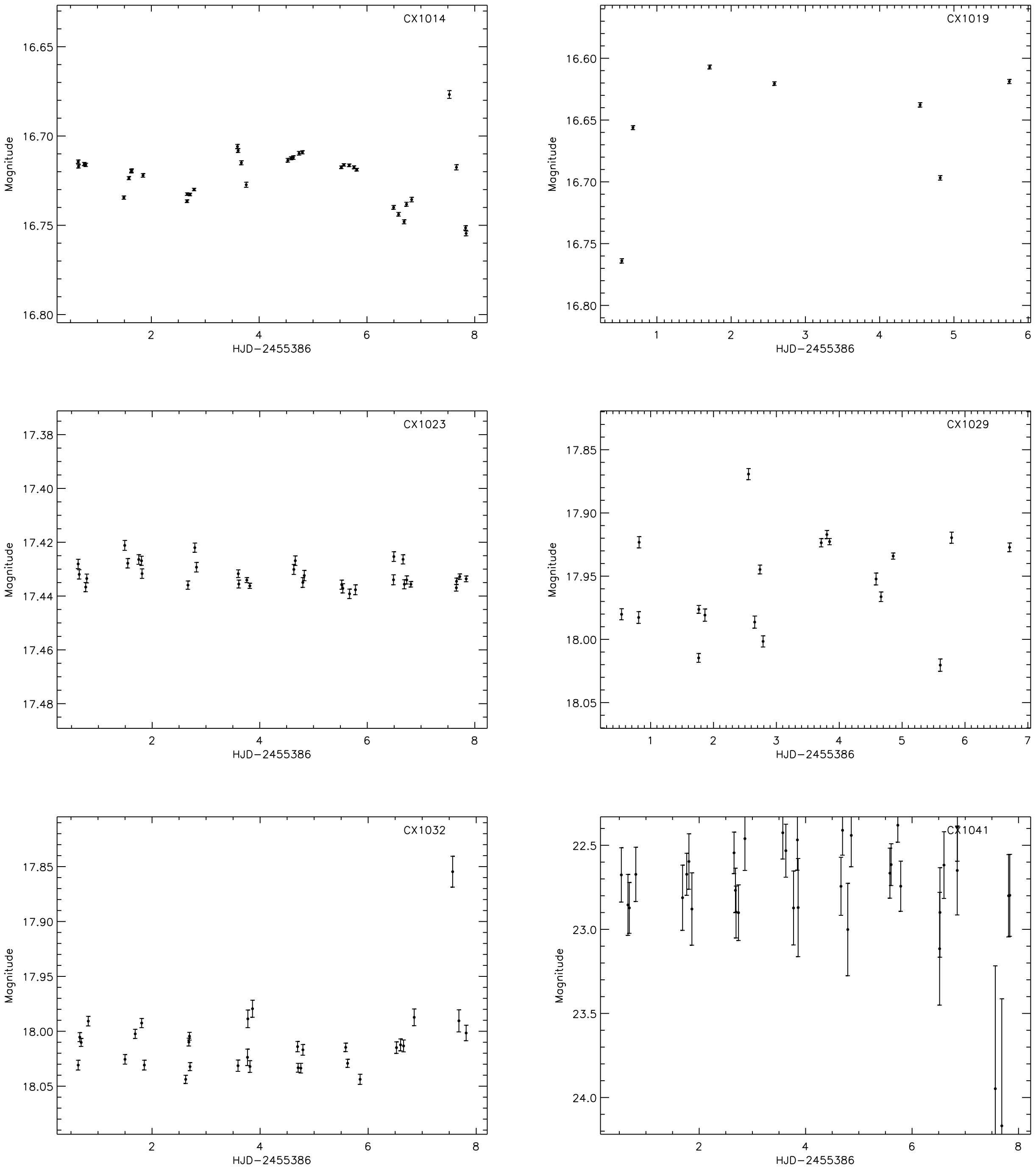

Figure A.17: CX1014, CX1019, CX1023, CX1029, CX1032, CX1041 Lightcurves

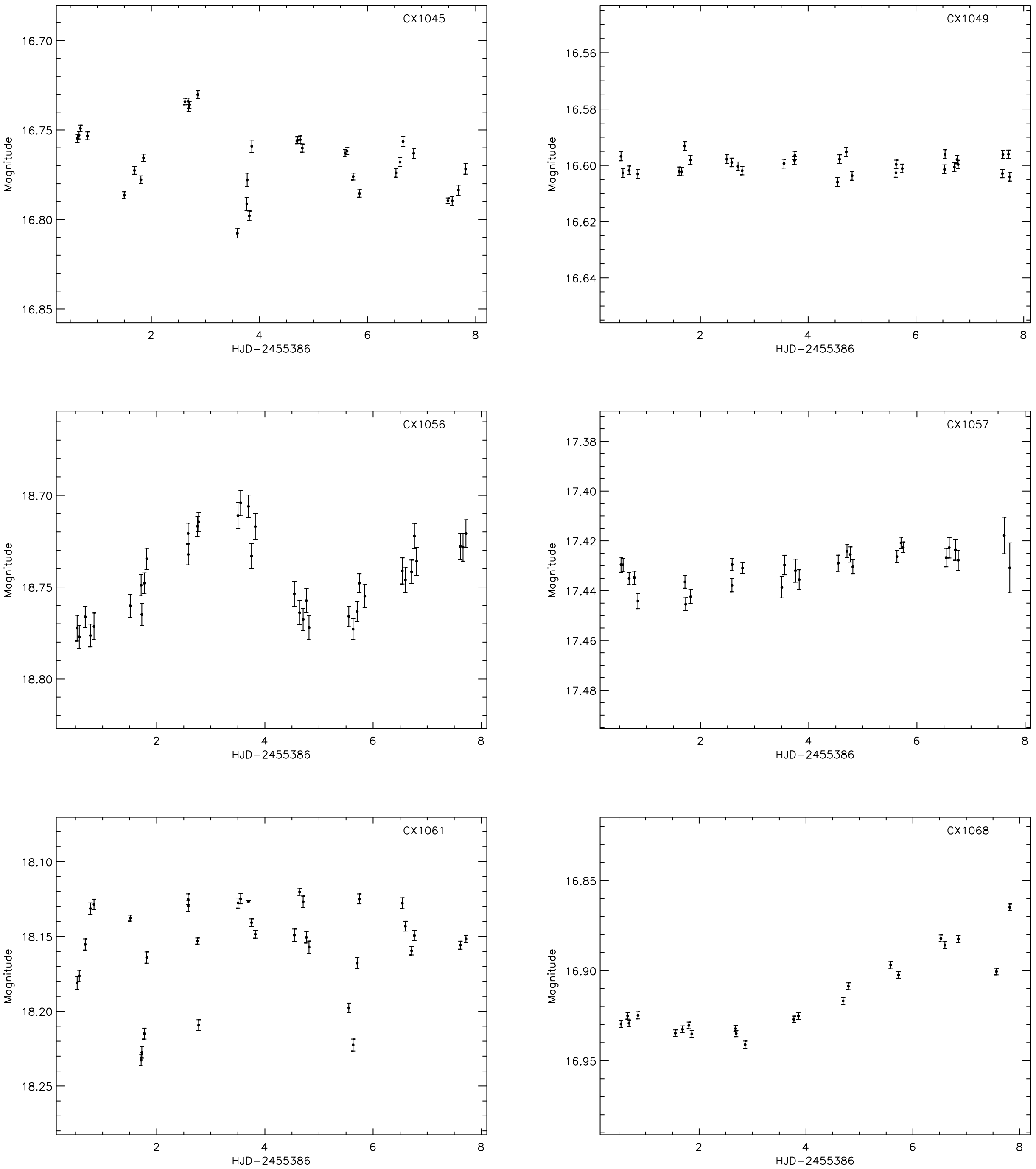

Figure A.18: CX1045, CX1049, CX1056, CX1057, CX1061, CX1068 Lightcurves

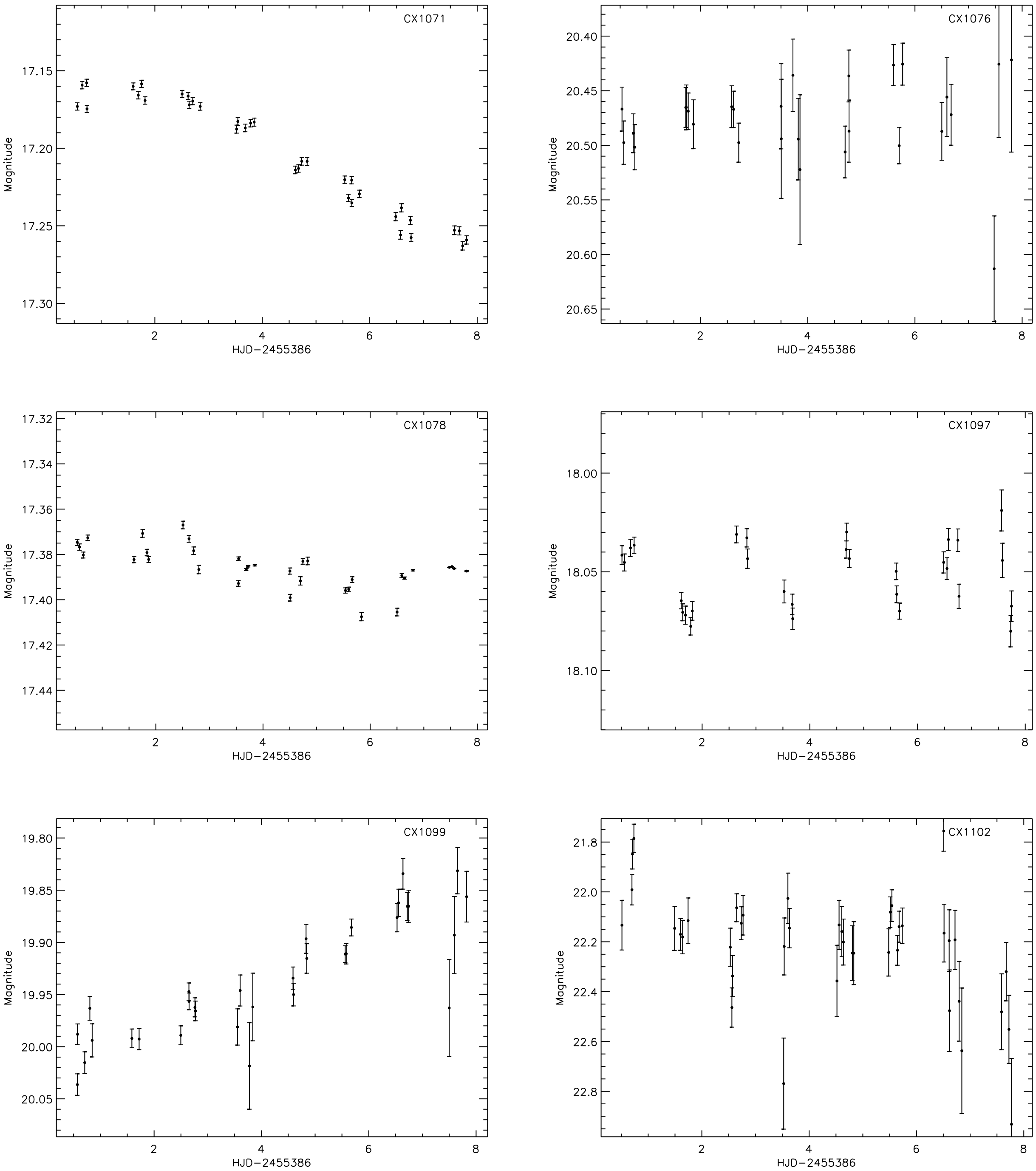

Figure A.19: CX1071, CX1076, CX1078, CX1097, CX1099, CX1102 Lightcurves

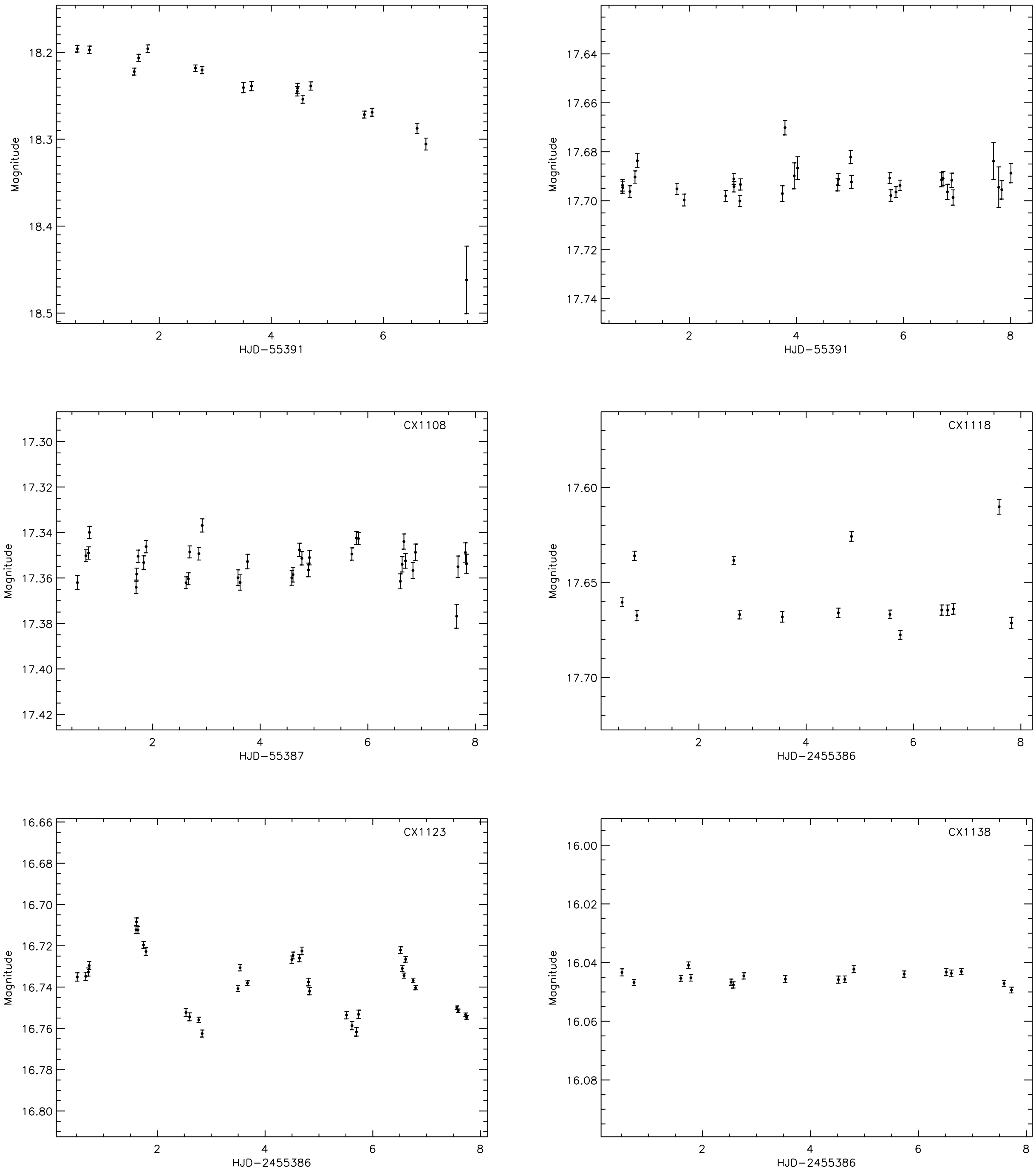

Figure A.20: CX1104, CX1107, CX1108, CX1118, CX1123, CX1138 Lightcurves

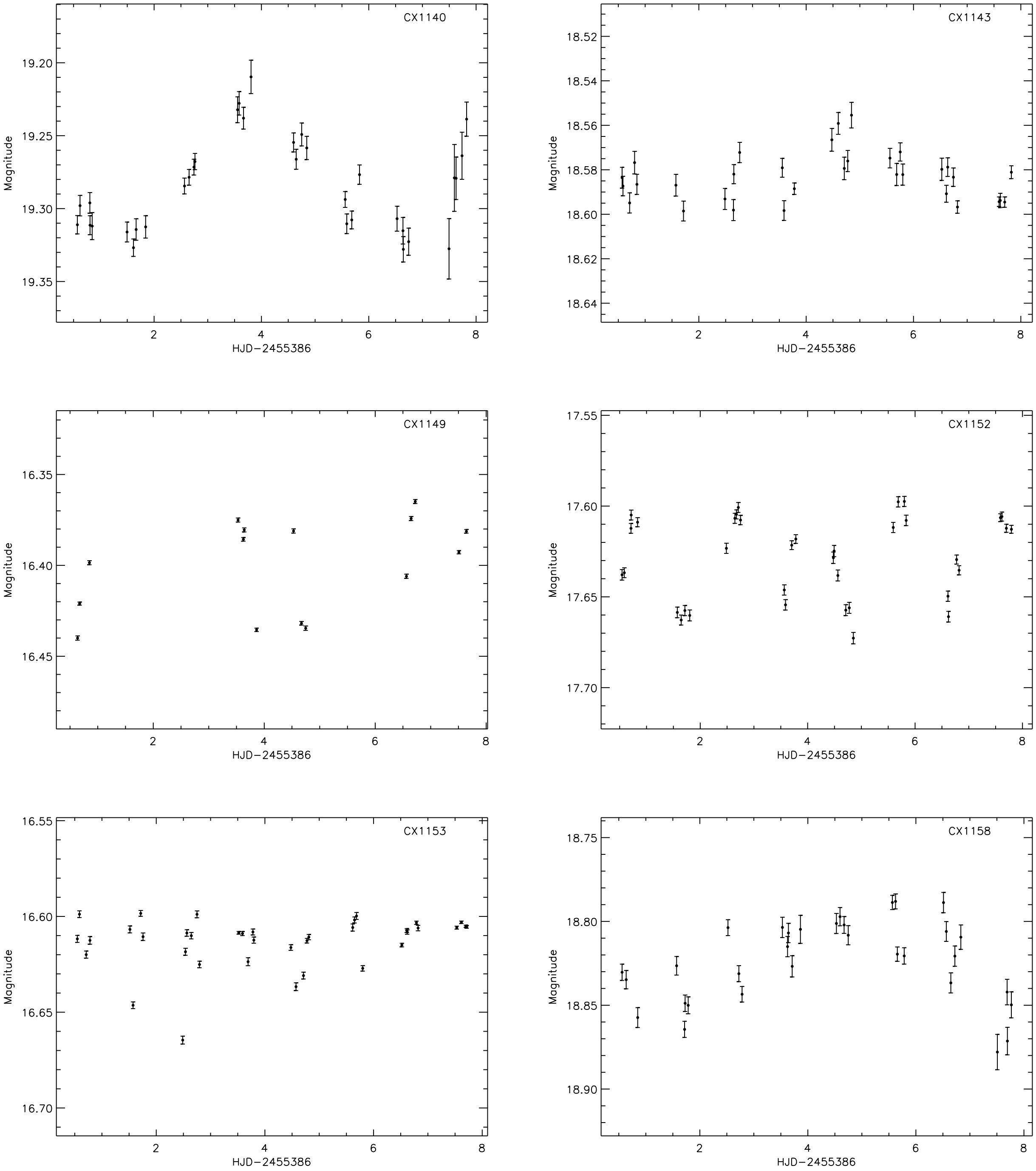

Figure A.21: CX1140, CX1143, CX1149, CX1152, CX1153, CX1158 Lightcurves

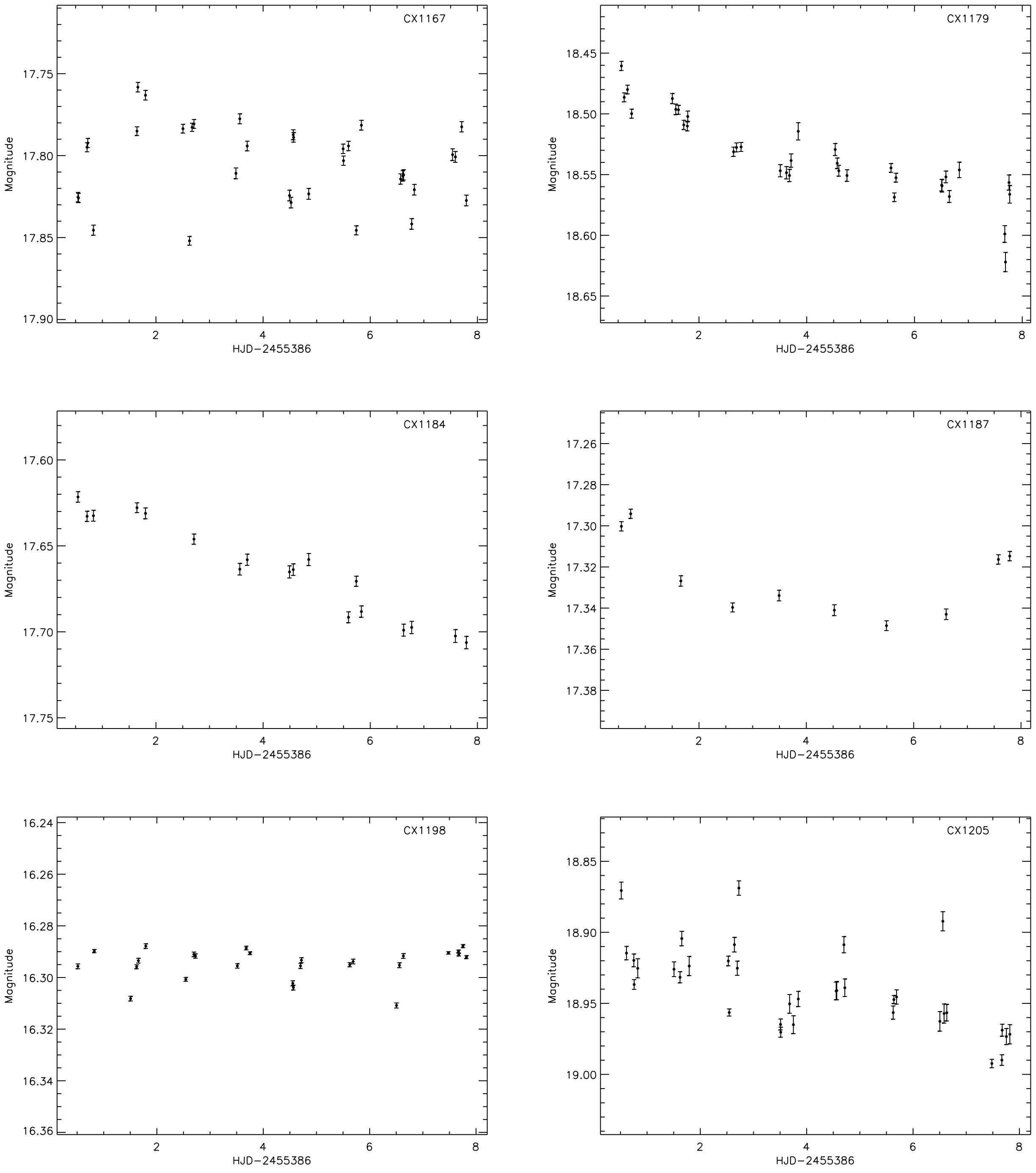

Figure A.22: CX1167, CX1179, CX1184, CX1187, CX1198, CX1205 Lightcurves

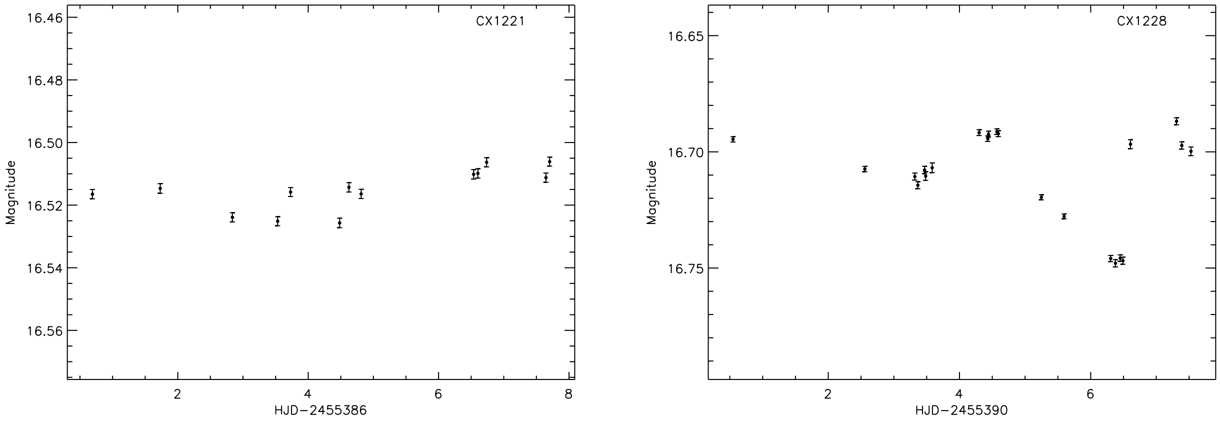

Figure A.23: CX1221, CX1228, Lightcurves

Appendix B: Permission to Reproduce Figures

B.1 Copyright Agreement with AAS

Reproduction of copyrighted materials The AAS is eager for the information published in its journals to reach the widest possible audience and it encourages the reuse of figures, tables, or other materials in review articles, textbooks, and other appropriate means of scholarly communication. To ensure the long-term access of the research community to its archives, the AAS holds the copyright on all copyrightable materials published in its journals, but the Society grants control of the right to reproduce the material to the original authors as long as they are alive.

B.2 Permission to use Figure 1.1

Hi Marc,

I'm a graduate student of Rob Hynes' at LSU writing my dissertation on optical variability of X-ray counterparts in the Galactic Bulge Survey, and I was wondering if I could reproduce Figure 6.3 (of the Roche potential) in my introductory chapter.

Cheers,

Chris Britt

Hi Britt,

Sure, no problem. I attached PS and PDF versions here. It would be cool if you would cite my thesis as a source (but then again, it's available under the Creative Commons licence on Wikipedia, though that's the bitmap version). If you have any questions, please let me know. Good luck with your thesis!

Cheers,

Marc.

Sent Thu, Jul 11, 2013 at 7:32 AM

B.3 Permission to use Figure 1.2

Hello Dr. Lattimer,

I am a graduate student at LSU writing my dissertation on optical variability of X-ray sources in the Galactic Bulge Survey, and I was wondering if I could reproduce figure 2 (on neutron star equations of state) from your 2007 paper with Maddapa Prakash published in Physical Reports, Volume 402, pg 109? I would like to use it in the introductory chapter of my dissertation to help build the narrative of why finding masses of neutron stars is important.

Cheers,

Chris Britt

Dear Christopher,

Absolutely you may use this figure in your dissertation. I am glad you find it helpful.

James Lattimer

Sent Thu, Jul 11, 2013 at 12:59 AM

B.4 Permission to use Figure 1.4 & Figure 1.5

Hi Dr. O'Brien,

I am a graduate student of Rob Hynes' doing part of my dissertation work on echomapping Sco X-1. In collaboration with you, actually, though it hasn't moved anywhere in the last 3 years, which will hopefully change after I finish my dissertation and have time to write up what we have as a paper. I would like to include figures 1 and 2 from O'Brien, Horne, Hynes, et al. 2002, MNRAS, 334, 426 in my introduction to help show what echomapping is. They very much help to make the idea clearer.

Cheers,

Chris Britt

Dear Chris

Sure, no problem. Sorry for the delay in getting back to you, your original email must have arrived just as I went on vacation. Good luck with the dissertation writing!

Regards

Kieran

Sent Mon, Aug 19, 2013 at 10:49 AM

B.5 Permission to use Figure 1.6

Hello Dr. Church,

I am a graduate student at LSU doing part of my dissertation on echomapping the Z-source Sco X-1, and I would like to use figure 1 from your 2011 review of Z sources. ADS is down at the moment, but it appears on arXiv.org as 1110.1281v1 I would greatly like to use this figure in my introduction to Z-sources as it helps show the distinction between Sco-like and Cyg-like Z-sources, as well as being a good example of what the Z-diagram looks like.

Thanks for your time,

Chris Britt

Dear Chris,

You are very welcome to use the figure. If you would like the original (as it may be better quality) please let me know. It will be a qdp file.

Best wishes, Mike Church

Sent Thu, Jul 11, 2013 at 3:49 AM

B.6 Permission to use Figure 5.18

chrisbritt86@gmail.com to e.m.ratti@gmail.com

date: Fri, Aug 16, 2013 at 5:27 PM

Hi Eva,

I wanted to reuse the lightcurve for CX93 with the sine fit in your paper in my dissertation (cited, of course). Since you're the first author on the paper, is it alright with you if I use the figure?

Cheers,

Chris

Hi Chris,

Of course, go ahead!

Cheers

Eva

Sent Sat, Aug 17, 2013 at 8:55 AM

Vita

Christopher Tillman Britt was born in Louisville, Kentucky, in March 1986. He received a BS in Physics with a concentration in Astronomy and a minor in Mathematics from Louisiana State University in May 2008. He enrolled in the Graduate School of LSU in August of the same year. He earned his Master's degree in 2012, and expects to complete his doctoral degree in August 2013.